Investigation of the Role Nonadiabatic Energy Relaxation Plays in Excited State Intramolecular Proton Transfer using Multidimensional Electronic-Vibrational Spectroscopy

Jason William Sandwisch

A dissertation

submitted in partial fulfillment of the

requirements for the degree of

Doctor of Philosophy

University of Washington

2023

Reading Committee:

Munira Khalil, Chair

Anne B. McCoy

Cody W. Schlenker

Program Authorized to Offer Degree:

Chemistry

University of Washington

Abstract

Investigation of the Role Nonadiabatic Energy Relaxation Plays in Excited State Intramolecular Proton Transfer using Multidimensional Electronic-Vibrational Spectroscopy

Jason William Sandwisch

Chair of the Supervisory Committee:
Professor Munira Khalil
Chemistry

Understanding the important mechanisms involved in photoinduced energy transfer in molecular systems is key to unlocking more efficient energy harvesting systems. Under specific conditions, nonadiabatic energy transfer, energy transfer that directly couples the electronic motion to that of the molecular vibrations is applied to explain how a 12 femtosecond proton transfer event occurs in a photoexcited molecular system. In this dissertation, the role of nonadiabatic coupling and nonadiabatic energy transfer on photoinduced intramolecular proton transfer molecular systems is explored using a subset of third order Fourier Transform techniques, termed electron-vibrational (EV) spectroscopies. These spectroscopic techniques combine an ultrabroadband near-ultraviolet (BBnUV) pump laser pulse which spans 370-440 nm

and a broadband mid-infrared probe laser pulse which span the fingerprint molecular region (1200-1600 cm^{-1}) on a class of organic molecules that undergo ultrafast intramolecular tautomerization reactions in the excited electronic state. These complexes are termed as excited state intramolecular proton transfer (ESIPT) complexes, and prove to be excellent reporters of the impact of nonadiabatic coupling on ultrafast structural transformations in molecular systems. The work presented here will advance the understanding of how coupled electronic and vibrational motions dictate ultrafast excited state proton transfer reactions. Ultrafast EV spectroscopy proves to be a viable method to explore the unique coupling of the electronic and vibrational degrees of freedom in complex molecular systems. To gain the best chemical insight, technical and experimental advancements of the EV spectrometer are implemented and discussed. The theory and design of a self-diffraction and transient grating cross correlation frequency resolved optical gating (FROG) pulse characterization method is introduced to characterize the pulses in the EV spectrometer. The generation of a BBnUV pump pulse that is used in the multidimensional spectroscopy experiments is improved. Lastly, a shot-to-shot pump-pulse phase cycling scheme is introduced and programmed into the EV spectrometer, which leads to a statistically-defined characterization of the noise floor used in the experiments. With the aid of EV spectroscopy and the advancements above, direct experimental evidence that nonadiabatic energy relaxation and transfer contribute to ESIPT in 10-hydroxybenzo[h]quinoline (HBQ), and its deuterated analog (DBQ) are discovered.

TABLE OF CONTENTS

LIST OF FIGURES

LIST OF TABLES

ACKNOWLEDGEMENTS

"It takes a village to raise a doctor" as goes the saying, and in my experience, this is very true. The work of this dissertation did not occur within a vacuum and was impacted by so many close friends, colleagues, groupmates, and mentors. For everyone who has crossed paths with me in this journey I thank you.

Specifically, this work would not exist if it were not for the guidance, support, and insights of my advisor Munira Khalil. Since first stepping foot in your office during visitation weekend and learning the details of spectral diffusion to stepping into lab to help troubleshoot laser problems, I have constantly valued and appreciated all the support you have given me over the course of my graduate students. To (now) Professor James Gaynor, thank you for closing College Inn down with me that first night. Your love of spectroscopy, science, attention to detail and soccer is not lost on me. Thank you for imparting the proper guidance and methodology required to appease the laser gods and for helping me refine the skills necessary to effectively manage the spectrometer. I hope that the "top of the league" mentality will persist. To my peer and groupmate Dr. Rob Weakly thank you for sharing the journey though graduate school together and "asking all the dumb questions." I am a better scientist because of you and I have thoroughly appreciated all the beers, late nights, and discussions we've had over the years. To my cohort members aka the "Chem Bois," Dr. Diana Roh, Dr. Sarah Sweger, Dr. Rob Weakly and Dr. Ryan Dirisio thank you for all the emotional support, study sessions during first year, presentation practices, and scientific troubleshooting over the years. I am glad that we've all officially made it across the finish line!

To the rest of the Khalil Krew, Joel, Zach, Tyler, Chelsea, Megan, Doyk, Amke, William, Ben, Caroline, Casey, Zhaoyuan: thank you for all the discussions we've had over the years, thanks for letting me ask stupid questions, and thank you for asking and challenging my understandings of science, data, lasers, soccer and anything else that came up. Thank you for your patience and allowing me to ramble on for hours about whatever we were chatting about. It amazes me how lucky I was to be able to get to collaborate with you all and I can't wait to see what awesome things you all find yourselves working on in the future!

To all my soccer, kickball, softball, indoor soccer, and baseball teammates thank you for accepting me even though you may have had no idea what I was working on and for allowing me to develop my skillset and to share time together.

To all my friends and family, thank you for making Washington home. Hayden, Zak, Eric, Riley, Gregory, and so many others: Thank you for being patient with me, even though I have gone days without responding to text messages. Thank you for accepting me and continuing to reach out and get me out of the house.

To my wife Jill Fenno. I still don't think we understood how long six years to a PhD was but our time together has made me a better person. The past six years have been the hardest of my life but have also been the best because they happened with you. You have taught me the importance of rest and taking time and space for myself. My best ideas have come after a weekend in the woods and for that, I have you to thank. And, last but not least, thank you to Cory Fenno whose endless face kisses made me smile even when I was struggling the most.

DEDICATION

To the late Professor Kenneth Hedberg

Chapter 1. INTRODUCTION

"All of the sciences grow out of common sense. They grow from curiosity, observation, reflection and then the refinement of observation, the refinement of analysis and by exploring and pushing things a little further than in ordinary life. Making them a little more extreme and abstract. And in this novelty then there are usually surprises for us. We have to talk differently about what we find. We find opportunities for exploration, as with the telescope, which simply could not be imagined within the framework of a completely non-technical life. The old ways of talking get so cumbersome and inappropriate that we make a big change, and one recreates one's way of describing this part of nature. – J. Robert Oppenheimer (Colorado University, 1961)

1.1 A Classical Assumption Revised: Born-Oppenheimer Approximation

The discovery and dictation of quantum mechanics at the turn of the 19th century brought about a fundamental change to the way scientists, researchers and academics think about the world and our observations of it[1-3]. Quantum mechanics, which simply describes the motions of atoms, particles and molecules in terms of discrete steps, postulates that energy absorbed or emitted from atomic particles exists in discrete energy levels, or in other words, the energy transfer within atomic states is made up of quanta, or quantized energy levels. The discovery of quantum mechanics was revolutionary because the observations and methodology used to describe these phenomena exist outside our everyday life and on the human scale energy transfer exists practically speaking continuously or behaves as described by classical mechanics. As chemists, those interested in the energetic transfer within - *intramolecular,* or between – *intermolecular,* particles the two defined schools of thought have presented a challenge in the way energetics are described in molecular systems. For one, on a scale between subatomic particles, individual atoms, molecules, macromolecules, complete biological systems, organisms and collections of organisms, a chemist seeks to address the board answer to what scale is accurate to fully describe a molecular system by quantum

mechanics over classical mechanics? And armed with this insight, how molecular systems can best be studied, described and harnessed to develop a better understanding of the energetic interface and exchange occurring on the molecular scale.

Max Born and Robert Oppenheimer[4] were some of the first to grabble with these questions. What was known in the early days and more so today, is when describing quantized energy levels not all particles, or degrees of freedom are quantized on the same energy scale. For example, electrons which are subatomic particles, most likely to participate in chemical reactions, are about 1/2000 the mass of the next largest particle responsible for chemistry the proton. Atoms that make up molecules are compounds of electrons, protons and neutrons, each atom is described by the number of protons. The protons along with the neutrons make up the relatively heavy nucleus of an atom while the less massive electrons exist in space outside the nucleus. Given the vast energy differences between the nucleus and the electrons, the amount of energy required to excite the different particles within a molecular can be orders of magnitude different. So, what Born and Oppenheimer postulated and effectively described was given the energy differences between the electrons and nucleus, the motion of electrons, or the electronic degrees of freedom, can be thought to be separable from the motion of the atomic nuclei, or nuclear degrees of freedom. In other words, when describing the total chemical system of the system, the molecular Hamiltonian operator (H) can be written as a separable sum of the kinetic energy of the nuclei (T_n), the kinetic energy of the electron (T_e), and the potential energy of the system (V) which depends on the interatomic distances (R) and the electron-electron distance (r), or $H_{tot} = T_n + T_e + V(r, R)$. The basis of the Born-Oppenheimer approximation (BOA) falling out from the fact that when applying the Hamiltonian to the

electronic wavefunction ($H_{tot}\,\psi_{el}$) the cross terms such as the nuclear kinetic energy operating on the electronic wavefunction cancel ($T_n\,\psi_{el} = 0$).

The Born-Oppenheimer approximation (BOA) has been a core principle in chemistry since its inception and has become a fundament underpinning in many theoretical works to help simplify the solution of the electronic energy in a chemical system. Recently in practice this simplification and assumption is typically at work in density functional theory (DFT) and perturbation theory[5-9]. The result of which has allowed many novel physical phenomena to be predicted and observed especially within the confines of the electronic energy levels. Given that most chemistry that occurs in nature occurs through the exchange, motion, or transfer of electrons in a chemical system applying the BOA has helped predict the geometry of many molecular systems[10]. Therefore, from a conceptual practice the BOA reduces much of the complexities around the mathematic representations and theoretical descriptions surrounding the energetic transformations taking place within molecular and chemical reactions through the seperation of variables of electronic states and nuclear states. However, the complete application of the BOA leads to some glaring inaccuracies in quantum mechanics, specifically the expected transition energies, lineshapes and timescales of molecular transitions. Or when for example the kinetic energy of the nuclei approaches or directly interacts with the motion of the electrons, as is the case during rapid geometric changes and chemical reactions. During chemical reactions there exists a dependence between the nuclei and electrons that should be accounted for to accurately describe molecular systems, as the motion of the positively charged nuclei directly impacts the negatively charged electron positions as was suggested by Edward Condon[11]. For the initial theory, the application of the BOA is justified for simple molecules such as diatomic molecules where the experimental transitions energies don’t deviate

substantially with the theoretical application of the BOA. However, as the molecular systems of interest become more complex so too have the theoretical errors and models associated with the BOA. The complete theoretical and experimental understanding and description of which is at the forefront of the motivation of this experimental work.

Though the application of the BOA presents a useful fundamental description and model for the interpretation of the energetic landscape of a molecule by breaking down the total energy of molecular system by its independent components, when multiple states, whether electronic or nuclear state, how do the states interact with each other? Fundamental work by Edward Teller[12] first postulated the effects of how multiple electronic states can exist and couple together during a chemical reaction or after an electronic state was excited, either chemically or photoinduced. Teller's fundamental work postulated in polyatomic systems there can exist multiple electronic states, or transitions and these electronic states can become degenerate at some point along the potential energy surface. Upon the degenerate energy point, or crossing point, the two electronic states interact with each other, leading to an avoiding crossing, through which a molecule can jump to an electronic state with a different allowed geometry. The extent to which electronic state mixing is allowed results in conditions where the newly formed electronic state is said to be adiabatically mixed or in the adiabatic picture, whereas when the states are not mixed, they are said to be nonadiabatically mixed.

Additional work of Renner[13], Herzberg and Teller[14] began to discuss the impact of the coupling between nuclear and electronic degrees of freedom following photoexcitation in polyatomic systems. The Renner-Teller effect was one of the first descriptions of a triatomic system that went beyond the BOA, in essence describing a 3-atom system in terms of the couplings between the nuclear and electronic energy levels. By assuming nuclear exchange

with electronic energy does not cancel for exceeding larger polyatomic systems it was found that theoretical models can do much better job at describing the energy of molecular transition or system[15-17] however the direct experimental observations of molecular systems with strongly coupled states and transitions through a conical interaction were not available. Michael Baer[18] summarized the advancements in quantum theory during the intermediate period advancements from Longuet, Higgins, Herzberg and Berry[19-21] where various expansions and coupling terms were added under the BOA to account for preliminary experimental spectroscopic results that came out. However various theoretical treatments such as the adiabatic-to-diabatic transformation were founds to be inconsistent with experimental results[22]. To this end, experimental observations of strong nuclear and electronic coupling, and interactions through a conical intersection are necessary to provide evidence of the existing theoretical models for optical transitions.

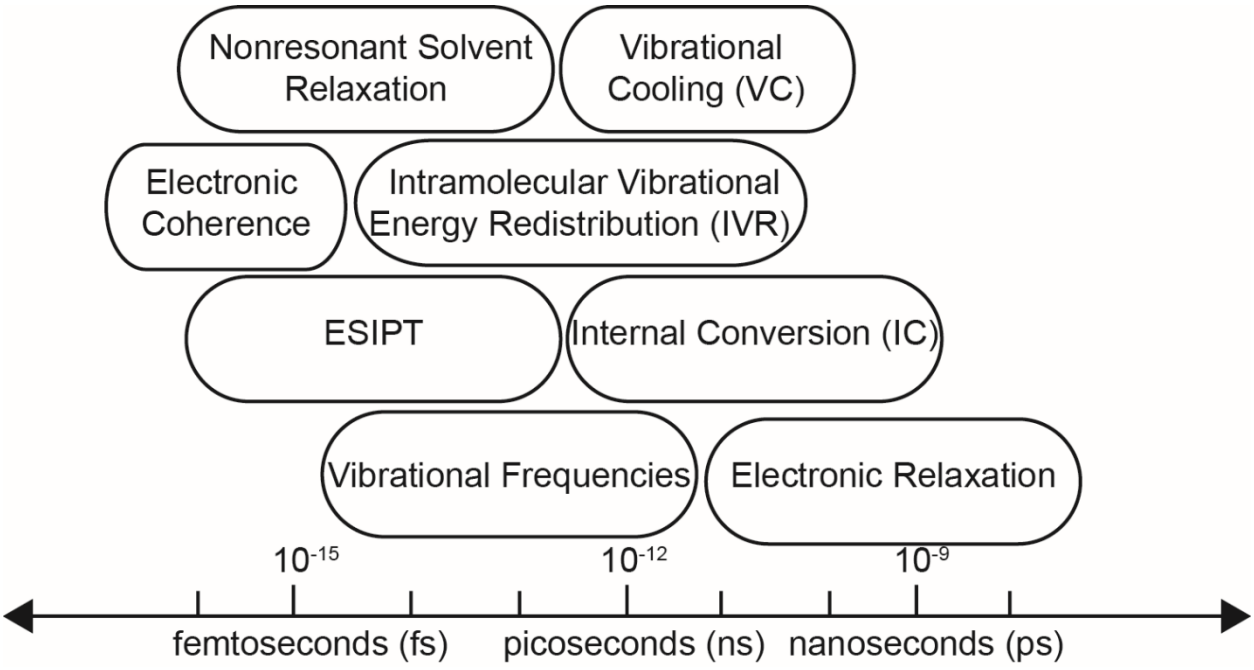

Figure 1-1. Relative timescales of ultrafast processing occurring in small molecules probed by ultrafast nonlinear spectroscopy, timescales adopted from May & Kuhn[23].

Accurate experimental observations that support or refute the applications of the BOA in quantum theory depend directly on the timescale of the observations being conducted. To adequately observe the breakdown of the BOA a proper experimental tool is needed which resolves the motion not only of the electronic degrees of freedom but also the nuclear degrees of freedom. Femtosecond (fs) laser nonlinear spectroscopy[24-28] has emerged in the recent decades, which combines a series of broadband short laser pulses that interact directly with a molecular system and provide experimental evidence of changes within the system as a series of difference spectra. Time-resolved nonlinear spectroscopy extends the experimental observables accessed by the technique to include spectroscopy changes as function a delay time, allowing the direct experimental observation of energetic and molecular structure changes as a result of the incident pump excitation pulse. Nonlinear spectroscopy has been utilized to experimentally determine rough timescales of electronic motion as well as vibrational rephasing and relaxation processes outlined in Figure 1-1. As illustrated, the timescales accessed have revealed various interfaces between electronic and nuclear motion in the femtosecond timescale and this timescale provides a window for the possible observation of non-BOA type systems and dynamics. As this thesis will show nonlinear spectroscopy provides a unique experimental handle for the experimentalist to observe changes occurring in a molecular system between the different nuclear and electronic degrees of freedom, which will provide experimental insight that can be used to expand on the theoretical framework of quantum mechanics.

1.2 EXCITED STATE INTRAMOLECULAR PROTON TRANSFER (ESIPT) – CHEMICAL REACTIONS IN THE EXCITED STATE

The BOA suggests that the nuclei and electronic motion do not exchange energy on a timescale sufficient for the nuclei to impact the electronic wavefunction and the corresponding molecular geometry. To test the validity of this approximation a molecular system and unique chemical phenomena which challenges the above postulate is needed. This thesis will focus on one such special case, excited state intramolecular proton transfer (ESIPT). ESIPT complexes exhibit a unique property where following photoinduced absorption of light, a concerted transfer of a proton and electron to separate reaction centers takes place[29-34]. ESIPT compounds exhibit large stoke shifts and typically contain strongly conjugated π-systems[35-38], the strong π-bonding weakens the hydrogen bond within the molecule while strengthening the electronic bonding, leading to a higher energy absorption in the near-UV and fluorescence in the near-IR spectral region. One such system that undergoes photoinduced ESIPT is 10-hydroxybenzo[h]quinoline (HBQ) shown in Figure 1-2. HBQ contains an exceptionally strong π-bonding system which includes the conjugation of the hydrogen bond, resulting in a very weak hydrogen bond coincidently this weak hydrogen bond is rapidly broken following photoexcitation of the electronic state with near-UV light (370-440 nm), HBQ undergoes sub-15 fs ESIPT, which corresponds to a single oscillatory period of the electronic ground state OH stretching mode, Figure 1-1.

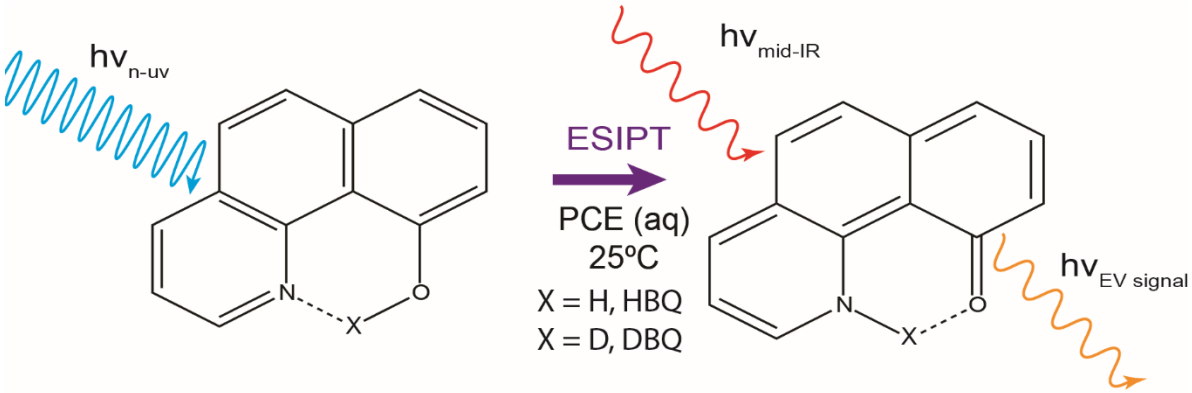

Figure 1-2.Schematic representation of ESIPT in 10-hydroxybenzo[h]quinoline (X =D) or its isotopic analog 10-duetrobenzo[h]quinoline (DBQ). Photoexcitation of a near-UV pulse leads to ESIPT in a nonpolar solvent tetrachloroethylene (PCE), following ESIPT EV spectroscopy is conducted using a broadband mid-IR probe pulse. The EV signal reports the change of the absorption of the probe dependent on the near-UV pump pulse.

The nonequilibrium change of the excited electronic state following ESIPT in HBQ has been extensively studied in prior work[39-47]. Time resolved fluorescence (TRF) experiments measured the rise of the large Stokes shift in the fluorescence signal with an onset time of ~13 fs[43] and showed spectrally shifted on 350 fs and 30 ps time scales[42]. These time constants were reported on the ESIPT growth of an S_2 keto* state, an internal conversion (IC) process from a closely lying S_2 keto* like state to the S_1 keto* and a solvent mediated vibrational cooling timescale, respectively. However, transient absorption experiments that primarily focus on electronic state dynamics only view what is occurring with the electronic state, which cast doubt on the assignment of the internal conversion pathway suggesting either non BO type energy transfer or other nuclear motion such as intramolecular vibrational relaxation (IVR) was taking place rapidly on the S_1 potential energy surface[41]. These observations were later supported by DFT computational work[47,48] however direct experimental evidence is lacking. Studies of the electronic potential energy surface have unlocked insights behind the overall ESIPT reaction mechanism and time scales of relaxation pathways in HBQ however a complete description of how the nuclear degrees of freedom impact the nonequilibrium relation pathways is needed to

drive a better understanding of how energy transfer occurs within the limits that the BOA breakdown. For instance, each of these studies assume the proton nuclei is solely responsible for the relaxation dynamics that are observed and are unable quantify how the excess kinetic energy from the ballistic proton motion modulates the relaxation dynamics[46]. Quantification of both the excess vibrational energy and kinetic energy in HBQ following ESIPT is required to fully map all reaction coordinates that govern the nonequilibrium dynamics in the excited state. These reaction coordinates may elucidate vibrational relaxation dynamics such as IVR which result from vibrational energy redistribution between vibrational modes and or show vibrational cooling (VC) processes are at play where excess energy from a hot vibrational level gets dissipated to lower vibrational energy levels. The work in this thesis will seek to address the questions of nuclear and electronic coupling and how nonadiabatic energy transfer process can impact assignments of energy transfer processes. This thesis will measure these phenomena with a novel time-resolved nonlinear spectroscopy technique geared to address these questions – Electronic-Vibrational Spectroscopy.

1.3 Measuring Excited state molecular dynamics of coupled electronic and vibrational degrees of freedom

Electronic-vibrational spectroscopy (EV) is an emerging third-order nonlinear, multidimensional Fourier transform (FT) spectroscopy technique that utilizes a sequence of optical and infrared femtosecond electromagnetic fields resonant with electronic and vibrational transitions in the system of interest. The resulting EV signal directly maps the extent of coupling between the vibrational and electronic degrees of freedom through vibronic coupling[49-53]. Illustrated in Figure 1-3 a 2D EV pulse sequence is a special third-order nonlinear spectroscopy method, in which 3 light matter interactions interact with a molecular system of interest in which

E_1 and E_2 are resonant with an electronic transition and E_3 and E_{sig} are resonant with a vibrational region of interest. In short EV spectroscopy measures the change in the vibrational coordinate, as a result of the resonant excitation of the electronic coordinate. If the vibrational coordinate is not impacted by the absorption of E_1 and E_2 then no change would be expected. Notable for third order spectroscopy techniques, the three pulses in the pulse sequence are separated by time delays, τ_1 and τ_2 which correspond to the pump pulse delay and the pump-probe delay times respectively, the work conducted in this thesis was conducted in the heterodyne pump-probe beam geometry where E_1 and E_2 are collinear with respect to each other and the signal pulse is governed by the probe resulting in a signal field that is geometrically on top the probe field. The interactions of the three incident electric fields and the signal field result in a four wave mixing process that is dependent on the geometric orientation of the incident electric fields. In the pump probe geometry, the signal and probe fields are spectrally dispersed using a monochromator and thus the probe-signal delay time, τ_3 is in practice zero in the cause of the heterodyne detection scheme.

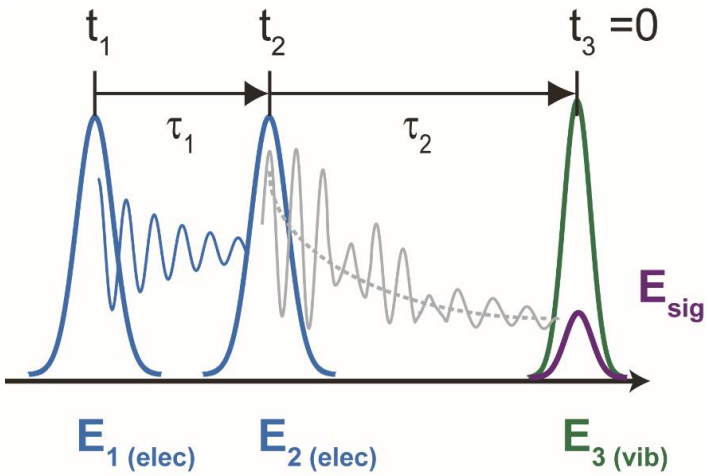

Figure 1-3. A cartoon diagram of a 2D EV heterodyne pulse sequence consisting of pump pulses (E_1 and E_2) which are resonantly excite the electronic coordinate and a probe pulse and signal pulse (E_3 and E_{sig}) which. The pump pulses are separated by the pump delay (τ1), with the typical pump-probe delay (τ_2) separating E_2 and E_3. The signal is spectrally dispersed using a spectrometer.

1.3.1 Linear or Nonlinear Spectroscopy

This thesis focuses on the experimental results and establishment of a high signal-to-noise 3D EV spectrometer, however linear spectroscopy is also used to characterize materials including systems that undergo ESIPT. As established, third order spectroscopy utilizes a series of three laser pulses to determine the change of a molecular system in some prepared state whereas linear spectroscopy characterizes a system through the use of a single laser pulse. Linear spectroscopy is a useful technique to characterize the ground state absorption profile of either the vibrational ground state or the electronic ground state through the use of Fourier transform infrared spectroscopy (FTIR) or near UV to visible (UV/vis) absorption spectroscopy. The main difference between the linear spectroscopy techniques is solely dependent on the frequency of light used in the experiment. Vibrational signatures report on the motion of nuclei within molecules and are resonantly excited around 100-4000 cm^{-1} depending on the vibrational mode of interest. Electronic absorption features on the other hand have a broad range of accessible spectroscopic signatures depending on whether the lowest energy transitions are of interest, high occupied molecular orbital to lowest unoccupied molecular orbital transitions (HOMO-LUMO) which occurs in the UV/VIS (12000- 30000 cm^{-1}) or other higher energy transitions are of interest such as core electronic excitation which can occur in the deep X-ray region. The vast difference in energy scales between the electronic and vibrational transitions is observed in linear spectroscopy. The presence of strongly coupled vibrations can be observed when splitting in a linear spectrum is observed, specifically the absorption of additional vibrational quanta across the HOMO-LUMO transition as represented in Figure 1-4. The additional quanta of excess

vibrational energy is represented by the Franck-Condon progression in the electronic excited state and can help identify the anharmonicity of the excited state[54,55].

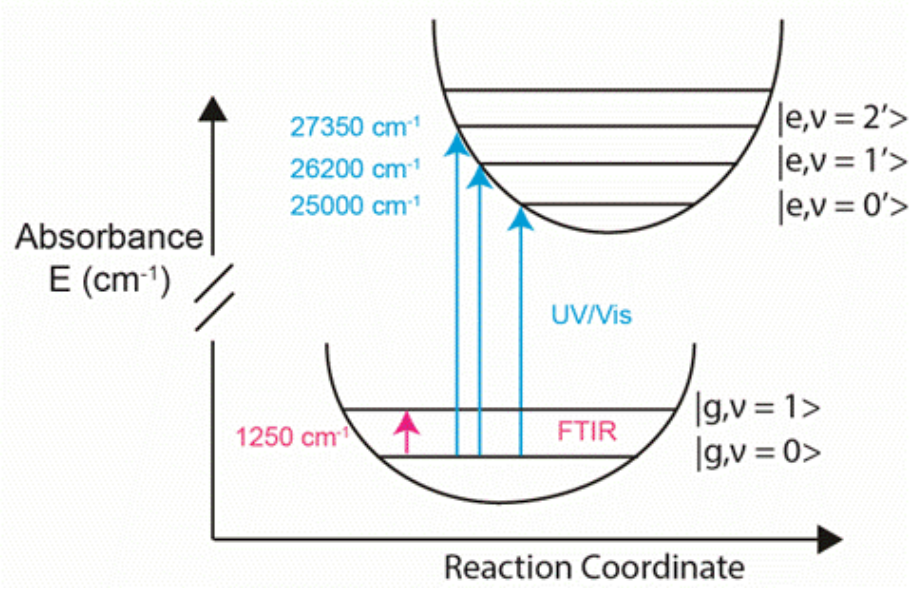

Figure 1-4. A cartoon diagram potential energy landscape probed by linear spectroscopy of a two electronic state system coupled to one vibrational mode. FTIR probes the ground state vibrational spectroscopy and reports a resonant transition of 1250 cm^{-1} in the ground electronic state. UV/Vis probes the absorption across the HOMO-LUMO transition and for strongly coupled vibrational modes maps the additional energy absorption of a coupled vibrational mode, here the addition of 1200 cm^{-1} corresponds to the addition of one quanta of energy in the vibrational mode and reports on the anharmonicity of the excited electronic state potential energy surface.

1.3.2 Pump Probe Spectroscopy – 1D EV

Linear spectroscopy provides insight behind the possible resonant transitions that can be accessed by third order spectroscopy however given the single light matter interaction and absorption pathway linear spectroscopy is limited to the dynamical information the technique can provide. In other words, the possible initial transitions are presented by linear spectroscopy but there is no time resolution of the technique. Third order spectroscopy bridges this gap and allows the experimentalist access to structural changes that occur as a function of delay time. For EV spectroscopy the simplest third experiment is 1D EV where τ_1 is held at zero and τ_2 is varied

therefore the dependent variables are solely the incident electric fields of the pump and probe and the delay time between the two. 1D EV on its own is a powerful technique, and provides a difference spectra in the IR spectral region and reveals differences in quanta of excess vibrational energy. Since the nuclear motion is encoded by the vibrational motion, the 1D EV difference spectra provide a snapshot of the effect the electronic excitation had on the nuclei and how the structure of the system changes and changed as a result. Understanding the structure of the molecular system as the system relaxes is at the core of what 1D EV attempts to experimentally provide. However, this simplicity results in only the inference of how the electronic and vibrational degrees of freedom are coupled together. To access the full picture of how energy is being transferred and coupled between the electronic and vibrational degrees of freedoms the third order experiment needed to be explained to account of the pump pulse delay time.

1.3.3 Multidimensional Spectroscopy – 2D and 3D EV

Fourier transform multidimensional experiments are an extension of the 1D experiments presented earlier and extend the spectral content from a difference spectrum to a 2D correlation map as shown in Figure 1-5. The correlation map extends the 1D spectra which reports solely on the change of the probed frequency region ω_3, to the excitation region by FT across all the pump pulse delay times. The FT across ω_1 couple each vibrational mode probed in ω_3 to the excitation frequency axis allowing the direct experimental determination of nonadiabatic energy transfer processes.

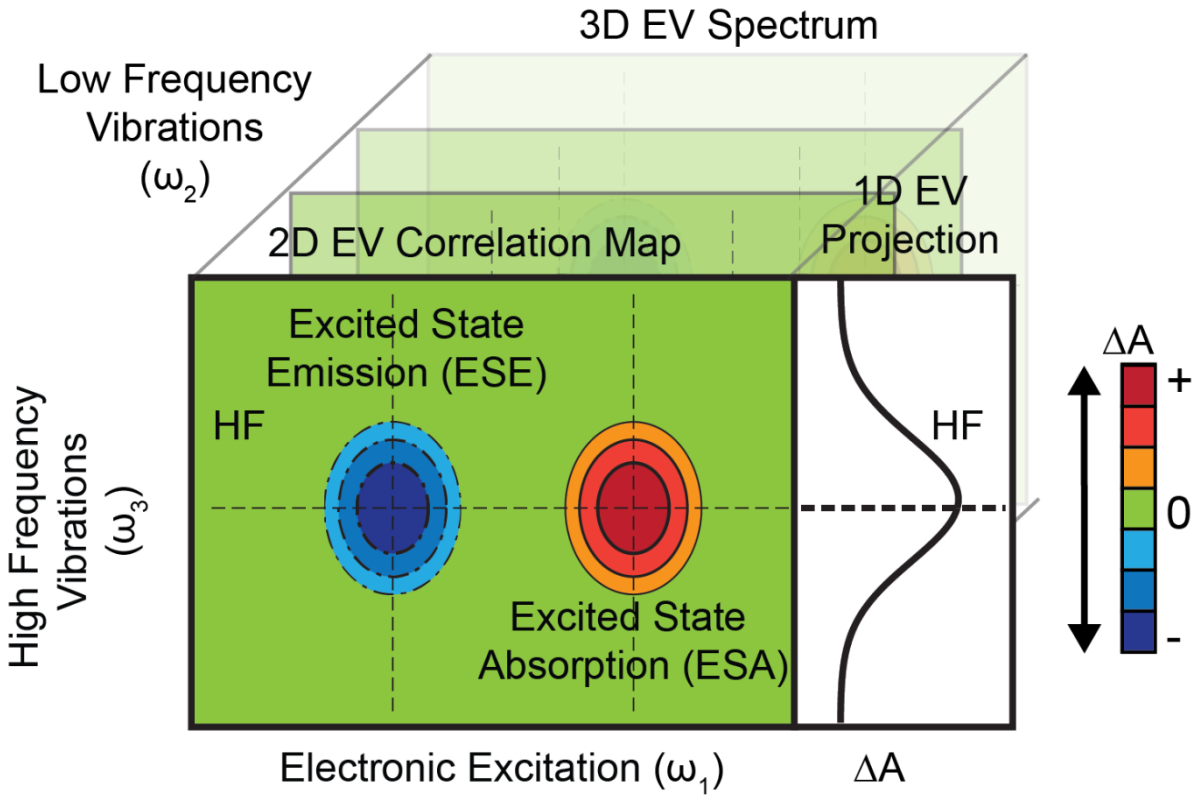

Figure 1-5. A cartoon 2D EV spectrum obtained by Fourier transforming along the time delay (τ_1) and spectrally dispersing the probe pulse ($\omega 3$). The 2D EV spectrum directly maps the correlations between the electronic transitions which lie within the bandwidth of the pump pulse of the vibrational modes resonant with the mid-IR probe. The projection across the electronic excitation axis is equivalent to a 1D EV spectrum. The 3D EV spectrum is obtained by Fourier transforming each 2D EV signal across a range of pump-probe delay times (τ_2) to obtain the ω_2 axis. The resulting data matrix reveals all the vibrations that are coupled to each other through the electronic excitation characteristics revealing the excited state IVR processes present in a molecular system.

Figure 1-5 shows the connection between 1D EV and 2D EV spectroscopy, a 3D EV spectrum is an extension of the ω_1-ω_3 correlation map into a 3rd dimension of the pump probe waiting time, τ_2. Correlations in ω_1 and ω_2 reveal how vibrational energy is transferred following the initial photoexcitation of the electronic transition. Understanding how vibrational energy transfer impacts the nonequilibrium relaxation pathways allows a direct experimental observable what happens during points along a potential energy surface where the BOA breaks down. Particularly if a negatively going excited state emission (ESE) pathway is revealed in a 2D EV

spectrum. ESE pathways have yet to be fully explained in the theoretical framework of EV spectroscopy as their presence indicates that electronic-vibrational energy transfer has occurring during the pump pulse delay time, the phenomenon of course not being allowing under the BOA. Additionally vibrational energy transfer during the pump pulse delay time can lead to anharmonic coupling between vibrations in an electronic excited state. IVR and VC processes would therefore be expected to be present and coherence transfer in ω_2 may reveal the specific vibrational energy redistribution taking place.

1.4 Dissertation Outline

In this thesis I present experimental and computation evidence of nonadiabatic energy transfer in a model ESIPT complex using EV spectroscopy. Chapter 2 of this work presents the optical and experimental advancements that I've made on the EV spectrometer to collect high signal-to-noise 3D EV spectra and the implementation of pulse characterization methods needed to support the claims made throughout this work. In chapter 3 I present the nonequilibrium relaxation model study of 10-hydroxy[h]benzoquinoline (HBQ), and its deuterated analog 10-(D)-hydroxy[h]benzoquinoline (DBQ) using 1D EV spectroscopy, which suggest that anharmonicity in the excited electronic state leads to excess vibrational energy participating in the IVR and VC on characteristic timescales. In chapter 4, the work from chapter 3 is expanded and a 2D EV and 3D EV study of HBQ is conducted to fully map the IVR pathways present following ESIPT. In chapter 4, I provide direct experimental evidence of nonadiabatic energy transfer taking place during the ESIPT in HBQ and reveal vibronic energy transfer results during ESIPT.

1.5 REFERENCES

1 Cohen-Tannoudji, C., Diu, B. & Laloë, F. *Quantum mechanics*. 2nd edn, (Wiley Hermann, 1977).

2 Townsend, J. S. *A modern approach to quantum mechanics*. 2nd edn, (University Science Books, 2012).

3 Albery, F. R. H. *Quantum Mechanics and Path Integrals*. (Dover Publications, 2010).

4 Born, M. & Oppenheimer, R. Zur Quantentheorie der Molekeln. *Annalen der Physik* **389**, 457-484 (1927). https://doi.org:https://doi.org/10.1002/andp.19273892002

5 Schnappinger, T., Jadoun, D., Gudem, M. & Kowalewski, M. Time-resolved X-ray and XUV based spectroscopic methods for nonadiabatic processes in photochemistry. *Chemical Communications* **58**, 12763-12781 (2022). https://doi.org:10.1039/d2cc04875b

6 Gaussian 09 (Gaussian, Inc., Wallingford, CT, USA, 2009).

7 Oliver, T. A., Lewis, N. H. & Fleming, G. R. Correlating the motion of electrons and nuclei with two-dimensional electronic-vibrational spectroscopy. *Proc Natl Acad Sci U S A* **111**, 10061-10066 (2014). https://doi.org:10.1073/pnas.1409207111

8 Yoneda, Y. *et al.* Electron-nuclear dynamics accompanying proton- coupled electron transfer. *Submitted* (2020).

9 Tiwari, V., Peters, W. K. & Jonas, D. M. Electronic energy transfer through non-adiabatic vibrational-electronic resonance. I. Theory for a dimer. *Journal of Chemical Physics* **147** (2017). https://doi.org:10.1063/1.5005835

10 Gross, L., Mohn, F., Moll, N., Liljeroth, P. & Meyer, G. The chemical structure of a molecule resolved by atomic force microscopy. *Science* **325**, 1110-1114 (2009). https://doi.org:10.1126/science.1176210

11 Condon, E. U. Nuclear Motions Associated with Electron Transitions in Diatomic Molecules. *Physical Review* **32**, 858-872 (1928). https://doi.org:10.1103/PhysRev.32.858

12 Teller, E. The Crossing of Potential Surfaces. *The Journal of Physical Chemistry* **41**, 109-116 (1937). https://doi.org:10.1021/j150379a010

13 Renner, R. Zur Theorie der Wechselwirkung zwischen Elektronen- und Kernbewegung bei dreiatomigen, stabförmigen Molekülen. *Zeitschrift für Physik* **92**, 172-193 (1934). https://doi.org:10.1007/BF01350054

14 Herzberg, G. & Teller, E. Schwingungsstruktur der Elektronenübergänge bei mehratomigen Molekülen. *Zeitschrift für Physikalische Chemie* **21B**, 410-446 (1933). https://doi.org:doi:10.1515/zpch-1933-2136

15 Baer, M. Introduction to the Theory of Electronic Non-Abiabatic Coupling terms in Molecular Systems. *Physics Reports* **358**, 75-142 (2002).

16 Mead, C. A. & Truhlar, D. G. On the determination of Born–Oppenheimer nuclear motion wave functions including complications due to conical intersections and identical nuclei. *The Journal of Chemical Physics* **70**, 2284-2296 (1979). https://doi.org:10.1063/1.437734

17 Yarkony, D. R. Conical Intersections: Diabolical and Often Misunderstood. *Accounts of Chemical Research* **31**, 511-518 (1998). https://doi.org:10.1021/ar970113w

18 Baer, M. Introduction to the theory of electronic non-adiabatic coupling terms in molecular systems. *Physics reports* **358**, 75-142 (2002). https://doi.org:10.1016/S0370-1573(01)00052-7

19 Berry, C. L., Nickols, C. & Swettenham, K. V. Transplacental Carcinogenesis with Radioactive Phosphorus: The Effects of Promoting Agents. *Human Toxicology* **3**, 45-50 (1984). https://doi.org:10.1177/096032718400300106l

20 Herzberg, G. & Longuet-Higgins, H. C. Intersection of potential energy surfaces in polyatomic molecules. *Discussions of the Faraday Society* **35**, 77 (1963). https://doi.org:10.1039/df9633500077

21 Longuet-Higgins, H. C. & Van Der Waals, J. H. Editorial. *Molecular Physics* **1**, 1-null (1958). https://doi.org:10.1080/00268975800100011

22 Hobey, W. D. & McLachlan, A. D. Dynamical Jahn-Teller Effect in Hydrocarbon Radicals. *The Journal of chemical physics* **33**, 1695-1703 (1960). https://doi.org:10.1063/1.1731485

23 May, V. & Kühn, O. *Charge and energy transfer dynamics in molecular systems*. 3rd, rev. and enl. edn, (Wiley-VCH, 2011).

24 Siegman, A. E. *Lasers*. (University Science Books, 1986).

25 Mukamel, S. *Principles of nonlinear optical spectroscopy*. (Oxford University Press, 1995).

26 Boyd, R. W. *Nonlinear optics*. 2nd edn, (Academic Press, 2003).

27 Tokmakoff, A. Time-Dependent Quantum Mechanics and Spectroscopy. *Lecture*, 272-272 (2014).

28 Vengris, M. Introduction to time-resolved spectroscopy. (2014).

29 Chou, P. T. & Wei, C. Y. Photophysics of 10-hydroxybenzo[h]quinoline in aqueous solution. *Journal of Physical Chemistry* **100**, 17059-17066 (1996). https://doi.org:10.1021/jp961368e

30 Chang, D. W., Kim, S., Park, S. Y., Yu, H. & Jang, D. J. Excited-state intramolecular proton transfer via a preexisting hydrogen bond in semirigid polyquinoline. *Macromolecules* **33**, 7223-7225 (2000). https://doi.org:10.1021/ma000126g

31 Lochbrunner, S., Wurzer, A. J. & Riedle, E. Ultrafast excited-state proton transfer and subsequent coherent skeletal motion of 2-(2′-hydroxyphenyl)benzothiazole. *Journal of Chemical Physics* **112**, 10699-10702 (2000). https://doi.org:10.1063/1.481711

32 K. Stock, T. B., and S. Lochbrunner Proton transfer and internal conversion of o-hydroxybenzaldehyde: coherent versus statistical excited-state dynamics. *Chem. Phys. Lett.* **354**, 7 (2002).

33 Hammes-Schiffer, S. & Soudackov, A. V. Proton-coupled electron transfer in solution, proteins, and electrochemistry. *Journal of Physical Chemistry B* **112**, 14108-14123 (2008). https://doi.org:10.1021/jp805876e

34 Weinberg, D. R. *et al.* Proton-Coupled Electron Transfer. (2012).

35 Mohammed, O. F., Luber, S., Batista, V. S. & Nibbering, E. T. J. Ultrafast branching of reaction pathways in 2-(2′-hydroxyphenyl) benzothiazole in polar acetonitrile solution. *Journal of Physical Chemistry A* **115**, 7550-7558 (2011). https://doi.org:10.1021/jp202277t

36 Mohammed, O. F., Xiao, D., Batista, V. S. & Nibbering, E. T. J. Excited-state intramolecular hydrogen transfer (ESIHT) of 1,8-Dihydroxy-9,10-anthraquinone (DHAQ) characterized by ultrafast electronic and vibrational spectroscopy and computational modeling. *Journal of Physical Chemistry A* **118**, 3090-3099 (2014). https://doi.org:10.1021/jp501612f

37 Barry, B. A. Reaction dynamics and proton coupled electron transfer: Studies of tyrosine-based charge transfer in natural and biomimetic systems. *Biochimica et Biophysica Acta - Bioenergetics* **1847**, 46-54 (2015). https://doi.org:10.1016/j.bbabio.2014.09.003

38 Dahal, D. *et al.* An NIR-emitting lysosome-targeting probe with large Stokes shift via coupling cyanine and excited-state intramolecular proton transfer. *Chemical Communications* **53**, 3697-3700 (2017). https://doi.org:10.1039/c7cc00700k

39 Chou, P.-t., Chen, Y.-c., Yu, W.-s., Chou, Y.-h. & Wei, C.-y. Excited-State Intramolecular Proton Transfer in 10-Hydroxybenzo [h] quinoline. **4500**, 1731-1740 (2001). https://doi.org:10.1021/jp002942w

40 Takeuchi, S. & Tahara, T. Coherent nuclear wavepacket motions in ultrafast excited-state intramolecular proton transfer: Sub-30-fs resolved pump-probe absorption spectroscopy of 10-hydroxybenzo[h]quinoline in solution. *Journal of Physical Chemistry A* **109**, 10199-10207 (2005). https://doi.org:10.1021/jp0519013

41 Tahara, T., Takeuchi, S. & Ishii, K. Observation of nuclear wavepacket motion of reacting excited states in solution. *Journal of the Chinese Chemical Society* **53**, 181-189 (2006). https://doi.org:10.1002/jccs.200600020

42 Kim, C. H. & Joo, T. Coherent excited state intramolecular proton transfer probed by time-resolved fluorescence. *Physical Chemistry Chemical Physics* **11**, 10266-10269 (2009). https://doi.org:10.1039/b915768a

43 Lee, J., Kim, C. H. & Joo, T. Active role of proton in excited state intramolecular proton transfer reaction. *Journal of Physical Chemistry A* **117**, 1400-1405 (2013). https://doi.org:10.1021/jp311884b

44 Hristova, S. *et al.* 10-Hydroxybenzo[h]quinoline: Switching between single- and double-well proton transfer through structural modifications. *RSC Advances* **5**, 102495-102507 (2015). https://doi.org:10.1039/c5ra20057a

45 Marciniak, H. *et al.* Dynamics of excited state proton transfer in nitro substituted 10-hydroxybenzo[h]quinolines. *Phys. Chem. Chem. Phys.* **19**, 26621-26629 (2017). https://doi.org:10.1039/C7CP04476C

46 Kim, J. W. *et al.* Non-Born-Oppenheimer Molecular Dynamics Observed by Coherent Nuclear Wave Packets. *Journal of Physical Chemistry Letters* **11**, 755-761 (2020). https://doi.org:10.1021/acs.jpclett.9b03488

47 Picconi, D. Nonadiabatic quantum dynamics of the coherent excited state intramolecular proton transfer of 10-hydroxybenzo[h]quinoline. *Photochem Photobiol Sci* **20**, 1455-1473 (2021). https://doi.org:10.1007/s43630-021-00112-z

48 Chansen, W. *et al.* Theoretical study on influence of geometry controlling over the excited-state intramolecular proton transfer of 10-hydroxybenzo[h]quinoline and its derivatives. *Computational and Theoretical Chemistry* **1113**, 42-51 (2017). https://doi.org:10.1016/j.comptc.2017.05.008

49 Gaynor, J. D., Sandwisch, J. & Khalil, M. Vibronic coherence evolution in multidimensional ultrafast photochemical processes. *Nature Communications* **10**, 5621-5621 (2019). https://doi.org:10.1038/s41467-019-13503-9

50 Gaynor, J. D. & Khalil, M. Signatures of vibronic coupling in two-dimensional electronic-vibrational and vibrational-electronic spectroscopies. *The Journal of Chemical Physics* **147**, 094202 (2017). https://doi.org:10.1063/1.4991745

51 Cho, M. & Fleming, G. R. Two-Dimensional Electronic − Vibrational Spectroscopy Reveals Cross-Correlation between Solvation Dynamics and Vibrational Spectral Di ff usion. (2020). https://doi.org:10.1021/acs.jpcb.0c08959

52 Gaynor, J. D., Weakly, R. B. & Khalil, M. Multimode two-dimensional vibronic spectroscopy. I. Orientational response and polarization-selectivity. *The Journal of Chemical Physics* **154**, 184201 (2021). https://doi.org:10.1063/5.0047724

53 Weakly, R. B., Gaynor, J. D. & Khalil, M. Multimode two-dimensional vibronic spectroscopy. II. Simulating and extracting vibronic coupling parameters from polarization-selective spectra. *The Journal of Chemical Physics* **154**, 184202 (2021). https://doi.org:10.1063/5.0047727

54 Luis, J. M., Bishop, D. M. & Kirtman, B. A different approach for calculating Franck-Condon factors including anharmonicity. *J Chem Phys* **120**, 813-822 (2004). https://doi.org:10.1063/1.1630566

55 Atkins, P. W. & De Paula, J. *Physical chemistry for the life sciences*. 2nd edn, (W.H. Freeman and Co. ;
Oxford University Press, 2011).

Chapter 2. DEVELOPMENT OF A HIGH SIGNAL-TO-NOISE 3D EV SPECTROMETER

The investigation of nonadiabatic energy transfer and vibronic coupling in organic systems requires the use of high signal-to-noise 3D EV spectrometer. In the following chapter the signal-to-noise of experiments conducted on organic ESIPT compounds will be quantified and shown to asymptotically approach the noise floor after collecting 1500 laser shots and will be shown to be about 1 mOD. The noise levels will be used to determine the relevant signal pathways and nonadiabatic energy transfer mechanism to a high degree of experimental certainty. To achieve high signal to noise ratios the implementation of proper experimental and pulse schemes including the generation of high powered BBnUV pump pulses, the characterization of pulses used and the implementation of pump pulse pair phase cycling as well as the implementation of a novel data collection scheme. The improvements, design and theory of which are presented in the chapter below.

2.1 AN EXPERIMENTALIST APPROACH TO MEASURING WEAK VIBRONIC SIGNALS

Implementation and experimental collection of multidimensional EV spectra has only recently been possible due in part to the technological advancement[1-6] and availability of commercially chirp pulse amplification[7-9] laser systems, advanced optics and optical coatings that are able to withstand the high peak powers resulting from these laser systems and most importantly the advancement in acousto-optic programmable dispersive filters (AOPDF) pulse shapers[9,10]. Pulse shaper allow the ability to generate phase stable pump pulse pairs which are necessary for the implementation of multidimensional spectroscopy[1,11,12], especially for use of multidimensional spectroscopy in the nUV spectral region. Furthermore, given the nature of the

weak signals generated in a third order multidimensional spectroscopy experiment resulting from a four wave mixing process (FWM) the signals induce are inherently very low, some being on the order of 1-2 μOD. Given the low signal to noise, the development of a 3D EV spectrometer with high signal-to-noise ratios is crucial.

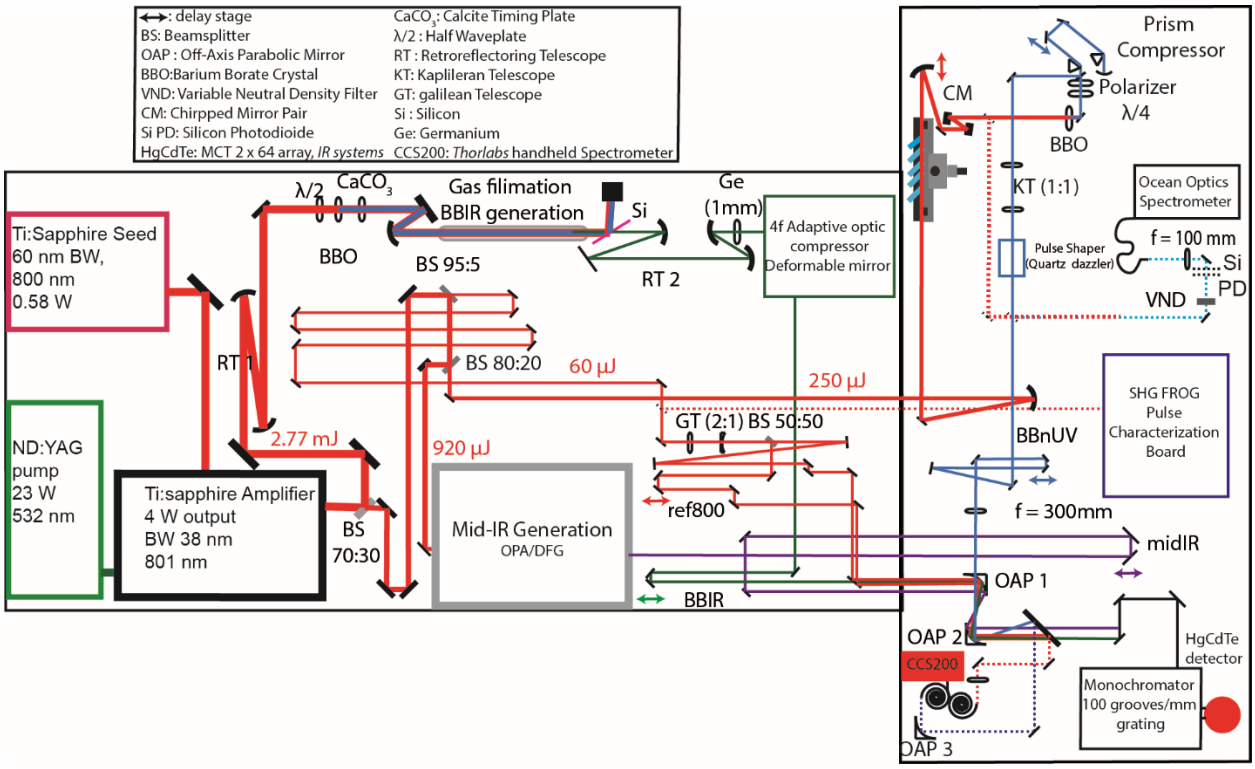

Figure 2-1. EV spectrometer experimental layout. A high power Ti:Sapphire regenerative amplifier (800 nm, 38 fs, 3.6-4.0 W, 1 kHz) laser system feeds 4 beam lines that are routed to the sample area. Two Mid-IR generation lines are routed to the sample area, a reference line and a BBnUV generation line. Various pulse characterization schemes and detectors are used to collect spectral, phase and temporal information about the generated laser pulses throughout the table. The generated Mid-IR laser pulses are detected using a 2 x 64 channel HgCdTe detector which is used to collect the EV signals of interest.

Laser technology has expanded tremendously over the past few decades in part to advancements in materials with higher damage thresholds, clean room manufacturing practices, and the development of new laser crystals. Ideally identical pulses, with identical powers, widths and shapes should be used in any photoinduced process to aid in the minimization of noise. In practice, the best noise floor that can be experimentally measured is the noise included by the

fluctuations of the laser power, spectrum, and beam shape resulting in some instrumental noise floor. In other words, increasing signal-to-noise ratios first comes from checking that the EV spectrometer is properly aligned and generating stable pulses on a shot-to-shot basis. Figure 2-1 shows a generalize schematic of the EV spectrometer used in this dissertation[13-17]. The diagram is roughly drawn to scale as laid out in the laboratory, note some items or beam lines could have been slightly changed from this writing. In general, the EV spectrometer is composed a chirped pulse amplification (CPA) laser system comprised of 3 components a Ti:Sapphire seed laser (60 nm BW, 800 nm, 0.48-0.58 W, 80 Mhz), a high powered Nd:YAG pump laser (19-20 W, 532 nm, CW), and a CPA based *Spectra-Physic* Spitfire XP Pro Ti:Sapphire regenerative amplifier (800 nm, 38 fs, 3.6-4.0 W, 1 kHz) which feeds 4 separate beam lines, 4 pulse characterization setups, a sample area, *Triax* Monochromator with 3 gratings, an *IR systems* 2 x 64 channel HgCdTe (mercury cadmium telluride, MCT) array detector, an high resolution (0.035 nm) near ultraviolet (355-445 nm, nUV) *Ocean Optics* spectrometer (*HR2000+*), and a *Thorlabs* spectrometer (0.2204 nm, 200-1100 nm, CCS200). Here performance ranges are listed for the laser system as over time the laser system degrades, a weekly catalog of laser performance is recorded to track laser system degradation, to regain optimal performance; translation of the seed Ti:Sapphire crystal should be performed every 9-12 months, power measurements of the pump laser should be performed monthly, if output drops below 19 W the output of the pump laser should be increased via the current output of pump on the system GUI. General alignment of the regenerative amplifier should be performed anytime the seed laser is turned off. To ensure longevity of the seed and amplifier semi-annual cleaning of the chillers and changing of the purge filter should be performed. Lastly, recording the uncompressed and compressed amplifier output should be performed to ensure the compressor grating is not misaligned or damaged. Over

time the compressor grating damage threshold can be exceeded causing distortions of the beam mode which can impact the performance of the beamlines. Optimal performance of EV spectrometer is directly tied to the performance and stability of the upstream laser output, if the system is not optimized additional experimental errors and instrumental noise are inevitable. Aside from power and qualitative beam mode analysis, the comparison of the seed spectrum with the CCS200 spectrometer can be used to assess whether crystal translation is needed. Furthermore, various Frequency Resolved Optical Gating (FROG) pulse characterization setups are included on the table to measure the phase and temporal duration of the reference line. Characterization of the reference beam line should be carried out after the seed laser is turned off to ensure the upstream laser output is compressed optimally.

Following optimization of the regenerative amplifier and quantification of the reference beam line, alignment of the mid-IR beam line to be used should be carried out. In this thesis a mid-IR probe that is generated from a collinear optical parametric amplification process followed by difference frequency generation (OPA/DFG) is used to span the 1200-1600 cm^{-1} fingerprint region of the IR spectrum[18]. For information regarding the broadband IR line (BBIR) see previous work[19,20], the BBIR line will not be further discussed in this work. The proper alignment of the OPA is critical to generate stable mid-IR pulses, of interest is the shot-to-shot stability of the mid-IR. Figure 2-2 shows an illustration of two mid-IR pulse trains as recorded by an oscilloscope, as shown two similar power pulse trains can result in drastically different shot-to-shot stability. In practice the stability of the mid-IR as generated from the OPA/DFG is dependent on the stability of the white light supercontinuum (WL) that is generated in the OPA process, therefore the compression of the upstream regenerative amplifier is set to achieve

optimal pulse compression of the WL, this setting is conducted before the alignment of the pump laser is done.

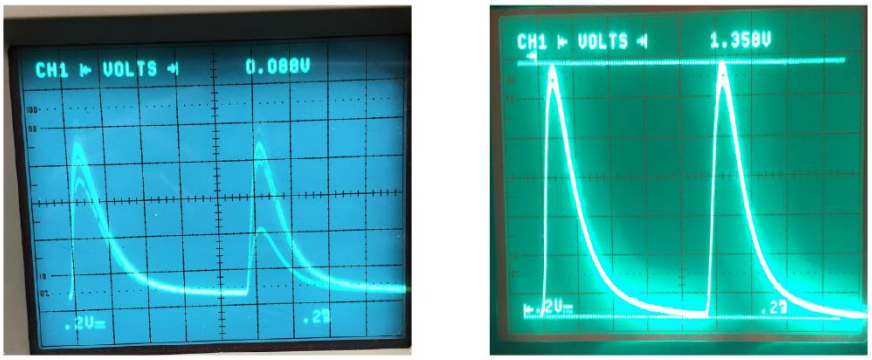

Figure 2-2. Mid-IR output from OPA/DFG generation, laser pulse stability as measured on an oscilloscope. Two measurement conditions read out similar power outputs on a detector plugged into a lock-in amplifier. Given the 100 MHz oscilloscope sensitivity the shot-to-shot instability is clearly observed in the left panel where there is less shot-to-shot noise in the right panel. Using the proper detectors with sensitive is critical to reduce unnecessary noise.

2.2 Generation of High Powered Broadband near-UV Pump Pulses for Ultrafast Electronic-Vibrational Spectroscopy

High powered, tens of microjoule compressed near-UV (nUV) pulses are desired for pumping in ultrafast spectroscopies[16,21-24] and generation of ultrashort deep UV pulses[25]. Furthermore, multidimensional EV experiments that study systems which absorb in this region in near-UV, for example light harvesting materials and molecules containing conjugated π systems which are the focus of this dissertation require the use a compressed broadband near-UV pump pulse. Here, the generation of broadband nUV (BBnUV) pulses that cover the full nUV spectral domain (370-440 nm) which is needed to extract a complete description of these systems[26] is described. The generation of a high-powered broadband near UV pulse for use in multidimensional EV spectroscopy is not intuitive and requires the use of pulse broadening optics, special selection of nonlinear materials and the proper technical implementation of the optical Kerr effect for nonlinear materials.

Past attempts to generate a BBnUV with the above requirements have largely struggled to either achieve proper power throughput, focusing instead to generate ultrabroadband pulse widths or have failed to generate sufficient broadening for use in an EV experiment[25-33]. The resolution and signal pathways that are resolved in a multidimensional EV spectrum are directly related to the pulse width of the pump pulses used. Therefore, it is critical to use the broadest pump pulses possible in EV experiments. Additionally, as is implemented in the EV spectrometer, multidimensional spectroscopies with UV excitation typically employ pulse shaping for sufficient phase stability of short wavelength pulses which will be discussed in the preceding sections, these pulse shaping devices often results in a 75-90% energy losses[28,34]. As a result, pulse energies of ~15-25 μJ are desired for spectroscopic experiments in the nUV. To this end, past nUV generation schemes that have been prepared offer either high power throughput at the expense of spectral coverage and temporal resolution or high spectral coverage and short time pulses at the expense of energy throughput.

Common generation methods of sub-20 fs BBnUV pulses include: the generation of nUV by using frequency mixing processes with broadband nonlinear optical parametric amplifiers (NOPAs)[28-31,35], inducing spectral broadening by self-phase modulation (SPM) by focusing in a hollow core fiber [25,26,36], and by angularly dispersing a fundamental pulse before frequency doubling to induce achromatic frequency doubling[33]. These generation methods of BBnUV suffer greatly from energy lost processes leading to compressed pulse conversion efficiencies ~1% and output energies being <5 μJ. For example, stable, short-duration pulses of a NOPA can be used to generate some nUV. However with optimal power outputs is typically 6-10 μJ in the 430-750 nm range[28-31,35], and Fourier limited nUV generation with NOPA generated pulses result in pulses down to 8 fs but are limited only to center frequencies 380 nm region

and have reduced pulse energies of 1-1.5 μJ[30]. Therefore, frequency doubling of a high powered broadened fundamental 800 nm pulse with a birefringent crystal such as a barium borate crystal (BBO) may offer greater power throughput for the generation of BBnUV pulse for EV spectroscopy. The generated doubled spectrum is dependent on satisfying phase matching conditions between a pulse and the birefringent media. Baum and coworkers[33] generated 120 nJ UV from a 1.25 μJ NOPA pulse using achromatic phase matching conditions in a thick BBO generating 21 nm broad pulses centered at 335 nm. Generating tens of microjoule BBnUV is thus not intuitive. By avoiding additional broadening and frequency mixing processes 55 μJ of compressed 400 nm can be generation from a 170 μJ fundamental Ti:Sapphire laser via three-wave mixing processes[31] the pulse duration and pulse width were reported as 32 fs and 6 nm, though this process provides high powered nUV pulses the narrow linewidth prevents the simple scheme from being useful in a multidimensional EV spectrometer. Conversely, recent work focusing on the maximization of pulse broadening has been shown by inducing SPM in gas-filled hollow core fibers (HCF) where theoretical pulse durations have approached the attosecond region[25,26,36]. However, to achieve the large broadening requires the use of 1.5 mJ of a 25 fs fundamental pulse, which was found to only generate 6 μJ of sub-5 fs BBnUV[26]. Additionally, questions of stability of the HCF pulses are raised owing to the fact that the pulse power dropped from 6 to 5 μJ observed over the course of 12 hours. Thus, the large power fundamental laser output may make it difficult to implement the technique. To circumvent this problem a new pulse broadening scheme was implemented to achieve high powered BBnUV pulses for use in multidimensional EV spectroscopy resulting in the generation of stable 20 μJ, sub-20 femtosecond (fs) nUV pulses which achieved the above requirements for the use in multidimensional EV spectroscopies. The demonstrated

method is implemented for all spectroscopic measurements collected in this dissertation and will be instrumental for the studies on ESIPT systems shown in the preceding chapters.

Here, the generation of a 20 µJ BBnUV laser pulses by doubling a broadened input fundamental pulse (38 fs, 800 nm) by inducing SPM in a series of thin fused silica plates is discussed. The general goal of the generation scheme is based off using a more efficiently generated broadened fundamental to drive a common frequency doubling set up. The broadening generation scheme is derived from the work of He et. al. and others[37-39]. The general experimental BBnUV generation scheme is shown in Figure 2-3. Briefly, a ca. 233 µJ portion of the output of a Ti:Sapphire regenerative amplifier (Spectra Physics Spitfire XP Pro, 4 W, 38 fs, 1 kHz) is focused over 1 meter focal distance with a concave mirror (Newport, 600-1000 nm HR coated) into a series of thin BK7 (VWR International micro cover glass, 22 x 30 x 0.14 mm) or fused silica (Valley Design Corp., 25 x 25 x 0.1 mm) which are set at Brewster's angle by minimization of reflective losses. To achieve ample SPM in a nonlinear media the beam must exceed the critical fluence 21.2 TW/cm2 in Fused Silica (FS) for a 100 µm plate at Brewster's angle[39]. The initial peak power of the fundamental pulse is 6.1 GW focused over a 1000 mm distance results in a beam fluence of 27.1 TW/cm^2 at the focus of our gaussian beam for an initially 12 mm diameter pulse. As the focused beam propagates through the nonlinear media, nonlinear processes governed by the Kerr effect result in enhanced spectral broadening, SPM and self-steepening which result in the generation of a broadband 800 nm pulse (BB800). For vast broadening to occur special attention must be given to the chirp of the input pulse, as is noted similarly for a HCF set up[40]. Although precompression schemes could be employed to the chirp of the incident fundamental pulse is contained by the dispersion requirements for pumping an OPA elsewhere in the EV spectrometer, therefore we observe a slight positive

chirp of the fundamental pulse and ultimately a slightly narrower pulse spectrum is achieved when accounting for the optimization of the chirp for the WL arm in the OPA.

The generation of a BB800 pulse involves careful placement of the thin plates made of a nonlinear media relative to one another and with respect to the input fundamental beam waist[39]. The placement of the first plate is about 10 cm before the focus of the beam and is set based on the maximal pulse broadening. After beam propagation through the first plate, self-steeping and SPM effects lead to an additional accumulation of pulse spectral broadening upon passing through successive plates. Upon each additional plate the nonlinear interactions within the thin plates drives spectral broadening while prolonging the beam waist of the focusing input beam, having a similar effect to a waveguide, plate positioning involves setting the thin plates at Brewster's angle by minimizing the intensity of the reflected fundamental pulse followed by placing the plates at optimal distance from each other which maximizes the SPM or spectra broadening of the BBnUV pulse, given the initial 233 μJ pulse no further pulse broadening affects were observed after the optimal placement of 5 plates FS plates. Recollimation of the BB800 pulse is done using a concave mirror (Newport, f =400 mm, low GDD HR coated 600-1000 nm) mounted on a translation stage account for different beam divergence profiles from the amount of self-focusing effects induced by the number of plates, special consideration should be noted when placing the recollimation lens as changes in plate position may affect the position of the recollimation lens. The pulse broadening effects are shown in Figure 2-3Figure 2-5 by the difference in spectral width of fundamental and BB800 pulses.

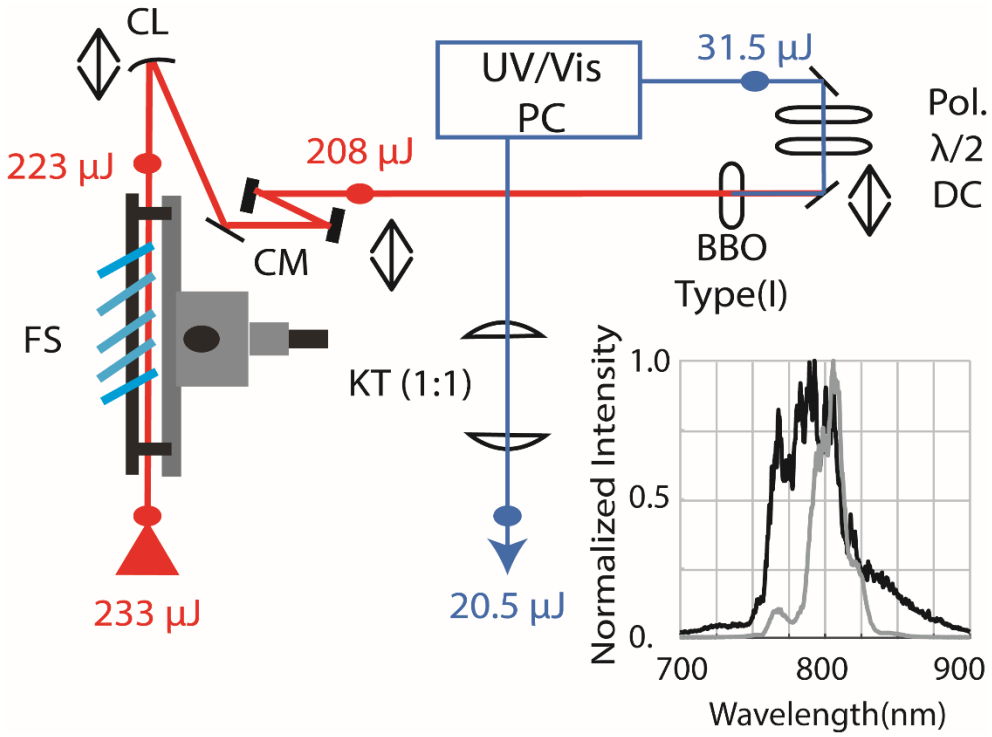

Figure 2-3. BBnUV pulse generation set up with measured pulse energies at various locations in the beam path. Inlet: Normalized intensity spectrum of broadened 800 nm pulse (Black) with FWHM 55.4 nm and incident fundamental pulse (Gray) with FWHM 21.4 nm. Black arrows denote a translation stage. FS: Fused Silica. CL: Concave Lens. CM: Chirped Mirrors. BBO: Barium Borate Oxide Crystal. DC: Dichroic Mirror. UV/vis PC: Double pass two prism, prism compressor. KT: recollimation Keplerian Telescope.

Self-focusing effect during the BB800 generation incur and can result in a change of the beam focusing profile. To avoid parasitic beam distortion effects, plates are set at Brewster's angle by minimizing reflection off the plates, and are separated by 1-2 cm. Both BK7 and FS plates were used to generate a BB800 pulse. We observed broader pulse generation in both the BB800 and BBnUV pulse when using FS thin plates as compared with slightly thicker BK7 plates. The broader spectrum is related to the plate thickness of the material, as we observed spectral broadening with up to 5 plates as compared with 4 for BK7. We observe stable BBnUV pulse generation with FS plates with an RMS ~1% over 12-16 hours as compared with 6-8 hour for BK7 generated BBnUV. The typical generated BB800 centers about 800 nm with a FWHM of 55.4 nm as compared with the incident fundamental FWHM of 21.4. With a total power lost

resulting from the broadening process of ~5%, with 223 µJ of BB800 being retrieved from the initial 233 µJ fundamental pulse. Due to the low pulse energy loss from the broadening procedure, the BB800 pulse can be put through a common doubling scheme, which can incur large energy lost in the doubling and compression processes.

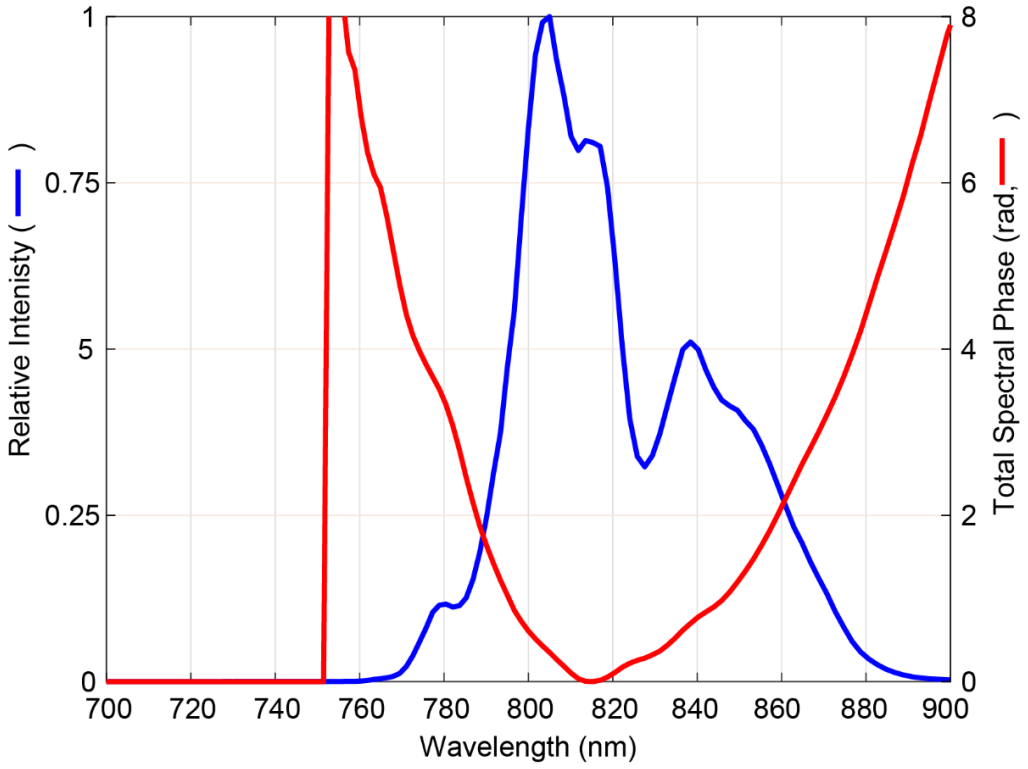

Figure 2-4. SHG FROG of BB800 used in the BBnUV generation scheme. The retrieved spectrum shown in blue shows a drop of intensity around 820 nm caused by the SPM induced in a series of FS plates. The spectral phase of the retrieved pulse shown in red, clearly shows the effect of the added GDD caused by both the FS plates and the broadening process, implementation of chirped mirrors counters the added GDD from the broadening process.

To provide the highest doubled intensity, the BB800 pulse can be reflected off a series of chirped mirrors (Newport, 10Q20UF.42) which add -45 fs^2 dispersion per bounce and are designed for chirp compression for 800 nm centered pulses as short at 10 fs. The effect of the broadening and SPM on the pulse by reporting the second order dispersion ($\varphi^{(2)}$) the group dispersion delay (GDD) and third order dispersion ($\varphi^{(3)}$) by fitting the spectral phase ($\varphi(\omega)$)

retrieved from an SHG FROG measurement of the fundamental compared with he boarded pulse as shown in Figure 2-4. The spectral phase was fit to a third order polynomial in which the quadratic ($\varphi^{(2)}(\omega- \omega_o)^2/2$) and cubic ($\varphi^{(3)}(\omega- \omega_o)^3/6$) terms were used to extract the dispersion. The broadening increased GDD from (-2,400 fs^2 to 12,100 fs^2) while decreasing $\varphi^{(3)}$ (750 fs^3 to -5,480 fs^3).

Chirp control is conducted by placing the first chirped mirror on a translation stage which can be moved in and out to control the amount of chirp added to the BB800 pulse prior to up conversion in a BBO type (I) crystal (Newlight Photonics, 50 μm or 100 μm thicknesses used here). The 5 FS plates add about 18 fs2 of GDD to the pulse and is compensated by the -90 fs^2 added by two reflections off the chirped mirrors. Overall, the doubled output power increases upon adding two chirp mirror reflections even though the reflections result in a pulse power lost from 223 μJ to 208 μJ into the BBO. A comparison of the BBnUV generation method is shown in Figure 2-5. Without broadening, a portion of the fundamental pulse can be doubled in a 100 μm thick type(I) BBO, of which the generated nUV pulse has a FWHM of 8.4 nm centered at 402.8 nm. This generation method is analogous to Grün and cowokers[31] and has a Fourier transform (FT) limit of 28 fs if properly compressed. After doubling the BB800 in a 100 μm type(I) BBO the bandwidth of the nUV pulse vastly increases with a FWHM of 18.4 nm centered at 402.8 nm. Which corresponds to a FT limit of 12 fs. However due to the bandwidth of the BB800 the entire spectrum of the BB800 can be upconverted in a 50 μm type(I) BBO. With the thinner BBO a BBnUV pulse with a FWHM of 36.0 nm centered at 404.7 nm is achieved. Which corresponds to a FT limit of 6.3 fs. The broadened nUV (BBnUV) pulse is then spectrally isolated and passes through a half waveplate before being routed to a UV prism compressor in a folded geometry (Newport 10SB10 prisms).

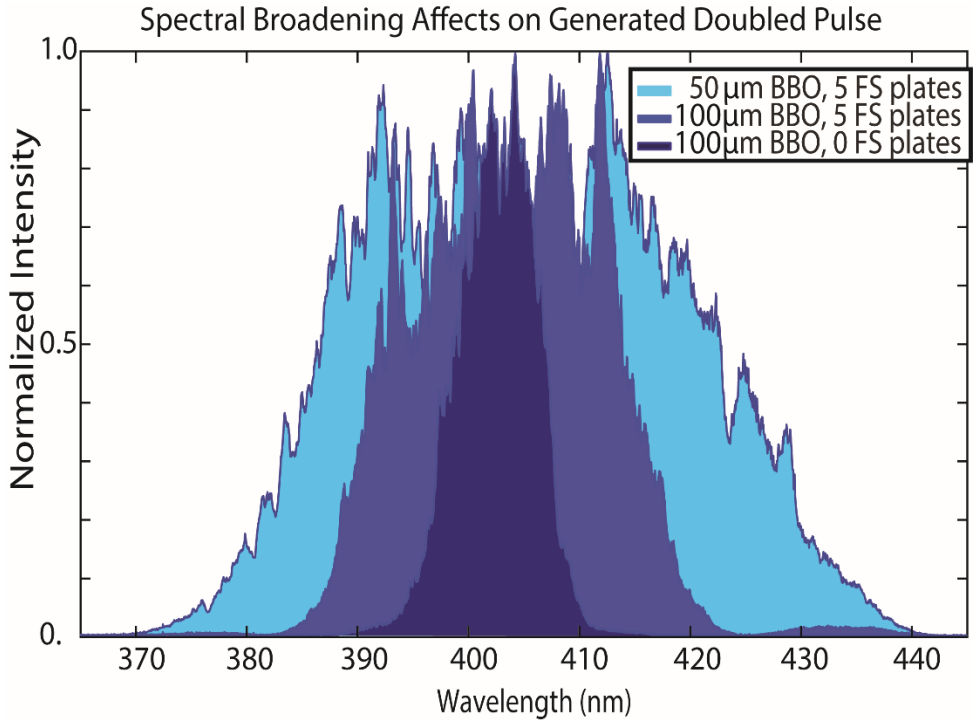

Figure 2-5. BBnUV spectra showing the effects of the spectral broadening on the generated frequency doubled spectrum shown by the doubling of a pulse generated from: the input fundamental 800 nm pulse with no broadening in a 100 µm BBO, the BB800 in a 100 µm BBO and the BB800 in a 50 µm BBO.

Overall, there are two main sources of pulse energy lost: doubling and compression, are important to note for this set up. Due to the thin BBO and phase mismatch bandwidth limitations, there was a large power loss between the pulse after passing through a prism compressor and the incident BB800 power. The pulse power generated following compression is 5.3 µJ when using a 50 µm thick BBO from the 208 µJ incident BB800 pulse after chirped mirror reflections. There is a noticeable power loss of ~35-40% when compressing the BBnUV using a prism compressor in addition to the losses dependent on phase mismatch efficiency of the doubling process for a given BBO thickness. Overall, for a 100 µm BBO we observed ~15% conversion efficiency as compared to ~3% for a 50 µm BBO. Noteworthy is the use of this generation and compression technique we achieve very high pulse power throughput giving leading to the ability to incur further shaping losses from a pulse shaper in a multidimensional EV experiment. To note, for the

50 μm thick BBO generated BBnUV the conversion efficiency, from the incident fundamental to the BBnUV power generated, is 2.3% still above the <1% efficiencies when HCFs are used[25,26,36] and 8.8% for the BBnUV generated from a 100 μm thick BBO. The generation of 31.5 μJ precompressed BBnUV of which up to 20.5 μJ compressed output is obtained when a BBnUV pulse is readily generated from a 100 μm thick BBO. Therefore, leading to the tens of microjoule power obtained is necessary for use in pumping multidimensional spectroscopy experiments.

2.3 Implementing a Characterization Scheme for a Broadband Near ultraviolet Pump Pulse

Following the generation of the BBnUV pulse proper compression of the pulse is needed to achieve high time resolution for use of the EV spectrometer. As discussed below, the generation of sub-20 fs BBnUV pulses is readily achieved for both pulses generated from a 50 μm BBO and 100 μm BBO shown in Figure 2-5. In tandem with the generation scheme the demonstration of typical pulse lengths between 15-18 fs is shown by implementation of broadband transient grating cross correlation frequency resolved optical gating (TG XFROG) spectrometer in tandem with proper compression techniques, mainly the use of UV-prism compressor or a pulse shaper can be employed.

2.3.1 Frequency Resolved Optical Gating (FROG) Pulse Characterization

To optimally compress the BBnUV pulses, a broadband TG XFROG pulse characterization technique was set up based on pioneering work by Ermolov and coworkers[41] and is summarized in the implemented set up in Figure 2-6. Briefly, FROG traces are used to measure ultrafast laser pulses by using a reference pulse to aid in the characterization of the intensity, phase and duration of that pulse[42,43]. This is carried out by collecting a spectrum of the

FROG signal as a function of the gating time between the pulses to be measured. In practice, the ultrafast laser pulses to be measured are temporally and spatially overlaid and sent into a nonlinear material to interact resulting in the 2 or more electric fields interacting causing an instantaneous nonlinear response in the material. That nonlinear interaction is analogous to the SHG generation method used to generate the BBnUV and results in the FROG signal field to be generated, this signal field for example when two identical pulses interact in a BBO crystal produce a SHG frog signal, at a specific frequency, ω, and time delay between the two pulses, τ.

$$I_{FROG}^{SHG}(\omega,\tau) = \left| \int_{-\infty}^{\infty} E(t)E(t-\tau)\mathrm{e}^{-i\omega t}\mathrm{d}t \right|^2 \tag{2.1}$$

As given in eq. 2.1 the measurement of a SHG FROG signal is dependent on the two laser pulse electric fields, *E*, that are to be characterized and on interaction between the two pulses in the nonlinear media. Since SHG is a second order nonlinear process, eq. 2.1 reveals that the individual phases of the incident laser pulses are indistinguishable resulting in the SHG FROG spectrograms that are collected to be symmetric with respect to the delay time. SHG FROG however is experimentally simple to set up and can be used to characterize the fundamental laser output readily. However, SHG FROG suffers from the fact that the signal produced is a second order process meaning the signal produced by SHG is dependent on the ability of a nonlinear media to produce the entire second harmonic of the beam to be characterized. For a fundamental laser pulse from a Ti:Sapphire system this is possible but for broadened nUV pulses SHG is not possible due to the lack of sufficient bandwidth in the nonlinear media.

Typical second order pulse characterization techniques, such as second harmonic generation FROG or pulse autocorrelations are unable to measure the total phase of a BBnUV pulse due to the lack of transparency and phase matching conditions for these techniques[41-43]. To

circumvent this issue the implementation of a third order pulse characterization techniques, Self-diffraction (SD) and TG XFROG characterization method were implemented to characterize the BBnUV and fundamental pulses at the sample area by crossing two identical fundamental pulses 800 nm laser pulses and the BBnUV pulse at a 3° crossing angles with respect to each other in a 25 μm FS plate (Valley Design Corp., 10 x 10 x 0.025 mm). The three pulses were routed to the main sample area of the EV spectrometer with the two references being focused off a gold off-axis parabolic mirror (OAP) with a four inch focal length. Special addition is given to the spot size of the incident fundamental pulses to ensure the tight overlap can be achieved. The crossing of the two 6 μJ portions of the fundamental pulse generate a phase grating with the periodicity of 15 μm[41]. The phase grating allows the characterization of the fundamental pulse (SD FROG) and the BBnUV (TG XFROG). At the optimized SD signal, temporal and spatial overlap of a 1-10 μJ portion of the BBnUV will lead to the BBnUV diffracting off the diffraction grating leading to the generation of TG XFROG signals, see Figure 2-6. FROG spectra are collected by temporal scanning either reference 2 with represent to reference 1 and collecting the SD signal at different time intervals or temporal scanning the BBnUV with respect to the SD signal for TG XFROG.

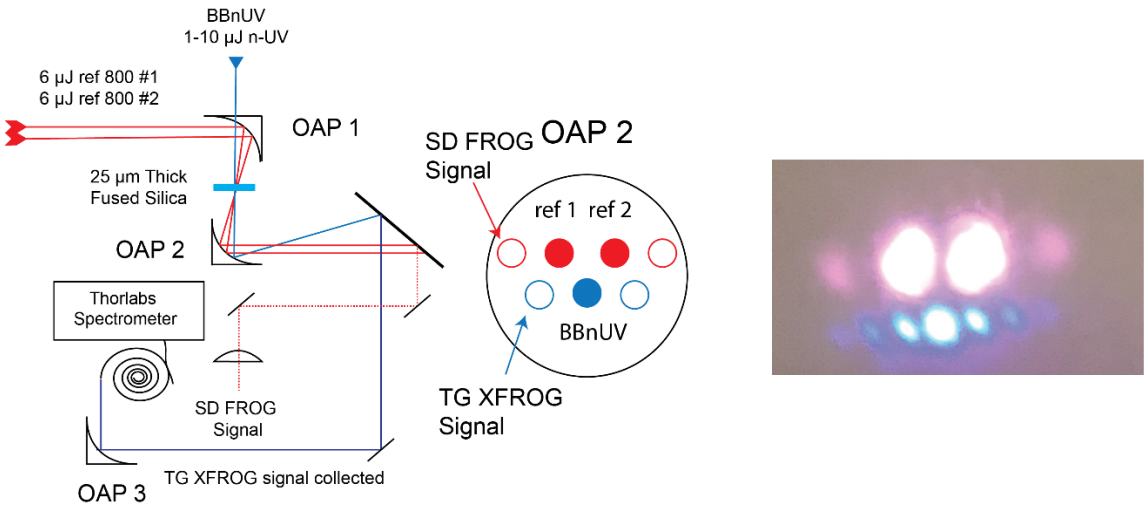

Figure 2-6. TG XFROG and SD FROG table schematic. Two identical reference 800 nm pulses are focused off OAP 1 into the sample area containing a 25 µm FS plate at a 3° crossing angle. When spatially and temporarily overlapped in the FS a SD signal will be generated for each of the diffracted arms of the references. At the optimized SD signal, temporal and spatial overlap of a the BBnUV will lead to the BBnUV diffracting off the diffraction grating leading to the generation of TG XFROG signals. The right panel shows an image taken right before OAP 2 from the lab when the SD and TG signals are present as well as an annotated diagram of the pulses. FROG spectra are collected by temporal scanning either reference 2 with represent to reference 1 and collecting the SD signal at different time intervals or temporal scanning the BBnUV with respect to the SD signal for TG XFROG.

The collection of a FROG spectrogram is done via a collection VI using LabVIEW. The VI collects a spectrum, typically using a handheld spectrometer (Thorlabs, CCS200) via a USB port, as a function of changing a pulse time delay using a retroreflecting mirror. The FROG signal is first routed to the spectrometer and focused into an optical fiber to be collected, special attention is given to ensure the laser pulse is coupled properly into the optic fiber. All retroflecting stages have been connected to a Newport XPS universal motion controller which is used to control the precise stage positions within 10 nm precision. The XPS is connected via an ethernet to the computer running the VI. This work focused on 3 timing stages, one which delays one of the reference arms (GROUP1), one which delays the mid-IR (GROUP 3) and one which delays the BBnUV (GROUP4), note the naming and stage connections in the XPS could have

been changed. The FROG collection VI connects to a specific stage which has been inputted and collects the spectrum of the FROG signal for a specific stage position, normally the strongest FROG signal is observed with the pulses which are characterized are temporally and thus the strongest temporal overlap is noted as time zero, as shown in the image in Figure 2-6. The experimentally measured FROG spectrograms of the TG FROG are shown for each experiment conducted and provide an excellent comparison between pump pulse conditions. Here we note the FROG signals fields are dependent on the convolution of three laser pulse interactions, for the SD FROG signal, the intensity of the FROG signal is given by the intensity of the diffraction grating produced.

$$I_{FROG}^{SD}(\omega,\tau)=\left|\int_{-\infty}^{\infty}E(t)^{2}E(t-\tau)\mathrm{e}^{-i\omega t}\mathrm{d}t\right|^{2} \tag{2.2}$$

As shown by eq. 2.2 the self-diffraction FROG signal is directly proportional to the three incident identical electric fields of the reference. Delaying one arm of fundamental pulse therefore establishes the SD FROG Spectrogram. Once a FROG spectrogram is collected the spectrogram is reduced to a square matrix to be used as an input field for the FROG retrieval algorithm[42]. The FROG retrieval algorithm attempts to fit the electric fields of the spectrogram, including the spectral and temporal phase, using a self-consistent field iterative procedure, of which the initial guess is important to prevent divergence in the algorithm. To ensure that the retrieval algorithm produces a satisfactory fit, data preprocessing procedures can be implemented to remove background noise from the experimentally collected matrices and help to converge the algorithm to an appropriate electric field in less computation time.

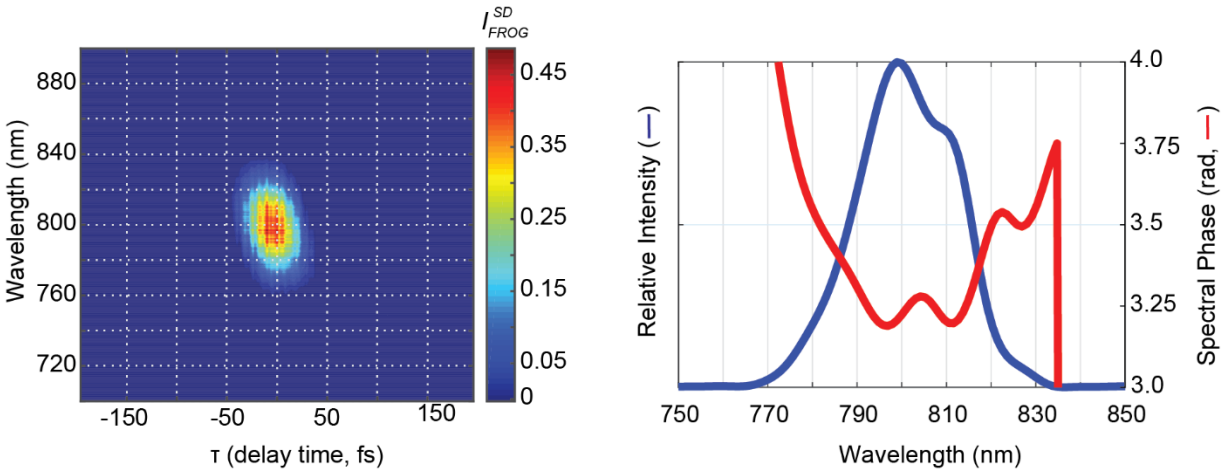

Figure 2-7. Representative SD FROG spectrogram collected with retrieved spectral phase and pulse spectrum. A spectrum of the SD FROG signal is collected scanning across -200 to 200 fs with respect to time zero, in 2 fs intervals. Of which the data matrix is reduced to including only the -197 to 197 delay times points and the spectral region from 700 to 900 nm to remove sampling errors of the first couple scans and to remove unnecessary data points, establishing a 908 x 197 data matrix. The spectrogram is further interpolated to a 256 x 256 square data grid before a FROG retrieval algorithm attempts to retrieve electric field which fits the spectrogram data set. The right panel shows a typical retrieved spectrum showing the effects of higher order spectral phase caused from compressor grating used in the regenerative amplifier. The spectral FWHM was 24.0 nm with a FROG algorithm error of 0.00649.

A representative SD FROG spectrogram is shown in Figure 2-7. Before all experiments shown, a SD FROG is measured before the measurement and characterization of the TG XFROG. Typical spectral FWHM and temporal FWHM retrievals for SD FROG spectrograms are between 22-26 nm and 42-52 fs depending on the performance of the laser system. Narrower and longer pulse durations found in the SD FROG is an indication of degradation of the laser system and should not be ignored.

2.3.2 Compression of a BBnUV pump pulse using TG XFROG

Following generation of the SD FROG signal, TG XFROG pulse characterization is performed. The strongest SD signal, found at time zero is generated before temporal and spatial overlap of the BBnUV pulse to be characterized, the Transient Grating signal then is routed to a spectrometer to collect the spectrogram of the FROG signal as a function of delay time of the

BBnUV. Here the phase matching conditions for the TG XFROG result orders of the TG XFROG which correspond to the SD signals as shown in Figure 2-6, the higher order TG signals contain signal contributions of the fifth and seven order SD signal and are blocked during the collection of the TG XFROG signal. The third order FROG signal is a double convolution of the incident reference electric field and the BBnUV as shown in eq 2.3.

$$I_{FROG}^{TG}(\omega,\tau)=\left|\int_{-\infty}^{\infty}E_{800}(t)^{2}E_{BBnUV}(t-\tau)\mathrm{e}^{-i\omega t}\mathrm{d}t\right|^{2} \tag{2.3}$$

Advantages of using TG XFROG for characterization of the BBnUV include the ability to phase match UV pulses, as the phasing matching condition is dependent on the SD grating produced in the nonlinear material and the diffraction grating period rather than the generation of a phasing matching condition in a nonlinear media. Additionally, the TG FROG signal comes out spectrally isolated with the same frequency as the incident pulse to be characterized. Given the later similar optics are used to route the TG signal to the spectrometer as are used to route the incident pulse to the sample area.

Following the generation of a TG XFROG of the BBnUV the spectral and temporal widths as well as the spectral and temporal phase of the incident pulse can be retrieved using the FROG retrieval algorithm. Upon obtaining the precise phase of the BBnUV the incident pulse can be properly compressed. Two compression methods are used in the EV spectrometer: a double pass UV prism compressor set up in the folded prism compressor geometry and the use of acoustic optical programable dispersive filter (AOPDF) pulse shaper. The effects of pulse compression with a signal prism compressor is explored below. For 2D EV and 3D EV experiments the pulse shaper is required as will be discussed in the preceding sections, for 1D EV experiments the pulse shaper is not needed however is often implemented to aid in the pulse

compression, as the temporal and spectral compression using a signal prism compressor is limited by the third order (TOP) and higher order phase imparted on the laser pulse by the prism material. Figure 2-8 shows the FROG spectrograms results when pulse compression is carried out with the aid of TG XFROG. The unoptimized spectrum revealed a pulse duration as measured by the full width at half maximal value (FWHM) of 387 fs whereas with optimized prism compressor setting the FWHM of the BBnUV is reduced to 31 fs.

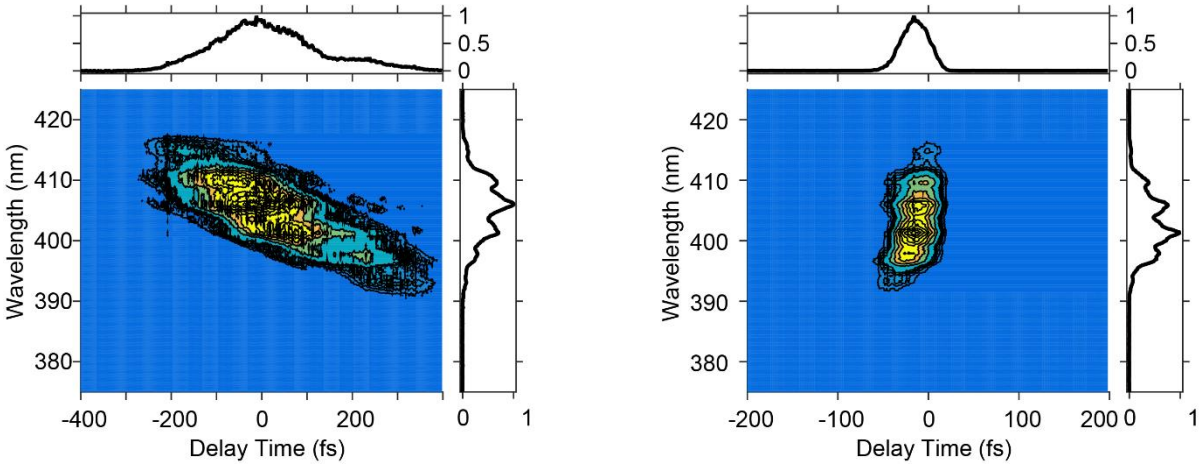

Figure 2-8. TG XFROG spectrum of BBnUV of the uncompressed compared with compressed output with a prism compressor. left: Initial pulse before optimization of prism compressor position. The FWHM of the temporal duration of the pulse was calculated to be 387 fs. right. FROG spectrograph following optimization of prism compressor with a FWHM of 31 fs length stated is convoluted with the ref 800 pulse duration. Here the slight curvature of the compressed pulse is illustrative of the TOP imparted by the prism compressor.

2.4 Generation of BBnUV Pump Pulses for Multidimensional Spectroscopy Using a Pulse Shaper

2.4.1 Use of an AOPDF pulse shaper to generate pump pulse pair for EV spectroscopy

As alluded to earlier, high powered BBnUV pump pulses are needed to generate pump pulse pairs using an AOPDF pulse shaper. The use of pulse shapers is commonplace in the multidimensional spectroscopy community[1,11,12] however is it not necessary in all experimental

setups[2,44-46] and can be carried out interferometrically, here due to the short cycle time of the UV pulses used (1.25-1.43 fs for 375-430 nm pulse) typical interferometric methods are unable to be used due to the uncertainty in the stage position in the spectrometer. Use of a AOPDF pulse shapers therefore is needed to generate pump pulse pairs for the ultrashort pulses generated in the nUV.

Briefly, an AOPDF pulse shaper is comprised of 3 components an RF generator carries a RF signal directly to a transducer which is coupled to a thick nonlinear crystal, a computer is connected to the RF generator and is calibrated to compute any series of custom RF waveforms that are sent to the crystal. Given the components involved the choice of calibrated waveforms and crystal type are important when determining the type of pulse shaper to use. Previous forms of the EV spectrometer[15] utilized a custom made potassium dihydrogen phosphate (KDP) crystal (*Fastlite* Dazzler) which was chosen to shape UV pulses between 200 and 450 nm. The KDP crystal (*Fastlite,* KUV50-65.130-240 440-B, SN 28879, RF generator: DC02KL88/T3) however cracked due to damage caused from the transduction of the RF, given the difficulty in custom crystallographic growth of the KDP crystal, the KDP dazzler was replaced with a quartz crystal dazzler (TF335-170-1-3-FL2, SN: 20061975-002, RF generator: GZ0655). The transparency of quartz in the nUV and transducer effectiveness in the nUV is significantly reduced compared with the KDP crystal. Great lengths in BBnUV generation and compression changes were needed to achieve optimal use of the quartz dazzler. Additionally, a new parameter calibration set was obtained from *Fastlite* to be able to shape BBnUV above 400 nm. This current parameter set allows the generation of pump pulse pairs from 360-430 nm with greatly reduced efficiency. Prior shaping efficiency of KDP-based Dazzler was stated at 5-10% however with the Quartz-based Dazzler shaping efficiency is between 0.25-1%

efficient between 380 and 420 nm, this low shaping efficiency practically speaking prevents the use of a 50 μm BBO generated spectrum to be used, see Figure 2-5, and instead a 100 μm BBO has been used for all pump pulses generated in this dissertation.

To generate a pump pulse pair to be used in a multidimensional EV experiment, the pulse shaper is placed directly inline of the generated BBnUV. The control computer is then synced to the regenerative amplifiers output to know the precise delay time between the ejected fundamental laser pulse and the time required for the pulse to travel to the pulse shaper, this value is directly controlled by the CH8 timing and is on the order of 2-5 μs. The control computer is also calibrated to determine the time the RF waveform takes to travel through the quartz crystal to "meet" the incident BBnUV pulse traversing the crystal. This takes about 22 μs. The remaining time between the 1 kHz pulse train is given to computer or stream a new RF waveform to sync with the next output pulse of the regenerative amplifier. The control computer GUI allows the user to manually set a waveform to be computed directly to the dazzler continuously. The GUI allows the user to generate any waveform within the calibrated window of 360-430 nm in the current configuration. Given this a useful waveform to optimize shaping and compression parameters is a waveform with does not create a pump pulse pair per say but shaped pump pulse with a pump pulse delay (τ_1) of zero. The user can input an RF waveform that shapes the nUV and adds or subtracts carrier envelop phase, first, second, third and fourth order spectral phase. This allows a further optimization control for the pump pulses to be fully compressed when arriving at the sample area. In other words, the dazzler can be used to directly compress the pump pulses, in the same way the UV prism compressor was used to compress the pulse from the TG XFROG output. In practice given the larger flexibility of the dazzler to control higher order spectral phase, the dazzler is used in most every

experiment in this thesis even if the pump pulse pair was not generated. As shown in Figure 2-9 use of the dazzler to shape the pump pulse further compresses the pump pulse to sub-20 fs and removes the higher order spectral phase characterizes that are shown in Figure 2-8.

Though shaping efficiency is extremely low with the quartz pulse shaper the efficiency of the generation scheme is vital to conduct multidimensional EV experiments. To this end the generation of up to 50 μJ of compressed BBnUV pulses was achieved by doubling the fundamental incident power. The higher pulse energies allowed the generation of up to 1.5 μJ of shaped pump pulses to be used in the multidimensional EV spectrometer. The reduced shaping efficiency of the quartz dazzler comes with a benefit, the quartz dazzler's RF generator is more powerful and contains a larger internal flash memory capacity than the KDP-based dazzler. This allows the ability to "stream" a fully series of waveforms directly to the quartz crystal, in essence allowing the generation of a complete 2D EV pulse sequence to collect a full τ_1 series in successive laser shots reducing the noise induced by long term laser drift. Utilization of the streaming process via an updated data acquisition program is a development that will ultimately allow the quantification of the spectrometers noise floor.

2.4.2 Generation of 2D EV spectroscopy using a phase cycling scheme

In addition to the streaming, phase cycling is implemented and shown to improve signal to noise ratios in the EV spectrometer. To generate a 2D EV signal typical experiments utilize the pump-probe heterodyne pulse geometry, this pulse geometry has the advantage of using the probe as a local oscillator and allows us to employ a collinear pump pulse pair for the experiment, or $k_{sig} = \pm k_3$ since $k_1 = -k_2$. The resulting signal field ($S_{sig}(\omega_3,t_2,t_1)$) that is generated, collinear and on top of the probe pulse, thus contains the following interactions.

$$S_{sig}(\omega_3,t_2,t_1) \sim |Epr(\omega_3) + i\omega_3[P_3^{(1)}(\omega_3) + P_{s2D}^{(3)}(\omega_3,t_2,t_1) + P_{pp}^{(3)}(\omega_3,t_2,t_1)]| \quad (2.4)$$

where $E_{pr}(\omega_3)$ is the electric field of the probe, $P_3^{(1)}(\omega_3)$ is the free-induction decay from the probe pulse, $P_{pp}^{(3)}(\omega_3,t_2,t_1)$ is the unwanted pump-probe signal resulting from interactions from either pump pulse 1 or pump pulse 2, and $P_{S2D}^{(3)}(\omega_3,t_2,t_1)$ is the desired third order macroscopic polarization term containing the EV signal interaction that is generated from the convolution of the third order material response and that of the three incident electric fields. To remove the contributions of unwanted pump-probe signal fields and reduce the overall experimental noise on the third order signal, incorporating phase cycling of the carrier envelop phase in the pump pulse pair is implemented to cancel the effects of the pump-probe signal generated by the heterodyne detected pulse geometry.

Several phase cycling schemes have been developed and implemented in prior multidimensional spectroscopy experiments[12,46,47], here we incorporate the waveform streaming option in our pulse shaper and conduct a 2 x 1 x 1 phase scheme to isolate the absorptive, real component of $P_{S2D}^{(3)}(\omega_3,t_2,t_1)$. For any multidimensional spectroscopy experiment proper control of the relative phases of each pulse is imperative to reducing uncertainty in the measured spectrum. The relative phase of the signal field (φ_s) is dependent on the relative phases of the incident electric fields and is given by the following expression in eq. 2.5.

$$\varphi = \varphi_{LO} - \varphi_s = (\varphi_{LO} - \varphi_3) - (\varphi_1 - \varphi_2) \quad (2.5)$$

where φ_{LO} is the phase of the local oscillator, $\varphi_{1,2,3}$ are the absolute phases of incident electric fields. For a 2 x 1 x 1 phase scheme the relative phase difference between the pump pulses 1 and 2 ($\Delta\varphi_{12} = \varphi_1 - \varphi_2$) is modulated between 0 and π for each experimental τ_1, τ_2, and ω_3.

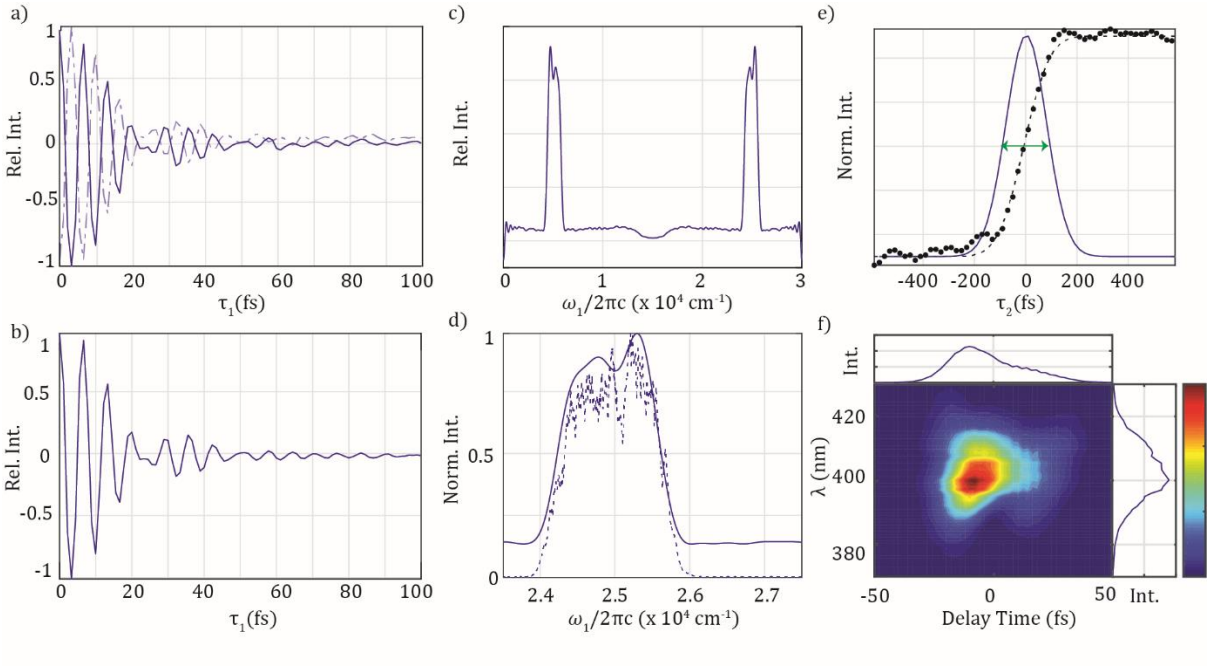

Figure 2-9. Pulse Characterization. a) Time Autocorrelation of 1 x 2π phase cycled pump pulse pair. *solid blue line* - 0π CEP phase; *dash-dotted blue line* - π CEP phase. b) Pump pulse time autocorrelation trace of after phase cycling subtraction. c) Frequency domain pump autocorrelation spectrum. The affect of undersampling is indicated by real spectral component being on the blue side of the nyguist line. d) Normalized autocorrelation spectrum overlaid with the measured pump spectrum showing good agreement between measured pulse spectrum and the autocorrelation. e) Measured experimental instrument response as reported by a 1D EV trace in a 250 µm thick Silicone wafer (black dots). The IRF of 185 fs is reported by a guassian fit (black dotted line) as the FWHM of rise (green arrow) of the third order response (blue line). f) TG XFROG contour plot of BBnUV pump pulse with the projections of the delay time and spectral domains shown to the top and right side of the contour plot. 20 evenly spaced contour levels report the spectral intensity of the FROG trace. The TG XFROG signal is convolved with a self-diffracted grating generated by two arms of the fundamental reference laser. The measured spectrogram was intropolated to a 256 x 256 data grid to process the spectral and temporal phase, the retreived FROG error was 0.0053, Temporal FWHM 16.0 fs and spectral FWHM 9.5 nm.

The effect of phase cycling the pump pulses is shown by an intensity autocorrelation interferogram. For the autocorrelation a pulse intensity measurement was recorded using a Silicone photodiode (Thorlabs, DET10A), see Figure 2-1, for 91 evenly spaced τ_1 delays from 0-100 fs for a $\Delta\varphi_{12}$ of 0 and π. The resulting interferograms are shown in Figure 2-9. The effect on the pulse intensity when relative phase between the pump pulses is changed is clearly exemplified by the π-shift in the interferogram. Here the absorptive component of the

autocorrelation is extracted by phase subtraction, resulting in the interferogram, upon Fourier transforming this time-domain trace the absorptive component of the autocorrelation is retrieved and shown. The effect of undersampling is present as the Nyquist limit is red of the true BBnUV spectrum. The lack of clear phase distortions is presented by the good agreement between the undersampled transformed autocorrelation and that of the pump spectrum as collected on a monochromator (Ocean Optics, HR2000+). The pump autocorrelation is also in good agreement with the TG XFROG temporal duration for the pump pulses used in the 2D EV experiments which shows a lack of higher order phase distortion than without the pulse shaper.

2.5 Highlighting Use of BBnUV Pump Pulses in a Sample 2D EV Spectrum of HBQ

To demonstrate the effectiveness of the pump pulse generation and characterization scheme I used the BBnUV pulses as pump pulses in a 2D EV experiment to study the role of vibronic coupling during ultrafast intramolecular excited state proton transfer (ESIPT) in 10-hydroxbenzo-[h]-quinolone (HBQ), an intramolecular hydrogen-bonded molecule with a π-conjugated backbone. The tunability of the BBnUV pulse is crucial to show that two vibronic states in HBQ are resonantly excited during the 2D EV experiment. The advancements in pulse generation lay the foundation for further studies on: Light harvesting, ESIPT, π-conjugated, and nanomaterial systems.

The advantage of spectral tunability of the BBnUV pulses is shown by 2D EV experiments of HBQ. Here two different spectrally tuned BBnUV pulses near the lowest energy transition of HBQ were used as pump pulses for 2D EV, denoted red and blue shifted. Note that after pulse shaping, pulse energies of 1.1 μJ were available before attenuation. The 2D EV experiments were conducted with a mid-IR probe centered ~1450 cm^{-1} to investigate the 1447

cm^{-1} excited state vibrational mode, a ring bending motion that shortens the proton donor-acceptor distance that will be further investigated in subsequent chapters. In HBQ, ESIPT occurs rapidly following photoexcitation. The excited electronic state resembles a proton transferred state and is nonadiabatically coupled to the 1447 cm^{-1} mode.

Comparison of the 2D EV excitation axis (ω_1) slices in Figure 2-10 highlight the key result and advantage of using the BBnUV generation scheme. When a slightly broader, red shifted pump pulse is used, two vibronic states are clearly resolved, at 25522 cm^{-1} and 25971 cm^{-1}. By comparison, the blue shifted pump spectrum only resolves the latter higher frequency vibronic state. The peak splitting of 449 cm^{-1} directly reports on the separation of the vibronic states. Comparison of additional probe frequencies (ω_3) in the 2D EV correlation map of the red shifted pump reveal different vibronic coupled modes with strikingly different peak positions along ω_1. The different ω_1 peak position informs reveals the excitation frequency dependent vibronic coupling for each high frequency mode. The spectrum shown below highlights the use of efficiently generated, tunable BBnUV pump pulses for 2D EV spectroscopy, which has enabled the discovery of multiple vibronic states participating in the ultrafast ESIPT in HBQ. In the following chapters 2D EV and 3D EV spectroscopy with the implemented BBnUV pulses will show the results of nonadiabatic energy transfer in HBQ and the radiative relaxation mechanism involved in excited state proton transfer complexes.

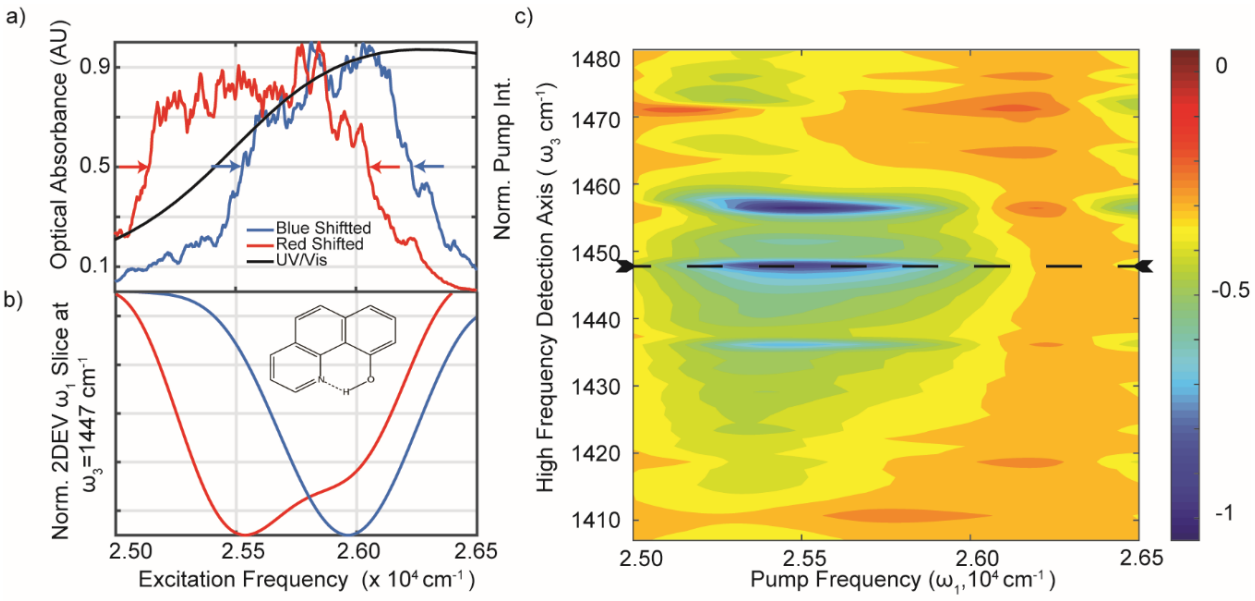

Figure 2-10. Highlighting use of BBnUV pump pulse in 2D EV spectrum of HBQ. a) Ground state electronic absorption spectrum of HBQ and corresponding normalized pump pulses used in the 2DEV experiment. The absorption spectrum corresponds to a sample concentration of HBQ of 50 mM dissolved in tetrachloroethane solution with a 50 μm pathlength (solid black). The red shifted pump spectrum (solid red) is centered at 25,594 cm^{-1} with a FWHM of 910 cm^{-1} while the blue shifted pump spectrum is centered at 25880 cm^{-1} with a FWHM of 698 cm^{-1}.b) 2D EV ω_1 slices at an ESA feature at 1447 cm^{-1} collected at a probe delay time of 200 fs. Each slice is normalized to itself between 0 and -1. The ω_1 slice obtained with a red shifted pump (solid red) depicts a double-well structure indicating two features contribute to the 2DEV spectrum centered at 25522 cm^{-1} and 25971 cm^{-1}, while the that obtained with a blue shifted pump (solid blue) displays a single feature centered at 25971 cm^{-1}. c) Normalized 2D EV correlation map obtained with red shifted pump pulses. Black dashed line indicates ω1 slice used in b). Contour map is constructed using 20 equally spaced contour levels between 0 and 1.

2.6 APPENDICES

2.6.1 EV spectrometer shot-to-shot data acquisition program implementation.

The generation of phase cycled, shot-to-shot 2D EV data was conducted using a new collection program that I programed to aid in the reduction of noise in the EV spectrometer. The collection program was written in LabVIEW and the front panel and GUI is shown in FHAGJDA. The program connects all the instruments needed to collect a 2D EV spectrum to a

centralized data collection computer as shown in the flow diagram in Figure 2-11. The first step of the LabVIEW program initializes all the necessary components needed to collect a 2D EV spectrum. As shown, the upstream laser system's timing delay generator (TDG) output a trigger pulse at the same time the 1 kHz laser pulse is ejected from the regenerative amplifier, see Figure 2-1. The trigger is transmitted to the DAQ board of the detector and the pulse shapers RF generator to be used as a 'start' signal for when the expected laser pulse will arrive, effective timing the system together. In separate calibration procedures the necessary integration time and delays necessary for the detector elements and RF signals to be collected and sent to their necessary components must be performed before the detector and pulse shapers are used in the 2D EV acquisition program, these calibration procedures are outlined by the respective manufacturers, and user manuals and are not discussed here.

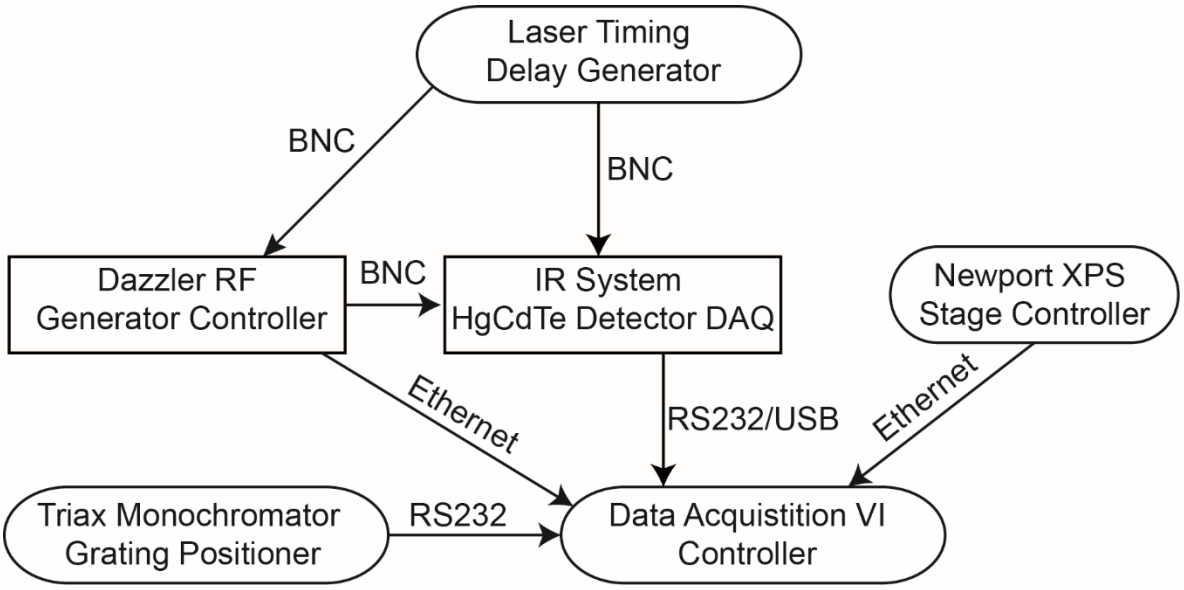

Figure 2-11. Connection flow diagram showing connections between instruments in use for the EV data acquisition program. The timing delay generator of the laser outputs a trigger signal which is carried by a BNC cable to the MCT detector DAQ board and the dazzler RF generator, this triggering signal times the detector and pulse shaper together. The XPS stage controller and Dazzler controller are connected to the data acquisition via ethernet ports whereas the detector and monochromator are connected using serial connectors. Before data collect the 4 instruments shown are initialized before a process is conducted.

The RF generator of the dazzler can be programmed to output a separate triggering signal, for when the RF generator is sending a signal to the crystal transducer. This programmability is important to be able to index when a specific RF pulse has been introduced to the pump pulse. Additionally, the DAQ board of the detector contains 16 external BNC channel inputs that can be programmed. For the 2D EV data acquisition program a BNC cable is attached from output of the RF generator box to the detector DAQ board. When the RF generator is on this sends a signal through the output of the RF to the detector allowing the detector sample VI to record the presence of a shaped pulse. As noted in an earlier section, the streaming process of the dazzler operates by using the internal memory of the RF generator to compute a series of up to 100,000 RF waveforms to be computed before the first waveform is sent to the crystal transducer. Unfortunately, the hardware of the detector only allows up to 10,000 laser shots to be collected in the internal memory of the DAQ, therefore we are limited to only collecting 10,000 laser shots at a time given the current detector limitations. Thus, for every 2D EV scan only 10,000 laser shots, or 10 seconds of data is collected at a time. However, during these 10 second times interval, the RF waveforms are computed and all the instruments in Figure 2-11 must be connected. Therefore, the first, 500-750 ms, of experimental time is typically ‘wasted’. Furthermore, when connecting a 3D EV data acquisition series, the pump-probe delay time, controlled by a delay stage, has to be scanned as well as if different probe frequencies are to be probed via the monochromator, the grating position has to be changed. To address these concerns the XPS stage controller, which connects 4 separate delay stages, see Figure 2-1, is connected and initialized into the VI as well as the Monochromator grating positioner. The XPS controller is connected via an ethernet port whereas the grating positioner is connected via an RS232 cable.

Overall, the data acquisition program process of operations is diagramed in Figure 2-12.

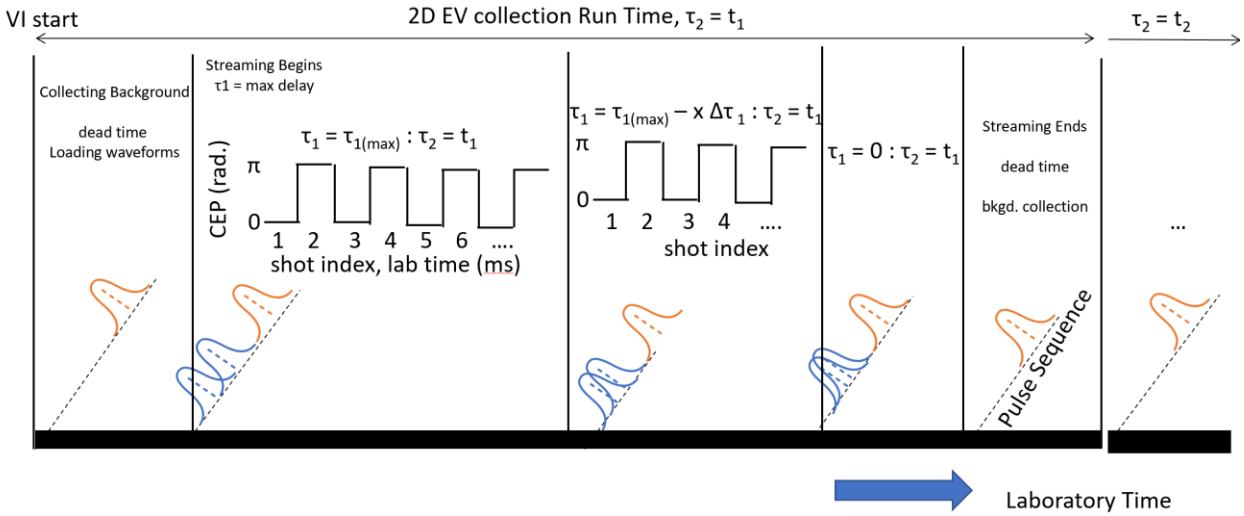

Figure 2-12. Cartoon Schematic detailing the data acquisition process in the EV data collection program. Upon setting the input parameters, a specific grating position is set, followed by setting a pump probe delay time, τ_2. A series of waveforms which include the number of pump pulse pair delays, τ_1 to be carried about, the amount of carrier envelop phases (CEP) to cycle between and the number of times the series will be repeated is established. Each CEP is cycled over the repetition length, followed by τ_1. The same waveforms are streamed for a particular τ_2 until the number of shots to be averaged is reached, then the delay stage is moved and the τ_1 and the CEP are scanned across for the next τ_2.

For each 3D EV data run the number of phases chosen for the phase cycling scheme to be collected, the number of pump-probe delay points τ_2, the number of pump pulse pair delays, τ_1 the number of grating positions and the number of scans to be averaged is considered. For a typical series the phases are scanned across first, for example if a 1 x 2π phase cycling scheme is introduced the carrier envelop phase (CEP) is cycled between 0 and π, in subsequent pulses. For each scan the CEP is cycled by the number of pattern repetitions before τ_1 is changed. The full τ_1 sequence for a specific grating position and τ_2 delay time is cycled. For instance, 1 x 2π phase cycling scheme, with 91 τ_1 delay times between 0 and 100 fs, and 40 repetitions will collect 2 x 91 x 40 or 7280 shots. If 3000 shots per point are to be collected this will result is 3000 ÷ 40 or 75 scans be collected for each τ_2 point in the series. In the next section the front panel of the data collection VI is shown and the expected signal to noise is discussed.

The front panel of the EV data acquisition program is shown in Figure 2-13 and shows all the necessary input parameters for the program. Here the filename and directory are appended with the specific scan number, τ_2 point, and grating position used in the scan. The input parameters for the pulse shaper also must be input, typically the dials tab and polynomial coefficient tabs are selected to input the dazzler phase and parameters. The amplitude of the RF accounts for the center frequency of the input BBnUV which can be tuned according to the angle of the BBO crystal in the BBnUV generation scheme. The phase values are read off from the proper values retrieved from the TG XFROG optimization procedure. The values for the IP address and port numbers for the XPS stage controller and dazzler control computer also have to be input to properly connect the program to the instruments. The Grating positions to scan over and the number of grating can be inputted following the array of τ_2 values to be input, note that at least two τ_2 points much be collected in order for the program to convert the array into string values to be converted to stage positions, therefore even if only one element of τ_2 array is selected the start and end values in the array must be different values. Lastly as described in the previous section, the τ_1 and CEP parameters are selected. Here, the input requires a minimum change of the τ_1, maximum change of τ_1 and the number of delay points. Note that if the values of the max and minimum delays can be swapped altering the order of the EV scan. In other words, whether the first τ_1 value is 0 fs or 100 fs depends on the order of the change of the delay parameters, this can affect the post processing and Fourier transform procedure. Finally, the number of CEP phases, N CEP is selected, which is also the same input parameter as the pattern size, pattern repetitions being described earlier and the number of shots to average being discussed earlier. Here, the N CEP can be 1,2,3 or 4 which alters the phase cycling procedures, in

this thesis only 1 x 2π phase cycling was implemented to maximize the overall cycle and duty time of the spectrometer.

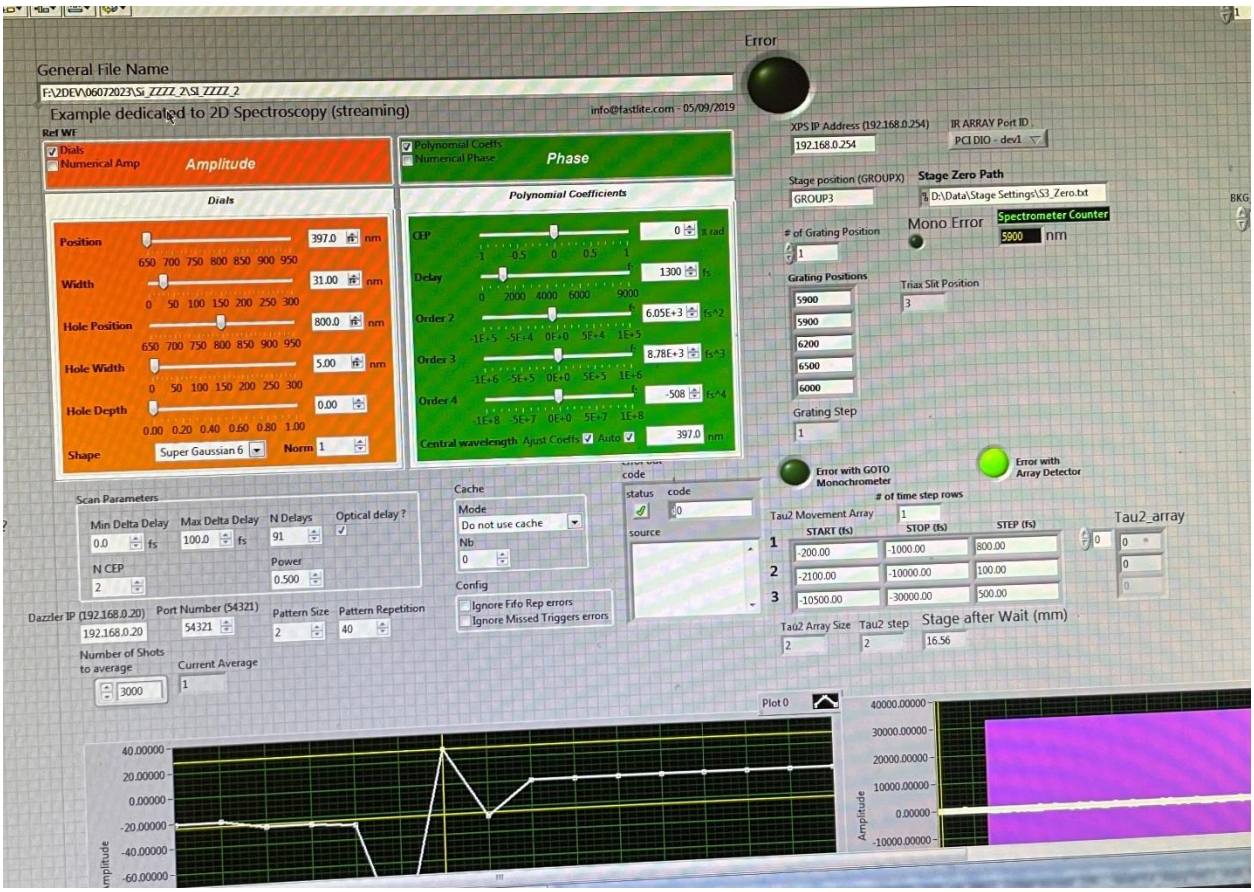

Figure 2-13. Front panel of the Data acquisition VI program showing the necessary input parameters to collect 3D EV spectra.

2.6.2 Quantification of 3D EV spectrometer signal to noise ratio

In the bottom portion of the program a series of arrays outputs the data collected by the VI. Here in the bottom right a pink block is shown. This block represents the external channel signal from the RF generator of the dazzler to the DAQ board of the MCT detector and signals the start of pulse shaping. A small dead space, before the presence of the pink RF signal, is manually input on the back end of the VI. This manual delay allows the Dazzler computer to compute and send the RF waveforms to be generated to the dazzler crystal and the dead time

varies between scans. Since the VI collects and saves every laser shot of collected by the MCT, a MATLAB script is used to reduce and average all the data with the same laser shot conditions, the script opens all the scan files and creates a 4D matrix of EV signal and sorts the data by pixel number (ω_3), τ_1 ,CEP and τ_2. For 4000 shots to be averaged, the standard error of a EV signal can be computed as a function of the running average signal value to find the optimal shots needed to resolve a EV signal pathway, shown in Figure 2-14.

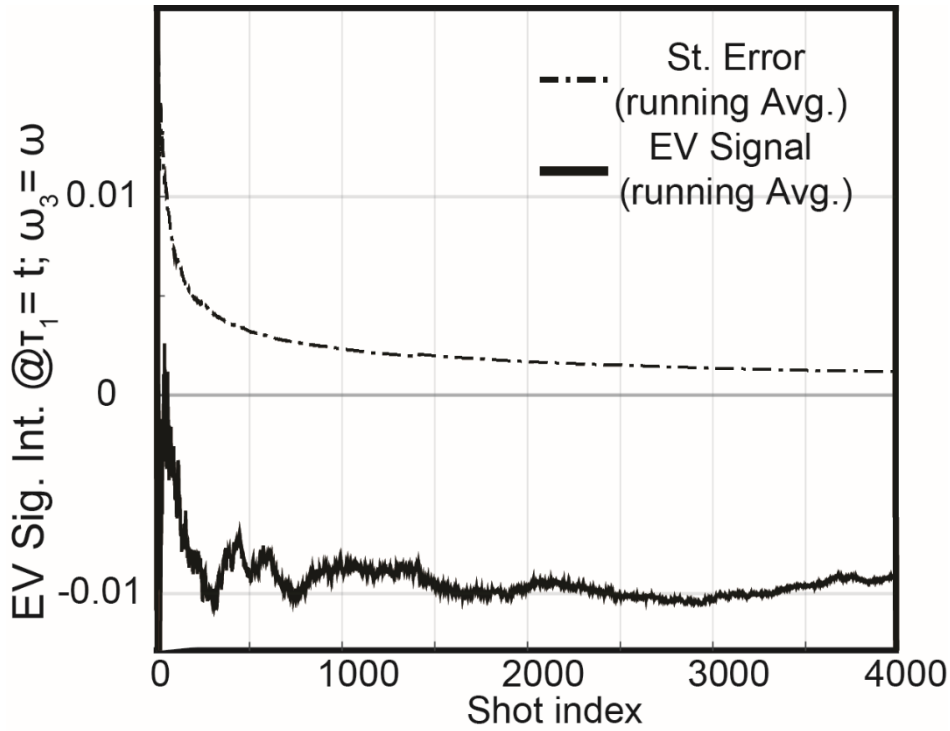

Figure 2-14. Quantification of signal-to-noise of 3D EV spectrometer. The running standard error and average of a EV signal at a induvial ω_3,τ_1, τ_2 point, shown by the dashed and solid black lines respectively. As the number of shots averaged together increase the standard error and average approach an asymptotic value expected to the limit of the 3D EV spectrometers noise floor after about 1500 shots.

The value of collecting signal intensity for every signal laser shot allows proper quantification of the noise floor of the 3D EV spectrometer after all prerequisites have been accounted for. In the example from Figure 2-14, two things are learned, first the noise floor is

approached after only 1500 laser shots to be averaged and secondly the noise floor is about 0.001 intensity units which roughly amounts to 1 mOD for the 1D EV experiment.

2.7 REFERENCES

1 Fuller, F. D. & Ogilvie, J. P. Experimental Implementations of Two-Dimensional Fourier Transform Electronic Spectroscopy. *Annu Rev Phys Chem* **66**, 667-690 (2015). https://doi.org:10.1146/annurev-physchem-040513-103623

2 Khalil, M., Demirdöven, N. & Tokmakoff, A. Coherent 2D IR spectroscopy: Molecular structure and dynamics in solution. *Journal of Physical Chemistry A* **107**, 5258-5279 (2003). https://doi.org:10.1021/jp0219247

3 Aue, W. P., Bartholdi, E. & Ernst, R. R. Two-dimensional spectroscopy. Application to nuclear magnetic resonance. *The Journal of Chemical Physics* **64**, 2229-2246 (1976). https://doi.org:10.1063/1.432450

4 Davies, J. H. Correlation spectroscopy. *Analytical Chemistry* **42**, 101A-112A (1970). https://doi.org:10.1021/ac60288a797

5 Tokmakoff, A. Orientational correlation functions and polarization selectivity for nonlinear spectroscopy of isotropic media. II. Fifth order. *Journal of Chemical Physics* **105**, 13-21 (1996). https://doi.org:10.1063/1.471859

6 Tokmakoff, A. Two-dimensional line shapes derived from coherent third-order nonlinear spectroscopy. *Journal of Physical Chemistry A* **104**, 4247-4255 (2000). https://doi.org:10.1021/jp993207r

7 Roth, M., Mehendale, M., Bartelt, A. & Rabitz, H. 2244-2246 Vol. 2243 (Institute of Electrical and Electronics Engineers (IEEE)).

8 Sung, J. & Silbey, R. J. Four wave mixing spectroscopy for a multilevel system. *Journal of Chemical Physics* **115**, 9266-9287 (2001). https://doi.org:10.1063/1.1413979

9 Verluise, F. L., V.; Cheng, Z.; Spielmann, C.; Tournois, P. Amplitude and phase control of ultrashort pulses by use of an acousto-optic programmable dispersive filter: pulse compression and shaping. *Opt Lett* **25**, 575-577 (2000). https://doi.org:https://doi.org/10.1364/OL.25.000575

10 Monmayrant, A. *et al.* Time-domain interferometry for direct electric-field reconstruction by use of an acousto-optic programmable filter and a two-photon detector. *Opt Lett* **28**, 278-280 (2003). https://doi.org:10.1364/ol.28.000278

11 Shim, S. H. & Zanni, M. T. How to turn your pump-probe instrument into a multidimensional spectrometer: 2D IR and Vis spectroscopies via pulse shaping. *Physical Chemistry Chemical Physics* **11**, 748-761 (2009). https://doi.org:10.1039/b813817f

12 Myers, J. A., Lewis, K. L., Tekavec, P. F. & Ogilvie, J. P. Two-color two-dimensional Fourier transform electronic spectroscopy with a pulse-shaper. *Opt Express* **16**, 17420-17420 (2008). https://doi.org:10.1364/OE.16.017420

13 Gaynor, J. D., Leger, J. & Khalil, M. JTu2A.8-JTu2A.8 (OSA).

14 Balasubramanian, M., Courtney, T. L., Gaynor, J. D. & Khalil, M. Compression of tunable broadband mid-IR pulses with a deformable mirror pulse shaper. *Journal of the Optical Society of America B* (2016). https://doi.org:10.1364/josab.33.002033

15 Gaynor, J. D., Courtney, T. L., Balasubramanian, M. & Khalil, M. Fourier transform two-dimensional electronic-vibrational spectroscopy using an octave-spanning mid-IR probe. *Opt Lett* **41**, 2895-2895 (2016). https://doi.org:10.1364/OL.41.002895

16 Gaynor, J. D., Petrone, A., Li, X. & Khalil, M. Mapping Vibronic Couplings in a Solar Cell Dye with Polarization-Selective Two-Dimensional Electronic–Vibrational Spectroscopy. *The Journal of Physical Chemistry Letters* **9**, 6289-6295 (2018). https://doi.org:10.1021/acs.jpclett.8b02752

17 Gaynor, J. D., Sandwisch, J. & Khalil, M. Vibronic coherence evolution in multidimensional ultrafast photochemical processes. *Nature Communications* **10**, 5621-5621 (2019). https://doi.org:10.1038/s41467-019-13503-9

18 Cerullo, G. & De Silvestri, S. Ultrafast optical parametric amplifiers. *Review of Scientific Instruments* **74**, 1-18 (2003). https://doi.org:10.1063/1.1523642

19 Balasubramanian, M., Courtney, T. L., Gaynor, J. D. & Khalil, M. Compression of tunable broadband mid-IR pulses with a deformable mirror pulse shaper. *Journal of the Optical Society of America B* **33**, 2033-2033 (2016). https://doi.org:10.1364/josab.33.002033

20 Balasubramanian, M., Reynolds, A., Blair, T. J. & Khalil, M. Probing ultrafast vibrational dynamics of intramolecular hydrogen bonds with broadband infrared pump-probe spectroscopy. *Chemical Physics* **519**, 38-44 (2019). https://doi.org:10.1016/j.chemphys.2018.11.018

21 Gaynor, J. D. & Khalil, M. Signatures of vibronic coupling in two-dimensional electronic-vibrational and vibrational-electronic spectroscopies. *The Journal of Chemical Physics* **147**, 094202 (2017). https://doi.org:10.1063/1.4991745

22 Bhattacharyya, P. & Fleming, G. R. Two-Dimensional Electronic-Vibrational Spectroscopy of Coupled Molecular Complexes: A Near-Analytical Approach. *Journal of*

Physical Chemistry Letters **10**, 2081-2089 (2019). https://doi.org:10.1021/acs.jpclett.9b00588

23 Arsenault, E. A., Yoneda, Y., Iwai, M., Niyogi, K. K. & Fleming, G. R. The role of mixed vibronic Q(y)-Q(x) states in green light absorption of light-harvesting complex II. *Nat Commun* **11**, 6011 (2020). https://doi.org:10.1038/s41467-020-19800-y

24 Arsenault, E. A., Yoneda, Y., Iwai, M., Niyogi, K. K. & Fleming, G. R. Vibronic mixing enables ultrafast energy flow in light-harvesting complex II. *Nature Communications* **11**, 1460-1460 (2020). https://doi.org:10.1038/s41467-020-14970-1

25 Conejero Jarque, E. *et al.* Universal route to optimal few-to single-cycle pulse generation in hollow-core fiber compressors. *Scientific Reports* **8**, 1-10 (2018). https://doi.org:10.1038/s41598-018-20580-1

26 Gueye, M., Nillon, J., Crégut, O. & Léonard, J. Broadband UV-Vis vibrational coherence spectrometer based on a hollow fiber compressor. *Review of Scientific Instruments* **87** (2016). https://doi.org:10.1063/1.4962699

27 Chang, H.-T. *et al.* Simultaneous generation of sub-5-femtosecond 400 nm and 800 nm pulses for attosecond extreme ultraviolet pump–probe spectroscopy. *Opt Lett* **41**, 5365-5365 (2016). https://doi.org:10.1364/ol.41.005365

28 Tseng, C.-h., Matsika, S. & Weinacht, T. C. Two-Dimensional Ultrafast Fourier Transform Spectroscopy in the Deep Ultraviolet. *Opt Express* (2009). https://doi.org:10.1364/oe.17.018788

29 Polli, D. *et al.* Broadband pump-probe spectroscopy with sub-10-fs resolution for probing ultrafast internal conversion and coherent phonons in carotenoids. *Chemical Physics* **350**, 45-55 (2008). https://doi.org:10.1016/j.chemphys.2007.12.021

30 Varillas, R. B. *et al.* Microjoule-level, tunable sub-10 fs UV pulses by broadband sum-frequency generation. *Opt Lett* **39**, 3849-3849 (2014). https://doi.org:10.1364/ol.39.003849

31 Grün, A., Austin, D. R., Cousin, S. L. & Biegert, J. Three-wave mixing mediated femtosecond pulse compression in β-barium borate. *Opt Lett* (2015). https://doi.org:10.1364/ol.40.004679

32 Liu, J., Okamura, K., Kida, Y., Teramoto, T. & Kobayashi, T. Clean sub-8-fs pulses at 400 nm generated by a hollow fiber compressor for ultraviolet ultrafast pump-probe spectroscopy. *Opt Express* **18**, 20645-20645 (2010). https://doi.org:10.1364/oe.18.020645

33 Baum, P., Lochbrunner, S. & Riedle, E. Tunable sub-10-fs ultraviolet pulses generated by achromatic frequency doubling. *Opt Lett* **29**, 1686-1686 (2004). https://doi.org:10.1364/ol.29.001686

34 Krebs, N., Pugliesi, I., Hauer, J. & Riedle, E. Two-dimensional Fourier transform spectroscopy in the ultraviolet with sub-20 fs pump pulses and 250-720 nm supercontinuum probe. *New Journal of Physics* (2013). https://doi.org:10.1088/1367-2630/15/8/085016

35 Rezvani, S. A. *et al.* Ultrabroadband tunable OPA design using a spectrally broadened pump source. *Opt Lett* **42**, 3367-3367 (2017). https://doi.org:10.1364/ol.42.003367

36 Kida, Y. & Kobayashi, T. Generation of sub-10 fs ultraviolet Gaussian pulses. *Journal of the Optical Society of America B* (2011). https://doi.org:10.1364/josab.28.000139

37 He, P. *et al.* High-efficiency supercontinuum generation in solid thin plates at 0.1 TW level. *Opt Lett* **42**, 474-477 (2017). https://doi.org:10.1364/Ol.42.000474

38 Lu, C.-H. *et al.* Generation of intense supercontinuum in condensed media. *Optica* **1**, 400 (2014). https://doi.org:10.1364/optica.1.000400

39 Cheng, Y.-C., Lu, C.-H., Lin, Y.-Y. & Kung, A. H. Supercontinuum generation in a multi-plate medium. *Opt Express* **24**, 7224-7224 (2016). https://doi.org:10.1364/oe.24.007224

40 Chang, H.-T. *et al.* Simultaneous generation of sub-5-femtosecond 400 nm and 800 nm pulses for attosecond extreme ultraviolet pump–probe spectroscopy. *Opt Lett* **41**, 5365-5365 (2016). https://doi.org:10.1364/OL.41.005365

41 Ermolov, A., Valtna-Lukner, H., Travers, J. & St.J. Russell, P. Characterization of few-fs deep-UV dispersive waves by ultra-broadband transient-grating XFROG. *Opt Lett* **41**, 5535-5535 (2016). https://doi.org:10.1364/ol.41.005535

42 Trebino, R. *Frequency-Resolved Optical Grating: The Measurement of Ultrashort Laser Pulses*. (Kluwer Academic Publishers, 2000).

43 Antoine Monmayrant, Sebastien Weber & Chatel, B. A newcomer's guide to ultrashort pulse shapingand characterization. *Journal of Physics B: Atomic, Molecular and Optical Physics* **43**, 103001 (2010). https://doi.org:10.1088/0953-4075/43

44 Khalil, M., Demirdöven, N. & Tokmakoff, A. Vibrational coherence transfer characterized with Fourier-transform 2D IR spectroscopy. *Journal of Chemical Physics* **121**, 362-373 (2004). https://doi.org:10.1063/1.1756870

45 Myers, J. A., Lewis, K. L. M., Tekavec, P. F. & Ogilvie, J. P. Two-color two-dimensional Fourier transform electronic spectroscopy with a pulse-shaper. *Opt Express* **16**, 17420-17428 (2008). https://doi.org:Doi 10.1364/Oe.16.017420

46 Shim, S.-H. & Zanni, M. T. How to turn your pump–probe instrument into a multidimensional spectrometer: 2D IR and Vis spectroscopiesvia pulse shaping. *Phys. Chem. Chem. Phys.* **11**, 748-761 (2009). https://doi.org:10.1039/B813817F

47 Zhang, Z., Wells, K. L., Hyland, E. W. J. & Tan, H.-S. Phase-cycling schemes for pump–probe beam geometry two-dimensional electronic spectroscopy. *Chemical Physics Letters* **550**, 156-161 (2012). https://doi.org:10.1016/j.cplett.2012.08.037

Chapter 3. VIBRATIONAL EXCITATION AND NONEQUILIBRIUM RELAXATION PROCESS FOLLOWING ESIPT

Herein, the coupled interplay of the motion of electrons and the motion of atomic nuclei is investigated for a model excited state intramolecular proton transfer (ESIPT) system, 10-hydroxy[h]benzoquinoline (HBQ), and its deuterated analog 10-(D)-hydroxy[h]benzoquinoline (DBQ). Quantitative measurements of the atomic displacement of the nuclei following photoinduced proton transfer are tracked utilizing 1D EV and 2D EV spectroscopies. The kinetic isotope dependence of the transferring proton is investigated. Statistical methods including singular value decomposition (SVD), target global analysis (TGA), and general Fourier transform analysis identify the high- and low-frequency vibrational modes that are coupled to the ESIPT process. Assignment of the modes is carried out with density functional theory (DFT).

The resulting 1D EV experiments show that following sub-15 femtosecond (fs) ESIPT in HBQ, two excited state absorption (ESA) regions report on proton acceptor modes centered around 1260 cm^{-1} and 1452 cm^{-1}. These ESA regions are found to be initially highly vibrationally excited and to relax on multiple timescales. During the initial relaxation of the 1452 cm^{-1} mode, an ultrafast decay is found to couple to the initial relaxation process suggesting the initial relaxation process is driven by an intramolecular vibrational redistribution (IVR) process. On a 17 ps timescale spectral up-frequency shifting is revealed and suggested to report on solvent mediated vibrational cooling (VC). An isotopic substitution of the benzoquinolinic proton is carried out to investigate the changes of the nonequilibrium relaxation process of DBQ. The resulting 1D EV spectrum of DBQ reveals following ESIDT reveals four strong ESA regions report on structural changes of the excited electronic state of DBQ which are assigned to two

backbone vibrations centered at 1467 cm^{-1} and 1509 cm^{-1}, a proton donor stretching mode at 1474 cm^{-1} and a proton acceptor dependent mode centered at 1367 cm^{-1}. TDDFT calculates and similar lineshape changes of the proton acceptor vibrational modes in HBQ and DBQ are suggested to exhibit IVR with a lifetime of 0.80 ± 0.05 ps and 1.2 ± 0.04 ps for HBQ and DBQ. Two additional decay time are measured across all coupled high frequency modes in HBQ and DBQ, an intermediate 17.0 ± 0.3 ps and 14.8 ± 0.4 ps decay assigned to solvent mediated vibrational cooling (VC) and a slow 377 ± 3 ps and 775 ± 12 ps decay representing the excited state lifetime. The results reveal that nonequilibrium dynamics on the proton acceptor mode undergo additional relaxation dynamics following ESIPT as compared with proton donor modes or backbone vibrations resulting from excess energy being dissipated in the proton acceptor modes following the proton transfer. The results motivate additional studies into the role proton vibronic states play in the IVR acceptor mode dependent relaxation and what role the excess kinetic proton energy plays in population of higher lying vibrational states of the IVR acceptor modes.

3.1 Studying the Excited State Photophysics of HBQ a Model ESIPT complex

Elucidating the mechanism of proton transfer is at the heart of a wide range of research in chemistry, biology and material sciences[1-4]. Recent photochemical studies[3,5-9] have set out to address the mechanism of proton transfer (PT) in photosynthesis. These works demonstrate that the fundamental mechanisms behind proton transfer is far from complete and that the key to understanding the charge and energy transfer mechanism involving PT lies with being able to directly map and correlate the specific radiative and nonradiative pathways in which PT takes place. The study of PT in molecules is not limited to a single reaction coordinate, as the work

here will demonstrate, but is directly coupled to both the relaxation of the electronic structure as well as specific vibrational modes which modulate the proton donor and proton acceptor distance (d_{DA}).

To characterize how PT is impacted by both anharmonic coupling of vibrational states and vibronic coupling between the electronic degrees of freedom and the individual vibrational modes, a systematic computational and experimental investigation on a model PT complex, 10-hydroxybenzo[h]quinoline (HBQ) will be conducted. HBQ contains an intramolecular hydrogen bond across its rigid three-member π-conjugated backbone. The rigidity of the π-conjugated system results in the hydrogen bond being very strong and makes HBQ a prime model system to study how anharmonic and vibronic couplings impact PT rate and the nonequilibrium relaxation dynamics in the excited state. The electronic properties and the ESIPT timescale of HBQ have been previously study by transient absorption[10-12], impulsive stimulated Raman[13-15], resonance Raman and time-resolved fluorescence spectroscopy[16] and postulate that the photophysics involve nonradiative relaxation following ESIPT and either involve ultrafast internal conversion (IC), vibrational cooling (VC) or intramolecular vibrational redistribution (IVR). HBQ exists entirely in the enol tautomer in the ground electronic state (S_0 (π))[17], however upon electronic photoexcitation to the S_1 (π^*) state HBQ undergoes ultrafast ESIPT inducing structural reorganization leading to the formation of keto tautomer that is stable in the excited state[18-21]. Relaxation to the ground state and back proton transfer then occur, reforming the ground state enol structure, see Figure 3-1. To fully map the anharmonicity and vibronic coupling present in HBQ isotopic labelling of the transferring proton and study of 10-deutroxybenzo[h]quinoline (DBQ) provides a synthetic tool to investigate the effect the proton coordinate directly couples to other vibrational modes in the system.

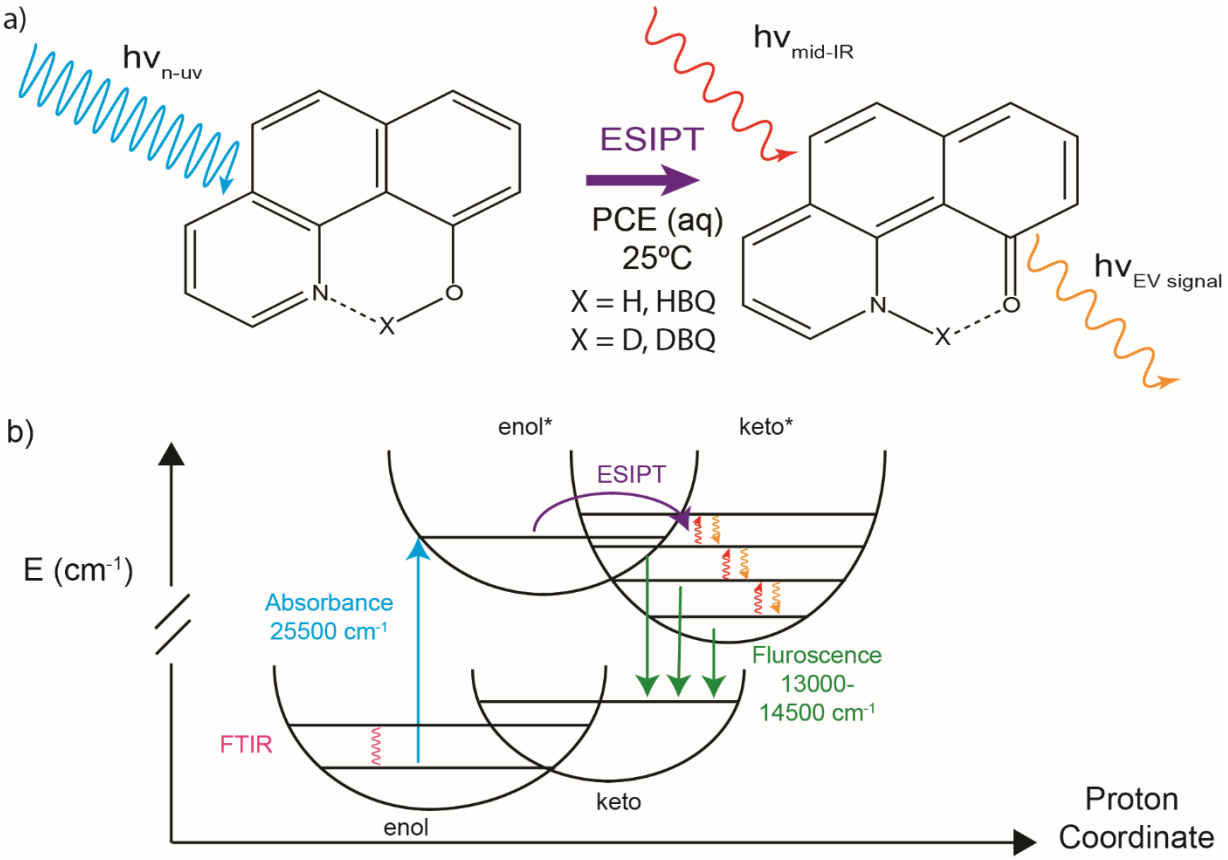

Figure 3-1 Excited State Intramolecular Proton Transfer (ESIPT) in isotopically labeled 10-Hydroxybenzo[h]quinoline (HBQ). a) System of interest, upon irradiation of a near-UV light rapid electronic and nuclear rearrangement in HBQ and DBQ occurs, causing the formation of the keto tautomer in the excited state. In this study, we probe the change of nuclear structural in the Excited keto* state after ESIPT using ultrafast mid-IR spectroscopy. b) Schematic of the system of interest potential energy. The system is initially in the enol ground state, FTIR (Pink, solid line) probes the vibrational structure of the ground state. UV-Vis absorption probes the allowed optical transition of the enol --> enol* state at 25500 cm-1 (blue, solid line). Transient mid-IR spectroscopy or 1D EV probes the vibrational structure of excited keto* state after ultrafast ESIPT occurs in the system of interest.

Chou and coworkers[18] first characterized the excited state photophysics of HBQ by deducing the keto state lived for 270 ps after photoexcitation and could be characterized by observing the fluorescence in the Stoke red-shifted spectral region. Later, time resolved fluorescence measurements in the same spectral region resolved the initial growth of the Stoke-shifted region[21] and fit constants of 13 (25) fs for HBQ (DBQ). These timescales were assigned based on the notion that the keto electronic state is populated in the 680-730 nm region,

suggesting that ESA in this region directly reports on the presence that the PT has occurred. However, this assignment creates a question regarding the nature of the excited state potential energy surface. Mainly, does the ESIPT occur mainly from an adiabatic electronic transition from the thermally populated enol transition state through an ultrafast internal conversion process or is the process mediated by nonadiabatic coupling of vibrational modes in which thermal energy is dissipated through the vibrations of the excited PT state. To address the question of how much nonadiabatic coupling plays in the ESIPT, a spectroscopy methods such as EV spectroscopy which directly probes the degree of nonadiabatic coupling in the excited electronic state is needed[22]. This is necessary since the prior nonlinear spectroscopy and fluorescence studies to date fail to directly probe the vibronic nature of the transition. For instance, time resolved fluorescence (TRF) measurements of HBQ and DBQ observe coherence oscillation in the emission of the 680-730 nm 'keto' fluorescence, if the ESIPT occurs through a adiabatic electronic transition the coherence of the vibrational modes is regularly expected to break through the internal conversion process[15,21]. Thus, supporting the initial claim made by Chou *et. al.*[23] that the remaining thermal energy in the system is dissipated through an internal conversion process between multiple electronic states, thus the oscillations of the TRF were assigned as electronic energy dissipation. However, recent work[10,17,24,25] have provided computation and transient absorption evidence which highlight that at early times, immediately following the ESIPT the keto state is predominately excited in the higher energy 680 nm region before relaxing over time towards the 730 nm emission. The frequency upshifting is accompanied with the presence of coherent low frequency vibrational modes that are on top of the keto emission suggesting that IVR processes are taking place. The latter studies also suggest that coherent nuclear wavepackets are superimposed on the electronic lifetimes of the keto

population and reveal IVR, VC and solvent reorganization play an active role in the nonequilibrium relaxation mechanism. Takeuchi *et. al.*[10] identified 4 low frequency vibrational modes were indirectly coupled to the keto emission in the excited state at 242 cm^{-1}, 392 cm^{-1}, 550 cm^{-1} and 692 cm^{-1}. Of the 4 low frequency vibrations the 242 cm^{-1} was assigned to a low frequency ring backbone bending mode that coupled strongly to the ν_{OH} stretching mode of the ground enol state. Interestingly this mode was also observed in the TRF studies[15,21], a latter IR pump/IR probe experiment which probed only the ground electronic state[26] and seen in impulsive stimulated Raman experiments[15]. Since the coherent oscillations were seen in multiple experimental procedures, even ones that were expected not to pick up on vibrations of the enol state, the question of how the ESIPT process proceeds through the excited state is again raised.

The technique of choice that can be used to address the role nonadiabatic coupling plays following ESIPT is electronic vibrational spectroscopy. Since the EV spectroscopy uniquely probes the change of the vibrations or nuclear degrees of freedom of the system following a change of the electronic degrees of freedom the technique can report directly how the two variables are coupled together, rather than indirectly reporting on the changes of the vibrational degrees of freedom like transient absorption (TA) or TRF. Additionally due to the advancements made in the generation of BBnUV pump pulses described in chapter 2 of this thesis, the exceptionally broadband pump pulses can be used to identify whether the vibrational modes indirectly observed in TRF and TA are formed from the ESIPT process itself or mediate the ESIPT nonadiabatically. Here, polarization-selective time-resolved 1D EV spectroscopy is performed to directly resolve the nonequilibrium structural dynamics involving the proton donor-acceptor and ring backbone vibrations of HBQ and DBQ. A new proposed nonequilibrium relaxation mechanism for HBQ and DBQ will be found and show that the ESIPT is directly

coupled to vibrational modes that exhibit proton donor and proton acceptor nuclei displacements in both the high frequency and low frequency region. The proton donor-acceptor and ring backbone vibrations located in the fingerprint region of the IR spectrum are directly probed during the 1D EV experiments as these vibrations are within the bandwidth of the pump pulses used in the experiment and provide an insight to the impulsive vibrational excitation involved in the ESIPT of HBQ and DBQ.

3.2 Experimental Methods

3.2.1 Sample Preparations and Steady State Spectra

This work utilized spectroscopic measurements of 3 separate samples, a HBQ, DBQ and PCE solvent sample. A 50 mM solution of HBQ (CAS: 33155-90-7) was dissolved in tetrachloroethane (PCE) and prepared from a commercially bought sample from TCI (>98% purity) without further purification. A 50 μM DBQ was prepared by isotopic substitution. A 50 mM HBQ in PCE was dissolved in a three-neck round bottom flask. Slow addition of a 3:1 stoichiometric ratio of sodium hydride was conducted. Extra caution should be exercised when adding sodium hydride, add slowly and dropwise to prevent quick buildup of hydrogen gas. During addition, the sample was kept under nitrogen and placed in an ice bath, while vigorously stirred to prevent excess hydrogen formation in the reaction sample. After hydrogen evolution, ~2 hours, was complete, an excess of deuterium oxide was added drop wise to react with any unreacted NaH and to replace the benzoquinolic hydrogen with a deuterium in the reaction vessel. The excess deuterium oxide prevented the reformation of the HBQ over the course of the experiment.

All steady state spectra were collected using a 50 mM concentration and a 50 μm pathlength using a fixed stationary FTIR cell. FTIR spectra were collected using a JASCO FT/IR-4100 spectrometer with 1 cm^{-1} resolution and are shown in Figure 3-4. UV-Vis spectra were obtained with a Jasco V-630 spectrometer with 1 nm resolution. The UV-Vis of HBQ and DBQ in PCE is shown below in Figure 3-2 and shows the electronic frequency region of interest. The UV-Vis shows the strong vibrational dependence of the ground electronic state of both HBQ and DBQ by revealing a vibronic progression in the S0 → S1 transition indicative of strong nonadiabatic coupling in ESIPT complexes. Here, the evolution of the excited state nonequilibrium relaxation mechanism following photoinduced ESIPT in HBQ and DBQ of the lowest lying vibronic transition 0→0', see Figure 3-2.

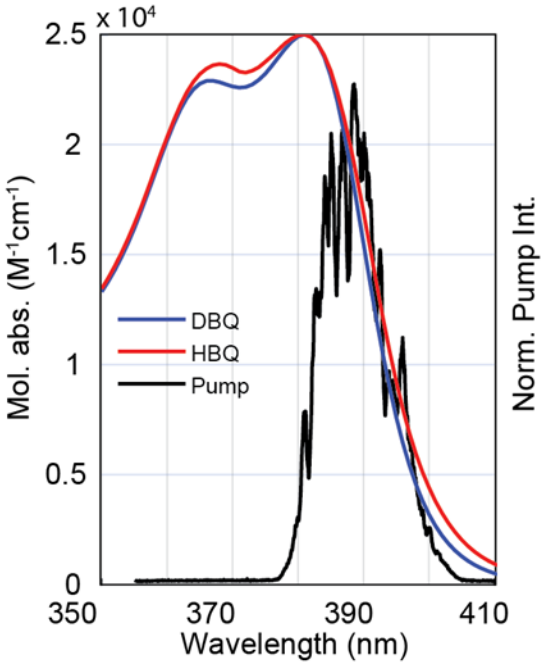

Figure 3-2. Electronic ground state spectra of HBQ and DBQ showing Vibronic progression of the S_0 ($\pi\pi$) → S_1 ($\pi\pi^*$) transition in HBQ (red solid) and DBQ (blue solid) plotted in molar absorptivity. The normalized pump spectrum (black solid) used in the 1D EV experiments probed the effect of exciting to the initially 0-0' enol* excited state.

Nonlinear spectra were collected for 50 mM samples of HBQ and DBQ in PCE prepared in N2 purged sample vials and flowed to the sample area using a Harrick Flow Cell. The flow

cell was constructed with a 1 mm thick CaF2 front window and 2 mm thick CaF2 back window separated by a 50 μm Teflon spacer. Special attention was placed on the DBQ sample to prevent air or water intrusion into the sample vessel containing the deuterium oxide layer. FTIR measurements collected after experimental runs confirmed negligible sample photodegradation for all 1D EV experimental runs.

3.2.2 Quantum Mechanical Calculations

Vibrational mode assignments of HBQ and DBQ were performed using TDDFT calculations performed on both the ground and first excited electronic state root of the HBQ and DQB (*for optimized structures see Appendix A)* using the Gaussian 16W package[27]. Optimization of the HBQ and DBQ ground state structures were performed using a tight convergence requirement with unrestricted B3LYP level of theory and 6-311++G(d,p) basis set, which is sufficient to accurately represent the enol ground state of the system[28]. Electronic transitions and vibrational frequencies were calculated using a B3LYP functional and the Aldrich Def2-TZVP basis set. The calculated UV-vis spectra of the optimized ground states are shown in Figure 3-3 were calculated for the first 6 electronic transition roots and qualitatively agree with previous computation work[17,24,28]. Under the calculation criteria, no effect of the isotopic substitution for the first 6 electronic roots was observed. The lowest electronic transition was centered at 363.86 nm with the second lowest transition being centered at 325.76 nm see Figure 3-3. The calculated UV-vis spectra thus support previous claims that the S_0 (π) à S_1 (π^*) transition is described by the UV-vis transition from 350-400 nm. To simulate the effect of a perturbation with 390 nm laser light, the excited state vibrational modes were obtained by TD-DFT calculation of the first excited state root. Vibrational mode calculations for the ground and excited state were performed

with anharmonic corrections for all modes using the *Hyak* supercomputer at the University of Washington, all vibrational modes computed returned non-negative transition energies. Optimization of the first excited state structure is notable for its obvious keto-like geometry and calculated fluorescence peaks at 598.5 nm and 426.5 nm for HBQ and DBQ.

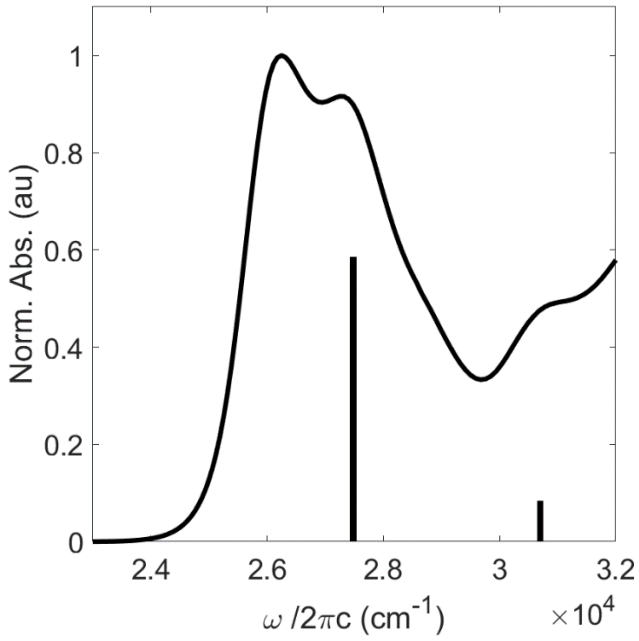

Figure 3-3 HBQ normalized UV-vis spectrum (solid black) overlaid with two lowest energy electronic transitions (black sticks). Lowest Energy transients were calculated using a B3LYP function and the Aldrich Def2-TZVP basis set.

3.2.3 Experimental Conditions for 1D EV and 2D EV spectroscopy of HBQ and DBQ

Polarization-selective 1D EV and 2D EV spectroscopy was conducted using a home-built spectrometer which has been previously described Figure 2-1[29-31]. Here, a sub-25 fs broadband near-UV (BBnUV) pulse covering the lowest energy vibronic transition, see Figure 3-2, was used as a pump pulse while a ~100 fs mid-IR probe pulse covering a broad range of IR-active vibrations in this system was used as the probe, see Figure 3-11. The third order signal was generated on top of the probe pulse in the collinear self-heterodyne pump-probe beam geometry.

The polarization-selective 1D EV experiments were performed by setting the polarization of the probe pulse at 45° with respect to the pump pulse before selectively choosing the polarization of interest with a second polarizer (analyzer) after the pulses interacted with the sample. Crossed (ZZYY) and parallel (ZZZZ) polarized 1D EV measurements were collected separately for all sample measurements. After the polarization of the probe was selected, the pump and probe beams were focused into the sample with the probe pulse reflection from an off-axis parabolic mirror (f=101.5 mm) and the pump focused through the back of the off-axis parabolic mirror with a UV antireflective-coated transmissive lens (f = 254 cm). Beam diameters at the focus were measured to be 200-240 μm and 185-200 μm with pulse energies of 400-500 nJ/pulse and 350-400 nJ/pulse for the pump and probe pulses, respectively. 1D EV pump-probe signals were generated at various pump-probe delay times, t_2, and controlled using a computer-controlled delay stage (Newport, XMS100). The pump-probe signal was routed to a spectrometer (Triax 190, Horiba Jobin Yvon) and spectrally dispersed using a 150 grooves/mm grating onto a 2×64 pixel mercury cadmium telluride (MCT) array detector (IR0144, Infrared Systems Development) resulting in ~1.5 cm^{-1} /pixel resolution. Multiple grating positions were selected to highlight key spectral changes in the experiment, for HBQ 7050 nm and 8000 nm grating positions were used and contained no spectral overlapping features while for DBQ 6850 nm, 7050nm and 7250 nm grating positions were stitched together. The delay time ranges used to measure the HBQ dynamics were: -1 ps to 2 ps using 20 fs time steps, from 2.1 ps to 10 ps with 100 fs time steps and from 20 ps to 500 ps using 10 ps time steps were collected for a total of 278 t_2 time points. The delay times for DBQ experiments were: -500 fs to 2 ps using 20 fs time steps, from 2.1 ps to 10 ps with 100 fs time steps, and from 20 ps to 480 ps using 10 ps time steps were collected for a total of 253 t_2 time points. For each experiment, 2000 difference spectra were collected

employing a 500 Hz chopper. A total of 10 (15) experimental runs for each grating position were collected, corresponding to a total of 20,000 (30,000) difference spectra per t_2 time point for HBQ (DBQ), for each polarization combination of the data presented.

2D EV spectra were collected for HBQ samples in the parallel polarization. Pump pulse pairs were generated with the aid of an acoustic optical programable dispersive filter (AOPDF) a total of 91 separate τ_1 delay time steps where collected, with a time step increment of 1.10 fs. Fourier transforming these delay steps meant under sampling according to the Nyquist limit for the pump pulses which was 0.64 fs, however, aliasing was not a factor as proper phase correction was considered to reconstruct the pump autocorrection spectrum without the effects of phase errors. The 2D EV correlation map was constructed from a single τ_2 waiting time of 200 fs, see polarization dependent 2D EV which is discussed later.

3.2.4 Global Target Analysis

Quantitative analysis of the time-resolved spectral evolution following ESIPT in HBQ and DBQ was preformed using target analysis with the Glotaran software package[32]. The fitted model incorporates two parallel components each with an irreversible sequential decay of increasing lifetimes (A→B and A→C→D→E). Due to the short IRF of the experiment, a nonresonant solvent response of TCE of ~100 fs was observed at early times in the time traces, therefore the first parallel component (A→B) accounted for solvent response see Figure 3-14. The second sequential component captures the time dependent spectral evolution in HBQ and DBQ following ESIPT. Here the sequential model (A→C→D→E) represents the population of each species as an exponential decay function where the change of absorptivity is denoted $\Delta A(\lambda, t) = \varepsilon_2(\lambda)c_2e^{-k_2t} + \varepsilon_3(\lambda)c_3e^{-k_3t} + \varepsilon_4(\lambda)c_4e^{-k_4t}$ with ε representing the absorptivity coefficient, c the concentration and *k* the decay coefficient for each species. Species 1 has the

same exponential form but represents the solvent response. Each species is convolved with a Gaussian function to account for the instrument response function and was fixed with a 120 fs response time measured using the nonresonant response time fix to a 250 μm thick silicon wafer (Figure 3-13). After fitting time zero, early time data was ignored to avoid spectral congestion from the free induction decay signal. Other global fit models were tested but did not reproduce the sub-ps dynamics as accurately as the current model due to the overlapping solvent and instrumental response at early times. The RMS of the final fits were 0.000866 for the spectrally stitched DBQ spectrum and 0.000422 and 0.000325 for the 7050 nm and 8000 nm grating positions of HBQ respectively. Within the decay of the IRF (k_1 = 80-104 fs^{-1}), a differential spectral artifact contribution is assigned to the nonresonant response of the TCE solvent, a separate parallel component accounts for this artifact whose initial spectral contribution is 20% (J_1 = 0.20). The remaining spectral contributions (J_2 = 0.80) are fit to sequential 3 component target model representing the solute nonequilibrium spectral dynamics. Given the solvent artifact decays on a similar timescale as the IRF, target modes using different initial spectral component values (J_1 = 0.05, 0.10, 0.15, 0.20 and 0.25) had negligible effect on the fitted time constants, here a value of 0.2 gave the best overall fit as determined by the RMS error.

with ε representing the absorptivity coefficient, c the concentration and *k* the decay coefficient for each species. Species 1 has the same exponential form but represents the solvent response. Each species is convolved with a Gaussian function to account for the instrument response function and was fixed with a 120 fs response time measured using the nonresonant response time fix to a 250 μm thick silicon wafer (Figure 3-13). After fitting time zero, early time data was ignored to avoid spectral congestion from the free induction decay signal. Other global fit models were tested but did not reproduce the sub-ps dynamics as accurately as the current model

due to the overlapping solvent and instrumental response at early times. The RMS of the final fits were 0.000866 for the spectrally stitched DBQ spectrum and 0.000422 and 0.000325 for the 7050 nm and 8000 nm grating positions of HBQ respectively. Within the decay of the IRF (k_1 = 80-104 fs^{-1}), a differential spectral artifact contribution is assigned to the nonresonant response of the TCE solvent, a separate parallel component accounts for this artifact whose initial spectral contribution is 20% (J_1 = 0.20). The remaining spectral contributions (J_2 = 0.80) are fit to sequential 3 component target model representing the solute nonequilibrium spectral dynamics. Given the solvent artifact decays on a similar timescale as the IRF, target modes using different initial spectral component values (J_1 = 0.05, 0.10, 0.15, 0.20 and 0.25) had negligible effect on the fitted time constants, here a value of 0.2 gave the best overall fit as determined by the RMS error.

3.3 Isotopic dependence of Ground State Fingerprint VIBRATIONAL MODES in HBQ and DBQ

Photoexcitation of HBQ results in ultrafast tautomerization reaction that occurs on the benzoquinolinic proton stretching coordinate from the enol to the keto form[28,33-36]. Though prior work has highlighted the timescale of the proton transfer, there remains question of how the proton transfer is initiated and whether the reaction proceeds through a adiabatic or nonadiabatic potential energy barrier[28]. A comprehensive understanding of the role that the benzoquinolinic proton and rigid π-conjugated backbone play in the excited state relaxation mechanism will be garnered and highlight the role vibronic couplings and high frequency vibrational modes play following ESIPT. To investigate the effect vibrational coupling plays in the ESIPT process a comprehensive study between different isotopes of the of the key nuclei, the benzoquinolinic proton, in HBQ is investigated. The fundamental basis of this study is to model how the

important nuclei impact the dynamics and kinetics of other reaction coordinates in both the ground and excited potential energy surface and act to measure the degree of anharmonicity in the system. To begin, the identification of the importance spectral characteristics of the ground state form of HBQ and DBQ are investigated.

Comparison of the ground state electronic spectra of HBQ and DBQ shows a change of the underlaying vibronic progression on the ground state enol state Figure 3-2. The ground electronic state spectrum of HBQ suggests the electronic state is strongly coupled to vibrational modes as indicated by the evident Frank-Condon like vibronic progression. The ground state electronic spectrum reveals two vibronic peaks, one centered about ~380 nm (0-0 transition) and the other centered about ~365 nm (0-1 transition) in both HBQ and DBQ, Figure 3-2. Interestingly though the vibronic progression centers appear to be little changed the amplitude of the 0-1 transition in DBQ is reduced from that of HBQ. Additionally, the line widths of the transitions appear to be narrowed in DBQ suggesting as exemplified by broader transition intensity on the red side of the spectrum.

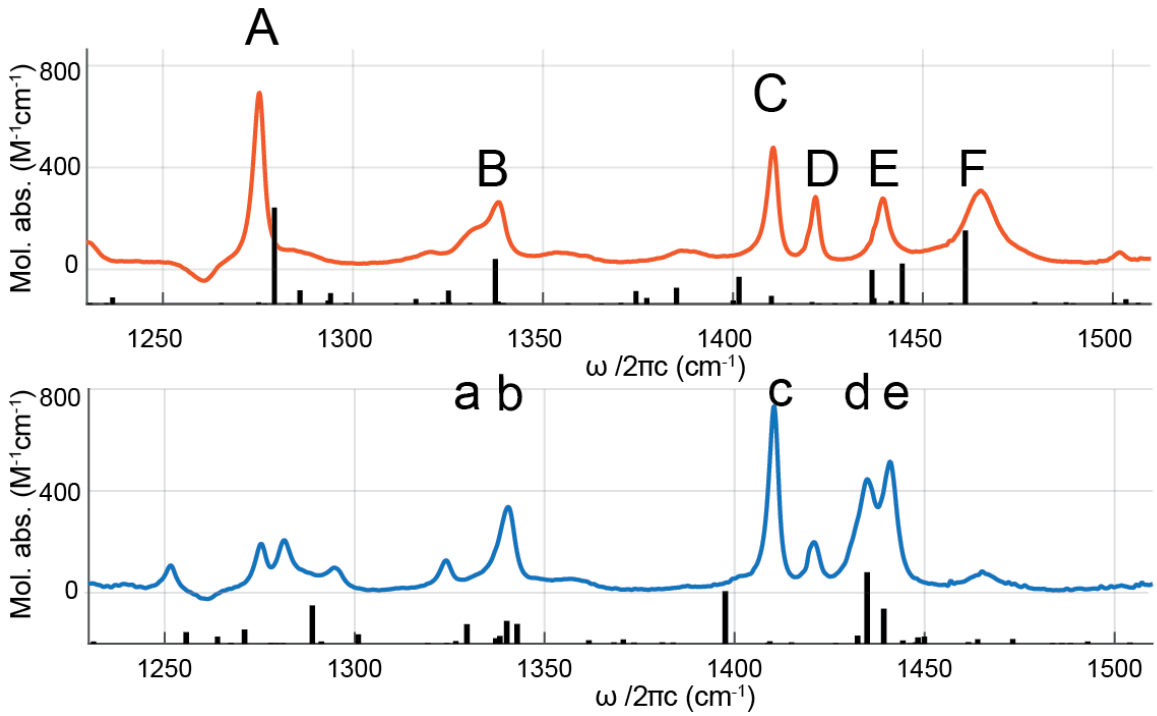

Figure 3-4 Ground state FTIR spectrum of HBQ (solid red) overlaid with DFT calculated ground state stick spectrum (black). Selected ground state vibrations are described by their harmonic energy mode from the DFT calculation. Ground state FTIR spectrum of DBQ (solid blue) overlaid with DFT calculated ground state stick spectrum (black). The changes of the multiple fingerprint vibrational modes elucidate that the benzoquinolinic proton is coupled with many vibrational modes in the ground state. Modes of interest are given a capital letter for HBQ and a lower case letter for DBQ and will be discussed in preceding sections.

To address the role of vibrational mode coupling in HBQ and DBQ, ground state electronic and vibrational spectra were compared to assess the extent the fingerprint vibrational modes and that of the benzoquinolinic hydrogen stretching mode depend on one other. As shown by the FTIR spectra of the fingerprint region (1200-1500 cm-1) in Figure 3-4, isotopic substitution of the benzoquinolinic hydrogen changes the amplitude and peak positions of nearly all ground state fingerprint vibrational mode. Here, the change in the peak amplitude of the vibrational modes is a direct result of the change in the overlap of the ground state transition dipole moment integral, simply put, the strength of the fingerprint vibration changes as a direct result of the isotopic substitution of the hydrogen. The change of frequency of the vibrational modes indicates the reduced mass of benzoquinolinic deuterium impacts the force constants of

most vibrational modes in the fingerprint region thus revealing the vibrational modes that are directly coupled to the benzoquinolinic hydrogen displacement, which is seen when comparing modes A, B, D, E and F in HBQ with a,d and e in DBQ.

To map the extent of how the high frequency mode are changing in the fingerprint region peak amplitudes and positions of ground state DFT frequency calculation with anharmonic corrections were conducted for HBQ and DBQ, Figure 3-4. Table 3-1 tabulates the vibrational modes with the largest amplitudes along with description of the ground state vibrational mode, the identification of the modes is characterized by the DFT transition frequency, see supplemental material. Anharmonic corrections compute the presence of combination, overtone and fundamental vibrational modes across the fingerprint region and reveal the major contributions to the ground state vibrational spectra. To aid in peak assignment, the solvent subtracted IR spectrum was fit to a sum of gaussians in the regions where the greatest 1D EV signals were observed, 1232-1282 cm^{-1} and 1400-1473 cm^{-1} for HBQ and 1361-1503 cm^{-1} for DBQ. To aid in the vibrational ground state peak assignments the regions of interest highlighted by the capital letters for HBQ and lower case letters in DBQ are fit to a series of gaussian peaks shown in Figure 3-9 and reveal the overall fits of the ground state vibrations are well described in Table 3-1. The fingerprint region of the ground and excited state contains vibrational modes described by backbone ring bending modes, carbonyl stretching modes, and bending modes that alter the proton donor, O atom, to proton acceptor, N atom distance. To differentiate the vibrational modes, mode descriptions are thus assigned based upon the character for the carbon chain holding the donor and acceptor to each other. A simplified mode label based on the DFT frequency label is given, superscripts denote excited state vibrational, while subscript H or D refers to HBQ or DBQ respectively.

Table 3-1. Selected ground state vibrational mode peak assignments of HBQ and DBQ with carbon labels denoted as carbons adjacent to the N and O atoms, with C_1 being bonded with the O and C_3 being bonded with the N. Subscripts: a) in unites of cm^{-1}, b) units of km/mol, c) modes are defined by COH bending mode N motion opposing bend is defines difference. oop: out of plane. ip: in plane.

HBQ Mode Label	Fit ω_{peak}[a]	DFT ω_{peak}[a]	DFT I_b	Mode Description	DBQ Mode Label	Fit ω_{peak}[a]	DFT ω_{peak}[a]	DFT I[b]	Mode Description
Peak **A**	1276.0	1279.3	72.8	C3-C2 str. w/C_1O-H rock	Peak **a**	1324.1	1329.5	12.8	C3-C2 str. w/C_1O-D bend
Peak **B**	1336.2	1337.5	35.5	C_1O-H wag ip w/N-C_3 str.	Peak **b**	1339.8	1340.0	15.0	C2-C1 str. w/C_1O-D bend
Peak **C**	1410.4	1401.6	22.6	ip N rock w/C_1-O-H bend[c]	Peak **c**	1410.2	1397.5	36.2	C3-C2 str. w/C_1O str.
Peak **D**	1440.0	1437.1	4.9	C_1-O-H sym. str	Peak **d**	1435.0	1434.8	50.5	C_1-O stretch
Peak **E**	1460.0	1444.6	34.4	C_1-O-H asym. str.	Peak **e**	1440.7	1439.3	24.7	C_1-O-D bend
Peak **F**	1466.2	1461.2	63.3	oop N rock w/C_1O-H bend[d]					

Comparing the computed DFT normal modes reveals the similar normal modes exhibit a frequency shift upon deuteration in the ground state. However, there are also a number of additional vibrational modes of which can be probed in the HBQ spectrum that aren't present in the DBQ spectrum. Furthermore, the majority of the computed fingerprint region vibrations are delocalized across the conjugated π-system backbone and contain a normal mode displacement that contains a ring vibrations in combination with a phenolic carbonyl stretch, bending mode or quinolinic nitrogen displacement. The assignment and identification of 6 fundamental ground state vibrations in HBQ and 5 fundamental ground state vibrations in DBQ are found in the probed fingerprint region about 1220-1500 cm^{-1}. Due to the delocalized nature of the ground state vibrational modes the vibrational modes that contain phenolic carbonyl displacements are challenging to describe but are shown by the molecular displacements in Figure 4-14.

The normal modes are predominately characterized by the nature of the proton donor-acceptor region of the molecule. Two vibrations that have similar character in and are carbonyl stretching modes are the **D**, **E** in HBQ and **c** and **d** in DBQ these normal modes contain similar

nuclei displacements and are affected by the deuteration of the benzoquilinic proton. The fundamental transition red shifts in DBQ as compared with HBQ, for example compared with the peak **E**. peak **d** red shifts by 9.8 cm^{-1} upon deuteration. Interestingly, this frequency upshift is not the same amongst similar fingerprint vibrations comparing the carbonyl bending modes of peak **F** with peak **e** the isotopic red shift is 21.9 cm^{-1} suggesting coupling of the proton is different amongst vibrational modes in the fingerprint region. The indirect effect the isotopic substation has on the vibrational transition frequency between the carbonyl bending and stretching frequencies highlights how the proton coordinate can couple with other vibrational modes in the ground state. This suggests that even in the ground state anharmonic coupling is playing an active role in dictating the potential energy surface, a observation which was confirmed by IR pump-IR probe experiments on HBQ and DBQ[26]. Strong anharmonic coupling of the vibrations indicates that nonadiabatic coupling can have an outsized impact on the nonequilibrium relaxation mechanism. Given HBQ and DBQ undergo rapid tautomerization in the excited state understanding the role the strong vibrational coupling plays during the course of the ultrafast internal conversion process using 1D EV can directly aid in the understanding of how the proton transfer is initiated and whether the reaction proceeds through a adiabatic or nonadiabatic potential energy barrier[28]

3.4 COMPUTATIONAL DETERMINATION OF ACTIVE VIBRATIONS INVOLVED IN ESIPT PROCESS BY TDDFT CALCULATIONS

To elucidate the role that nonadiabatic coupling of the fingerprint vibrational modes to the proton transfer coordinate and the electronic rearrangement plays following ESIPT, TDDFT calculations were conducted to identify the major vibrational modes that couple to the excited state potential energy surface. Here, computational methods used to probe the excited state

fingerprint vibrations that participate in the excited state relaxation mechanism are obtained using excited state TD-DFT calculations with anharmonic corrections. Computationally, TD-DFT frequencies were calculated on the optimized first excited state root (S_0 (π) → S_1 (π^*)). The results of the excited state TD-DFT calculations as compared with the ground state DFT normal modes suggest the vibrations present in the ground state are completely altered following proton transfer. Since the benzoquilinic proton in the enol configuration is an active coordinate in the carbonyl stretching and stretching modes the loss of this coordinate directly impacts the vibrational transition frequencies of the fingerprint vibrational modes. Lost are the present of the vibrations localized on the proton donor side of HBQ and DBQ are gained are the vibrational transitions on the proton acceptor region of the molecule, or the quinolinic nitrogen region.

Following ESIPT the hydrogen (deuterium) accepting nitrogen plays a more active role in the fingerprint vibrational modes in both HBQ and DBQ. Along the calculated first excited state root, both HBQ and DBQ adopt a fully keto optimized geometry where the hydrogen (deuterium) binds to the quinolinic nitrogen resulting in a change in character for the excited state vibrational modes. Table 3-2 compares the excited state normal mode coordinates for two fundamental vibrational modes of the keto* geometry. These modes are denoted by their capitalization as was used in the ground state: HBQ, capital letters, and DBQ lowercase letter however the excited state vibrations are denoted by the use of a prime. The two vibrational modes denoted below will be assigned to the ESA regions seen in the 1D EV spectrum, however the isotope dependence of Peak **A**' and Peak **b**' is noteworthy as these two peaks report on similar displacements of the normal mode coordinates, each of which incorporates a newly formed carboxylate stretching with a displacement of the proton acceptor quinolinic nitrogen coordinate. Peak **A'** with a vibrational transition energy of 1448.9 cm^{-1} is 82 cm^{-1} blue shifted

from the deuterated mode of the same normal mode displacement of 1366.9 cm^{-1}. The difference between the calculated isotope effect of the ground and excited state suggests in the excited state the degree of anharmonic coupling between the proton coordinate and the fingerprint vibrations is strongly than that of the ground state.

Table 3-2. Selected excited vibrational mode peak assignments of HBQ and DBQ with carbon labels denoted as carbons adjacent to the N and O atoms, with C_1 being bonded with the O and C_3 being bonded with the N. Subscripts: a) in unites of cm^{-1}, b) units of km/mol, c) modes are defined by COH bending mode N motion opposing bend is defines difference. oop: out of plane. ip: in plane.

HBQ Mode Label	*DFT* $\omega_{peak}{}^{a}$	DFT I^{b}	Mode Description	*DBQ Mode Label*	*DFT* $\omega_{peak}{}^{a}$	DFT I^{b}	Mode *Description*
	1268.4	74.2	H-N-C_3 rock w/ *ip* C_1=O str.		1366.9	11.6	D-N-C_3 aym. str. w/ C_2-C_1=O sym. str.
	1448.9	30.2	H-N-C_3 aym. str. w/ C_2-C_1=O sym. str	Peak **b'**	1473.8	44.1	D-N-C_3 bend w/ C_2-C_1=O rock

In summary, ground, and excited state TD-DFT frequency calculations reveal the fingerprint region molecular vibrations in HBQ and DBQ are very delocalized and many directly coupled to the benzoquilinic hydrogen (deuterium). Upon excitation to the first excited state the system adopts a keto molecular geometry and relaxes along a highly anharmonicity excited state potential energy surface. Comparison of the fundamental fingerprint vibrational modes reveals the main fundamental vibration modes that couple to the excited state have different vibrational character than the ground state shifting from oxygen-containing (carbonyl) stretching and bending character to nitrogen-contain bending character. Isotopic substitution of the benzoquilinic hydrogen in HBQ red shifts the vibrational transitions which couple to the hydrogen transfer reaction coordinate and suggests the anharmonic coupling of the excited keto state is greater than that of the ground state.

3.5 1D EV SPECTROSCOPY CAPTURES TIME-DEPENDENT SPECTRAL CHANGES OF VIBRATIONS REPORTING ON ESIPT IN HBQ

DFT and TD-DFT calculations elucidate that fingerprint vibrational modes in HBQ and DBQ are strongly coupled to the proton transfer coordinate and that isotopic substitution of the benzoquinolinic hydrogen alters the vibrational coupling in this region. 1D EV seeks to experimentally confirm and extract the time-resolved structural dynamics and nonradiative relaxation mechanism of HBQ and DBQ following ESIPT by monitoring how the population of the fingerprint vibrational modes change as a result of the selective motion of the transferring hydrogen (deuterium) following photoexcitation. Time-resolved 1D EV spectrum of HBQ and DBQ are shown in Figure 3-5 and Figure 5, respectively, and were collected with a mid-IR probe that captured the fingerprint vibrational modes of interest, see supplemental information for pulse characterization. The HBQ 1D EV spectrum in Figure 3-5, reveals 3 GSB features (negative signals) where strong sharp transitions are centered at 1276 cm^{-1}, 1410 cm^{-1}, and 1422 cm^{-1}, which were previously assigned to Peak A, B and D in the ground state respectively, Table 3-1. The GSB transitions correspond to vibrational transitions in the enol tautomer and therefore as the keto excited state relaxes back to the ground state a small amplitude increase in the GSB peaks is observed from comparison of the early and late time pump-probe traces.

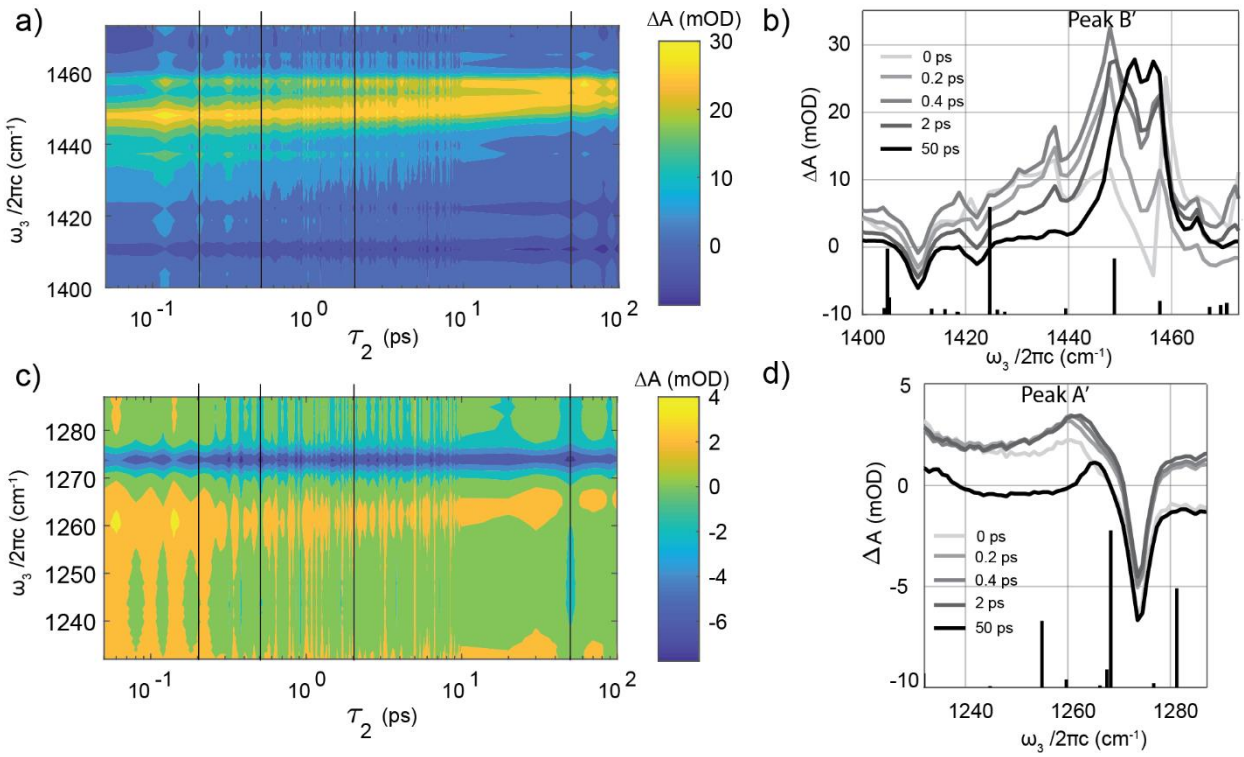

Figure 3-5. Isotropic 1D EV experimental traces of HBQ**.** a-b) 7050 nm grating position. c-d) 8000 nm grating position. a, c) show full experimental contour maps. Mode specific vibrational cooling, shown by time dependent frequency upshifting is observed for Peak **A'** and **B'** modes. Dynamic spectral frequency up-shift indicates that IVR and VC processes are prevalent in the nonequilibrium relaxation mechanism of HBQ following ESIPT. b,d) Highlight selected pump probe frequency slices at the black vertical slides with the TDDFT calculated excited state vibrational mode stick spectrum overlaid.

Given the large electronic structural change following the enol to keto tautomerization, vibrations in the excited state are greatly displaced from their corresponding ground state vibrations, i.e., the spectral distribution of vibrational transitions in the excited state will be different for modes coupled to the ESIPT confirming the computation evidence. The two excited state 2 ESA features (positive signal) identified by the 1D EV spectrum are assigned to Peak A' and B' from Table 3-2. Interestingly **A'** is observed to be slightly redshifted from a ground state vibration, **A** which contains similar normal mode displacement even accounting for the proton transfer coordinate, in contrast to **B'** which is a very board, strong transition, 30 mOD, which is spectrally convoluted and spectrally overlapped with peak **D**, **E** and **F**.

Though peaks **A'** and **B'** vary in amplitude and report on different vibrational modes both ESA contain some degree of spectral frequency up shifting as evident by the change of peak positions for all the strong sharp transitions over multiple timescales. For example, at early times, 0.2 ps, the ESA **B'** is centered between 1437 cm^{-1} and 1448 cm^{-1} with a maximum amplitude of 17 mOD and 32 mOD respectively but by 2 ps the absorption drops to 8 mOD and 28 mOD while intensity grows in at 1448 cm^{-1} and 1458 cm^{-1}, the corresponding decline of the 1437 cm^{-1} and 1448 cm^{-1} and growth of the 1458 cm^{-1} transitions continues until 50 ps when the absorbance of the 1438 cm^{-1} is near 1 mOD and at 26 mOD at 1452 cm^{-1}. The same spectral phenomenon also occurs, albeit with less overall peak intensities, at 1255, 1261, 1266 cm^{-1} frequencies. Spectral up shifting was observed in the earlier TRF and TA measurements on HBQ and DBQ but was indicated to be caused by solvent cooling[17,19,21,23], given the direct frequency upshifting observation in 1D EV IVR process is more likely. However, spectral shifting in the 1D EV impacts peak assignment given the intense for example, is between transferred from 1437 cm^{-1}, 1448 cm^{-1} and 1458 cm^{-1} transitions and TDDFT calculations shows different combination bands in this spectral region it is unknown whether the ESA observe is reporting on 1 vibration or many. To address the peak assignment concern global target analysis is used to isolate the spectral components which dynamically change over the course of the 1D EV dataset.

3.5.1 Global target analysis reveals timescales of nonequilibrium relaxation dynamics.

Target analysis quantifies the different spectral components or species associated with different spectrum (SADS) that are present in each spectrum and fits the corresponding population lifetimes of each spectral component[32,37,38]. Global Target Analysis was conducted to extract the SADS and time components of the isotropic 1D EV spectrum of HBQ and DBQ the results of the HBQ target model are shown in Figure 3-6. The compartmental model used in the

target analysis separated four components into two parallel paths: a three components sequential pathway and single spectrum.

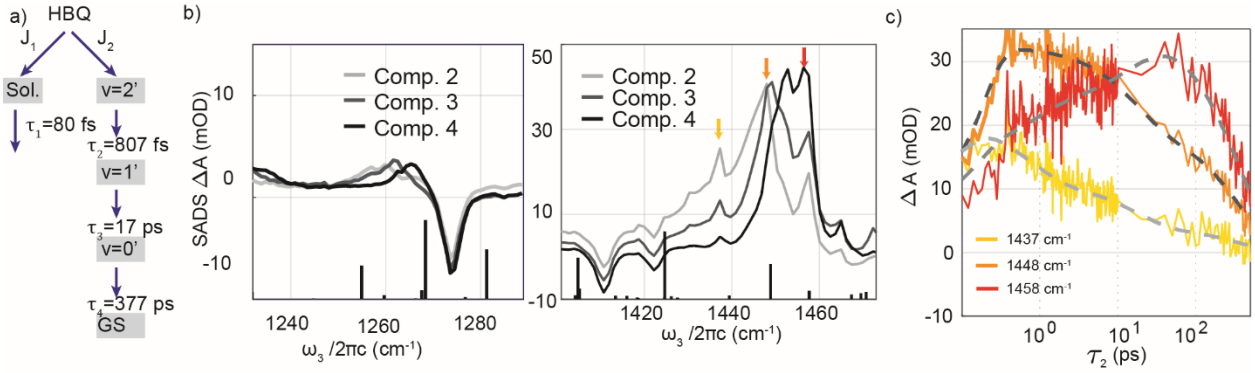

Figure 3-6. Target Analysis of transient IR spectra of HBQ reveal Vibrational Cooling timescale. a) Compartmental Model used to conduct target analysis, initial populations of parallel components, J_1 and J_2 were 0.2 and 0.8 respectively and corresponding component lifetimes indicating Vibrational cooling timescale. b) SADS components for k_2, k_3 and k_4 overlaid with computed TDDFT excited state vibrational modes (stick spectrum). Colored arrows denote ω_3 positions are shown in the transient pump probe slices shown in panel c. c) Selected transient pump-probe slices showing vibrational cooling in the peak b' region the target analysis quantifies the lifetimes of the hot vibrational states after ESIPT as indicated in Figure 3-1. and how there is a mode specific vibrational cooling that has an isotropic dependent lifetime.

artifact component that encompasses the nonresonant solvent response. For the corresponding analysis this same compartmental model was used for each spectrum analyzed yet extracted different SADS and spectral lifetimes for HBQ and DBQ systems. The target analysis resulted in the SADS lifetimes given in Figure 3-6a for HBQ. For HBQ the fast non-resonant solvent response occurred within the instrumental response of 120 fs and is denoted as, τ_1, with extracted lifetimes of 80 fs, 104 fs for HBQ and DBQ respectively. The remaining parallel pathway contains the remaining three components, denoted as 2, 3 and 4 Figure 3-6. The 2nd SADS component fit time constants of 0.80 ± 0.05 ps, the 3rd SADS component grows in as the 2nd component decays and has a lifetime of 17.0 ± 0.3 ps and the 4th SADS component is a long-lived component, with a lifetime of 377 ± 3 ps. The target model thus shows a clear frequency shifting of both ESA peaks in HBQ.

3.5.2 Quantification of anharmonic coupling and vibrationally relaxation mechanism in HBQ

To garner insight behind the vibrational cooling process occurring in the 1D EV spectra the 3 major components of the SADS spectra of peak B' were fit to a series of 3 Gaussian functions to match the number of SADS spectra found in the target mode. The peak was fit to a sum of 3 gaussian functions of the form,

$$\Delta A_{SADS} = \sum_{i=1}^{3} a_i e^{(x-b_i)^2/2c_i^2}$$

,

with the resulting fitted parameters given in Figure 3-7. Where a_i represents the amplitude of peak i, b_i represents the center position peak i and c_i represents the standard deviation. Table 3 lists the peak area, center position and full-width-half-maximum (FWHM) , of the fitted gaussian peaks and is visualized in Figure 3-7. Comparison of the three peaks revealed the amplitude of the red-shifted features declined across SADS components. At early times, the SADS components revealed the 3 peaks centered at 1439cm^{-1}, 1448cm^{-1}, and 1457 cm^{-1}. The evolution of the spectral intensity is assigned to the thermally cooling of the peak B' vibrational mode via three vibrational quanta of excitation ν = 2',1',0' corresponding to a vibrational progression of the **B'** calculated normal mode. The spectral intensity and width of the hot vibrational states is larger at early times. For instance, the broad peak centered at 1438 cm^{-1} is fit to a 20 cm^{-1} width and corresponds to a sub-ps homogeneous lifetime.

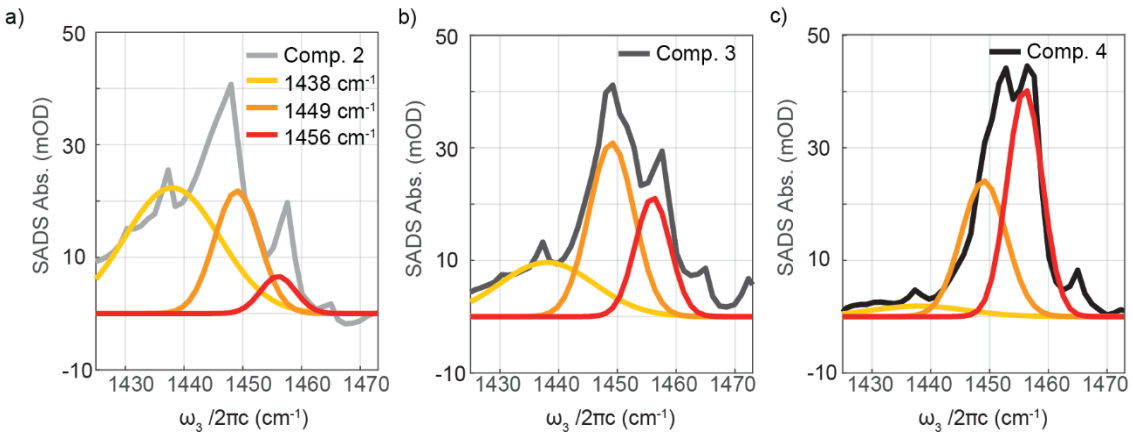

Figure 3-7. Vibrational cooling in HBQ illustrated by fit of SADS components, frequency upshifting is indicative of the anharmonic potential energy surface of the keto* state. Fit of SADS components, a) component 2 (light grey, solid), b) component 3 (dark grey, solid) and c) component 4 (black, solid). The fits indicate the dominate vibrational state of the 1456 cm^{-1} vibrational mode upshifts over the vibrational cooling times of 807 fs and 17 ps. The SADS spectra shown are fit to three gaussians curves with a constant width, and frequency using nonlinear least squares method. The 1438 cm^{-1} peak (yellow, solid) corresponds to the ν'=2 and is lifetime broadened to 20 cm^{-1} and makes up the majority of component 2, the vibrational energy then shifts to the ν'=1, 1449 cm^{-1} peak (orange, solid) and lastly to the ν'=0, 1456 cm^{-1} peak (red, solid).

3.5.3 1D EV spectral Analysis of DBQ

Changes of the potential energy surface in the ground state were readily identified by changes in the IR frequencies between HBQ and DBQ. Upon deuteration the nonequilibrium dynamics of DBQ are expected to be impacted compared to HBQ dude to the difference in anharmonic coupling of the excited state. As was shown in the previous section, the isotropic 1D EV spectrum of HBQ revealed the presence of time-dependent spectral frequency shifting of the vibrational modes that are were attributed to both peak **A'** and **B'** which both reported on fingerprint vibrational modes modulating proton donor and acceptor distances. From the TD-DFT analysis, upon isotopic of the benzoquinolinic hydrogen in the 1360-1520 cm^{-1} spectral region DBQ reveals a harmonic shift of Peak **a'** by up to 82 cm^{-1} in the excited state, given the

similar HBQ model peak **B'** exhibited a large spectral up frequency shift, the 1D EV of DBQ is analyzed to provide insight behind the ESIDT process.

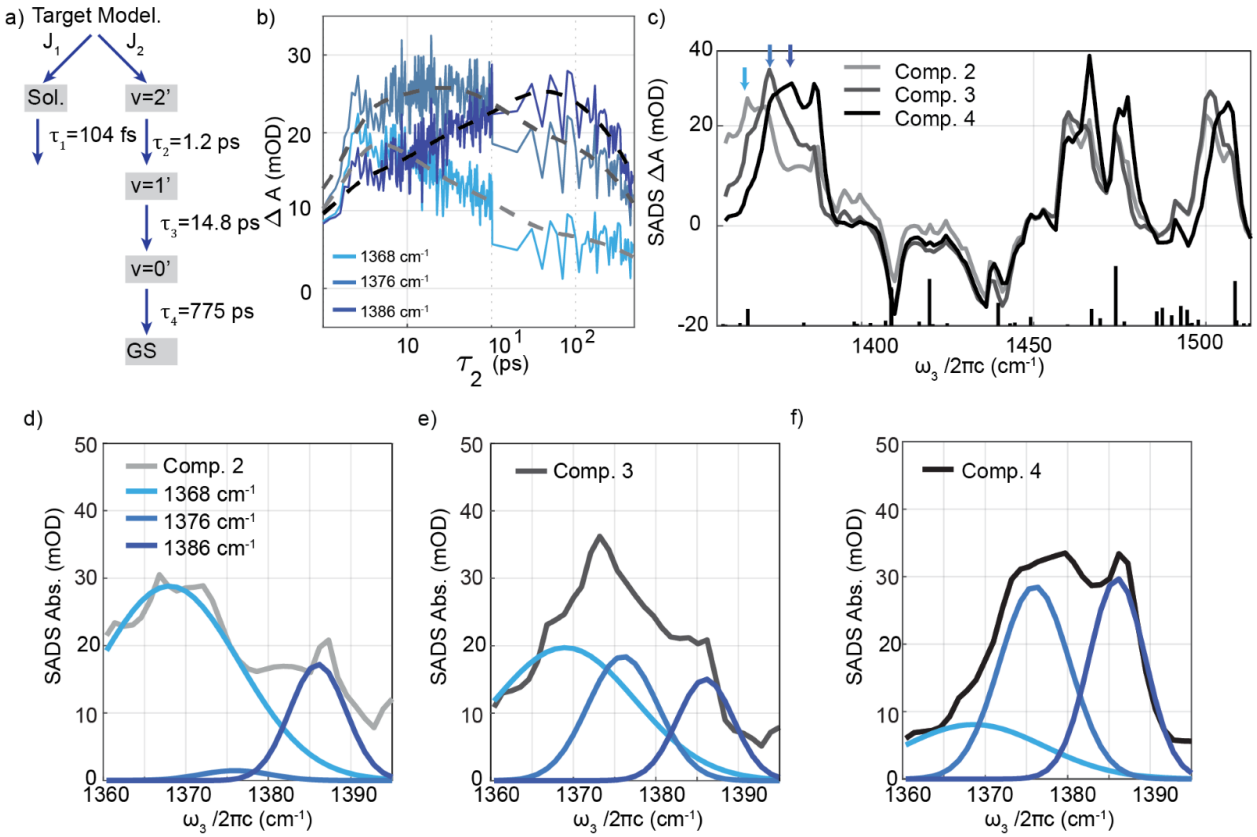

Figure 3-8. Isotopic Dependence of Vibrational Cooling, nonequilibrium relaxation process of DBQ. a) Compartmental Model used to conduct target analysis fit to the DBQ transient mid-IR spectrum. Due to the isotopic dependence of the deuterated proton, IVR and VC occurred at a lower frequency ESA and were observed to be kinetically slowed compared to HBQ. b) selected pump probe time traces of the DBQ 1D EV (blue, solid lines), with target model fit shown (dashed lines). c) Species associated difference spectra (SADS) of DBQ 1D EV (solid black lines) overlaid with the TDDFT excited state vibrational modes (black, stick spectrum) showing the dynamic frequency upshifting occurring in the 1386 cm^{-1} ESA. d-f) Fit of SADS components d) component 2 (light grey, solid), e) component 3 (dark grey, solid) and f) component 4 (black, solid).

To elucidate ESA peak assignments for the 1D EV spectrum of DBQ, the intense TD-DFT vibrational modes are overlaid in Figure 5a. Interestingly, in general the fundamental excited vibrational modes in DBQ are weak compared to combination bands, suggesting for

DBQ there is greater anharmonicity of the excited state than in HBQ. The strong ESA features in DBQ are assigned to the corresponding TD-DFT vibrational modes with the highest intensity with ESA peaks centered at 1374 cm-^{1}, 1458 cm^{-1}, 1475 cm^{-1} and 1503 cm^{-1} assigned as: ν'$_{D,48}$, ν'$_{D,15\text{-}30}$, ν'$_{D,52}$, and ν'$_{D,10\text{-}27}$ respectively see Table 2. Of these peaks the fundamental vibrational modes, ν'$_{D,48}$, ν'$_{D,15\text{-}30}$ and ν'$_{D,52}$, contain displacement along the d_{DA} coordinate with the combination band ν'$_{D,15\text{-}30}$ made up of low frequency ring backbone bends vibrations and the combination band ν'$_{D,10\text{-}27}$ comprised of vibrations that are perpendicular to the d_{DA} coordinate, out-of-plane vibrations. The 4 ESA features in DBQ contain vastly different molecular displacements, but the change of absorptivity of the modes was similar ~20-25 mOD in comparison to HBQ where only the ν'$_{H,50}$, and ν'$_{H,51}$ peaks had this large of peak intensities. In HBQ the ν'$_{H,50}$, and ν'$_{H,51}$ peaks contained evidence of frequency up-shifting which is observed for the 4 ESA features in DBQ however there is an appreciable difference between the frequency up-shifting in the 1360-1390 cm^{-1} region, the ν'$_{D,48}$ mode that containing carbonyl stretching characterize, from that of the other 3 ESA features. Frequency up-shifting in the 1360-1390 cm^{-1} region exhibits a frequency shifting on 2 time-scales similar to frequency upshifting to what is observed in the 1420-1460 cm^{-1} frequency region of HBQ. In DBQ an initial population grows at 1366 cm^{-1} in the first 0.4 ps, which decays as a population grows in at 1374 cm^{-1} during a 2 ps timescale before a last frequency up-shift occurs to 1381 cm^{-1} at long times. As evidence by the pump probe time traces the ν'$_{D,15\text{-}30}$, ν'$_{D,52}$, and ν'$_{D,10\text{-}27}$ modes also undergo frequency up-shifting at long times but not in the short timescale, indicating there is a mode specific vibrational population transfer process that is occurs in HBQ and DBQ. Additionally, the presence of vibrational up-shifting across multiple vibrational modes of DBQ indicates that vibrational energy redistribution following ESIDT also occurs on an anharmonic excited state

potential energy surface. To quantify and extract the relevant population lifetimes and nonequilibrium dynamics occurring in the excited state potential energy surface after ESIP(D)T a quantitative method that extracts the dependent spectral and temporal components of the entire 1D EV spectrum is needed: Target Analysis.

For HBQ the fast non-resonant solvent response occurred within the instrumental response of 120 fs and is denoted as, τ_1, with extracted lifetimes of 80 fs, 104 fs for HBQ and DBQ respectively. The remaining parallel pathway contains the remaining three components, denoted as 2, 3 and 4 in Figs. 6b. and 6e. The 2nd SADS component fit time constants of 0.80 ± 0.05 ps (1.22 ± 0.04 ps) for HBQ (DBQ) and yields a kinetic isotope effect (KIE) of 1.53 ± 0.11. The 3rd SADS component grows in as the 2nd component decays and has a lifetime of 17.0 ± 0.3 ps (14.8 ± 0.4 ps) for HBQ (DBQ) and yields a KIE of 1.15 ± 0.04. The 4th SADS component is a long-lived component, with a lifetime of 377 ± 3 ps (775 ± 12 ps) for HBQ (DBQ) and yields a KIE of 2.06 ± 0.04. Interestingly the target analysis shows the SADS components have isotopic dependent lifetimes.

Figure 3-8 illustrates the spectral upshifting of the proton (deuterium) accepting normal modes in HBQ and DBQ across the SADS components and shows narrowing blue shifted features in the $\nu'_{H,51}$ *and* $\nu'_{D,48}$ modes. Additionally, though a clear VC progression can be fit, during the sub-ps timescale, peaks centered at 1439 cm^{-1} and 1458 cm^{-1} in HBQ and a peak centered at 1387 cm^{-1} in DBQ, in plane backbone combination bands, are seen to have non-zero peak intensity on top of the broad v=2' in HBQ as well as overlapping spectral intensity that is blue shifted from the v = 0' vibrational mode. The in plane combination bands have altering intensities over the first ps after ESIPT (Figure 3-6) suggesting that IVR between proton acceptor

modes and low frequency in plane ring bending modes is occurring on the same timescale as the VC relaxation timescale from v =2' to v = 1'.

modes. Additionally, though a clear VC progression can be fit, during the sub-ps timescale, peaks centered at 1439 cm^{-1} and 1458 cm^{-1} in HBQ and a peak centered at 1387 cm^{-1} in DBQ, in plane backbone combination bands, are seen to have non-zero peak intensity on top of the broad v=2' in HBQ as well as overlapping spectral intensity that is blue shifted from the v = 0' vibrational mode. The in plane combination bands have altering intensities over the first ps after ESIPT (Figure 3-6) suggesting that IVR between proton acceptor modes and low frequency in plane ring bending modes is occurring on the same timescale as the VC relaxation timescale from v =2' to v = 1'.

3.6 APPENDICES

3.6.1 Ground State Vibrational Mode Fit of HBQ and DBQ

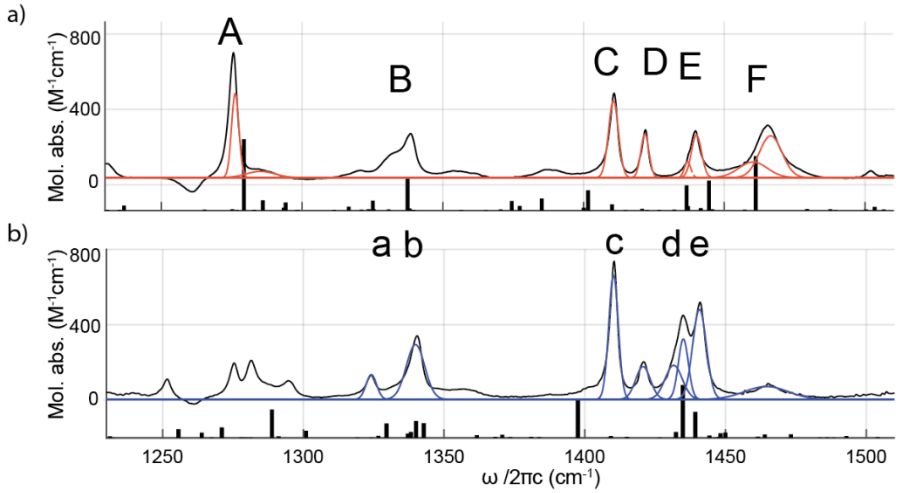

Figure 3-9. Gaussian peak fit of FTIR spectrum for a) HBQ (solid orange) and b) DBQ (solid blue) overlaid with ground electronic state DFT calculations stick spectrum with main peaks labeled by their corresponding regions of interest discussed in text. Solid black line indicates solvent subtracted FTIR of HBQ (top) and DBQ (bottom).

3.6.2 Pixel Calibration curve and probe spectrum

The pulse energies for this experiment were between 850-950 nJ/pulse for the pump energy and 400 nJ/pulse for the probe. A FTIR before and after the experiment revealed no difference in optical or IR absorption of the sample indicated the sample did not photodegrade over the course of the experiment. The probe spectrum was calibrated to the sample spectrum and a water line spectrum to determine the pixel calibration axis in ω_3,Figure 3-10 shows the pixel calibration curve and calibrated probe spectrum overlaid with the DBQ FTIR and water vapor spectrum, as shown the pixel resolution is about ~1 cm^{-1}. The calibrated probe spectrum for HBQ is shown in and shows tail of the probe spectrum in the red side of the mid-IR spectrum.

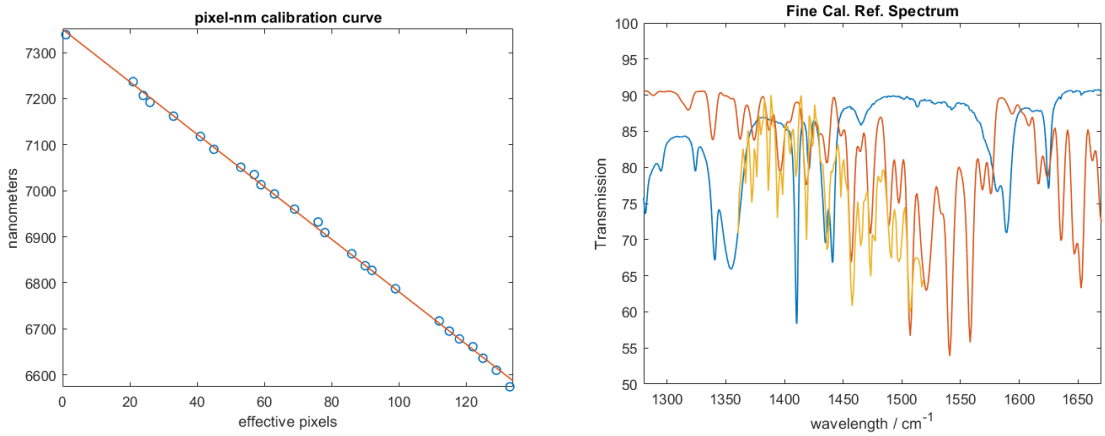

Figure 3-10. Calibration curve (*left*) and calibrated probe spectrum overlaid with DBQ FTIR spectrum and water vapor spectrum (*right*).

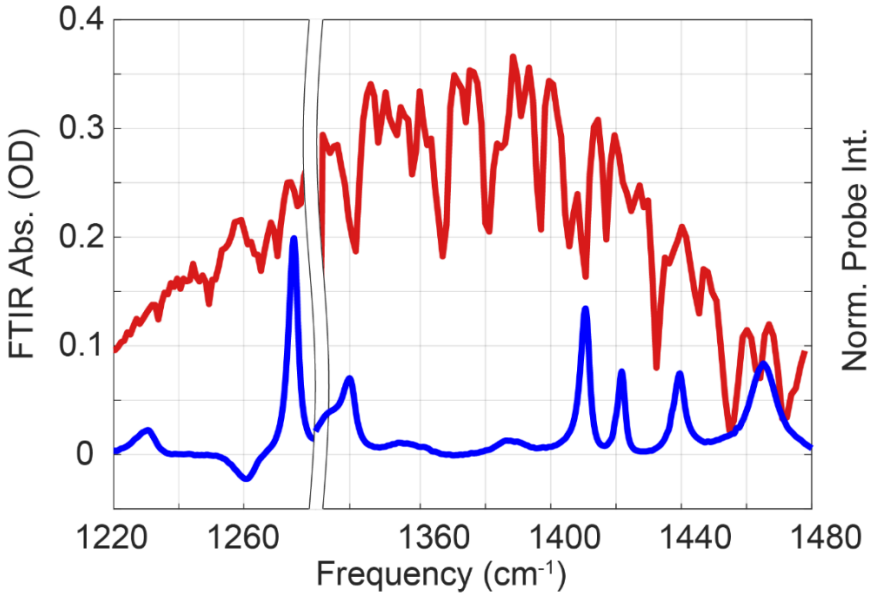

Figure 3-11. 50 mM HBQ dissolved in PCE with 50 μm pathlength FTIR (blue) overlaid with normalized probe spectrum (red). Probe spectrum covers entire high frequency regions of interest in HBQ and DBQ.

3.6.3 Characterization of Instrumental Response Function and BBnUV Pump Pulses

The BBnUV pulse was centered at 390 nm for the experiments above to capture the red edge of the $\pi \rightarrow \pi^*$ transition in HBQ and DBQ, see Figure 3-2. The pulse was compressed using a double-pass UV prism compressor and to further reduce the effects of third dispersion a UV pulse shaper (Fastlite), see section in *Chapter 2*. The BBnUV pulses were characterized using a TG XFROG which retrieved pulse duration of 18 fs used in the experiment, see Figure 3-12.

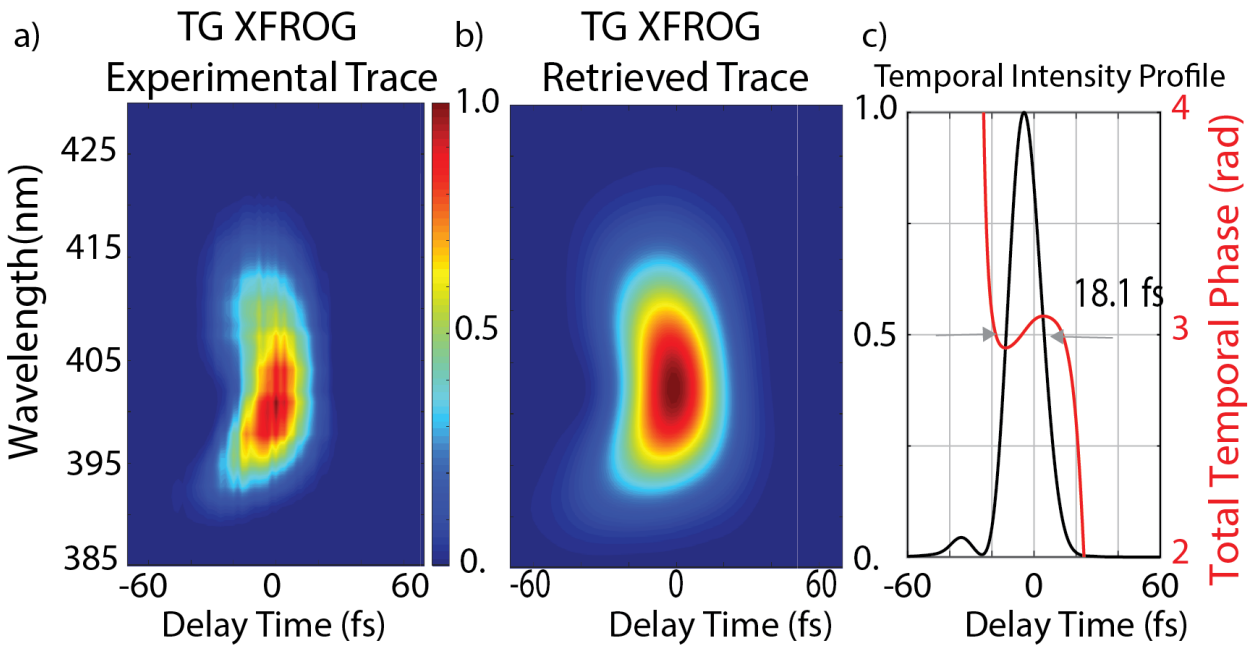

Figure 3-12. Pump pulse characterization using TG XFROG. Representative TG XFROG result of pulse generated from a) 100 µm type (I) BBO crystal. Additional higher order spectral phase is seen due to UV fused silica prism material dispersion. b) Retrieved TG XFROG. Minimum FROG error a) 0.01002, trace used a 256 grid sized. c) Retrieved temporal pulse characterization with a full width half max of 18.05 fs (black solid). Retrieved temporal phase (solid red) shows resulting third order phase caused by use of the UV fused silica prism compressor.

Characterization of the spectrometer's instrumental response function (IRF) was conducted by overlapping the broadband near-UV pump with the OPA/DFG generated mid-IR pulses in a 100 µm thick silicon wafer, see Figure 3-13. From the spectrally dispersed signal, A gaussian function convolved with a single exponential was fit to the raw data and gives the fit the resulting peak width at half max was 120 fs, the corresponding line shape is given from the derivative of the time fit.

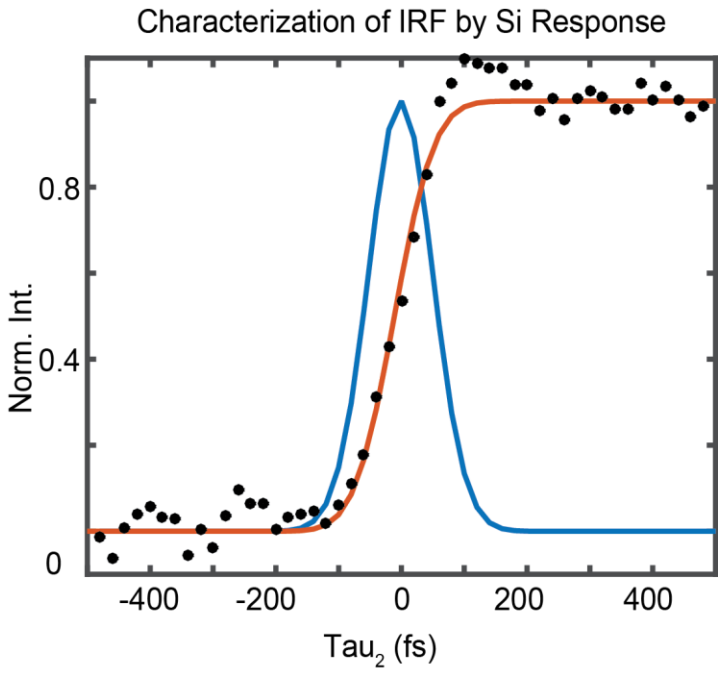

Figure 3-13. Characterization of the instrumental response function. Cross-correlation time of pump and probe pulses in a 250 μm thick Si wafer. Black dots are normalized intensity of response taken with 20 fs time steps. A gaussian function convolved with a single exponential was fit to the raw data and gives the fit (red solid line) the resulting peak width at half max was 120 fs, the corresponding line shape is given from the derivative of the time fit.

3.6.4 1D EV of PCE solvent

The collection of a control, the solvent, allows better quantification of the underlying population dynamics in the first ps. Here, we map the nonresonant response of the PCE solvent under the same laser conditions that allows the quantification of the solvent response and fit of the solvent response to a parallel branching pathway in the target analysis. The 1D EV study of PCE reveals that an 80-104 fs decay was present when no sample was imparted in the sample area. For the PCE solvent scans the delay time ranges used to measure the dynamics were: -1 ps to 2 ps using 20 fs time steps, collected over the full spectral range of the HBQ, DBQ experiments. A sample 1D EV spectrum is shown in Figure 3-14 and shows the absence of any

signal from the solvent in the region probed in the HBQ and DBQ study. Here, a nonresonant response is generated by heating of the solvent during the laser pulse interaction of the pump and probe in PCE and lasts for about 100 fs.

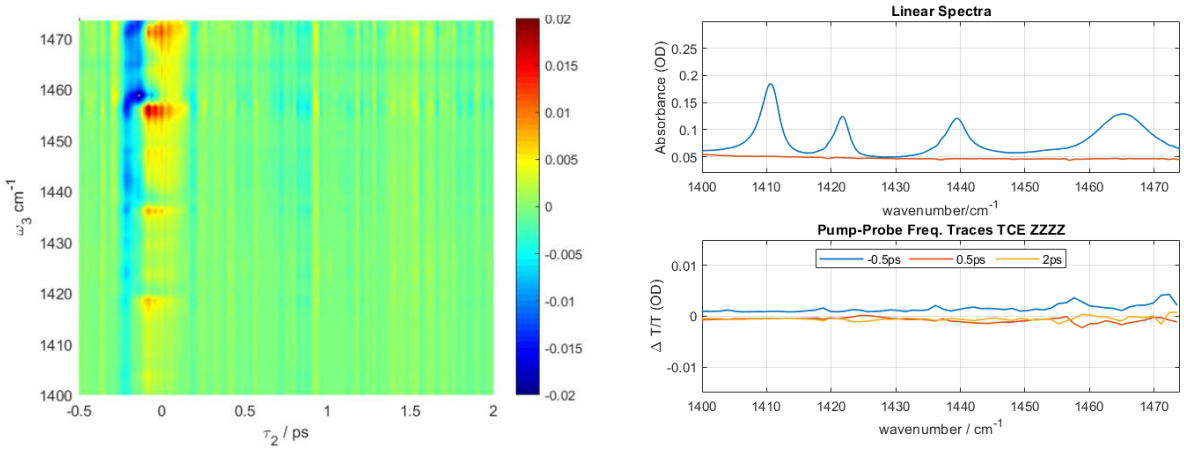

Figure 3-14. PCE 1D EV spectrum shows nonresonant solvent response at early times. Left) The 1D EV Correlation map at the 7050 nm grating position, during the first 100 fs and the solvent nonresonant response is generated by heating of the solvent during the laser pulse interaction of the pump and probe in PCE. Right, top) FTIR of region of interest, HBQ (solid blue line) and PCE (solid red line) showing the absence of any appreciate IR vibration is the region of interest. Right, bottom) select pump probe time traces at -500, 500 and 2,000 fs following photoexcitation, after the quick decay no featured signal is present in solvent 1D EV spectrum.

3.7 REFERENCES

1 Hammes-Schiffer, S. & Soudackov, A. V. Proton-coupled electron transfer in solution, proteins, and electrochemistry. *Journal of Physical Chemistry B* **112**, 14108-14123 (2008). https://doi.org:10.1021/jp805876e

2 Goyal, P. & Hammes-Schiffer, S. Role of active site conformational changes in photocycle activation of the AppA BLUF photoreceptor. *Proc Natl Acad Sci U S A* **114**, 1480-1485 (2017). https://doi.org:10.1073/pnas.1621393114

3 Parada, G. A. *et al.* Inverted Region. *Science* **475**, 471-475 (2019).

4 Goings, J. J. & Hammes-Schiffer, S. Nonequilibrium Dynamics of Proton-Coupled Electron Transfer in Proton Wires: Concerted but Asynchronous Mechanisms. *ACS Central Science* **6**, 1594-1601 (2020). https://doi.org:10.1021/acscentsci.0c00756

5 Cotter, L. F., Rimgard, B. P., Parada, G. A., Mayer, J. M. & Hammarstr, L. Solvent and Temperature E ff ects on Photoinduced Proton-Coupled Electron Transfer in the Marcus Inverted Region. (2021). https://doi.org:10.1021/acs.jpca.1c05764

6 Markle, T. F. & Mayer, J. M. Concerted proton-electron transfer in pyridylphenols: The importance of the hydrogen bond. *Angewandte Chemie - International Edition* **47**, 738-740 (2008). https://doi.org:10.1002/anie.200702486

7 Tiwari, V., Peters, W. K. & Jonas, D. M. Energy transfer: Vibronic coherence unveiled. *Nature Chemistry* **6**, 173-175 (2014). https://doi.org:10.1038/nchem.1881

8 Tiwari, V., Peters, W. K. & Jonas, D. M. Electronic energy transfer through non-adiabatic vibrational-electronic resonance. I. Theory for a dimer. *Journal of Chemical Physics* **147** (2017). https://doi.org:10.1063/1.5005835

9 Tiwari, V., Peters, W. K. & Jonas, D. M. Electronic resonance with anticorrelated pigment vibrations drives photosynthetic energy transfer outside the adiabatic framework. *Proceedings of the National Academy of Sciences* **110**, 1203-1208 (2013). https://doi.org:10.1073/pnas.1211157110

10 Takeuchi, S. & Tahara, T. Coherent nuclear wavepacket motions in ultrafast excited-state intramolecular proton transfer: Sub-30-fs resolved pump-probe absorption spectroscopy of 10-hydroxybenzo[h]quinoline in solution. *Journal of Physical Chemistry A* **109**, 10199-10207 (2005). https://doi.org:10.1021/jp0519013

11 Schriever, C. *et al.* The interplay of skeletal deformations and ultrafast excited-state intramolecular proton transfer: Experimental and theoretical investigation of 10-hydroxybenzo[h]quinoline. *Chemical Physics* **347**, 446-461 (2008). https://doi.org:10.1016/j.chemphys.2007.10.021

12 Marciniak, H. *et al.* Dynamics of excited state proton transfer in nitro substituted 10-hydroxybenzo[h]quinolines. *Phys. Chem. Chem. Phys.* **19**, 26621-26629 (2017). https://doi.org:10.1039/C7CP04476C

13 Kim, C. H. & Joo, T. Coherent excited state intramolecular proton transfer probed by time-resolved fluorescence. *Physical Chemistry Chemical Physics* **11**, 10266-10269 (2009). https://doi.org:10.1039/b915768a

14 Lee, J. & Joo, T. Photophysical model of 10-Hydroxybenzo[h]quinoline: Internal conversion and excited state intramolecular proton transfer. *Bulletin of the Korean Chemical Society* **35**, 881-885 (2014). https://doi.org:10.5012/bkcs.2014.35.3.881

15 Kim, J. W. *et al.* Non-Born-Oppenheimer Molecular Dynamics Observed by Coherent Nuclear Wave Packets. *Journal of Physical Chemistry Letters* **11**, 755-761 (2020). https://doi.org:10.1021/acs.jpclett.9b03488

16 Zhang, L., Fassioli, F., Fu, B., She, Z.-S. & Scholes, G. D. Modeling Excited-State Proton Transfer Using the Lindblad Equation: Quantification of Time-Resolved Spectroscopy with Mechanistic Insights. *ACS Physical Chemistry Au* **3**, 107-118 (2023). https://doi.org:10.1021/acsphyschemau.2c00038

17 Hristova, S. *et al.* 10-Hydroxybenzo[h]quinoline: Switching between single- and double-well proton transfer through structural modifications. *RSC Advances* **5**, 102495-102507 (2015). https://doi.org:10.1039/c5ra20057a

18 Chou, P. T. *et al.* Excited-state intramolecular proton transfer in 10-hydroxybenzo[h]quinoline. *Journal of Physical Chemistry A* **105**, 1731-1740 (2001). https://doi.org:10.1021/jp002942w

19 Takeuchi, S. & Tahara, T. Coherent Nuclear Wavepacket Motions in Ultrafast Excited-State Intramolecular Proton Transfer: Sub-30-fs Resolved Pump−Probe Absorption Spectroscopy of 10-Hydroxybenzo[h]quinoline in Solution. *The Journal of Physical Chemistry A* **109**, 10199-10207 (2005). https://doi.org:10.1021/jp0519013

20 Schriever, C. *et al.* The interplay of skeletal deformations and ultrafast excited-state intramolecular proton transfer: Experimental and theoretical investigation of 10-hydroxybenzo[h]quinoline. *Chemical Physics* **347**, 446-461 (2008). https://doi.org:10.1016/j.chemphys.2007.10.021

21 Lee, J., Kim, C. H. & Joo, T. Active role of proton in excited state intramolecular proton transfer reaction. *Journal of Physical Chemistry A* **117**, 1400-1405 (2013). https://doi.org:10.1021/jp311884b

22 Gaynor, J. D. & Khalil, M. Signatures of vibronic coupling in two-dimensional electronic-vibrational and vibrational-electronic spectroscopies. *The Journal of Chemical Physics* **147**, 094202 (2017). https://doi.org:10.1063/1.4991745

23 Chou, P.-t., Chen, Y.-c., Yu, W.-s., Chou, Y.-h. & Wei, C.-y. Excited-State Intramolecular Proton Transfer in 10-Hydroxybenzo [h] quinoline. **4500**, 1731-1740 (2001). https://doi.org:10.1021/jp002942w

24 Chansen, W. *et al.* Theoretical study on influence of geometry controlling over the excited-state intramolecular proton transfer of 10-hydroxybenzo[h]quinoline and its derivatives. *Computational and Theoretical Chemistry* **1113**, 42-51 (2017). https://doi.org:10.1016/j.comptc.2017.05.008

25 Kumpulainen, T., Lang, B., Rosspeintner, A. & Vauthey, E. Ultrafast Elementary Photochemical Processes of Organic Molecules in Liquid Solution. *Chemical Reviews* **117**, 10826-10939 (2017). https://doi.org:10.1021/acs.chemrev.6b00491

26 Balasubramanian, M., Reynolds, A., Blair, T. J. & Khalil, M. Probing ultrafast vibrational dynamics of intramolecular hydrogen bonds with broadband infrared pump-probe spectroscopy. *Chemical Physics* **519**, 38-44 (2019). https://doi.org:10.1016/j.chemphys.2018.11.018

27 Gaussian 09 (Gaussian, Inc., Wallingford, CT, USA, 2009).

28 Kim, J. *et al.* Non-Born-Oppenheimer Molecular Dynamics Observed by Coherent Nuclear Wave Packets. *J Phys Chem Lett* **11**, 755-761 (2020). https://doi.org:10.1021/acs.jpclett.9b03488

29 Gaynor, J. D., Courtney, T. L., Balasubramanian, M. & Khalil, M. Fourier transform two-dimensional electronic-vibrational spectroscopy using an octave-spanning mid-IR probe. *Opt Lett* **41**, 2895-2895 (2016). https://doi.org:10.1364/OL.41.002895

30 Gaynor, J. D., Petrone, A., Li, X. & Khalil, M. Mapping Vibronic Couplings in a Solar Cell Dye with Polarization-Selective Two-Dimensional Electronic–Vibrational Spectroscopy. *The Journal of Physical Chemistry Letters* **9**, 6289-6295 (2018). https://doi.org:10.1021/acs.jpclett.8b02752

31 Gaynor, J. D., Sandwisch, J. & Khalil, M. Vibronic coherence evolution in multidimensional ultrafast photochemical processes. *Nature Communications* **10**, 5621-5621 (2019). https://doi.org:10.1038/s41467-019-13503-9

32 Snellenburg, J. J., Laptenok, S. P., Seger, R., Mullen, K. M. & van Stokkum, I. H. M. Glotaran: A Java-Based Graphical User Interface for the R Package TIMP. *J Stat Softw* **49**, 1-22 (2012). https://doi.org:DOI 10.18637/jss.v049.i03

33 Stefan Lochbrunner, A. J. W., and Eberhard Riedle. Microscopic Mechanism of Ultrafast Excited-State Intramolecular Proton Transfer: A 30-fs Study of 2-(2‘-Hydroxyphenyl)benzothiazole. *J. Phys. Chem. A* **107**, 11 (2003). https://doi.org:https://doi.org/10.1021/jp035203z

34 Takeuchi, S. & Tahara, T. Coherent Nuclear Wavepacket Motions in Ultrafast Excited-State Intramolecular Proton Transfer: Sub-30-fs Resolved Pump−Probe Absorption Spectroscopy of 10-Hydroxybenzo[h]quinoline in Solution. *The Journal of Physical Chemistry A* **109**, 10199-10207 (2005). https://doi.org:10.1021/jp0519013

35 Hristova, S. 10-Hydroxybenzo[h]quinoline: switching between single- and double-well proton transfer through structural modifications. *RSC Advances* **5**, 12 (2015). https://doi.org:10.1039/c5ra20057a

36 Marciniak, H. *et al.* Dynamics of excited state proton transfer in nitro substituted 10-hydroxybenzo[h]quinolines. *Phys Chem Chem Phys* **19**, 26621-26629 (2017). https://doi.org:10.1039/c7cp04476c

37 Lynch, M. S., Cheng, M., Van Kuiken, B. E. & Khalil, M. Probing the photoinduced metal-nitrosyl linkage isomerism of sodium nitroprusside in solution using transient infrared spectroscopy. *Journal of the American Chemical Society* **133**, 5255-5262 (2011). https://doi.org:10.1021/ja110881n

38 Van Stokkum, I. H. M., Larsen, D. S. & Van Grondelle, R. Global and target analysis of time-resolved spectra. *Biochimica et Biophysica Acta - Bioenergetics* **1657**, 82-104 (2004). https://doi.org:10.1016/j.bbabio.2004.04.011

Chapter 4. VIBRONIC COHERENCE MEDIATES BREAKDOWN OF THE BORN-OPPENHEIMER APPROXIMATION IN ULTRAFAST EXCITED STATE INTRAMOLECULAR PROTON TRANSFER

Elucidating the role that coupled vibration and electronic degrees of freedom play following excited state intramolecular proton transfer (ESIPT) is key to understanding the role vibronic coupling plays in ultrafast relaxation processes in photoexcited systems. Herein, we employ ultrafast 3D EV spectroscopy and computational methods to observe the nonequilibrium relaxation processes following sub-15 fs ESIPT in 10-hydroxybenzo[h]quinoline (HBQ). We observe the presence of an excited state emission feature to the red of the HOMO-LUMO electronic transition which is modulated by a 755 cm^{-1} and a 1405 cm^{-1} vibronic coherence. We conclude the early time vibronic coherences facilitates the breakdown of the Born-Oppenheimer Approximation leading to ultrafast nonadiabatic proton transfer and the subsequent formation of a vibrationally excited keto state. We find that ultrafast intramolecular vibrational redistribution occurs within 800 fs couples the delocalized proton acceptor bending vibrations to up to 16 separate low frequencies which taken together amount for the stoke shift energy. The results reveal the role that vibrational energy transfer, vibronic coherence, and vibrational coupling play in a fundamental photophysical process and show how strongly coupled vibrational states can play an active role in nonadiabatic energy transfer.

4.1 Role Nonadiabatic and Vibrational Coupling has on ESIPT in HBQ

4.1.1 ZZZZ polarized 1D EV analysis of HBQ

In the prior chapter I showed the isotopic 1D EV analysis of HBQ and identified 2 main spectral components in the spectrum and their characteristic lifetimes. This chapter will focus on an analysis of the parallel polarized EV analysis of HBQ. The effects of vibronic coupling in the ESIPT process are explored through the lens of the local vibrational modes that indirectly couple to the PT coordinate. Herein, we investigate the fingerprint vibrational modes that contain proton donor, carbonyl stretching character of the GS enol form and amino bending character in the excited keto form. Figure 1 shows the ground state FTIR, BBnUV pump, and excited state 1D EV spectra of HBQ dissolved in an aprotic, nonpolar solvent tetrachloroethylene (PCE). The ground state vibrational spectrum of HBQ in the fingerprint region reveals 5 strong, sharp vibrational modes are present at 1344 cm^{-1}, 1410 cm^{-1}, 1422 cm^{-1}, 1437 cm^{-1}, and 1440 cm^{-1}. The five modes, denoted by their gaussian vibrational mode number are assigned as ν_{46}, ν_{48}, ν_{49}, ν_{50}, and ν_{51} respectively, correspond to fundamental modes as computed from a sufficient[1,2] level of DFT frequency calculation utilizing the unrestricted B3LYP level of theory and 6-311++G(d,p) basis set with anharmonic corrections (see Appendix A). Each mode is delocalized and contains a combined local motion of the proton donor carboxylate group and vibrations from the backbone. Here, the five modes are assigned by the motion of the carboxylate group: [C-O-H rock], [C-O-H bend], [C-O-H sym. Str.], [C-O-H asym. Str.], and [C-O-H bend], respectively. To simulate the effect of photoinduced ESIPT in HBQ, we conducted TDDFT frequency calculations with the same basis set on the HOMO-LUMO transition to determine the frequencies of thermally relaxed keto excited state. We note upon simulating the transition the thermally relaxed geometry adopts a keto geometry and in the same fingerprint frequency region is dominated by fundamental modes that are described by combination of delocalized nuclear modes containing [C-N-H] amino group bends, here we highlight the ν'_{47}, ν'_{48}, and ν'_{51} modes

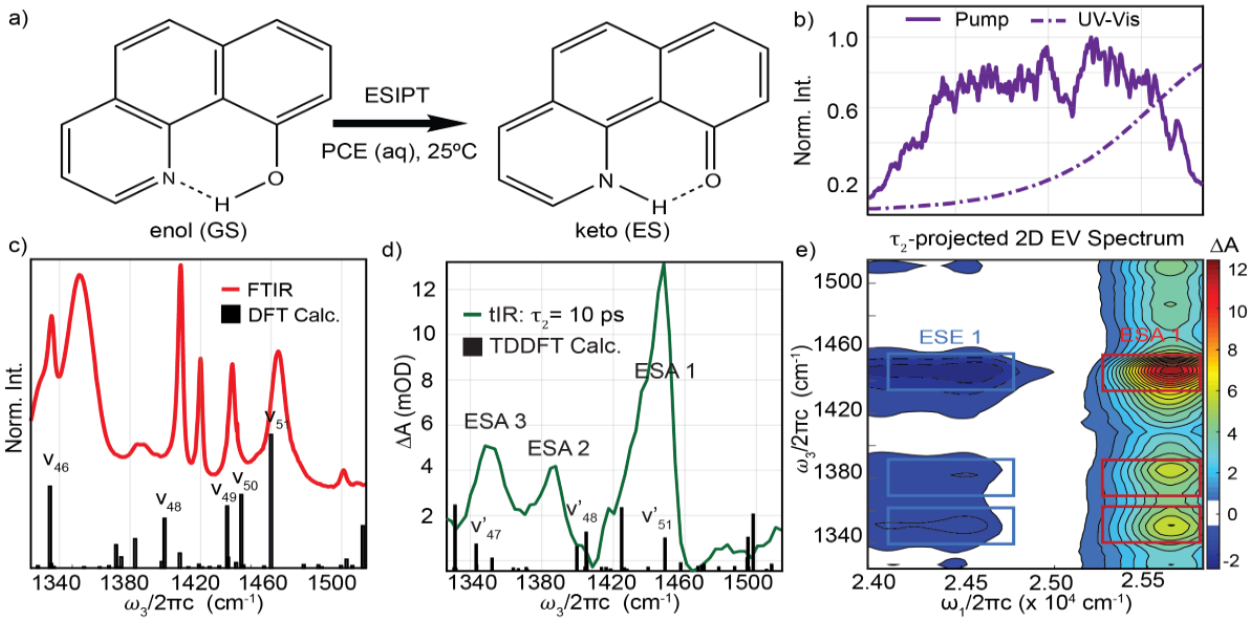

Figure 4-1. Electronic Vibrational Spectroscopy of model ESIPT system. Probes change to delocalized proton donor and proton accepting high frequency modes that couple to a resonant photoexcitation process on the electronic ground state. a) Schematic of system of interest upon photoexcitation of a broadband nUV laser pulse 10-Hyroxybenzo[h]quinoline undergoes a rapid tautomerization from the enol ground state (GS) to keto excited state (ES). b) A resonant compressed pump pulse, solid purple line, excites the red edge of the HOMO-LUMO transition of the electronic ground state, represented as the dashed purple line of the UV-Vis absorption spectrum. c) Initial ground state enol spectrum, solid red line, the local GS vibrational modes report on the high frequency modes excited during the ESIPT process and include delocalized ring breathing modes with significant C-O-H stretching and bending character as provided by ground state DFT calculations (black sticks). 5 strong fundamental vibrational modes are identified from the FTIR at 1344 cm^{-1}, 1410 cm^{-1}, 1422 cm^{-1}, 1437 cm^{-1}, and 1440 cm^{-1} are assigned to ν_{43}, ν_{48}, ν_{49}, ν_{50} and ν_{51} respectively. d) 1D EV spectrum of HBQ at 10 ps (see Figure 4-7). The representative pump probe frequency slice reveals the presence of 3 broad ESA. The 3 ESA features are assigned to 3 fundamental vibrations in the excited keto state for our TDDFT calculations ν'_{47}, ν'_{48}, and ν'_{51} which contain significant C-N-H proton acceptor character. (See Figure 4-14). e) τ_2-averaged 2D EV absorption spectrum reveals the presence of a low amplitude negative ESE peaks that couple to the same high frequency vibrational modes that are present in the 1D EV (Green, solid line) shown by the ω_1 projection.

which correspond to similar frequencies of that of the ground state and are labeled in Figure 4-1. The computed IR spectra of the ground state enol and excited state keto form of HBQ provides a theoretical basis for spectra interpretation of the experimental transient IR spectra, for instance, positive excited state absorptions (ESA) features should correspond to keto proton acceptor

frequencies and negative ground state bleach (GSB) features report on the repopulation of the ground state enol, proton donor frequencies.

Experimentally, the proton donor and acceptor vibrational modes are monitored using a combination of multicolor ultrafast nonlinear spectroscopic techniques: 1D EV, 2D EV and 3D EV, all of which resonantly excite the HOMO-LUMO transition and monitor the change of absorption of the mid-IR fingerprint region as a function of time delay time. Following the resonant photoexcitation, electronic redistribution occurs on the same timescale as an optical cycle of the O-H stretch, ~12 fs[3,4]. Figure 4-1. we show the mid-IR transient infrared spectrum at 10 ps delay time which clearly displays three positive peaks centered between 1415-1460 cm^{-1}, 1370-1390 cm^{-1} and 1345-1365 cm^{-1} representing excited state absorptions (ESAs) of the non-equilibrium keto species: ESA 1, ESA 2 and ESA 3 and are assigned to the ν'_{47}, ν'_{48}, and ν'_{51} gaussian modes. In chapter 3, lineshape and frequency changes of the ESA regions were reported and suggested to directly couple nonadiabatically to the ESIPT where vibrational cooling and IVR processes were concluded to be the main nonequilibrium relaxation channel of the keto* state. In brief, 1D EV showed n>1 vibrational excitation in the ESA 1 mode and using a sequential kinetics fit the non-equilibrium vibrational relaxation of HBQ occurs on 3 separate timescales, a 0.8 ps ultrafast intramolecular vibrational redistribution, a 10-17 ps vibrational cooling process and a long ~300 ps lifetime of the keto state. Though 1D EV can reveal spectral changes to the local vibrational reporters in HBQ, identify the excited state spectrum is dominated by the keto electronic state geometry and highlight the specific vibrational modes that vibronically couple to the ESIPT process, the nature and difference between these high frequency reporters is not clear. Here we report the 2D EV and 3D EV spectra of HBQ which identify an previously unresolved excited state emission (ESE)

signature that arises from a τ_1 coherence transfer resulting from breakdown of the Born-Oppenheimer approximation, and elucidates the low frequency skeletal modes that couple the proton acceptor vibrations via τ_2 coherence-to-coherence transfer during the early time IVR process.

4.1.2 2D EV of HBQ

Figure 4-1 shows the τ_2-averaged 2D EV absorption spectrum taken from averaging the 2D EV surfaces over the first 900 fs of τ_2 waiting times. Compared with the 1D EV spectrum the 2D EV spectrum resolves additional features across the excitation spectrum (ω_1) revealing additional cross peaks that couple the electronic and vibrational motion (ω_3) together. Highlighted by the red boxed areas, the 3 positive ESA features that were resolved in the 1D EV in the detection axis (ω_3) are revealed to couple to ω_1 = 25300-25800 cm^{-1} with peak center frequency of 25640 cm^{-1}. Interestingly, we observe 3 excited state emission (ESE) peaks about ω_1 = 24200-24700 cm^{-1} in the 2D EV spectrum, centered about 24550 cm^{-1} as denoted by the 3 blue boxed areas, these negative features each fall to the red of the ground state absorption, Figure 4-1. Thus, we rule out the possibility that these are GSB transitions. Interestingly, previous reports[5-9] of 2D EV spectra have failed to resolve the presence of an ESE feature which couple to the same ω_3 transition, whereas theoretical frameworks[10-14] have failed to predict the presence of an ESE feature in arising to the red side of an ESA pathway. Below, we report and detail how the presence of these ESE pathways arises from τ_1 coherence transfer resulting from breakdown of the Born-Oppenheimer approximation.

4.2 Evidence of Vibronic Coherence Transfer mediates PT in T_1

Figure 4-2 provides a detailed description of two possible nonsecular pathways that can give rise to the ESE features. For ESE features to be observed to the red of the ground state electronic absorbance in an EV experiment a coherence-to-coherence transfer occurs during the pump-pulse delay time, τ_1. Given the fast ESIPT rate we deduce this coherence transfer occurs between the excited state population in the Franck Condon region which contains enol-like geometry and a highly excited vibrational keto state. Following the τ_1 coherence-to-coherence transfer a new coherence state is formed following the interaction with the second pump pulse forming a coherent state between the initially populated hot enol* state and the thermally excited keto* state. This coherent state releases energy corresponds to the energy difference between the peak absorbance of the ESA and peak emission of the ESE, we find the difference of 1090 cm^{-1} for ESA/ESE 1. To confirm whether the τ_1 coherence transfer is occurring a oscillatory feature in the ESE with respect to τ_1 should be present. To test this, we perform a short time Fourier analysis of the integrated ESA and ESE regions in the 2D EV time domain spectrum we use a 5-fs wide sliding Fourier transform window across the entire τ_1 region of 100 fs to determine the τ_1 - integrated signal intensity for each center τ_1 point, see Figure 4-11. Figure 4-2. shows the resulting analysis, during the first 40 fs following photoexcitation, in the ESE region we find that the time-domain ESE signal is modulated by two frequencies 755 and 1405 cm^{-1} which were fit via a exponential convolved with two sinusoids shown by the inset in Figure 4-2. Interestingly, the coherence transfer which characterizes the ESE signal is not observed in ESA, and the ESA signal decays to via simple exponential. This result suggests that during the same time period of photoexcitation, the ESIPT processes the modulation of the ESE region is present and is coupled to two separate vibrational frequencies.

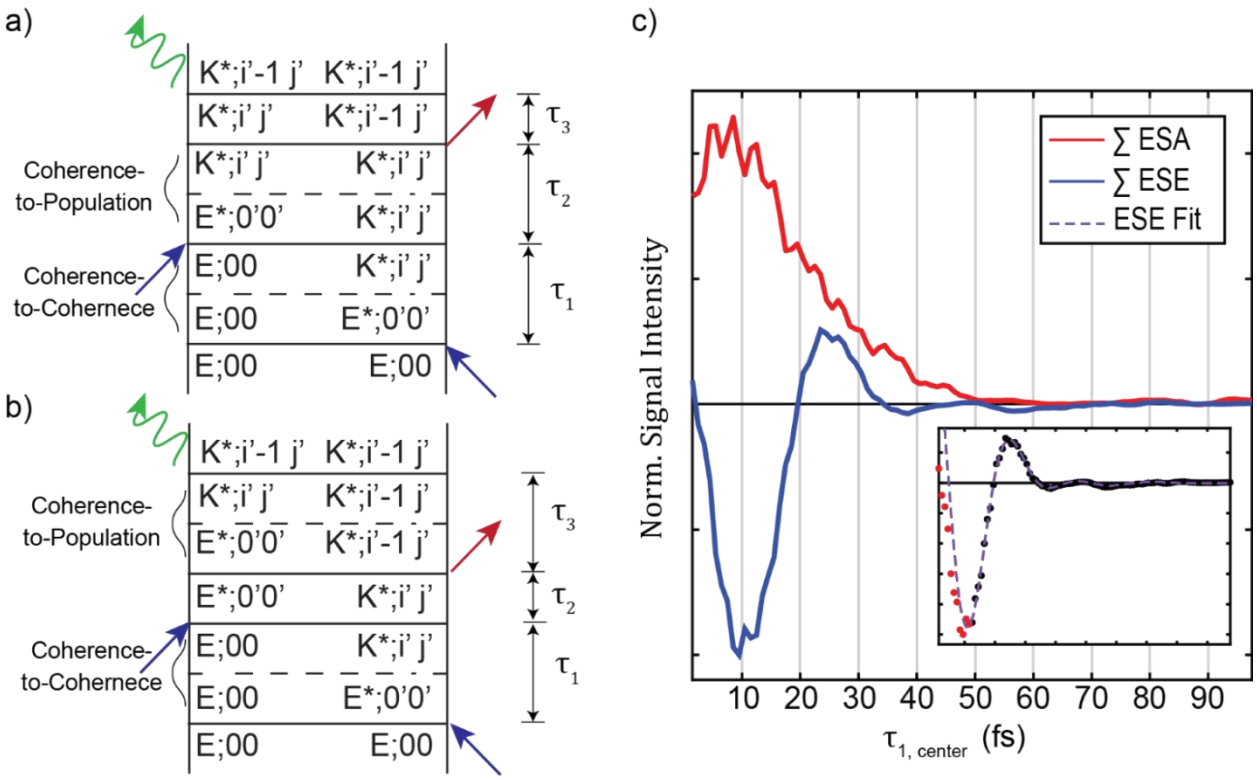

Figure 4-2. Rapid coherence-to-coherence transfer during the ultrafast ESIPT elucidates the excited state emission signal observed by 2D EV spectroscopy. An oscillatory beat in the ESE signal persists through the 12 fs ESIPT and IRF, in contrast to the simple decay of nature of the ESA signal, providing evidence for τ_1 coherence transfer. a) and b) show two plausible nonsecular Feynmann diagrams that can result in the observed ESE 2D EV signal. Following photoexcitation, coherence transfer occurs between the enol, GS and Keto, ES, which produces a beating frequency on top of the emitted signal which dephasing during τ_1. A second coherence to population transfer terminates the signal in a population state either during τ_2 (a)) or τ_3 (b)). c) τ_1 dependent 2D EV signal contribution of ESA 1 and ESE 1, see Figure 4-11. The ESA has an appreciable intensity at τ_1=0 fs and decays over 40 fs. The ESE grows in over the first 12 fs and then clearly oscillates in τ_1. Inset. Time domain fit of the ESE signal shown in c) to a sum of 2 decaying sinusoids with a decay constant of 12 ± 2 fs and frequencies 755 ± 50 cm^{-1} and 1405 ± 90 cm^{-1}.

4.3 Born Oppenheimer Approximation breakdown and Nonadiabatic coupling via a 772 cm^{-1} vibrational mode

The discovery of τ_1 coherence transfer confirms the violation of the BO approximation during the first 40 fs following photoexcitation. Further evidence of the BO breakdown is

garnered from the assigned modes that mediate the coherence transfer, interestingly the 755 cm^{-1} frequency is within our uncertainty to prior Raman experimental data and theoretical work[1] which suggested that a 794 cm^{-1} Raman mode is directly correlated with a nonadiabatic non-BO vibrational motion during the ESIPT. Here, we assign the 755 cm^{-1} vibration to an out-of-plane vibrational mode that is perpendicular to the electronic transition of the ESIPT, see Fig 3e. The presence of an assigned out-of-plane vibration that couples to the ESE region is notable since the experiments were conducted in an all parallel beam geometry suggesting that the perpendicular vibrational modes we observe are due in fact to IVR or fermi resonance between two closely lying vibrational modes. In fact, the importance of OOP vibrations which are involved with the breakdown of the BO region have been observed in other ultrafast ESIPT complexes mainly *o*-hydroxybenzaldehyde[15] and in hydroxyanthraquinone[16] which were found to mediate the nonequilibrium relaxation time following PT. Furthermore, the role that vibrational redistribution in ESIPT complexes has been debated[17,18] though not fully observed. IVR and other vibrational induced thermal relaxation mechanisms involving ESIPT has been suggested to result in the large stoke shifts which characterize ESIPT systems, for example low temperature fluorescence measurements of an similar compound to HBQ, an HBT derivative was found to show decreases in the stoke shift at lower temperatures[17,19] this trend was determined to be dependent on the degree of Intermolecular charge transfer within the system suggesting the vibrational redistribution and vibronic coupling have a strong correlation to the stoke shift in ESIPT systems including HBQ. HBQ has one of the fastest ESIPT rates measured and the one of the largest stoke shifts ~11,000 cm^{-1} amongst studied ESIPT system. Additionally, the observed nonequilibrium dynamics which involve the rapid τ_1 coherence-to-coherence transfer, the observed OOP vibrations that modulate the coherence transfer and the underlying solvent

independent vibrational cooling suggest the system would have a very vibrationally mixed, anharmonic excited state keto state.

4.4 ANHARMONIC COUPLING OF THE VIBRATIONAL MODES DRIVES NONEQUILIBRIUM IVR PROCESS FOLLOWING ESIPT IN HBQ

The degree of anharmonicity in HBQ and the extent that initially thermally populated vibrational states play in IVR following the photoinduced ESIPT was measured using 3D EV spectroscopy. Here the added advantage of 3D EV over 2D EV is the ability to resolve the τ_2 coherence-to-coherence transfer which eludes the vibrational couplings that exist between the keto proton acceptor modes and the skeletal modes in HBQ. To determine the vibrational couplings between the keto proton acceptor modes and the skeletal modes 2D EV frequency-frequency correlation maps were experimentally collected for a series of pump-probe waiting times at 12.5 fs intervals over the first 800 fs which corresponded to the decay of the fast

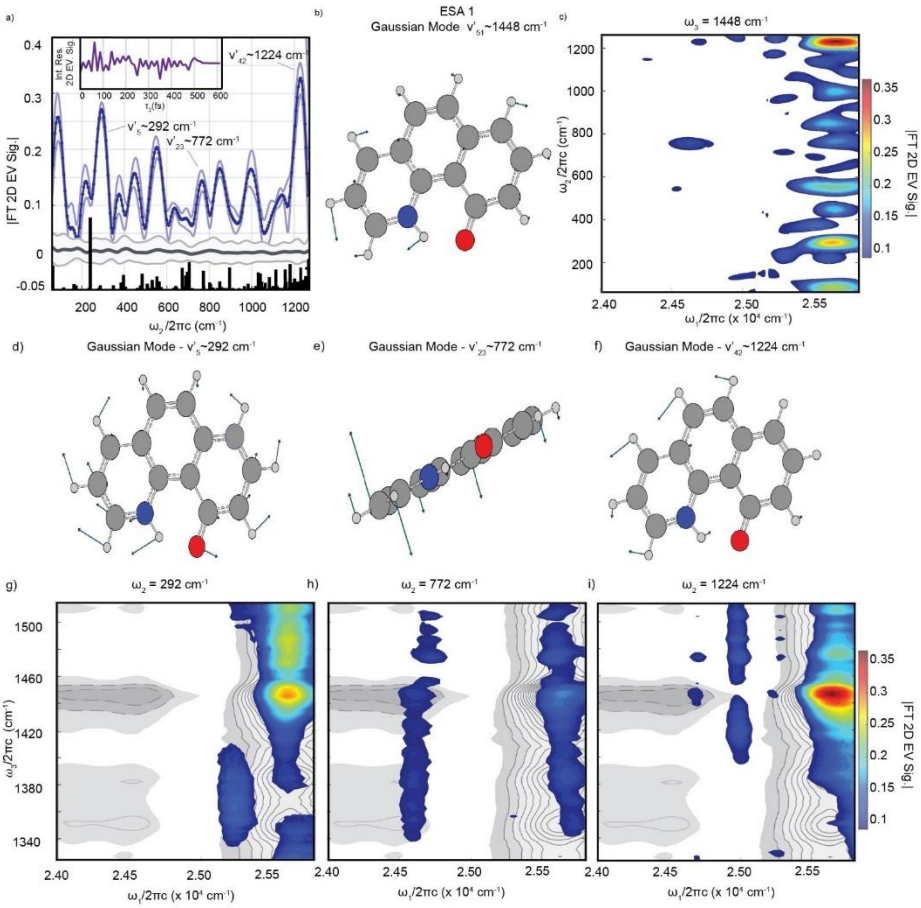

Figure 4-3. Early τ_2 3D EV Fourier Analysis reveals vibrational coherence beating in excited state absorption. a) Time-Fourier Analysis of ESA 1 during first 700 fs pump-probe delay time. Solid, black line - Integrated 2D EV signal of ESA 1 (ω_3 = 1444-1452 cm^{-1}, ω_1 = 25500-25700 cm^{-1}) revealing 14 resolved low frequency vibrational coupling that are outside the noise (gray solid line) and the standard errors shown as corresponding shaded regions. inset - The residuals of the integrated 2D EV signal following subtraction of the population dynamics (solid, purple line). The presence of a strong high frequency oscillation corresponds to a 1224 cm^{-1} mode which is resolved outside the 1333 cm^{-1} Nyquist limit (region near which are not shown) and outside the noise (solid, grey line). b) Schematic representation of TDDFT mode that corresponds to ESA 1, ν'_{51}, which contains proton acceptor bending character. c) 3D EV Correlation map of a slice at 1448 cm^{-1} corresponding to the dominate frequency in the ESA 1 mode. The strong coupling across three separate electronic regions at 24500, 25250 and 25640 cm^{-1} with the latter corresponding to the Time-Fourier Analysis where the 14 separate frequency regions found couple to the high frequency region. The separate resolved frequency at ω_2 = 772 cm^{-1} , ω_1 = 25640 cm^{-1} suggests a τ_2 coherence-to-coherence transfer is present. d-f) Selected TDDFT mode that corresponds to frequencies of interest. g-i) Quantum Coherence Beat Maps of selected skeletal vibrational modes show different delocalized vibration couple to different ESA and ESE nonadiabatic relaxation processes in HBQ. Quantum Beat slices at selected ω_2 frequencies. The quantum coherence beating maps shown as the colored contours maps between the absolute value of the maximum and 95% confidence interval of the noise.

component from the 1D EV data. The inset in Fig. 3a shows the residuals of the integrated 2D EV signal for the boxed ESA 1 mode after fitting to a signal exponential decay. Briefly, we averaged the pixels across the ω_1 and ω_3 spectral region and fit the population decay to 1.04 ps exponential which is inline with the population decay as determined from the global analysis of the 1D EV results. Following population subtraction, the residuals are Fourier transformed to provide the correlation map shown in Figure 4-3. A similar procedure is carried out the noise, denoted as pixels of the white area in Figure 4-3. Figure 4-10 shows the corresponding ω_2 correlation map informs the lower frequency skeletal modes which couple to ESA 1 and thus the vibrational modes that are coupled together during the ultrafast IVR process. Here, 14 separate frequencies are resolved outside our error and present within the frequency area below the Nyquist limit of 1334 cm^{-1}. A summary of the vibrational energy ladder is shown in Fig. 4 for ESA 1, ESA 2 and ESA 3. Though the degree of vibrational coupling may at first be surprising, earlier transient absorption experiments by Tahara and others[3,4,20,21] identified four coherent vibrational frequencies that coupled to the keto emission at around 242, 392, 550 and 692 cm^{-1} during the first ps following ESIPT. Furthermore, recent impulsive stimulative Raman experiments identified[1] four additional Raman modes at 794, 842, 990 and 1346 cm^{-1}. Together with the 3D EV correlation map, a strong degree of anharmonicity and vibrational mode mixing is present during the first ps following PT in HBQ.

To further map out which vibrations are coupled to the high frequency ESA and ESE vibrational modes we map the full 3D EV correlation map landscape to determine which vibrational frequencies in the keto excited state are correlation with respect to one other. To perform this, we conduct a similar population fit for each ω_1 and ω_3 pixel pair to obtain a ω_1-ω_2-ω_3 map. The correlation map of ω_1 versus ω_2 at the center frequency of the ESA 1, ω_3 = 1448 cm^{-}

[1] is shown in Figure 4-3. with the white shaded areas representing data within the noise level. Interestingly across the 1448 cm^{-1} slice we can see three separate coupling regions across ω_1 centered at 24500, 25250 and 25640 cm^{-1}, for the latter the coupling amplitude appear to be the strongest which correlates with the rise of the excited state absorption amplitude from the strong ground state absorption and reveals the 14 separate frequencies which couple to the ESA 1 region described earlier. Here we highlight three of these coupled modes that occur at the 292 cm^{-1}, 772 cm^{-1} and 1224 cm^{-1} which we assign to the TDDFT fundamental modes of ν'_5, ν'_{23}, and ν'_{42}, respectively and illustrated in Figure 4-3(d-f). The former and latter vibrational modes highlight the electronic coupling dependence between the 3 ESA modes described by the 2D EV spectrum, Fig. 1e. The 292 cm^{-1} mode assigned previously been identified as an in-plane backbone bend that directly couples with the proton transfer coordinate[1,4,21] is clearly resolved to couple here to the proton acceptor bending mode of ESA 1. However, we observe that this mode only weakly couples with ESA 2 and ESA 3, as evidenced by the weak coupling strengths at ω_1 = 25650 cm^{-1} and 1386 cm^{-1} and 1352 cm^{-1} rather modest coupling amplitude at ω_1 = 25250 cm^{-1}, Figure 4-3g. which indicate that different IVR pathways and vibrational couples occurs for the different vibrational ESA pathways. This observation is further solidified by the presence of the strongly coupled 1224 cm^{-1} vibration to only ESA 1, Figure 4-3i. surprisingly the coupling strength to this higher frequency delocalized proton acceptor bending mode and that to ESA 1 is not coupled to either the ESE pathways or ESA 2 or ESA 3. 1D EV experiments, Figure 4-6 identified that ESA 1 was unique in the degree of vibrational cooling process amongst the fingerprint vibrational modes, however the strong couplings between different low frequency skeletal modes revealed by the 3D EV clearly highlight that ESA 1 participates in a strongly

coupled ultrafast IVR process. A full experimental picture of the vibrational mode

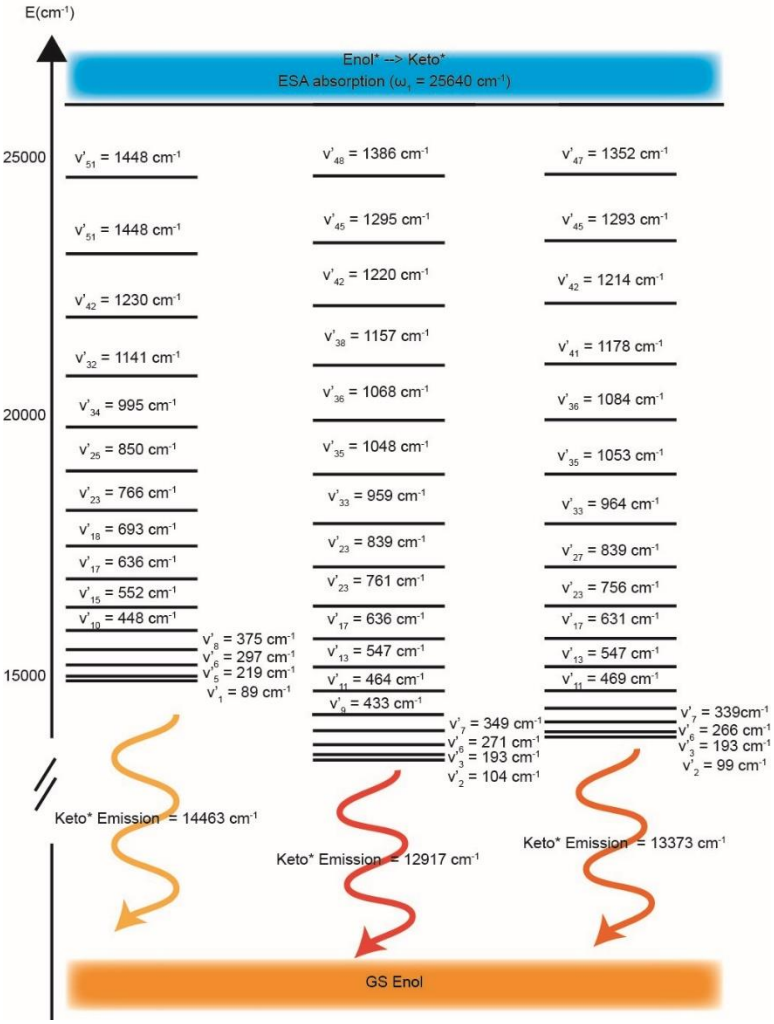

Figure 4-4. Excited State Potential Energy Ladder following ESIPT of HBQ. Following PT the 3D EV coherence maps elucidate the ultrafast IVR pathways for the 3 separate fingerprint region ESAs. The hotly excited ESA 1 mode contains two quanta of vibrational energy, deduced from the 1D EV analysis, whereas ESA 2 and ESA 3 mix with additional lower frequency vibrational modes. Addition of the total vibrational energy involved in the ultrafast IVR process shows the large stoke shift of HBQ is attributed to the excess vibrational energy of the keto excited state.

couplings involved between ESA 1, ESA 2 and ESA 3 is presented in Figure 4-4. Which highlights the frequencies that couple to each of the ESA mode, here by adding up all vibrational frequencies resolved by the 3D EV spectrum in ω_2 we are able to account for the large stoke shifts that is observed in TA experiments on HBQ during the first ps following photoexiciation.[21,22] We note that the large stoke shifts[3,4,21] observed in HBQ (9000-11000 cm^{-1})

are fully accounted for by the excess vibrational energy dissipated in the ultrafast IVR process following ESIPT.

Interestingly, we see a strong coupling between the ω_2 = 772 cm^{-1} OOP skeletal mode and the ω_1 = 24500 cm^{-1} ESE 1 feature which is within the experimental error of the 755 cm^{-1} modes we assigned from the τ_1- coherence-to-coherence transfer fitting. Though we are unable to resolve the second vibration at 1405 cm^{-1}, given our Nyquist sampling limit, here the combined presence of ESE 1, the τ_1, and τ_2-coherence-to-coherence transfer indicate that this OOP vibrational mode directly plays a role in mediating the breakdown of the Born-Oppenheimer approximation via a direct vibronic coherence transfer between the Franck Condon enol* state through the 772 cm^{-1} to a vibrationally hot keto excited state. The added experimental resolution from 3D EV directly measures the first coherence transfer followed by a second coherence transfer across τ_2 which puts the system back into a population before the signal field is emitted illustrated by the nonsecular pathway in Figure 4-2a. Though 3D EV confirms this secular pathway, we do not discount the second secular pathway illustrated in Figure 4-2b.

4.5 MULTIMODAL POTENTIAL ENERGY LANDSCAPE DEDUCED FROM 3D EV SPECTROSCOPY

A detailed description of the nonequilibrium relaxation mechanism in a well-studied ESIPT complex, HBQ, was conducted via a suite of nonlinear spectroscopic techniques and computational approaches. Utilizing 2D EV experiments, we determined that the ESIPT process in HBQ violates the Born Oppenheimer approximation and undergoes a unique τ_1 coherence-to-coherence vibronic energy transfer process facilitated by a 755 cm^{-1} and a 1405 cm^{-1} vibrational modes. 3D EV spectral analysis revealed that the ESIPT is a complex process involving many coupled vibrational coordinates and that up to 14 vibrational coordinates were observed to

couple to an important highly vibrationally excited ESA mode at 1448 cm^{-1}. Three separate vibrational modes in the excited proton transferred state were observed to couple to the same electronic transition, but different high frequency vibrations and low-frequency vibrations indicating the nonequilibrium relaxation process in HBQ occurs on a multidimensional landscape for ESIPT. We observe the multidimensional landscape during the first ps following photoexcitation on a hotly excited vibrational state of the keto state which accounts for the large stoke shifts observed in this model ESIPT system. Tools sensitive to coupled electronic and vibrational motions are crucial for manipulating and controlling this important process. 3D EV will be an important tool to understand photoinduced proton transfer and proton coupled electron transfer in complex systems.

4.6 EXPERIMENTAL METHODS

The general experimental and theoretical description of the multidimensional electronic vibrational (EV) spectroscopy experiment have been described elsewhere[5,11-13]. Briefly, the pulses used in the spectroscopy experiments are split from a fundamental Ti:Sapphire regenerative amplifier (Spectra Physics XP Pro, 800 nm, 3.85 W, ~38 fs, 1 kHz). The experiments utilized a broadband near ultraviolet (BBnUV) pump, a mid-IR probe, and a portion of the fundamental pulse. The BBnUV pulse was generated from the second harmonic of a spectral broadened fundamental pulse (430 μJ, 38 fs, 800 nm). The spectral broadening procedure is outlined elsewhere[5,23,24], here five 100 μm thick fused silica plates (Valley Design, FS-243) were placed near the focused of the fundamental pulse. The BBnUV was linearly chirped using a UV prism compressor (Newport 10SB10) before being compressed and shaped by an acoustic optic programmable dispersive filter (AOPDF) pulse shaper (Fastlite UV-Dazzler). The mid-IR probe is generated from difference frequency generation of the two outputs of a

home built two pass optical parametric amplifier and is routed to the sample area via a delay stage (Newport ILS150PP) which controls the τ_2 timing of the experiments. Before arriving to the sample area, the polarization of the mid-IR is set at 45° with respect to the pump with a ZnSe polarizer (Thorlabs, WP25H-Z). The detected polarization was set using a second ZnSe polarizer that was placed immediately after the sample cell and was being used as an analyzer. The polarization was set to 'S', parallel with respect to the pump for the data set discussed in this study. The pulse energies were between 850-950 nJ/pulse for the pump energy and 400 nJ/pulse for the probe. A FTIR before and after the experiment revealed no difference in optical or IR absorption of the sample indicated the sample did not photodegrade over the course of the experiment. Additionally, a pump-power dependence for the absorption difference at 1448 cm^{-1}, Figure 4-5 shows the nonlinear experiment was conducted inside the linear pulse energy regium.

As shown in Figure 4-5, 2D EV experiments were collected using advances in our broadband-nUV pump generation scheme. For each 2D EV spectrum a total of 3,000 laser shots were collected for each $\tau 1$, $\tau 2$, and $\omega 3$ surface using a homebuilt LabView VI that incorporates the Fastlite streaming option of our pulse shaper. To generate each averaged 2D EV spectrum, 75 scan files are collected, a scan consisting of 40 complete τ_1-series 2D EV spectra containing the spectrally dispersed IR intensity of 10,000 shots of the laser and are saved on a data file. The first ~1,360 and last ~1,360 shots are averaged together and are collected as a pump off background for each scan. A series of 7,280 pump-pulse waveforms are calculated and sent to the Fastlite RF generator, upon receiving a triggering signal, the waveforms are then sent to the pulse shaper and act to generate a new pump-pulse pair with a specific carrier envelop phase (CEP) and $\tau 1$ delay for each laser shot for the next 7,280 laser shots. Within the 7,280 waveforms sent to the dazzler the 1 x 2π phase cycling scheme and series of 91 evenly spaced τ_1 points between 0-100 fs in

1.11 fs steps were calculated and are cycled 40 times through. A separate homebuilt MATLAB script reads in each of the 75 scan data files per τ_2 point and parses the pump on data into a 4 x 4 matrix [CEP, τ_1, τ_2, ω_3]. By cycling through an entire 2D EV spectrum's pump CEP and $\tau 1$ in less than 0.2 seconds the effect of laser drift are greatly reduced, compared with averaging data collection that was previously done[5]. Additionally, since a single-shot 2D EV spectrum was collected 3000 times the standard errors of the signal intensities can be calculated for the data collected in this experiment and are shown when possible.

A total of 57 $\tau 2$ 2D EV spectrums were collected for HBQ and 9 $\tau 2$ 2D EV spectra were collected for the solvent PCE. To further reduce the impact of long-term laser drift in our experimental noise throughout the HBQ experiment the entire subset of data was broken down into 2 parts: first τ_2 points in the range of $0 \leq \tau 2 \leq 600$ fs were scanned followed by $\tau 2$ points in the range of $587.5 \leq \tau 2 \leq 20$ ps. The first subset was additionally divided into 22 $\tau 2$ scans that were spaced in 25 fs steps from $12.5 \leq \tau 2 \leq 537.5$ fs and a second subset of 25 $\tau 2$ scans that were spaced in 25 fs steps from $0 \leq \tau 2 \leq 600$ fs. The final data subset scanned $\tau 2$ of 575 fs, 600 fs, 700 fs, 800 fs, 900 fs, 1 ps, 5 ps, 10 ps, 15 ps and 20 ps. Time zero was set from the an midpoint of the rise in an integrated 1D EV trace of a silicon wafer see Figure 2-9 and the 1D EV of HBQ, Figure 4-6. The solvent only PCE 2D EV scanned 9 $\tau 2$ scans that were spaced in 100 fs steps from $0 \leq \tau 2 \leq 900$ fs.

4.7 Appendices

4.7.1 Sample Preparation and Linear spectroscopy

The study herein was conducted using a 50 mM solution of 10-hydroxybenzo[h]quinoline (HBQ) in tetrachloroethylene (PCE). The sample was prepared from a reaction grade 98.0+%,

pure stock purchased from TCI America (CAS: 33155-90-7). The sample was prepared without further purification and dissolved in an anhydrous 99% pure solution of tetrachloroethylene (CAS 127-18-4) purchased from Millipore Sigma. To avoid the effects of adverse health effects from PCE, special care was taken to prevent environmental exposure and release of PCE during spectroscopic measurements including containing samples in an enclosed container, in closed flow cell loops and airtight stationary cells that prevented the release of solvent. Spectroscopic measurements were conducted on a portion of the 50 mM HBQ sample and the pure PCE solvent. The UV-vis and FTIR linear spectroscopic characterization were collected on a JASCO V-630 and JASCO FT/IR 4100 spectrometers. UV-vis and FTIR measurements were collected on a ~100 μL portion of the sample and solvent were transferred to a FTIR stationary cell containing two 4 mm thick CaF2 windows separated by a 50 μm Teflon spacer.

For nonlinear spectroscopy experiments a ~10-15 mL portion of the sample or pure solvent was transferred to a septum capped 20 mL scintillation vial. A sample flow cell (Harrick) was prepared with a 50 μm pathlength (a 50 μm Teflon spacer sandwiched between two 2 mm CaF2 windows) the sample flow cell was connected to two Viton tubes (Masterflex) each capped with a 22-gauge needle which pierced the septum of the sample vial. One side of the tubing was wrapped around a peristatic pump which ran continuously to refresh the sample volume at the focus of the laser shot to avoid multi-excitation events. To avoid laser induced damage of the CaF2 windows the sample cell was raster scanned in the perpendicular direction of the beam focus. FTIR and UV-vis spectrum of the sample before and after nonlinear experiments confirmed no significant laser induced degradation of the sample. Additionally, pump power

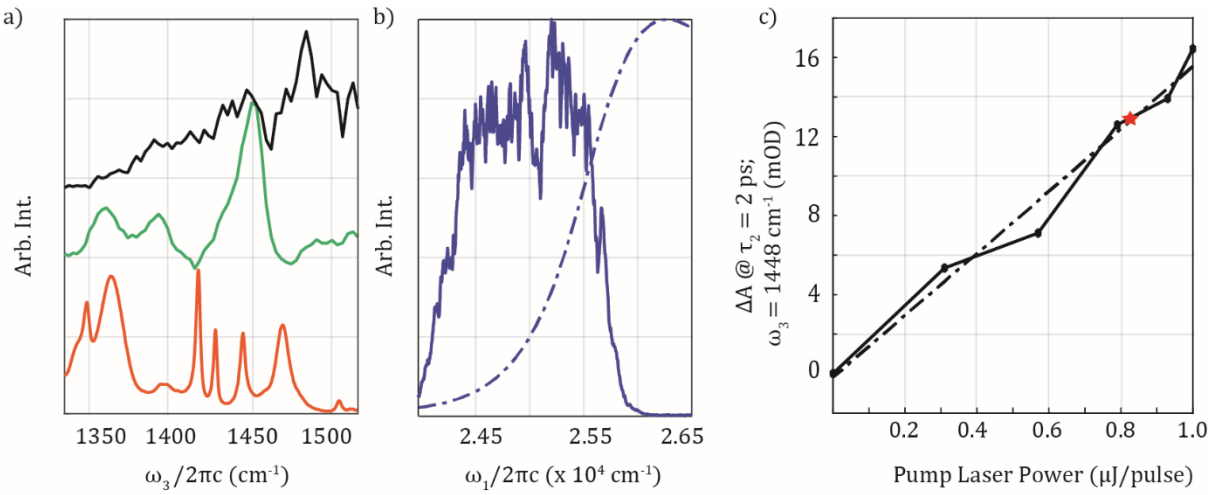

Figure 4-5. Pulse spectra and ground state experimental spectrum for ZZZZ polarizated EV experiments on HBQ in PCE. a) Probed frequency region effect showing ground state, excited state and probe spectrum. Black solid line – representive mid-IR probe spectrum used in nonlinear spectroscopy experiments displaced by arbitary scalar, dips in spectrum are a result of atmospheric water absorption. Green solid line – Integrated 3D EV spectrum offset by arbitrary constant. Red Solid line – FTIR spectrum of a 50 mM HBQ sample with a 50 μm pathlength. b) Pump frequency region, representive near-UV pump (solid blue line) overlayed with ground electronic state spectrum (dash-dotted blue line). c) Linear pump power dependence curve. Excited state absorption peak at 1446 cm^{-1} at a 2 ps pump-probe delay time (solid black line) increases linearily with pump laser power (fitted data dash-dotted black line). Red Star indicates pump-power used for experiments.

fluence measurement, see Figure 4-5c, show a linear increase in pump-probe signal with increasing pump energies, indicating sample conditions are sufficient to prevent photodegradation and nonlinear photon absorption processes, the experiments herein, were conducted with a pump power indicated by the red star.

The electronic ground state spectrum is shown in Figure 4-5b and includes a single ππ → ππ* type transition between 25000 – 28500 cm^{-1} (the S0 → S1 transition) and a ππ → πn type transition between 29500 – 32000 cm^{-1} (the S0 → S2 transition). Both the S0 → S1 transition and the S0 → S2 transition exhibit vibronic splitting of the electronic transition (not shown), the origin of which is not clear from the preceding experiment nor is addressed in this study. The maximum absorption of a 50 mM HBQ sample with a 50 μm pathlength is 1.08 OD at 381 nm

whereas the maximum absorption of the S0 → S2 transition is 0.57 at 309 nm. Herein, the red edge of the S0 → S1 transition is excited using a nUV pump pulse whom spectrum is shown in Figure 4-5b.

The ground state vibrational absorption spectrum of HBQ in the fingerprint region is shown in Figure 4-5a. The spectrum presents six sharp strong transitions (1338 cm^{-1}, 1354 cm^{-1}, 1411 cm^{-1}, 1422 cm^{-1}, 1439 cm^{-1}, and 1466 cm^{-1}) and two weak transitions (1388 cm^{-1}, 1502 cm^{-1}). The solvent ground state vibrational absorption spectrum (not shown) exhibits a strong transition which overlaps entirely with the 1354 cm^{-1} transition of Figure 4-5a and therefore assigned as the only resonant solvent vibrational feature. The seven vibrations in the HBQ are assigned as ring bending vibrational modes, the OD of which in a 50 mM solution with a 50 μm pathlength are 0.15, 0.07, 0.18, 0.12, 0.12, 0.13 and 0.05 from reddest peak to blue.

4.7.2 1D EV of HBQ and PCE

As described in the preceding section, the signal of the 2D EV can contain additional third order signals which can offset the true materials response. Normalization of the 2D EV spectrum was conducted by fitting the 2D EV, $\tau_1 = 0$ trace to that of the 1D EV spectrum at a specific τ_2. The 1D EV spectrum used for normalization was collected by averaging 2000 laser shots per difference spectrum while step scanning over a range of -5 ps to 300 ps, a differential stepping range was utilized to reduce data acquisition, a total of 5 τ_2 scans were collected. From -5 ps to 1 ps; 1 ps time intervals were used, from 1 ps to 2 ps, 20 fs time intervals were used, from 2.1 ps to 10 ps, 100 fs time intervals were used, and from 11 ps to 300 ps; 1 ps steps were used for a total of 526 τ_2 per 1D EV scan. The difference spectra was divided by a well averaged (5000

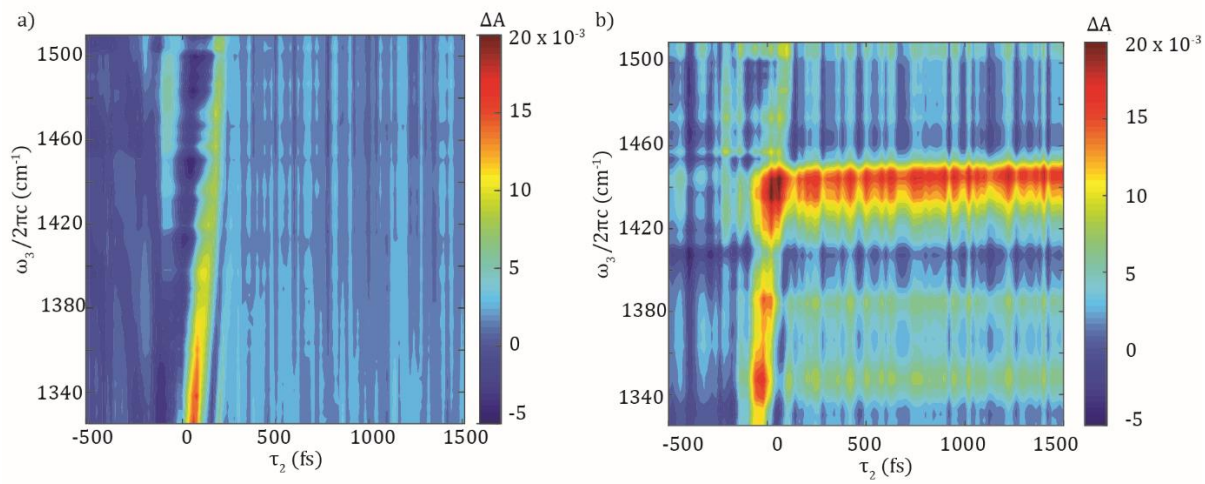

Figure 4-6. Early time transient mid-IR correlation maps plotted with contour levels at 5% intervals to maximum signal of HBQ. a) Correlation map of non-resonant solvent response of Tetrachloroethylene at ZZZZ polarizzation. Correlation map of HBQ at ZZZZ polarizzation, the slight chirp within the first 100 fs also is shown in solvent.

laser shot) pump off sample spectrum to obtain a ΔT/T spectrum before conversion to a ΔA spectrum. The early time 1D EV spectrum is shown in Figure 4-6, for the PCE solvent and sample respectively. The comparison of the early time (-500-1500fs) spectrum reveals the duration and frequency of a slightly chirped non-resonant solvent response. The solvent is not electronically resonant with the pump frequency and therefore the thermalization of the solvent and the chirp of the Mid-IR probe is indicated by the first ~200 fs about time zero. The linearly chirped non-resonant positive response of PCE about 1340-1380 cm^{-1} is also presented in HBQ 1D EV, which clearly indicates the effect of the solvent at early times. After the depletion of the non-resonant solvent response the presence of 3 positive excited state absorption (ESA) features at 1351 cm^{-1}, 1386 cm^{-1}, and 1442 cm^{-1} as well as 1 negative ground state bleach (GSB) feature at 1411 cm^{-1} are clearly identifiable in the sample. The ESA features directly report on the evolution of the local vibrational modes in the excited state keto* state, which is populated after photoinduced ESIPT of HBQ. For the excited state vibrational modes TDDFT calculations aid in the peak assignments and are assigned as the ν'_{47}, ν'_{48}, and ν'_{51} vibrational modes respectively

(see Supplementary Table 1 and Supplementary Figure 6). Of note, is the dependence of the assigned fingerprint vibrational modes to that of proton acceptor NHO bending character and in plane backbone breathing character. Unsurprisingly, these vibrational modes are dependent heavily on the proton motion resulting from the photoinduced ESIPT and can be thought to be coupled directly to the ultrafast $\pi \rightarrow \pi^*$ transition that takes place immediately following photoexcitation (within our IRF), which is exemplified from the lack of any measurable rise of each of the ESA features at 1351 cm^{-1}, 1386 cm^{-1}, and 1442 cm^{-1}.

4.7.3 Global Target Analysis of 1D EV spectra

At long times in the 1D EV spectrum (not shown) each of the ESA features exhibits characteristic frequency upshifting similar to the reported nonequilibrium dynamics described in Chapter 3. The frequency upshifting here is attributed to vibrational cooling in each of the vibrational modes that couple to the proton acceptor region of the molecule. To denote the main features present in the 1D EV spectrum the assigned nomenclature to the 3 excited state absorption mode regions in descending order from highest energy to lowest energy, here the region between 1420 -1460 cm^{-1} is ESA 1, 1375 -1390 cm^{-1} is ESA 2, 1325 -1365 cm^{-1} is ESA 3. To determine the relevant population decay times a global target analysis was done on the 1D EV data set using the compartment target model shown in Figure 4-7a[25]. The target model was fit using the Java based Glotaran fitting software package[25-27] and returned a fit error value of 0.0014. The model incorporated two parallel pathways one that decayed in 127 fs and simulated the nonresonant response of the PCE solvent (A→B), see preceding section and Figure 4-7, and one that pertained to a 3-step sequential pathway of the population decay over time (B→C,

C→D, D→E). The sequential pathway fits each decay step to an exponential decay which is assumed to be associated with a spectral population decay:

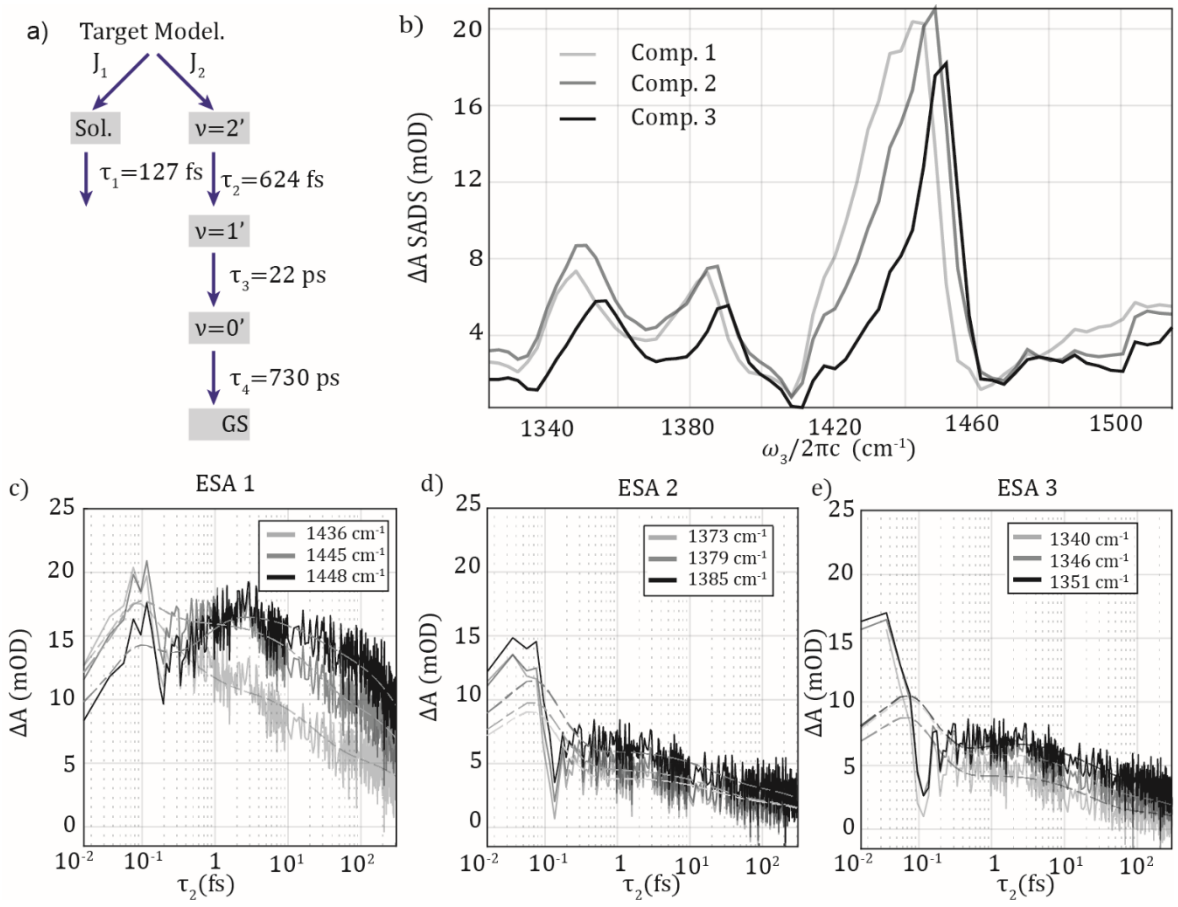

Figure 4-7. Global Target Anaylsis of 1D EV Spectrum of a 50 mM HBQ in PCE in the ZZZZ polarization condition. a) Schematic of component model used to model vibration cooling dynamics of the excited electronic state for HBQ in Glotaran. The initial conditions for J_1 and J_2 were fixed at 0.2 and 0.8 repectively with an analysis error of 0.0014[18,19], the retreived time contants are shown. b) SADS for 3 components modeling the vibrational cooling, the spectral blue shifting between components 1 to 3 is pronounced for the ESA 1 and is less pronounced for ESA 2 and ESA 3. c-e) Selected transient pump-probe slices overlaid with target model fit. c) Fitted time traces for ESA 1 at 1436, 1445 and 1448 cm^{-1}. d) Fitted time traces for ESA 2 at 1373, 1379 and 1385 cm^{-1}. e) Fitted time traces for ESA 3 at 1340, 1346 and 1351 cm^{-1}.

$\Delta A(\lambda, t) = \varepsilon_1(\lambda)c_1e^{-k_1t} + \varepsilon_2(\lambda)c_2e^{-k_2t} + \varepsilon_3(\lambda)c_3e^{-k_3t}$, in which the equation coefficient relates to the absorptivity coefficient, concentration and decay time components of each decay step. The target model was convolved with an 80 fs gaussian instrument response function.

, in which the equation coefficient relates to the absorptivity coefficient, concentration and decay

time components of each decay step. The target model was convolved with an 80 fs gaussian instrument response function.

Alternative models were also used to fit the data without improvement of the error, to avoid overfitting the 4-component model was chosen as the fit incorporated the fewest components that reproduced the data well. The slight spectral chirp seen in Figure 4-6 was ignored due to the presence of spectral artifacts caused from detector noise and atmospheric water absorption around time zero, these artifacts were subtracted from the 3-step decay model using a single early time decay component that was fit to an initial amplitude of 0.2 (J_1), the remaining spectral amplitude at early time was fit to the 3-step decay model. The species associated difference spectra (SADS) of the resulting fit is shown in Figure 4-7b and shows the spectra components of the 3-step sequential pathway which reproduce the ESA frequency upshifting effect. Spectral frequency upshifting is present in ESA 1,2, and 3 in the SADS however upon inspection of the time traces fits for each ESA mode, Figure 4-7c-e, the population of the blue frequencies in ESA 2 and ESA 3 is not seen to increase as evident as in ESA 1. This suggests whereas vibrational cooling is clearly present in ESA 1, ESA 2 and ESA 3 appear to undergo a different nonequilibrium relaxation pathway more attuned to an electronic potential solvent reorganization rather than pure vibrational cooling.

4.7.4 2D EV data acquisition, data processing and noise correction procedures

As described in the methods section, 2D EV experiments were collected using advances in our broadband-nUV pump generation scheme. For each 2D EV spectrum a total of 3,000 laser shots were collected for each τ_1, τ_2, and ω_3 surface using a homebuilt LabView VI that incorporates the Fastlite streaming option of our pulse shaper. To generate each averaged 2D EV

spectrum, 75 scan files are collected, a scan consisting of 40 complete τ_1-series 2D EV spectra containing the spectrally dispersed IR intensity of 10,000 shots of the laser and are saved on a data file. The first ~1,360 and last ~1,360 shots are averaged together and are collected as a pump off background for each scan. A series of 7,280 pump-pulse waveforms are calculated and sent to the Fastlite RF generator, upon receiving a triggering signal, the waveforms are then sent to the pulse shaper and act to generate a new pump-pulse pair with a specific carrier envelop phase (CEP) and τ_1 delay for each laser shot for the next 7,280 laser shots. Within the 7,280 waveforms sent to the dazzler the 1 x 2π phase cycling scheme[9] and series of 91 evenly spaced τ_1 points between 0-100 fs in 1.11 fs steps were calculated and are cycled 40 times through. A separate homebuilt MATLAB script reads in each of the 75 scan data files per τ_2 point and parses the pump on data into a 4 x 4 matrix [CEP, τ_1, τ_2, ω_3]. By cycling through an entire 2D EV spectrum's pump CEP and τ_1 in less than 0.2 seconds the effect of laser drift is greatly reduced, compared with averaging data collection that was previously done[4] and improve the signal to noise. Additionally, since a single-shot 2D EV spectrum was collected 3000 times the standard errors of the signal intensities can be calculated for the data collected in this experiment and are shown when possible. All other aspects of the experimental setup were the same as the 1D EV experiment, see sections above.

A total of 57 τ_2 2D EV spectrums were collected for HBQ and 9 τ_2 2D EV spectra were collected for the solvent PCE, see Figure 4-8. To further reduce the impact of long-term laser drift in our experimental noise throughout the HBQ experiment the entire subset of data was broken down into 2 parts: first τ_2 points in the range of $0 \leq \tau_2 \leq 600$ fs were scanned followed by τ_2 points in the range of $587.5 \leq \tau_2 \leq 20$ ps. The first subset was additionally divided into 22 τ_2 scans that were spaced in 25 fs steps from $12.5 \leq \tau_2 \leq 537.5$ fs and a second subset of 25 τ_2 scans

that were spaced in 25 fs steps from $0 \leq \tau_2 \leq 600$ fs. The final data subset scanned τ_2 of 575 fs, 600 fs, 700 fs, 800 fs, 900 fs, 1 ps, 5 ps, 10 ps, 15 ps and 20 ps. Time zero was set from the an midpoint of the rise in an integrated 1D EV trace of a silicon wafer see Figure 4-5 and the 1D EV of HBQ Figure 4-6. The solvent only PCE 2D EV scanned 9 τ_2 scans that were spaced in 100 fs steps from $0 \leq \tau_2 \leq 900$ fs.

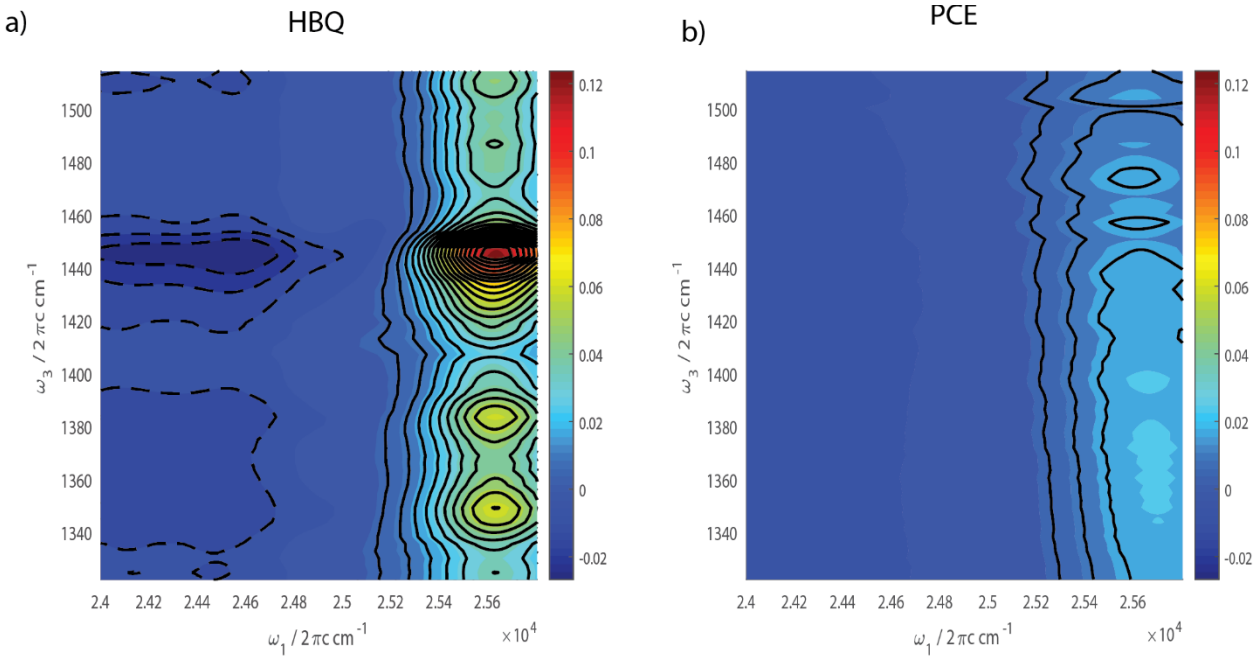

Figure 4-8. τ_2-averaged 2D EV Correlation Maps. a) ZZZZ-polarized HBQ 2D EV spectrum averaged over 52 τ_2 spectra between 0-900 fs. b) ZZZZ-polarized solvent 2D EV spectrum averaged over 9 τ_2 spectra between 0-900 fs. Featureless positive residual intensity from non-resonant heating of the solvent at early waiting times. Contour levels drawn at positive intensity in 20 equally spaced solid contour lines (0.006 OD) between 0 and 0.12 OD. The negative going contour lines were spaced at (-0.006 OD levels), the 0 OD level contour line was not drawn.

To generate 2D EV frequency-frequency correlation maps for each τ_2 2D EV spectrum, traditional Fourier transforming methods were first implemented to convert the time domain data to a ω_1- frequency: ω_3-frequency correlation map (ω_1 vs. ω_3), or simply the 2D EV spectrum for each τ_2 time. Before Fourier transforming the raw data was first normalized to the 1D EV data set using a previously established method[5]. Briefly, to ensure proper normalization between the

phase cycling data set and the normal pump-probe chopped data set, the time domain 2D EV signal is first normalized to the 1D EV for each τ_2 value. This is done by first, taking the 1D EV data set and cubic spline interpolated to have finer timesteps than was collected, 1D EV collection was done with 20 fs steps in the first 1 ps where 2D EV spectra were collected ever 12.5 fs in τ_2. Next the 2D EV (τ_1 = 0 fs) 1D EV spectra was fit to the actual 1D EV spectrum with a linear scalar and offset to generate the 2D EV normalized signal time domain signal. The optimized scalar and offset values are than applied for each time domain 2D EV (τ_1, ω_3, τ_2) signal intensity. We note the scalar and offset values applied to the data set initially set at 1, and 0 respectively and some data fits deviated from these values by more than 10% however when conducting the analyzes presented below the overall conclusions and results did not alter the underlying observations, even though the absolute Fourier transformed frequencies differed slightly.

More advanced τ_1 Fourier transform filtering were implemented for see next section for a detailed explanation regarding τ_1 and ω_1 coherence transfer. All other data analysis was conducted on the 2D EV spectrum generated from τ_1-dependent change in absorption data set generated after implementing the phase cycling difference ($\Delta\varphi_{12}(\tau_1,\omega_3,\tau_2)$) , dividing by the pump off spectrum (I_{off}) and converting to absorption units ($\Delta A(\tau_1,\omega_3,\tau_2)$ = -log(1+ $\Delta\varphi_{12}(\tau_1,\omega_3,\tau_2)$/ I_{off})). The resulting time domain signal thus has the form similar to the pump autocorrelation given in Figure 2-9. A 5th order polynomial Savitzky-Golay filter with a frame of 11 is applied to the absorptive signal, before zero-padding to 2048 points and applying a hyperbolic tangent function with a 40-fs center and 5 fs width to smooth out the data at long values of τ_1. The resulting processed time dependent signal is Fourier transformed and the real portion of the FT is repeated for each of the 3,000 2D EV spectrum collected. The standard error

and averaged 2D EV for each τ_2, ω_1, ω_3 were calculated in this way.

To remove any unwanted effect of any sampling or τ_2 coherence beating the τ_2-averaged 2D EV correlation maps are plotted for HBQ and the PCE solvent in Supplemental Figure 6. The 52 τ_2 2D EV HBQ spectra spanning 0-900 fs were averaged together and the 9 τ_2 2D EV solvent spectra were averaged together. From Supplemental Figure 6 the main spectral areas of interest and that are further discussed in the main text are resolved in both the excited state emission (ESE), negative going blue region, and the positive excited state absorption (ESA) areas as red regions. Though not thoroughly discussed in the main text 2 additional weak ESE regions are resolved the HBQ spectrum, ESE 2 and ESE 3 which are centered around ω_1 = 24300 – 24600 cm^{-1} along the excitation axis and the for ESE 2, ω_3 = 1382 -1392 cm^{-1} and ESE 3 ω_3 = 1347 - 1357 cm^{-1}. Interestingly these two ESE regions appear to correspond to the ESA 2 and ESA 3 regions, and we assign their peaks to a similar τ_1 coherence transfer process that gives rise to the stronger ESE 1 feature. Given the weaker amplitude of the ESE 2 and ESE 3 feature we are unable to resolve, above the noise, any τ_2-coherence transfer or ω_2 peaks in the discussion of 3D EV spectral analysis.

4.7.5 3D EV Time-Frequency Analysis – τ_2 coherence transfer and Vibronic Coupling of Vibrational Manifold to ESIPT in HBQ.

Implementation of pump pulse phase cycling to our EV spectrometer enables the reduction of signal to noise and quantification of background noise in the 2D EV spectrum. Given this technological improvement in our experiment the full utility of the third order spectroscopy experiment can be realized. To this end, a 3D EV spectrum can be obtained by varying, in fine time steps, the pump-pulse delay time (τ_2) with respect to the 2D EV pulse train and can provide time domain changes in the 2D EV signals. In other words, accessing the

τ_2 coherence transfer in an EV experiment requires high duty cycle, and high signal to noise. The global target analysis of the 1D EV experiment, see Figure 4-7, collected during the same laser run, reveals the initially hotly excited vibrational state present after ultrafast ESIPT decays on a 624 fs timescale, in order to map the coherence transfer pathways and intramolecular vibrational redistribution in the initial excited state the 52 τ_2 2D EV spectra were generated with a 12.5 fs time step interval to give a complete energetic landscape of the energy relaxation process. The convenient time step interval results in a frequency Nyquist sampling limit of 1333 cm^{-1} which approaches the lower frequency end of the detected probe frequency, therefore the higher energetic couplings of the mid-IR detection frequency are not explored as these frequencies would either be impulsively excited through the bandwidth of our pump pulse or not be resolvable as they would propagate faster than our gating probe pulse. Within this framework 3D EV spectra were collected; the data was processed as described below.

From the prepared data matrix, ω_2 correlation maps were generated from typical Fourier transform methods from the time domain data sets. To map the effects of τ_2 coherence transfer and its role in the nonadiabatic relaxation mechanism we perform a Fourier transform of the residuals after removal of the population dynamics in the first 600 fs to mirror the resulting decay of observed by the 1D EV spectrum. Here the selected frequency regions that are described by the ESA 2, ESA 3 and ESE 1 as described in Figure 4-1 are investigated. The resulting integrated Fourier transform correlation maps were produced and reveal sufficient signal to noise and are shown in Figure 4-9.

To generate the frequency domain correlation maps the population dynamics of the integrated signals for each ESA and ESE was subtracted. The population dynamics were

nonlinear least squares fit to a sum of 3 exponential functions of the form shown below, the fitted exponential decay and amplitudes for the integrated ESA 1 under the same analysis procedure.

$$S(\omega_1, \tau_2, \omega_3) = A_1 e^{-\frac{1}{k_1}\tau_2} + A_2 e^{-\frac{1}{k_2}\tau_2} + A_3 e^{-\frac{1}{k_3}\tau_2}$$

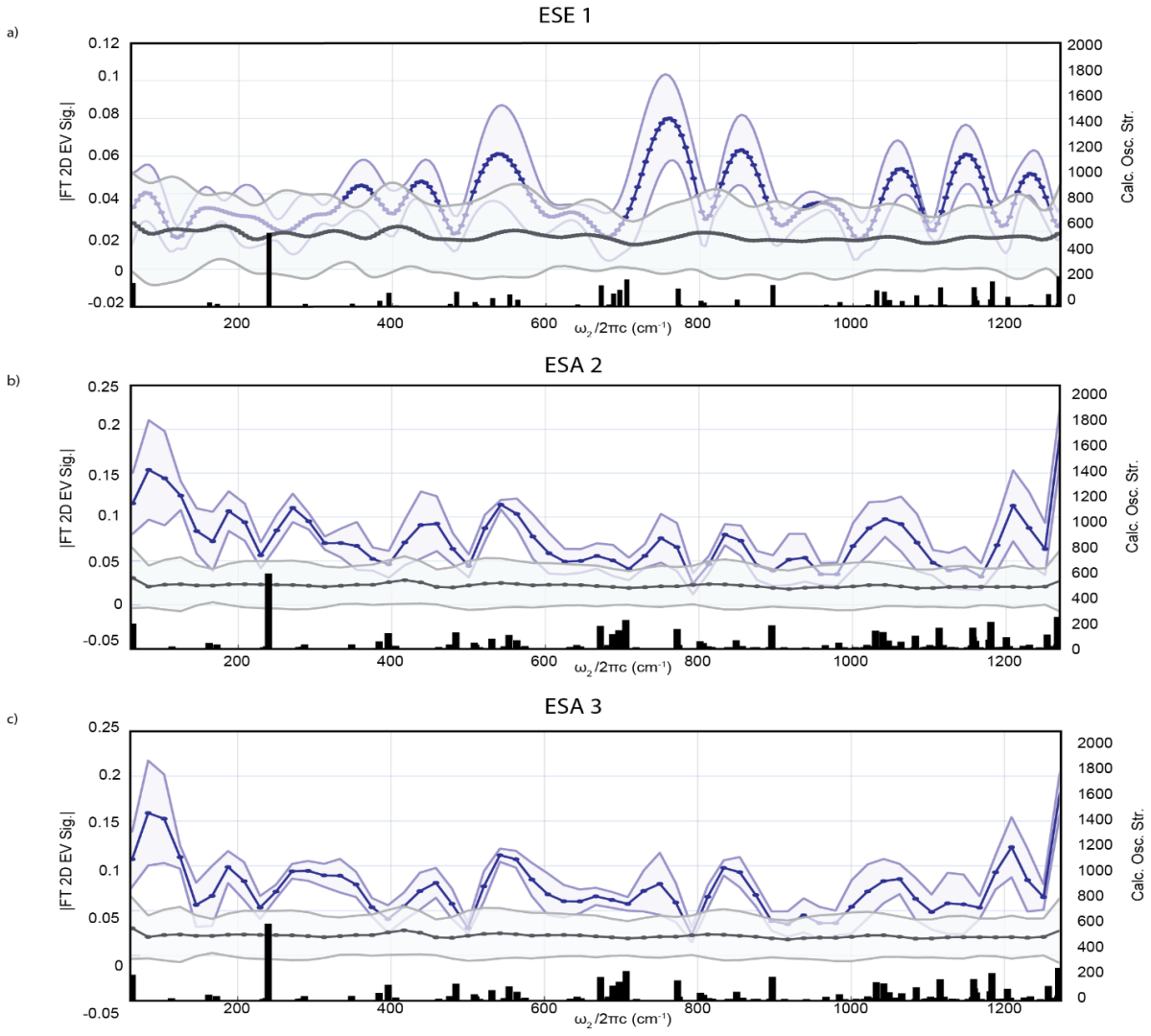

Figure 4-9. Integrated ω_2-coherence maps of ESE1, ESA 2, ESA 3 reveal resolved low frequency vibrational couplings differ between ESA 1, but are present. For all maps, black stick spectra show the frequencies of the TDDFT normal modes with anharmonic correction , the black solid line is the noise floor with the shaded areas corresponding to ±σ, for the noise, gray area and the region of interest, purple area. purple line correspond to the coherence map of the region of interest: a) ESE 1 - ω_1 = 24200-24700 cm^{-1}, ω_3 = 1415-1460 cm^{-1}, b) ESA 2 - ω_1 = 25300-25800 cm^{-1}, ω_3 = 1370-1390 cm^{-1}, b) ESA 3 - ω_1 = 25300-25800 cm^{-1}, ω_3 = 1345-1365 cm^{-1}.correlation maps are given by Table 4-1. An inlet in Figure 4-3 shows the resulting residuals of.

Overall, the fits remove any population dynamics or baseline caused from the Instrument response function in the 2D EV signal. The noise floor was

Table 4-1. Population dynamics fit parameters used in correlation maps of integrated ω_2-coherence maps.

Mode	A_1	k_1 (ps)	A_2	k_2 (ps)	A_3	k_3 (ps)
ESA 1	0.4304	1.037	-0.9613	0.36	0.0568	0.03
ESA 2	-0.0056	25.16	0.0397	0.36	-0.0989	0.03
ESA 3	-0.0217	15.38	0.0650	0.36	-0.1131	0.03
ESE 1	-0.0062	3.13	0.0096	0.36	-0.0285	0.03

characterized by the Fourier analysis of all pixel points with +/- 5% the maximum 2D EV signal about a 0 intensity value in the averaged τ_2 2D EV, the corresponding error bars are the standard deviation from each of these noise points. Following subtraction of the population dynamics the integrated residual signal was filtered via a hyperbolic tangent with a center of 525 fs and width of 10 fs for all correlation maps presented here, unless otherwise stated. The corresponding correlation plots were thus produced from the fast Fourier transform of the filtered time domain traces, see Figure 4-3 and Figure 4-9. The standard deviation of the frequency domain was produced from reproducing the fitting and filtering procedure for each pixel in the integration region and was added to the frequency domain traces for each ESA and ESE investigated and thus the correlations maps clearly produce ω_2 frequency correlations that are resolved.

Upon investigation of the integrated ω_2 correlation maps, the low frequency modes that couple to each of the ESA and ESE vibrational modes following the ultrafast ESIPT is revealed. Here, we observe many different low frequency vibrational modes coupled to the first decay component of HBQ. The low frequency modes provide detailed mechanistic understanding to the vibronic relaxation mechanism in HBQ and provide a route specific pathway for Intramolecular vibrational redistribution (IVR). In other words, the ω_2 correlation maps provide insight to which

vibrational modes are coupled to the ESA 1, ESA 2, ESA 3 and ESE 1 proton acceptor bending vibrational modes that are probing after the ESIPT has taken place.

To illustrate the vibronic coupling and vibrational mixing taking place in the first 1 ps following photoexcitation in HBQ, we report the 3D EV correlation maps for the entire sampled frequency space. The 3D EV correlation maps were created following a similar procedure as the

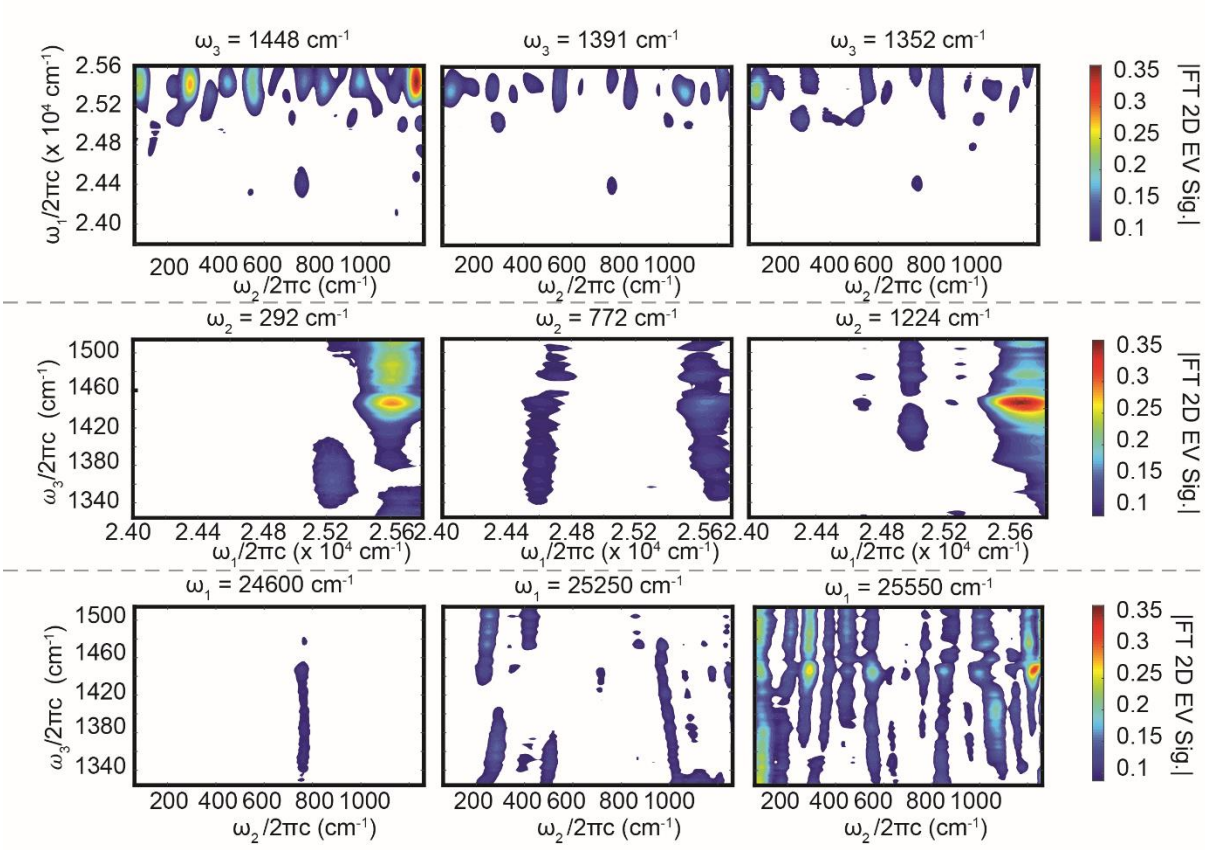

Figure 4-10. 3D EV Correlation Map revealing the vibronic coupled potential energy landscape in HBQ. Top row: 3D EV correlation maps at different ω_3 slices showing the 3 main regions of interest, ESA 1, ESA 2 and ESA 3. The projections along the ω_1 axis reveal a single significant ω_2 couples to the ESE region at lower frequencies in ω_1. The ESA region centered about 25550 cm^{-1} reveals the strongly coupled low frequency modes which couple to each ESA region. Middle Row: Correlation Maps of selected ω_2 frequencies, 292, 772 and 1224 cm^{-1} reproduced from the main text to highlight the coupling strength between the vibronic modes, the 292 cm^{-1} project reveals a second region which couples to the ESA 2 and ESA 3 region in ω_1 indicating the three ESA regions have different nonadiabatic coupling pathways. Bottom Row: Correlation Maps of selected ω_1 frequencies. The ESE region is clearly shown to couple to the 760 cm^{-1} whereas the strong ESA 1 which is centered at 25550 cm^{-1} is shown to couple to different low frequency modes that ESA 2 and ESA 3 which contain coupling to the 25250 cm^{-1} in ω_1.

integrated ω_2 coherence spectrum except that the ω_2 frequency space was deduced for every [ω_1, ω_3] pixel for the given τ_2 range. An iterative, nonlinear least squares fit of the population dynamics was subtracted for each point, in a similar matter as the integrated spectral region procedure, with the benefit of fully mapping the coherences produced during the pump-probe dimension. The same hyperbolic tangent filter was applied to the residuals before Fourier transforming the data matrix, here the data was zero padded to 2048 points in ω_2.

The procedure above resulted in a [ω_1, ω_2, ω_3] data matrix, and reports the nonadiabatic coupling between vibrational modes in the fingerprint region and the electronic degrees of freedom. The data matrix provides the correlation maps for each ESA and ESE region or interest. The major frequency slices for each frequency axis are shown in Figure 4-10. As described earlier the correlation maps report on the extent of the vibronic coupling and vibrational mode mixing in the excited state. Here, the vibrational modes of the Keto* state and that these fingerprint vibrational modes couple to a host of different low frequency modes. For ESA 1 we resolve up to 14 different low frequency vibrational modes that couple to the strong proton bending mode, see main text. ESA 1 is clearly the predominate vibrational mode however the ESA 2, ESA 3 and ESE 1 modes also couple to multiple low frequency modes in ω2. We quantify the fully coupled potential energy in Supplemental Table 2 and Figure 4-4. To aid in the discussion we report the low frequency modes which were found to couple to the ESIPT process in the stimulated Raman experiments recently performed by Taiha Joo and coworkers[28]. What is of interest is that many of the modes which were reported but, in the Raman, and previous transient absorption[29,30] experiments are also resolved in the 3D EV correlation maps. Here, with 3D EV spectroscopy we identify the specific modes that couple to the fingerprint modes to provide more specific detail regarding the nonequilibrium energy transfer mechanism in HBQ.

The correlation maps and 3D EV time analysis clearly indicated the presence of multiple coherences that propagate during the pump-probe waiting time. In the next section we will identify two vibrational modes which couple and propagate during τ_1.

Table 4-2. ω_2 - Vibronic Coupling Frequencies from 3D EV Correlation Maps shown in Figure 4-10.

ESA 1: *ω_3 = 1444 – 1452 cm^{-1}* *ω_1 = 25500 – 25700 cm^{-1}*		**ESA 2:** *ω_3 = 1382– 1392 cm^{-1}* *ω_1 = 25500 – 25700 cm^{-1}*		**ESA 3:** *ω_3 = 1347– 1357 cm^{-1}* *ω_1 = 25500 – 25700 cm^{-1}*		**ESE 1:** *ω_3 = 1444 – 1452 cm^{-1}* *ω_1 = 24300 – 24600 cm^{-1}*		**Joo (2021)[1]**
ω_2 (cm^{-1})	|EV FT int.|	ω_2 (cm^{-1})	|EV FT int.|	ω_2 (cm^{-1})	|EV FT int.|	ω_2 (cm^{-1})	|EV FT int.|	ω (cm^{-1})
89	0.26	104	0.16	99	0.16			
219	0.14	193	0.13	193	0.12			237
297	0.27	271	0.14	266	0.09			
375	0.12	349	0.10					396
448	0.16	433	0.09					
		464	0.10	469	0.09			
552	0.20	547	0.14					543
636	0.09	636	0.09	631	0.10			
693	0.08							688
766	0.14	761	0.11			760	0.08	794
850	0.17	839	0.11	839	0.13	855	0.06	842
995	0.16	959	0.08	964	0.08			990
		1048	0.14	1053	0.10			
		1068	0.14	1084	0.10	1063	0.05	
1141	0.12	1157	0.10	1178	0.07	1147	0.07	
1230	0.33	1220	0.13	1214	0.09	1235	0.05	1205

4.7.6 ω_1-excited state emission coherence time analysis

To describe the ultrafast energy transfer process following photoexcitation in HBQ concepts relating the notion that population-to-coherence energy transfer and coherence-to-population energy transfer processes explain the nonadiabatic energy transfer that moderates the ESIPT process are introduced described by Figure 4-2 here the data analysis procedure is described. To this end, we performed a short time-frequency Fourier analysis across τ_1 in the ESA 1 and ESE 1 frequency regions. Recall that the 2D EV analysis revealed for the ESE the

signal started from zero intensity grows in during the characteristic proton transfer time then oscillates in a characteristic frequency beating pattern. Whereas the ESA signal intensity started from a signal maximal and decayed in a simple exponential time scale. Prior 3D EV experiments have failed to measure a clear ESE pathway as is shown by our experiments on HBQ, thus for completeness and to assess the level of confidence in our assessment on the presence of the coherence in τ_1 we performed multiple time-frequency analyses for different time-frequency windowing functions which are summarized in Figure 4-11 below.

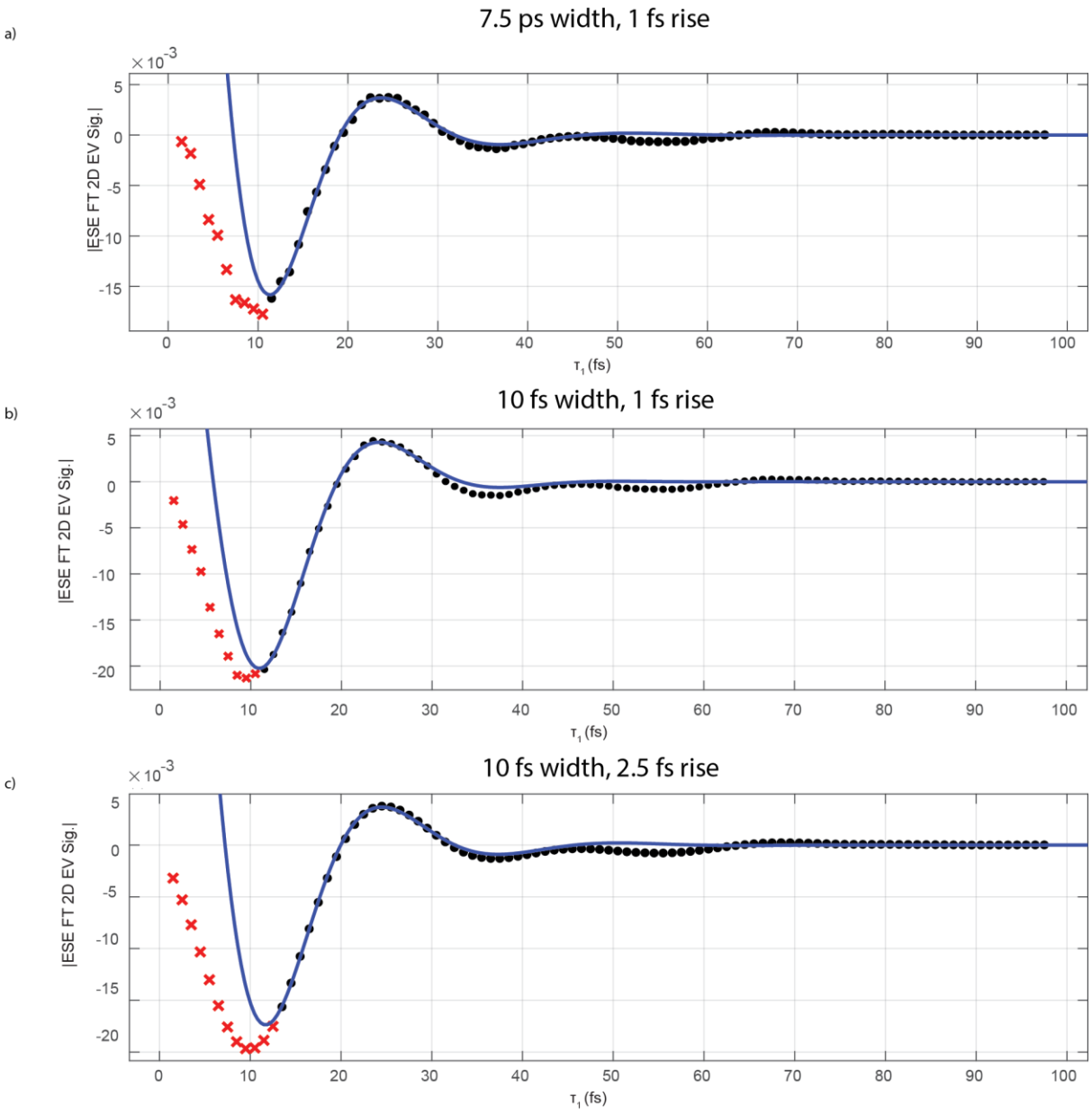

Figure 4-11. Short-Time frequency Analysis on ESE 1 Revealing τ_1-population-to-coherence transfer occurs for multiple short time windowing function, a double sided hyperbolic tangent filter was applied for the τ_1

Briefly, a short time-frequency analysis was performed on the integrated frequency region of the ESE for all τ_2 scans. The short time-frequency analysis was performed by multiplying a double sized hyperbolic windowing function of different widths and rise times to the raw time-domain data set. The windowing function was slide across the data set in 1 fs intervals to reproduce a τ_1 time domain trace. Following application of the short time windowing

function the resulting time domain traces were plotted and nonlinearly least squares fit to two sinusoids convolved with a damping exponential function. Fourier time windowing function were used to with the filter in the main text being a 5 fs width and 1 fs rise. The resulting fits resulted in a characteristic frequency between 800-1000 cm^{-1} and a higher lying frequency around 1300-1500 cm^{-1} depending on the windowing function used. Of note, we exclude in our fit the first 12 fs of data points. By excluding these data points the fitted function reproduces the fit well, see supplemental figure 7 and main text figure 2. The first 12 fs are excluded to take into an account the rapid changes occurs during the ESIPT process, it is of note the fit to the remaining data clearly does not capture the phase or frequency of the ESE region within the first 12 fs and the growth of the ESE signal intense is of much lower frequency, suggesting the rise of the ESE occurs at different frequency.

4.7.7 Lineshape and Center line Slope Analysis of 2D EV spectroscopy

The study herein utilized a multidimensional EV spectrometer that probes how the direct coupling from a nUV broadband laser pulse affects and is coupled to the structural changes in HBQ. The third order spectroscopy experiment extends the information content that can be accessed from a traditional pump probe experiment (1D EV) to two additional degrees of freedom, the ω_1 (excitation frequency), and ω_2 (coherence frequency) degrees of freedom. One analysis method that is commonly employed to analysis multidimensional spectroscopy, including 2D EV spectra, is center line slope analysis[10]. Herein, a series of 52 early τ_2 waiting times is analyzed for CLS deviations and I conclude that no resolvable backwards center line slope is observed across the 2D EV series, below we present an explanation.

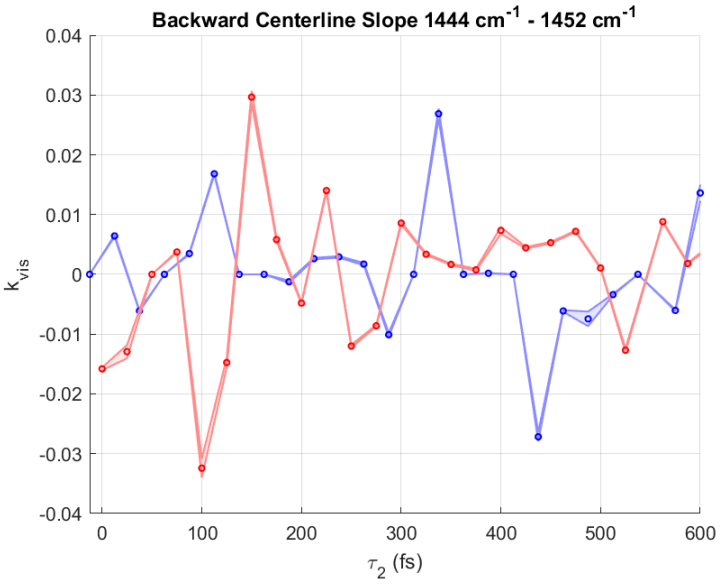

Figure 4-12. Backwards center cine slope Analysis of ESA 1 region for the two separates experimental 2D EV runs, denoted by color. For each experimental run and for the dataset the values fluctuated about 0, indicating no correlation between the electronic and vibrational degrees of freedom, confirming the ESA 1 feature does not report on the initial photoexcited population.

CLS analysis is useful when attempting to quantify whether the electronic or vibrational transition energies are correlated, and what the vibrational dephasing times for the coupled transition is[31,32]. Here we implement the procedure, previously established in Oliver and Fleming[32], to determine the CLS for each of the ESE and ESA regions of interest. Briefly, the CLS is calculated from taking a linear fit of the 2D EV signal maxima along either the excitation axis or detection axis for a particular feature in a 2D EV spectrum. In each of our analyses the CLS over the early waiting times appeared to fluctuate about zero without a clear positive or negative trend. Qualitatively this is seen in Figure 4-8, from the τ_2-averaged 2D EV each ESA and ESE feature which appear to have a horizontal peak maximum (minimum for the case of the ESE) with respect to the excitation axis.

Accurate quantification of the CLS for any multidimensional spectrum requires the resolution of the detection and excitation axes to be relatively equal. For 2D EV spectra this

presents a problem given the resolution of the detection axis in our experiment is limited by the resolution of a grating and the corresponding seperation of MCT detector elements, here a single grating position dispersed light spanning from 1514 to 1324 cm^{-1} across 64-pixel elements leading to a detection resolution of 2.97 cm^{-1}. The resolution of the excitation axis on the other hand, was determined from zero padding to 2048 frequency points from the Fourier transformed signal, which results in resolution of 14.66 cm^{-1}. Given the large mismatch and relatively low resolution in our experiment in order to induce a CLS than is non-zero the 2D EV spectrum is cubic spline interpolated along the excitation and detection axes to 0.5 cm^{-1} resolution, upon conducting the interpolation the CLS for each ESA and ESE determined and found to remain fluctuating about zero as shown in the CLS shown in Figure 4-12.

The corresponding CLS analysis suggests there is no correlation between the electronic degrees of freedom and the vibrational degrees of freedom in this experiment however the determination of whether the CLS analysis is a good method to analysis our 2D EV spectra is called into question. A recent 2020 account on CLS in 2D EV spectra was presented by Cho and Fleming[10] which describes in detail the resulting CLS based on a model of 1 electronic transition coupling to 1 vibrational transition. This model presents some clear deviations and underlining assumptions which appear to deviate from the spectra of HBQ. For instance, based on the 1 electronic transition coupled to 1 vibrational transition model a 2D EV spectrum should contain GSB features to the red of a corresponding electronic energy gap of ν_{eg}, while ESA features should present themselves to blue side of the GSB that is resonant with a $\nu_{e'g}$ gap. However, in the 3D EV experiment of HBQ this relationship is not observed. Additionally, their work suggests there should be an FCCF or nodal slope that relates the electronic transition to the vibrational transition correlation function, but in HBQ the slope is also not observed.

Accordingly, the lack of a CLS in our data may be attributed to the fact there is a strong association to the solvent. However, once again this is not evident in HBQ as the case stems from the fact that PCE is a very nonpolar as well as aprotic solvent which has been attributed to having very little interaction with the system. Therefore, the lack of a clear CLS is evidenced to that fact that in HBQ many vibrational modes couple to the electronic transition of interest, which interfere with, and cancel out any CLS that may be present in our experimental data, the many vibrational modes theory accurately describes the current system as being exceedingly anharmonic a point shown by the evidence of Vibrational cooling and intramolecular vibrational redistribution in the present system. The resulting anharmonicity of the system further explains why anisotropic datasets could not accurately be compiled for HBQ, given the broad pump bandwidth used in this study. The presence of multiple vibrational modes coupling to the electronic transition moment further supports the claim of an ESE pathway in the 2DEV spectrum, which is revealed to red of the eg transition at around 24500 cm^{-1}, based on the framework laid out by Cho and Fleming any ESE pathways would be to the blue of the resulting ground state absorption spectrum, which is not present in this work.

Lastly, the peak maxima of the 3 ESA features and the peak minima of ESE 1 were analyzed to determine whether any electronic transition or dark state arise following the ESIPT in HBQ, see . Overall, the peak maxima and minima do not shift significantly though there appears to be a fluctuation of the peak centers about ω_1 across the early τ_2 2D EV spectra. Here, we find the 3 ESA peak maxim fluctuation about 25620 cm^{-1} though the amplitude of the peak centers fluctuates with differing amplitude across the 3 modes. For ESA 1 (ω_3 = 1446 cm^{-1}) the

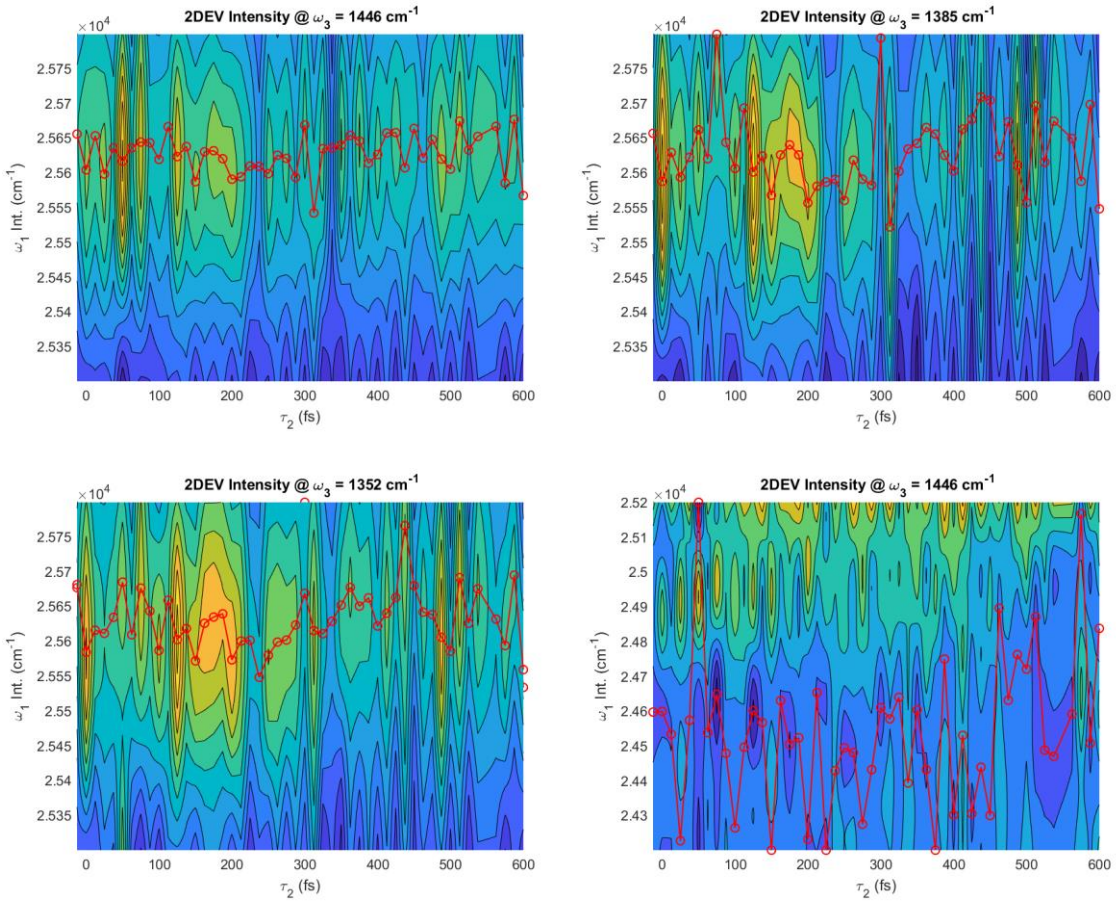

Figure 4-13. ESA and ESE ω_1 peak positions during τ_2. *Top left:* ESA 1 peak position centered at ω_3 = 1446 cm^{-1}.*Bottom Left:* ESA 2 peak position centered at ω_3 = 1385 cm^{-1}. *Top Right:* ESA 3 peak position centered at ω_3 = 1352 cm^{-1}. *Bottom Right:* ESE 1 peak position centered at ω_3 = 1446 cm^{-1}. For each panel the corresponding peak maxima/minima is denoted as a red point with the corresponding trend represented as a red line. For the ESAs the peak maximas do not change significantly over the first 600 fs of delay times.

observed fluctuation range is within 60 cm^{-1} which accounting for chosen ~15 cm^{-1} Fourier transform resolution is not significant, the peak intensity fluctuations for ESA 2 (ω_3 = 1385 cm^{-1}) and ESA 3 (ω_3 = 1352 cm^{-1}) are significantly less pronounced but have a larger range from 25550 – 25750 cm^{-1}. For each ESA feature the peak shifts across τ_2, though with fluctuating absolute peak intensities which suggests the peak center amplitudes are a result of τ_2 coherences rather than the rise or decay of various electronic transitions. Given there is no clear change to the peak maxima center the peak maxima fluctuation across ω_1 for the ESA modes we assign the

peak shifting in ω_1 to be from intramolecular vibrational redistribution coherence transfer observed in the ESA modes, rather than any indication of early sub-picosecond Internal conversion process. Lastly, the peak shifting in ESE 1 was much more pronounced however we assign the peak shifting to arise from a separate τ_2 coherences, see main text and SI note below. The overall minimum of the 2D EV spectrum in the lower frequency range is almost an order of magnitude less intense suggesting a more significant impact of solvent intensity, see Figure 4-8 and intensity borrowing caused by the τ_2 coherence transfer process.

4.7.8 Computation assignment of vibrational modes from Gaussian Calculations

To aid in the assignment of vibrational mode and low frequency modes observed in the 3D EV experiments, computation support was proved by DFT and TDDFT calculation using the assignments of HBQ were performed using the Gaussian 16W package[15]. Briefly the ground state optimized structure of HBQ was performed utilizing a tight convergence requirement with unrestricted B3LYP level of theory and 6-311++G(d,p) basis set, which is sufficient to accurately represent the enol ground state of the system[1,2]. The optimized ground state structure is provided in Appendix A. Following the optimization of the HBQ ground state structure the first 3 electronic transitions and vibrational frequencies were calculated using a B3LYP functional and the Aldrich Def2-TZVP basis set. The lowest electronic transition was centered at 363.86 nm with the second lowest transition being centered at 325.76 nm. The calculated UV-vis spectra thus support previous claims that the S0 (π) → S1 (π^*) transition is described by the UV-vis transition from 350-400 nm.

Table 4-3. Vibrational Mode assignments of the keto* electronic state as computed from TDDFT calculations of the first excited state root of the geometry optimized structure of HBQ. Subscripts: a in unites of cm-1, b units of km/mol,. oop: out of plane. op: out of phase. ip: in phase.

Vibrational Mode Label	*DFT Anharmonic* ω_{peak}[a]	*DFT Anharmonic Correction*[a]	DFT I[b]	Mode Description
ν'_1	62.6	2.9	2.9	Out of plane, Wobble
ν'_5	239.5	8.19	33.8	In-plane backbone bend
ν'_6	283.8	-4.5	2.2	Out of plane, Wobble
ν'_8	384.0	3.2	4.5	In-plane backbone wag
ν'_{10}	475.7	7.6	3.0	Out of plane, Wobble
ν'_{15}	553.6	1.0	13.3	In-plane backbone rock
ν'_{17}	641.6	7.9	3.2	Out of plane, Wobble
ν'_{18}	705.6	28.1	37.2	Out of plane, Wobble
ν'_{23}	772.4	14.5	27.4	Out of plane, Wobble
ν'_{25}	806.5	-9.8	7.0	C2-C1=O str. Backbone squeeze
ν'_{29}	1064.4	130.8	12.2	Out of plane, Wobble
ν'_{31}	1048.7	93.9	1.3	Out of plane, Wobble
ν'_{32}	1118.5	150.6	4.7	Out of plane, Wobble
ν'_{34}	1019.9	-8.8	5.4	N-H ring breath w/C2-C1=O str.
ν'_{42}	1223.6	-13.7	4.2	H-N-C3 bend
ν'_{47}	1343.3	-30.6	22.8	H-N-C3 bend w/ op C2-C1=O bend
ν'_{48}	1399.6	-19.8	21.4	H-N-C3 bend w/ ip C2-C1=O bend
ν'_{51}	1448.9	-28.8	30.2	H-N-C3 rock w/ op C2-C1=O rock

To simulate the effect of a perturbation with 390 nm laser light, the excited state vibrational modes were obtained by TDDFT calculation of the first excited state root. The vibrational mode calculations for the ground and excited state were performed with anharmonic corrections for all modes using the Hyak supercomputer at the University of Washington, all vibrational modes computed returned non-negative transition energies with exact frequencies, selected normal modes discussed in the main text and that were assigned by to the ESA observed by the 1D EV and 3D EV experiments are highlighted in Supplementary Figure 8 and Table 4-3. We note, the optimization of the first excited state structure is notable for its obvious keto-like geometry and calculated fluorescence peaks at 598.5 nm and 426.5 nm for HBQ and the

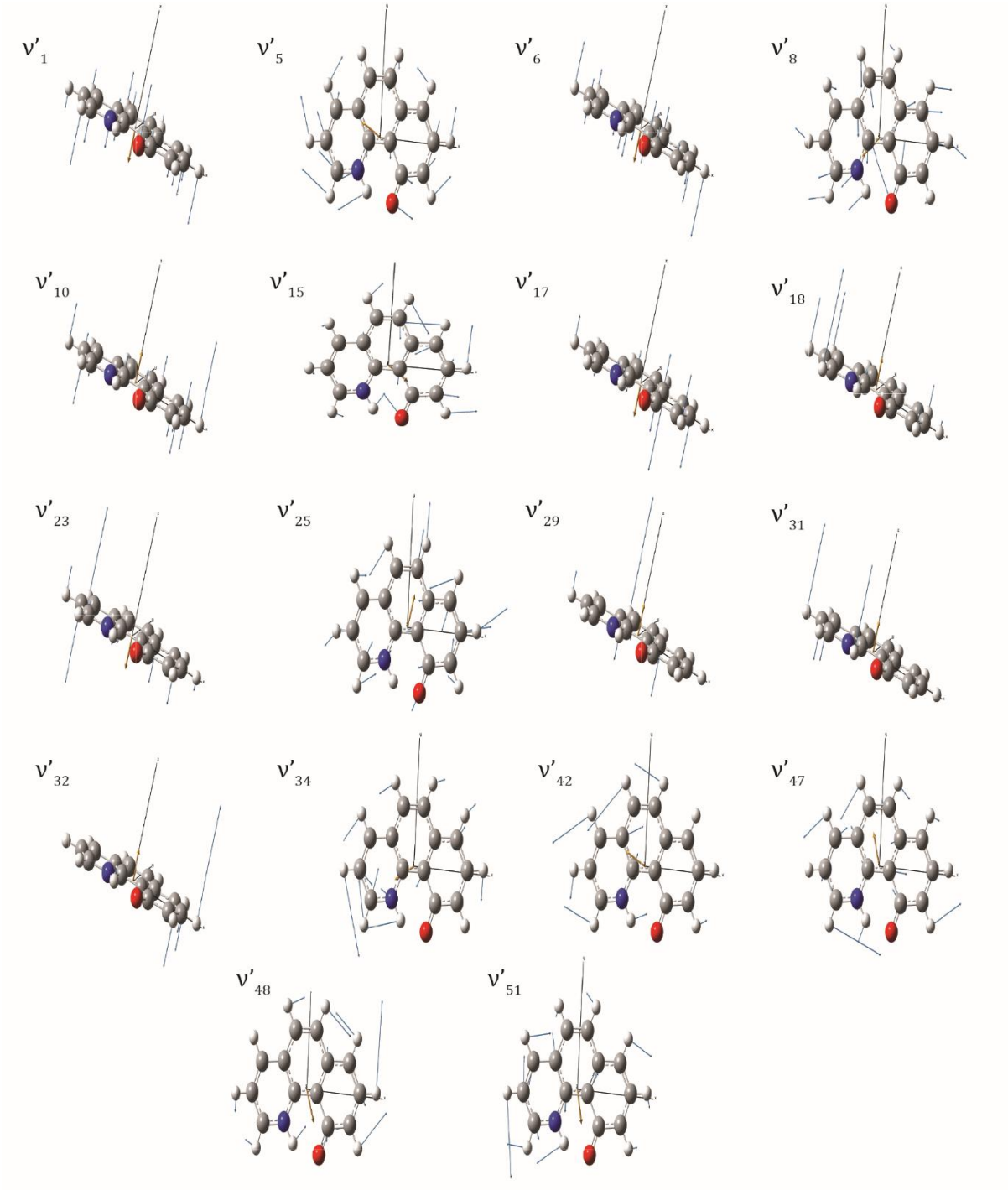

Figure 4-14. Selected excited state keto conform normal mode Vibrational Modes. Individual atomic displacements are shown by the solid blue arrows with the overall transition dipole moments shown by the gold arrow. Out-of-plane butterfly and wobble modes are shown looking down the y-axis whereas in-plane vibrational modes are shown looking down the z-axis, see included Cartesian axis.

computed harmonic frequencies. The total anharmonic X matrix which can be used to calculate the anharmonic frequency corrections for each vibrational model is reported in Appendix A.

4.8 REFERENCES

1 Kim, J. *et al.* Non-Born-Oppenheimer Molecular Dynamics Observed by Coherent Nuclear Wave Packets. *J Phys Chem Lett* **11**, 755-761 (2020). https://doi.org:10.1021/acs.jpclett.9b03488

2 Hurley, J. J. M. & Zhu, L. Excitation Energy-Dependent, Excited-State Intramolecular Proton Transfer-Based Dual Emission in Poor Hydrogen-Bonding Solvents. *J Phys Chem A* **126**, 5711-5720 (2022). https://doi.org:10.1021/acs.jpca.2c03668

3 Junghwa Lee, T. J. Photophysical Model of 10-Hydroxybenzo[h]qionoline: Internal Conversion and Excited State Intramolecular Proton Transfer. *Bull. Korean. Chem. Soc.* **35**, 5 (2014). https://doi.org:https://doi.org/10.5012/bkcs.2014.35.3.881

4 Hristova, S. 10-Hydroxybenzo[h]quinoline: switching between single- and double-well proton transfer through structural modifications. *RSC Advances* **5**, 12 (2015). https://doi.org:10.1039/c5ra20057a

5 Gaynor, J. D., Sandwisch, J. & Khalil, M. Vibronic coherence evolution in multidimensional ultrafast photochemical processes. *Nat Commun* **10**, 5621 (2019). https://doi.org:10.1038/s41467-019-13503-9

6 Arsenault, E. A., Yoneda, Y., Iwai, M., Niyogi, K. K. & Fleming, G. R. Vibronic mixing enables ultrafast energy flow in light-harvesting complex II. *Nat Commun* **11**, 1460 (2020). https://doi.org:10.1038/s41467-020-14970-1

7 Arsenault, E. A., Yoneda, Y., Iwai, M., Niyogi, K. K. & Fleming, G. R. The role of mixed vibronic Q(y)-Q(x) states in green light absorption of light-harvesting complex II. *Nat Commun* **11**, 6011 (2020). https://doi.org:10.1038/s41467-020-19800-y

8 Arsenault, E. A. *et al.* Concerted Electron-Nuclear Motion in Proton-Coupled Electron Transfer-Driven Grotthuss-Type Proton Translocation. *J Phys Chem Lett* **13**, 4479-4485 (2022). https://doi.org:10.1021/acs.jpclett.2c00585

9 Arsenault, E. A., Bhattacharyya, P., Yoneda, Y. & Fleming, G. R. Two-dimensional electronic-vibrational spectroscopy: Exploring the interplay of electrons and nuclei in excited state molecular dynamics. *J Chem Phys* **155**, 020901 (2021). https://doi.org:10.1063/5.0053042

10 Cho, M. & Fleming, G. R. Two-Dimensional Electronic-Vibrational Spectroscopy Reveals Cross-Correlation between Solvation Dynamics and Vibrational Spectral

Diffusion. *J Phys Chem B* **124**, 11222-11235 (2020). https://doi.org:10.1021/acs.jpcb.0c08959

11 Gaynor, J. D. & Khalil, M. Signatures of vibronic coupling in two-dimensional electronic-vibrational and vibrational-electronic spectroscopies. *The Journal of Chemical Physics* **147**, 094202 (2017). https://doi.org:10.1063/1.4991745

12 Gaynor, J. D., Weakly, R. B. & Khalil, M. Multimode two-dimensional vibronic spectroscopy. I. Orientational response and polarization-selectivity. *The Journal of Chemical Physics* **154**, 184201 (2021). https://doi.org:10.1063/5.0047724

13 Weakly, R. B., Gaynor, J. D. & Khalil, M. Multimode two-dimensional vibronic spectroscopy. II. Simulating and extracting vibronic coupling parameters from polarization-selective spectra. *The Journal of Chemical Physics* **154**, 184202 (2021). https://doi.org:10.1063/5.0047727

14 Gelzinis, A., Augulis, R., Butkus, V., Robert, B. & Valkunas, L. Two-dimensional spectroscopy for non-specialists. *Biochim Biophys Acta Bioenerg* **1860**, 271-285 (2019). https://doi.org:10.1016/j.bbabio.2018.12.006

15 K. Stock, T. B., and S. Lochbrunner Proton transfer and internal conversion of o-hydroxybenzaldehyde: coherent versus statistical excited-state dynamics. *Chem. Phys. Lett.* **354**, 7 (2002).

16 Berenbeim, J. A. *et al.* Excited state intramolecular proton transfer in hydroxyanthraquinones: Toward predicting fading of organic red colorants in art. *Science Advances* **5**, eaaw5227 (2019). https://doi.org:10.1126/sciadv.aaw5227

17 Li, Y., Dahal, D., Abeywickrama, C. S. & Pang, Y. Progress in Tuning Emission of the Excited-State Intramolecular Proton Transfer (ESIPT)-Based Fluorescent Probes. *ACS Omega* **6**, 6547-6553 (2021). https://doi.org:10.1021/acsomega.0c06252

18 Sedgwick, A. C. *et al.* Excited-state intramolecular proton-transfer (ESIPT) based fluorescence sensors and imaging agents. *Chemical Society Reviews* **47**, 8842-8880 (2018). https://doi.org:10.1039/c8cs00185e

19 Dahal, D. *et al.* An NIR-emitting lysosome-targeting probe with large Stokes shift via coupling cyanine and excited-state intramolecular proton transfer. *Chemical Communications* **53**, 3697-3700 (2017). https://doi.org:10.1039/c7cc00700k

20 Marciniak, H. *et al.* Dynamics of excited state proton transfer in nitro substituted 10-hydroxybenzo[h]quinolines. *Phys Chem Chem Phys* **19**, 26621-26629 (2017). https://doi.org:10.1039/c7cp04476c

21 Takeuchi, S. & Tahara, T. Coherent Nuclear Wavepacket Motions in Ultrafast Excited-State Intramolecular Proton Transfer: Sub-30-fs Resolved Pump−Probe Absorption

Spectroscopy of 10-Hydroxybenzo[h]quinoline in Solution. *The Journal of Physical Chemistry A* **109**, 10199-10207 (2005). https://doi.org:10.1021/jp0519013

22 Stefan Lochbrunner, A. J. W., and Eberhard Riedle. Microscopic Mechanism of Ultrafast Excited-State Intramolecular Proton Transfer: A 30-fs Study of 2-(2‘-Hydroxyphenyl)benzothiazole. *J. Phys. Chem. A* **107**, 11 (2003). https://doi.org:https://doi.org/10.1021/jp035203z

23 He, P. *et al.* High-efficiency supercontinuum generation in solid thin plates at 0.1 TW level. *Opt Lett* **42**, 474-477 (2017). https://doi.org:10.1364/Ol.42.000474

24 Lu, C.-H. *et al.* Generation of intense supercontinuum in condensed media. *Optica* **1**, 400 (2014). https://doi.org:10.1364/optica.1.000400

25 Snellenburg, J. J., Laptenok, S. P., Seger, R., Mullen, K. M. & van Stokkum, I. H. M. Glotaran: A Java-Based Graphical User Interface for the R Package TIMP. *J Stat Softw* **49**, 1-22 (2012). https://doi.org:DOI 10.18637/jss.v049.i03

26 van Stokkum, I. H. M., Larsen, D. S. & van Grondelle, R. Global and target analysis of time-resolved spectra. *Bba-Bioenergetics* **1657**, 82-104 (2004). https://doi.org:10.1016/j.bbabio.2004.04.011

27 Mullen, K. M. & van Stokkum, I. H. M. TIMP: An R package for modeling multi-way spectroscopic measurements. *J Stat Softw* **18** (2007).

28 Kim, J. *et al.* Non-Born–Oppenheimer Molecular Dynamics Observed by Coherent Nuclear Wave Packets. *The Journal of Physical Chemistry Letters* **11**, 755-761 (2020). https://doi.org:10.1021/acs.jpclett.9b03488

29 Takeuchi, S. & Tahara, T. Coherent nuclear wavepacket motions in ultrafast excited-state intramolecular proton transfer: Sub-30-fs resolved pump-probe absorption spectroscopy of 10-hydroxybenzo[h]quinoline in solution. *Journal of Physical Chemistry A* **109**, 10199-10207 (2005). https://doi.org:10.1021/jp0519013

30 Marciniak, H. *et al.* Dynamics of excited state proton transfer in nitro substituted 10-hydroxybenzo[h]quinolines. *Phys. Chem. Chem. Phys.* **19**, 26621-26629 (2017). https://doi.org:10.1039/C7CP04476C

31 Wu, E. C. *et al.* Two-dimensional electronic-vibrational spectroscopic study of conical intersection dynamics: An experimental and electronic structure study. *Physical Chemistry Chemical Physics* **21**, 14153-14163 (2019). https://doi.org:10.1039/c8cp05264f

32 Oliver, T. A., Lewis, N. H. & Fleming, G. R. Correlating the motion of electrons and nuclei with two-dimensional electronic-vibrational spectroscopy. *Proc Natl Acad Sci U S A* **111**, 10061-10066 (2014). https://doi.org:10.1073/pnas.1409207111

APPENDIX A – DFT CACLUATION OUTPUT DATA OF HBQ AND DBQ

Throughout the previous chapters, results from DFT and TDDFT calculations were commonly referred to and referenced. A summary of the key data outputs is shown below. In each of the calculations a common optimized geometry was used, the geometry is the starting point for computes and was computed independent of the vibration and electronic state root calculations discussed through this thesis. Aside from the geometry optimized structure, the anharmonic corrections and vibrational frequencies of the ground and electronic state for HBQ and DBQ are tabulated in addition to the full X matrix for the excited keto vibrations. The X matrix can be used to determine the individual displacements of the keto vibrations for HBQ.

Gaussian ground state enol geometry optimized structure used for DFT and TDDFT frequency and excited state energy calculations.

C	-3.54315900	-0.37558900	0.00000000
C	-2.96321800	0.87842200	0.00000100
C	-1.56234500	1.00559200	0.00000100
C	-0.78715800	-0.18816400	0.00000000
C	-2.70436300	-1.49734700	-0.00000200
C	-0.89783000	2.27526300	0.00000300
C	0.65747600	-0.11540800	0.00000000
C	1.28057100	1.16760200	0.00000100
C	0.45831500	2.34618100	0.00000300
C	2.68493700	1.26938400	0.00000200
H	3.14555500	2.25047300	0.00000300
C	3.46151200	0.12379200	0.00000100
C	2.87007300	-1.14258200	-0.00000100
C	1.48554300	-1.27811600	-0.00000200
H	-1.50042100	3.17716600	0.00000400
H	-4.61850200	-0.50177900	-0.00000100
H	-3.57758500	1.77273800	0.00000200
H	-3.12083900	-2.49980200	-0.00000300
H	0.95393400	3.31101900	0.00000400
H	4.54299100	0.20284400	0.00000100
H	3.47346800	-2.04233300	-0.00000200
O	0.96841200	-2.52320900	-0.00000300
H	-0.02255000	-2.42764700	-0.00000300
N	-1.38078200	-1.41017000	-0.00000200

Gaussian ground state enol fundamental Vibrational Transition matrix with anharmonic corrections of HBQ

Fundamental Bands

	Mode(n)	Status	E(harm)	E(anharm)	Aa(x)	Ba(y)	Ca(z)
L	1(1)	active	3204.115	3096.913	0.039541	0.018596	0.012652

L	2(1)	active	3197.278	3092.638	0.039540	0.018596	0.012652
L	3(1)	active	3186.798	3032.901	0.039541	0.018596	0.012652
L	4(1)	active	3183.870	3058.165	0.039542	0.018595	0.012652
L	5(1)	active	3174.458	3036.088	0.039541	0.018596	0.012652
L	6(1)	active	3171.350	3054.969	0.039542	0.018597	0.012652
L	7(1)	active	3167.179	3009.497	0.039543	0.018595	0.012652
L	8(1)	active	3165.011	3039.106	0.039542	0.018597	0.012652
	9(1)	active	3098.866	2704.781	0.039604	0.018683	0.012699
H	10(1)	active	1667.199	1614.926	0.039527	0.018585	0.012648
L	11(1)	active	1652.845	1623.522	0.039527	0.018587	0.012648
	12(1)	active	1629.376	1592.007	0.039529	0.018587	0.012645
	13(1)	active	1611.575	1570.066	0.039520	0.018586	0.012644
H	14(1)	active	1570.683	1545.389	0.039527	0.018587	0.012645
	15(1)	active	1539.759	1506.687	0.039531	0.018589	0.012646
H	16(1)	active	1512.606	1461.174	0.039529	0.018591	0.012647
	17(1)	active	1471.587	1444.559	0.039540	0.018588	0.012648
	18(1)	active	1456.644	1437.111	0.039533	0.018594	0.012651
H	19(1)	active	1431.907	1401.600	0.039523	0.018590	0.012644
H	20(1)	active	1423.403	1385.147	0.039513	0.018581	0.012641
	21(1)	active	1365.676	1337.474	0.039523	0.018582	0.012643
	22(1)	active	1349.984	1325.152	0.039519	0.018588	0.012644
	23(1)	active	1322.432	1294.136	0.039524	0.018583	0.012644
	24(1)	active	1302.801	1279.332	0.039523	0.018590	0.012647
	25(1)	active	1262.244	1236.761	0.039543	0.018589	0.012648
L	26(1)	active	1235.380	1223.850	0.039525	0.018591	0.012645
H	27(1)	active	1230.618	1201.093	0.039539	0.018587	0.012646
L	28(1)	active	1197.414	1206.224	0.039547	0.018596	0.012651
	29(1)	active	1171.946	1160.199	0.039545	0.018597	0.012651
	30(1)	active	1154.324	1144.499	0.039552	0.018595	0.012650
	31(1)	active	1102.882	1093.349	0.039538	0.018598	0.012651
	32(1)	active	1089.399	1068.747	0.039539	0.018596	0.012650
	33(1)	active	1047.648	1033.107	0.039535	0.018592	0.012646
	34(1)	active	1033.904	1018.948	0.039542	0.018594	0.012648
	35(1)	active	996.433	1033.954	0.039532	0.018595	0.012653
H	36(1)	active	977.755	1067.647	0.039538	0.018594	0.012653
	37(1)	active	967.347	967.307	0.039541	0.018594	0.012653
H	38(1)	active	964.559	1134.465	0.039532	0.018595	0.012653
H	39(1)	active	895.126	890.173	0.039545	0.018593	0.012653
	40(1)	active	880.015	870.201	0.039547	0.018593	0.012649
H	41(1)	active	873.852	928.901	0.039527	0.018577	0.012643
L	42(1)	active	853.132	779.757	0.039531	0.018593	0.012652
H	43(1)	active	847.031	973.632	0.039540	0.018592	0.012652
	44(1)	active	822.452	814.566	0.039545	0.018598	0.012651
	45(1)	active	799.091	819.874	0.039541	0.018595	0.012654
H	46(1)	active	771.968	789.169	0.039544	0.018596	0.012653
H	47(1)	active	741.590	735.927	0.039544	0.018597	0.012654

	48(1)	active	732.294	722.032	0.039544	0.018596	0.012651
	49(1)	active	693.983	685.664	0.039542	0.018592	0.012650
	50(1)	active	651.697	660.404	0.039547	0.018598	0.012654
	51(1)	active	589.256	602.118	0.039543	0.018597	0.012655
H	52(1)	active	581.224	578.783	0.039542	0.018595	0.012652
	53(1)	active	558.034	560.602	0.039550	0.018598	0.012650
	54(1)	active	521.488	522.596	0.039545	0.018600	0.012656
	55(1)	active	519.672	516.832	0.039553	0.018598	0.012651
	56(1)	active	509.731	506.546	0.039546	0.018598	0.012651
	57(1)	active	493.503	498.974	0.039541	0.018598	0.012656
	58(1)	active	422.472	416.253	0.039540	0.018601	0.012656
	59(1)	active	413.818	407.316	0.039552	0.018594	0.012656
	60(1)	active	390.751	387.971	0.039552	0.018596	0.012643
	61(1)	active	290.945	287.073	0.039536	0.018600	0.012657
	62(1)	active	250.456	242.443	0.039571	0.018591	0.012646
	63(1)	active	230.011	219.868	0.039549	0.018597	0.012657
	64(1)	active	207.399	206.415	0.039535	0.018599	0.012658
	65(1)	active	114.180	111.295	0.039540	0.018597	0.012659
	66(1)	active	90.971	84.974	0.039511	0.018602	0.012660

Gaussian excited state keto fundamental Vibrational Transition matrix with anharmonic corrections of HBQ

Fundamental Bands

	Mode(n)	Status	E(harm)	E(anharm)	Aa(x)	Ba(y)	Ca(z)
H	1(1)	active	3241.497	3115.636	0.039815	0.018236	0.012514
	2(1)	active	3231.869	2945.089	0.039779	0.018299	0.012540
H	3(1)	active	3204.403	3084.117	0.039814	0.018236	0.012514
L	4(1)	active	3201.096	3048.322	0.039814	0.018235	0.012513
L	5(1)	active	3192.678	3059.670	0.039815	0.018234	0.012513
H	6(1)	active	3189.753	3058.950	0.039814	0.018236	0.012514
L	7(1)	active	3187.187	3113.327	0.039815	0.018234	0.012513
L	8(1)	active	3170.002	3015.515	0.039816	0.018235	0.012513
L	9(1)	active	3169.151	3080.893	0.039815	0.018235	0.012513
	10(1)	active	1688.491	1632.570	0.039801	0.018224	0.012508
	11(1)	active	1590.106	1547.014	0.039800	0.018229	0.012510
	12(1)	active	1578.037	1543.082	0.039805	0.018226	0.012509
	13(1)	active	1555.426	1508.582	0.039809	0.018231	0.012510
	14(1)	active	1525.567	1495.662	0.039809	0.018231	0.012509
	15(1)	active	1494.442	1469.520	0.039802	0.018232	0.012509
	16(1)	active	1477.651	1448.872	0.039793	0.018231	0.012509
	17(1)	active	1455.396	1424.671	0.039800	0.018231	0.012510
	18(1)	active	1431.995	1404.814	0.039802	0.018231	0.012509
	19(1)	active	1419.400	1399.609	0.039811	0.018232	0.012511
	20(1)	active	1373.852	1343.279	0.039803	0.018225	0.012507

	21(1)	active	1352.193	1322.260	0.039802	0.018222	0.012506
	22(1)	active	1309.159	1289.433	0.039783	0.018225	0.012506
	23(1)	active	1297.142	1268.377	0.039805	0.018220	0.012503
	24(1)	active	1279.747	1254.947	0.039806	0.018228	0.012507
H	25(1)	active	1237.317	1223.632	0.039805	0.018229	0.012508
	26(1)	active	1200.774	1181.603	0.039802	0.018222	0.012504
H	27(1)	active	1194.060	1201.820	0.039816	0.018235	0.012512
	28(1)	active	1182.686	1161.630	0.039821	0.018228	0.012509
	29(1)	active	1167.462	1157.968	0.039821	0.018236	0.012513
H	30(1)	active	1135.372	1114.139	0.039820	0.018235	0.012513
	31(1)	active	1094.251	1083.154	0.039812	0.018237	0.012513
	32(1)	active	1060.949	1040.948	0.039816	0.018232	0.012510
	33(1)	active	1028.673	1019.894	0.039825	0.018228	0.012509
	34(1)	active	999.961	983.218	0.039813	0.018231	0.012508
	35(1)	active	967.963	1118.534	0.039805	0.018234	0.012514
L	36(1)	active	954.803	1048.732	0.039807	0.018227	0.012511
H	37(1)	active	950.736	895.888	0.039810	0.018223	0.012510
H	38(1)	active	933.593	1064.405	0.039809	0.018235	0.012515
	39(1)	active	871.601	857.405	0.039821	0.018231	0.012514
	40(1)	active	859.212	849.450	0.039814	0.018232	0.012510
	41(1)	active	831.553	1031.136	0.039816	0.018233	0.012515
	42(1)	active	816.255	806.476	0.039823	0.018234	0.012512
H	43(1)	active	811.320	802.284	0.039807	0.018237	0.012516
H	44(1)	active	757.898	772.401	0.039810	0.018238	0.012516
H	45(1)	active	739.051	774.588	0.039817	0.018236	0.012516
L	46(1)	active	703.314	688.473	0.039819	0.018234	0.012512
H	47(1)	active	701.550	718.993	0.039814	0.018237	0.012516
	48(1)	active	684.301	672.353	0.039814	0.018233	0.012512
L	49(1)	active	677.427	705.558	0.039810	0.018238	0.012516
	50(1)	active	633.782	641.642	0.039824	0.018237	0.012516
	51(1)	active	568.583	563.556	0.039817	0.018237	0.012515
	52(1)	active	552.154	553.135	0.039825	0.018235	0.012512
	53(1)	active	550.643	566.684	0.039817	0.018237	0.012517
	54(1)	active	533.035	530.776	0.039822	0.018236	0.012512
H	55(1)	active	492.987	507.897	0.039819	0.018237	0.012518
	56(1)	active	490.383	483.910	0.039826	0.018238	0.012512
H	57(1)	active	468.156	475.715	0.039812	0.018237	0.012518
	58(1)	active	404.481	395.780	0.039827	0.018232	0.012518
	59(1)	active	380.791	383.949	0.039833	0.018234	0.012504
	60(1)	active	352.658	348.175	0.039821	0.018240	0.012519
	61(1)	active	275.654	283.842	0.039809	0.018240	0.012519
	62(1)	active	244.452	239.514	0.039847	0.018230	0.012508
H	63(1)	active	196.046	162.213	0.039826	0.018237	0.012520
H	64(1)	active	159.365	172.187	0.039816	0.018239	0.012521
	65(1)	active	102.936	113.729	0.039789	0.018245	0.012523
	66(1)	active	59.668	62.587	0.039808	0.018241	0.012527

Gaussian excited state keto fundamental Vibrational Transition matrix with anharmonic corrections of DBQ

Fundamental Bands

	Mode(n)	Status	E(harm)	E(anharm)	Aa(x)	Ba(y)	Ca(z)
L	1(1)	active	3204.018	3090.709	0.039014	0.018590	0.012594
L	2(1)	active	3197.275	3053.933	0.039013	0.018590	0.012595
L	3(1)	active	3186.796	3095.091	0.039014	0.018590	0.012594
L	4(1)	active	3183.862	3063.283	0.039015	0.018589	0.012594
L	5(1)	active	3174.436	3043.023	0.039014	0.018590	0.012594
L	6(1)	active	3171.307	3023.418	0.039015	0.018590	0.012595
H	7(1)	active	3167.142	3013.477	0.039016	0.018589	0.012594
H	8(1)	active	3164.417	3033.450	0.039014	0.018589	0.012594
	9(1)	active	2261.645	2051.275	0.039081	0.018654	0.012631
	10(1)	active	1659.680	1621.954	0.039000	0.018579	0.012590
	11(1)	active	1641.095	1604.526	0.039002	0.018579	0.012590
	12(1)	active	1626.250	1588.105	0.039005	0.018581	0.012589
	13(1)	active	1611.522	1572.985	0.038993	0.018580	0.012586
	14(1)	active	1548.251	1513.159	0.039004	0.018583	0.012588
H	15(1)	active	1534.571	1504.046	0.039006	0.018583	0.012590
	16(1)	active	1472.036	1449.938	0.039012	0.018583	0.012590
	17(1)	active	1464.870	1439.283	0.038997	0.018586	0.012591
H	18(1)	active	1456.565	1434.843	0.039006	0.018588	0.012594
	19(1)	active	1427.178	1397.531	0.038992	0.018574	0.012582
H	20(1)	active	1370.164	1340.050	0.038983	0.018576	0.012585
	21(1)	active	1355.725	1329.531	0.039007	0.018578	0.012588
	22(1)	active	1326.043	1300.955	0.038998	0.018578	0.012588
	23(1)	active	1312.732	1288.857	0.038999	0.018582	0.012589
	24(1)	active	1280.528	1255.666	0.039014	0.018587	0.012590
H	25(1)	active	1238.010	1231.283	0.038997	0.018581	0.012587
H	26(1)	active	1231.127	1200.862	0.039013	0.018583	0.012590
L	27(1)	active	1199.101	1210.135	0.039016	0.018590	0.012593
	28(1)	active	1172.159	1156.908	0.039018	0.018591	0.012594
	29(1)	active	1157.791	1153.039	0.039024	0.018588	0.012593
	30(1)	active	1122.988	1110.873	0.039007	0.018589	0.012592
	31(1)	active	1093.031	1075.439	0.039009	0.018591	0.012593
	32(1)	active	1075.468	1049.683	0.039006	0.018585	0.012591
	33(1)	active	1042.478	1027.954	0.039015	0.018586	0.012589
	34(1)	active	1019.390	998.329	0.039009	0.018587	0.012589
	35(1)	active	996.385	1033.843	0.039006	0.018588	0.012596
H	36(1)	active	977.711	1066.971	0.039011	0.018588	0.012596
H	37(1)	active	967.033	966.096	0.039014	0.018588	0.012596
H	38(1)	active	964.502	1134.691	0.039005	0.018589	0.012596
H	39(1)	active	893.839	895.621	0.039019	0.018587	0.012596

	40(1)	active	879.858	870.306	0.039024	0.018587	0.012591
	41(1)	active	857.943	863.327	0.039000	0.018590	0.012596
H	42(1)	active	849.561	962.545	0.039014	0.018589	0.012596
	43(1)	active	821.106	813.529	0.039019	0.018591	0.012593
	44(1)	active	799.348	818.399	0.039014	0.018589	0.012596
H	45(1)	active	773.302	789.737	0.039017	0.018590	0.012596
H	46(1)	active	741.590	736.186	0.039017	0.018591	0.012597
	47(1)	active	732.038	724.423	0.039017	0.018589	0.012594
	48(1)	active	692.949	684.464	0.039017	0.018586	0.012592
H	49(1)	active	661.701	686.312	0.039011	0.018585	0.012594
H	50(1)	active	618.900	590.798	0.039002	0.018575	0.012588
H	51(1)	active	589.255	604.574	0.039016	0.018591	0.012597
H	52(1)	active	580.588	577.281	0.039014	0.018589	0.012595
	53(1)	active	554.356	557.373	0.039022	0.018591	0.012593
	54(1)	active	520.798	520.739	0.039019	0.018593	0.012599
	55(1)	active	515.851	514.697	0.039025	0.018592	0.012594
	56(1)	active	505.094	499.965	0.039019	0.018592	0.012593
	57(1)	active	493.501	499.233	0.039014	0.018592	0.012598
	58(1)	active	420.826	415.468	0.039013	0.018594	0.012599
	59(1)	active	411.258	405.712	0.039024	0.018589	0.012598
	60(1)	active	384.817	381.337	0.039021	0.018590	0.012586
	61(1)	active	289.869	285.850	0.039009	0.018594	0.012600
	62(1)	active	246.641	239.624	0.039038	0.018584	0.012588
	63(1)	active	229.978	219.935	0.039027	0.018590	0.012600
	64(1)	active	207.001	206.440	0.039009	0.018593	0.012600
	65(1)	active	114.167	111.728	0.039013	0.018591	0.012602
	66(1)	active	90.540	85.198	0.038984	0.018596	0.012603

Gaussian excited state keto fundamental Vibrational Transition matrix with anharmonic corrections of DBQ

Fundamental Bands

	Mode(n)	Status	E(harm)	E(anharm)	Aa(x)	Ba(y)	Ca(z)
H	1(1)	active	3241.434	3116.734	0.039382	0.018222	0.012465
H	2(1)	active	3204.405	3084.104	0.039381	0.018222	0.012464
L	3(1)	active	3201.124	3048.293	0.039381	0.018221	0.012464
L	4(1)	active	3192.748	3065.409	0.039383	0.018220	0.012464
H	5(1)	active	3190.043	3057.754	0.039382	0.018222	0.012464
L	6(1)	active	3187.179	3105.582	0.039382	0.018221	0.012464
H	7(1)	active	3169.973	3025.467	0.039383	0.018221	0.012464
L	8(1)	active	3169.186	3076.961	0.039383	0.018221	0.012464
	9(1)	active	2382.045	2228.018	0.039358	0.018268	0.012484
	10(1)	active	1670.649	1619.090	0.039363	0.018212	0.012459
	11(1)	active	1585.449	1546.865	0.039364	0.018218	0.012461
	12(1)	active	1569.330	1526.643	0.039371	0.018213	0.012460

	13(1)	active	1532.880	1495.347	0.039371	0.018217	0.012459
	14(1)	active	1517.330	1487.373	0.039363	0.018215	0.012458
	15(1)	active	1483.703	1473.839	0.039366	0.018221	0.012462
	16(1)	active	1467.695	1449.100	0.039360	0.018219	0.012460
	17(1)	active	1438.625	1408.696	0.039379	0.018216	0.012459
	18(1)	active	1424.425	1406.937	0.039369	0.018220	0.012462
	19(1)	active	1399.903	1366.916	0.039370	0.018212	0.012460
	20(1)	active	1369.639	1338.191	0.039369	0.018212	0.012456
	21(1)	active	1338.665	1315.746	0.039372	0.018208	0.012456
	22(1)	active	1307.928	1285.523	0.039342	0.018210	0.012457
	23(1)	active	1284.009	1264.256	0.039377	0.018210	0.012454
	24(1)	active	1242.596	1224.260	0.039366	0.018216	0.012460
	25(1)	active	1217.204	1192.586	0.039384	0.018211	0.012456
	26(1)	active	1200.358	1179.733	0.039370	0.018209	0.012455
H	27(1)	active	1192.911	1203.582	0.039384	0.018221	0.012462
	28(1)	active	1169.142	1160.143	0.039388	0.018223	0.012464
H	29(1)	active	1135.219	1117.161	0.039389	0.018221	0.012463
H	30(1)	active	1108.646	1098.089	0.039387	0.018220	0.012462
H	31(1)	active	1092.635	1071.942	0.039378	0.018223	0.012464
	32(1)	active	1043.440	1028.155	0.039384	0.018217	0.012460
	33(1)	active	1002.168	985.916	0.039380	0.018216	0.012458
	34(1)	active	967.899	1114.057	0.039372	0.018220	0.012465
	35(1)	active	953.177	1015.787	0.039371	0.018223	0.012466
	36(1)	active	934.142	1059.842	0.039377	0.018222	0.012466
	37(1)	active	931.476	913.847	0.039405	0.018217	0.012462
	38(1)	active	872.815	872.544	0.039387	0.018218	0.012465
	39(1)	active	850.403	841.558	0.039383	0.018218	0.012460
	40(1)	active	833.573	1044.617	0.039384	0.018219	0.012465
	41(1)	active	816.090	806.190	0.039390	0.018221	0.012462
	42(1)	active	811.305	816.980	0.039375	0.018223	0.012467
	43(1)	active	760.929	791.552	0.039377	0.018223	0.012466
H	44(1)	active	740.708	768.859	0.039383	0.018222	0.012466
H	45(1)	active	709.278	735.042	0.039382	0.018216	0.012463
	46(1)	active	702.626	697.128	0.039386	0.018220	0.012463
H	47(1)	active	700.038	699.012	0.039384	0.018222	0.012466
	48(1)	active	679.438	667.683	0.039379	0.018218	0.012462
H	49(1)	active	670.407	686.262	0.039379	0.018220	0.012465
	50(1)	active	628.582	627.966	0.039390	0.018222	0.012467
H	51(1)	active	565.780	566.856	0.039385	0.018223	0.012466
H	52(1)	active	550.356	553.386	0.039391	0.018221	0.012463
H	53(1)	active	548.528	548.691	0.039385	0.018223	0.012467
	54(1)	active	532.011	529.571	0.039389	0.018222	0.012462
	55(1)	active	491.417	512.779	0.039387	0.018223	0.012468
	56(1)	active	490.326	484.124	0.039393	0.018224	0.012462
	57(1)	active	468.101	464.945	0.039379	0.018223	0.012468
	58(1)	active	403.359	395.684	0.039393	0.018219	0.012468

59(1)	active	379.580	383.218	0.039401	0.018220	0.012454
60(1)	active	348.074	333.923	0.039388	0.018226	0.012470
61(1)	active	274.903	280.051	0.039377	0.018226	0.012470
62(1)	active	241.693	237.317	0.039414	0.018217	0.012459
63(1)	active	195.968	183.524	0.039393	0.018223	0.012470
64(1)	active	159.361	169.470	0.039383	0.018226	0.012471
65(1)	active	102.028	95.470	0.039356	0.018232	0.012474
66(1)	active	59.650	54.699	0.039375	0.018228	0.012478

Total Anharmonic X Matrix from TDDFT Frequency calculations on first excited state root geometry optimized structure.

	1	2	3	4	5
1	-0.523409D+02				
2	-0.876087D+00	-0.133726D+03			
3	-0.996398D+01	-0.198791D+01	-0.276390D+02		
4	-0.405605D-01	-0.665194D+00	-0.540096D+00	-0.423955D+02	
5	-0.182001D+00	-0.903243D+00	-0.335122D+01	-0.496258D+01	-0.316496D+02
6	-0.277368D+01	-0.509456D+01	-0.100634D+03	-0.434353D+00	-0.596757D+01
7	0.222478D-01	0.157276D+00	-0.417611D+00	-0.242005D+02	-0.280301D+02
8	0.828731D-01	-0.284411D+00	-0.373458D-01	-0.593326D+01	-0.425901D+02
9	0.399265D-01	-0.183107D+00	-0.301969D-01	-0.230853D+02	-0.153402D+02
10	0.729654D+00	-0.852557D+01	0.273807D+00	-0.263734D+00	0.629314D+00
11	0.148361D+01	-0.379148D+01	0.260228D+01	0.191043D+01	0.658908D+01
12	0.325463D+00	-0.227088D+01	0.563468D-01	0.836046D+01	0.187365D+01
13	0.826775D+01	-0.130336D+02	0.133080D+01	0.915774D-01	0.671086D+00
14	0.195324D+00	0.180037D+01	0.632248D+00	0.273321D+01	0.104240D+00
15	-0.173084D+00	-0.362516D+00	0.869551D+00	0.162840D+01	0.432751D+01
16	0.795244D+00	-0.425564D+01	0.486808D+01	0.138313D+00	-0.172737D+00
17	-0.165188D+01	-0.257353D+01	0.781828D+00	-0.129983D+00	0.386822D+00
18	-0.182340D+00	-0.260599D+01	-0.350159D+00	-0.286232D+00	0.532420D+00
19	0.447252D+00	0.432592D+00	0.529501D+00	-0.248813D+00	-0.323010D+00
20	-0.242836D+01	-0.904658D-01	0.111596D+01	-0.129941D+01	0.554448D+00
21	0.617034D+00	-0.121563D+01	-0.193928D+00	-0.134694D+00	0.141988D+00
22	-0.306890D+00	-0.302283D-01	-0.593306D+00	0.143004D+00	-0.547320D+00
23	-0.524242D+00	-0.288181D+01	-0.637183D+00	-0.882768D+00	-0.231957D+00
24	-0.251940D+01	0.116134D+00	-0.390472D+00	-0.187733D+01	-0.769477D+00
25	-0.162703D+01	-0.195535D+01	-0.152603D+01	-0.223731D+00	-0.142166D+01
26	-0.255514D-01	0.115592D+01	-0.277125D+00	-0.143944D+01	-0.829788D+00
27	-0.152685D+01	-0.541454D+00	-0.445172D+00	-0.114537D+01	-0.121393D+01
28	-0.286469D+01	-0.469806D+01	-0.606054D+00	-0.248552D+01	-0.448636D+00
29	-0.122764D+01	-0.243493D+01	-0.120361D+01	-0.407281D+00	-0.303363D+01
30	-0.146607D+01	-0.251851D+01	-0.382009D+01	-0.557926D+00	-0.413743D+00
31	-0.313194D+00	-0.601147D+00	-0.120431D+00	-0.659896D+01	-0.130317D+00
32	-0.118534D+01	-0.396081D+00	-0.607811D+00	-0.169353D+00	-0.270273D+00

33 0.982421D-01 -0.288474D+01 -0.105027D+01 -0.678569D-01 -0.150003D+00
34 -0.429307D+00 -0.312541D+01 -0.780809D+00 -0.572343D+00 -0.157007D+00
35 -0.132265D+00 0.667835D+00 0.984606D-01 -0.400076D+01 -0.229702D+00
36 -0.280564D+01 0.133101D+02 -0.415844D+01 -0.229051D+00 -0.267351D+00
37 -0.160019D+01 0.204675D+02 -0.240906D+01 -0.382882D+00 -0.586603D+00
38 0.118906D+00 -0.215829D+00 -0.157783D+00 0.311546D-01 -0.506949D+01
39 -0.314395D-01 0.194211D+01 0.135214D-01 -0.878657D+01 -0.736214D+00
40 -0.957694D-01 0.174590D+01 -0.250771D+00 -0.142214D+00 -0.317517D+00
41 -0.224801D+00 0.139756D+01 -0.199957D+00 -0.482727D+00 -0.653804D+00
42 -0.189832D+00 0.405422D+00 -0.189445D+00 -0.272314D+00 -0.317674D+00
43 -0.756686D+00 -0.220582D+01 -0.194991D+01 -0.106922D+01 -0.371133D+01
44 -0.788995D+01 -0.351088D+01 -0.466195D+01 -0.728259D+00 -0.138459D+01
45 0.454313D-02 -0.168020D+00 -0.121819D+00 -0.770961D+00 -0.348356D+01
46 -0.105866D+00 -0.252037D+00 -0.596046D-01 -0.186584D+00 -0.115808D+00
47 -0.387913D+01 -0.133957D+01 -0.419236D+00 -0.377290D+01 -0.317948D+00
48 -0.338938D+00 -0.118927D+01 -0.232873D+00 -0.303582D-03 -0.269814D-01
49 -0.946685D+01 -0.266594D+00 -0.185809D+01 -0.319776D+00 -0.265253D-01
50 -0.291021D+00 -0.547716D-01 -0.145643D+00 -0.634787D+00 -0.987462D+00
51 -0.670526D-01 -0.121180D+01 -0.216263D-01 -0.141291D+00 -0.298195D-01
52 0.213914D-01 0.104885D+01 -0.129658D-01 -0.141793D+00 0.494319D+00
53 -0.645113D+00 -0.298680D-01 -0.448479D+00 -0.345181D+00 -0.112620D+00
54 -0.418460D-01 0.354645D+00 -0.845983D-01 0.248184D-01 0.209230D+00
55 -0.213929D-01 -0.307048D+00 -0.157969D+00 -0.272728D+00 -0.509114D+00
56 -0.602977D-01 0.317911D+00 0.340879D-01 -0.105099D+00 0.228116D+00
57 0.264336D-01 0.422002D+00 -0.401833D-03 -0.237309D+00 -0.141047D-01
58 0.127381D+00 0.222872D+01 -0.290901D-01 -0.311952D-01 0.147311D+00
59 0.979922D-02 0.759841D+01 0.302989D-01 -0.274187D+00 0.149093D+00
60 -0.471831D+00 -0.812835D-01 -0.438515D+00 -0.141925D+00 -0.285528D+00
61 0.233276D-01 0.606055D+00 0.133334D+00 -0.533263D-01 -0.109954D+00
62 0.260745D+00 -0.224203D+01 -0.137296D-01 -0.143262D-01 0.739138D-01
63 -0.194717D+00 -0.218378D+00 -0.200730D+00 -0.349206D+00 -0.372435D+00
64 -0.163521D+00 -0.651049D-01 0.279075D+00 -0.393435D+00 -0.891430D-01
65 0.155516D+00 0.870809D+00 0.486959D+00 -0.887402D-02 0.107468D+00
66 -0.257157D+00 0.410562D+01 -0.201333D+00 -0.667087D+00 -0.248634D+00

	6	7	8	9	10
6	-0.279481D+02				
7	-0.242133D+01	-0.268181D+02			
8	-0.618577D+00	-0.156184D+02	-0.298851D+02		
9	-0.782580D+00	-0.473133D+02	-0.457110D+02	-0.237530D+02	
10	-0.342446D+00	-0.431241D+00	-0.151720D+01	0.167129D+01	-0.240393D+01
11	0.325513D+01	0.114998D+01	-0.250557D+01	-0.176247D+01	0.209635D+01
12	0.274584D+00	0.106074D+02	0.855947D+00	0.456916D+01	0.324352D+01
13	0.623196D+01	0.262113D+00	0.121514D+00	0.169041D+00	-0.111034D+01
14	0.588948D+00	0.960547D+00	0.148927D+01	0.798682D+01	-0.154992D+01
15	0.583252D+00	0.328671D+01	0.769133D+00	0.106197D+01	-0.515463D+01
16	0.323281D+01	-0.309044D+00	-0.302401D+00	0.304697D+00	-0.818669D+01

17 0.338257D+00 0.123448D+01 0.142374D+01 0.242421D+01 -0.919659D+01
18 0.156492D+00 0.446564D+00 0.185857D+00 0.377822D-01 -0.341445D+01
19 0.354329D+00 0.704943D+00 0.100503D+01 0.629573D+00 -0.436690D+01
20 0.144219D+01 -0.138725D+00 0.221351D+00 -0.140644D+00 -0.578019D+01
21 0.156467D+00 0.901359D+00 -0.456109D-01 -0.172862D+00 -0.432904D+01
22 -0.387001D+00 0.796346D+00 -0.831082D+00 -0.283636D+00 -0.288256D+01
23 -0.770642D+00 -0.728388D-01 0.127110D+00 -0.103453D+00 -0.660794D+01
24 -0.353569D+00 -0.979588D+00 -0.152703D+01 -0.693501D+00 -0.159560D+01
25 -0.193883D+01 0.467358D+00 -0.147258D+01 -0.140535D+00 -0.322074D+01
26 -0.314546D+00 -0.101054D+01 -0.539153D+00 -0.888394D+00 -0.196534D+01
27 -0.643166D+00 0.375552D+01 -0.217752D+01 0.633860D-01 -0.183773D+01
28 -0.816737D+00 -0.999393D+00 -0.102977D+01 -0.141818D+01 -0.249549D+01
29 -0.136109D+01 -0.101496D+01 -0.251844D+01 -0.169518D+01 -0.330144D+01
30 -0.445032D+01 -0.481349D+00 -0.536545D+00 -0.334876D+00 -0.234862D+01
31 -0.148462D+00 -0.111881D+01 -0.123985D+00 -0.525103D+00 -0.532439D+00
32 -0.846579D+00 -0.610978D+00 -0.881976D+00 -0.872350D+00 -0.310441D+01
33 -0.110590D+01 -0.268860D+00 -0.257913D+00 -0.268389D+00 -0.193396D+01
34 -0.892173D+00 -0.225944D+00 -0.202153D+00 -0.196560D+00 -0.250487D+01
35 0.141806D+00 -0.286424D+01 -0.108930D+01 -0.507976D+01 -0.675295D+00
36 -0.360188D+01 -0.761789D-01 0.953398D-01 -0.128718D+00 -0.123153D+01
37 -0.191992D+01 -0.149211D+00 -0.410663D+00 -0.311569D+00 -0.326933D+01
38 -0.171369D+00 -0.887630D+00 -0.959254D+01 -0.206116D+01 -0.228497D+01
39 0.240515D-01 -0.336790D+01 -0.431905D+00 -0.157835D+01 -0.103803D+01
40 -0.145782D+00 0.154697D+00 -0.717856D+00 -0.134337D+00 -0.817722D+00
41 -0.186088D+00 -0.157927D+01 -0.296521D+00 -0.548578D+00 -0.173766D+01
42 -0.199118D+00 -0.114539D+00 -0.455740D+00 -0.632423D+00 0.322799D+00
43 -0.287236D+01 -0.922307D+00 -0.130258D+01 -0.554285D+00 -0.207742D+00
44 -0.642515D+01 -0.414877D+00 -0.475880D+00 -0.250828D+00 0.477999D+00
45 -0.259692D+00 -0.268192D+01 -0.180896D+01 -0.125938D+01 -0.141519D+01
46 -0.481699D-01 0.348136D+00 -0.246675D+00 -0.124635D+00 -0.263812D+01
47 -0.448556D+00 -0.955425D+00 -0.317026D+00 -0.534260D+00 -0.354584D-01
48 -0.208131D+00 0.456239D-01 0.269015D-01 -0.299665D-01 -0.659700D+00
49 -0.246845D+01 -0.279872D+00 0.180770D-01 -0.112773D+00 0.676380D+00
50 -0.183821D+00 -0.520242D+00 -0.647503D+00 -0.519404D+00 -0.107397D+01
51 -0.189901D-02 -0.479528D-01 -0.268940D-01 -0.296332D-01 -0.551519D+00
52 -0.210859D-01 0.149700D+01 -0.335751D-01 0.390354D+00 -0.697040D+00
53 -0.463141D+00 -0.269281D+00 -0.646382D-01 -0.185345D+00 -0.607488D+00
54 -0.189458D+00 0.671326D+00 -0.113627D+00 0.200143D+00 -0.106187D+01
55 -0.237741D+00 -0.170968D+00 -0.729479D+00 -0.275351D+00 -0.677554D+00
56 -0.171610D-01 0.680880D+00 -0.560970D-01 0.200260D+00 -0.153873D+00
57 -0.671301D-01 -0.414367D+00 -0.116874D-01 -0.360750D-01 0.128169D+00
58 -0.194118D-01 0.309719D+00 -0.790403D-01 0.640422D-01 -0.119490D+01
59 0.726923D-01 0.488475D+00 -0.717989D-02 0.113563D+00 -0.531487D+00
60 -0.220025D+00 -0.137727D+00 0.664069D-01 -0.576815D-01 -0.104576D+01
61 0.821575D-01 0.165442D+00 0.204088D-01 0.379755D+00 -0.282413D+00
62 -0.748104D-01 0.203809D+00 -0.297074D-01 0.752561D-01 -0.121400D+01

63 -0.147214D-02 -0.786302D+00 -0.615922D-01 -0.362810D+00 -0.364712D+00
64 0.220107D+00 0.170791D+00 0.175988D-01 0.309734D-01 -0.142419D+00
65 0.365078D+00 0.119851D+00 0.142456D+00 0.337862D+00 -0.223906D+00
66 -0.187552D-01 0.384600D-02 0.108874D+00 0.268892D+00 0.243055D+00
        11   12   13   14   15
11 -0.225489D+01
12 -0.401904D+01 -0.600171D+01
13 -0.785922D+01 -0.213182D+01 -0.475987D+01
14 -0.348827D+01 -0.742095D+01 -0.173708D+01 -0.448787D+01
15 -0.533207D+01 -0.480593D+01 -0.235654D+01 -0.362176D+01 -0.197315D+01
16 -0.782660D+01 -0.209981D+01 -0.624710D+01 -0.179250D+01 -0.226885D+01
17 -0.447703D+01 -0.281902D+01 -0.255976D+01 -0.301629D+01 -0.185062D+01
18 -0.277133D+01 -0.399552D+01 -0.471950D+01 -0.209972D+01 -0.257951D+01
19 -0.399895D+01 -0.458561D+01 -0.211774D+01 -0.547047D+01 -0.204278D+01
20 -0.375033D+01 -0.115738D+01 -0.658299D+01 -0.210881D+01 -0.203699D+01
21 -0.500757D+01 -0.346902D+01 -0.458769D+01 -0.181875D+01 -0.181978D+01
22 -0.304232D+01 -0.340847D+01 -0.116937D+01 -0.185959D+01 -0.256571D+01
23 -0.156585D+01 -0.167720D+01 -0.920195D+00 -0.153420D+01 -0.148354D+01
24 -0.150352D+01 -0.192930D+01 -0.105742D+01 -0.333006D+00 -0.159622D+01
25 -0.158272D+01 -0.471621D+00 -0.311613D+01 -0.664836D+00 -0.585248D+00
26 -0.953068D+00 -0.530422D+01 -0.451623D+00 -0.206384D+01 -0.148930D+01
27 -0.157319D+01 -0.597841D+00 -0.125883D+01 -0.132236D+01 0.194996D+01
28 -0.118637D+01 -0.129417D+01 -0.306538D+01 -0.134583D+01 -0.118116D+01
29 -0.187271D+01 -0.902754D+00 -0.114485D+01 -0.947476D+00 -0.187536D+01
30 -0.300655D+01 -0.722677D+00 -0.308932D+01 -0.114565D+01 -0.609397D+00
31 -0.108756D+01 -0.232170D+01 -0.259770D+00 -0.371197D+01 -0.444298D+00
32 -0.174534D+01 -0.143886D+01 -0.257808D+01 -0.100042D+01 -0.790306D+00
33 -0.856945D+00 -0.763714D+00 -0.309830D+01 -0.405578D+00 -0.665914D+00
34 -0.102935D+01 -0.865617D+00 -0.834814D+00 -0.163203D+01 0.412556D+00
35 -0.125959D+01 -0.569842D+00 0.466662D-01 0.490429D+00 -0.980813D-02
36 -0.921557D-01 -0.328023D+00 -0.261051D+00 -0.158680D+00 -0.292778D+00
37 -0.393557D+00 -0.539665D+00 -0.532367D+00 -0.409518D+00 -0.653997D-01
38 -0.141543D+01 -0.678540D-01 -0.439410D+00 0.319200D+00 0.196591D+00
39 -0.384648D+00 -0.672807D+00 0.188597D-01 -0.431648D+00 -0.109105D+01
40 -0.684066D+00 -0.515588D+00 -0.201234D+01 -0.222302D+00 -0.812549D+00
41 -0.167519D+01 -0.954333D+00 -0.290911D+00 -0.776506D+00 -0.291094D+00
42 -0.891684D+00 -0.205221D+01 -0.541280D+00 -0.899691D+00 -0.523346D+00
43 -0.110105D+01 -0.394427D+00 -0.116550D+00 0.268404D+00 -0.635920D+00
44 0.212256D+00 -0.390547D-01 -0.212437D+01 0.530026D+00 -0.457750D+00
45 -0.510081D+00 -0.147855D+00 0.922001D+00 0.422994D+00 -0.411524D+00
46 -0.504244D+00 -0.660746D+00 -0.135993D+01 -0.678718D+00 -0.588313D+00
47 0.177072D+00 0.555813D+00 -0.404404D+00 0.658697D-01 -0.239698D+00
48 -0.660497D+00 -0.435064D+00 -0.740567D+00 -0.542149D+00 -0.527493D+00
49 0.723198D-01 -0.355118D+00 -0.911733D+00 0.639053D+00 0.127977D+00
50 -0.967319D+00 -0.774854D+00 -0.513248D+00 -0.223791D+00 -0.136406D+01
51 -0.730948D+00 -0.706006D+00 -0.966640D+00 -0.996710D+00 -0.279784D+00

52 -0.153130D+01 -0.949078D+00 -0.109153D+00 -0.386394D+00 0.643684D+00
53 -0.390877D+00 -0.150811D+00 -0.139550D+00 -0.256214D+00 -0.400063D+00
54 -0.959171D+00 -0.396880D+00 -0.973463D+00 -0.152196D+01 0.226667D+00
55 -0.473334D+00 -0.505122D+00 -0.318096D+00 -0.525650D-01 0.498189D-02
56 -0.694021D+00 -0.167135D+01 -0.625853D+00 -0.829191D+00 0.239420D+00
57 -0.509059D+00 -0.379827D+00 -0.592039D-03 -0.420102D+00 -0.271176D-01
58 -0.499885D-01 -0.353354D+00 -0.103694D+01 -0.618462D-02 -0.217413D+00
59 -0.144467D+00 -0.130591D+01 -0.960463D+00 -0.265708D+00 0.121437D+00
60 -0.305088D+00 -0.291741D+00 -0.612346D+00 -0.367544D+00 -0.448865D+00
61 -0.208431D+00 -0.277282D+00 -0.146320D+00 0.204389D+00 0.525500D-02
62 -0.124391D+01 0.483249D+00 0.634586D+00 0.563410D+00 0.711000D+00
63 -0.561780D+00 -0.463558D+00 -0.256768D+00 -0.400757D+00 -0.880912D+00
64 -0.856249D-01 0.143336D-01 0.463828D-01 -0.523960D+00 -0.179360D-01
65 -0.519629D-01 0.733144D-01 0.134672D+00 0.348413D+00 0.185277D+00
66 -0.182786D+00 0.427433D+00 0.127682D+00 -0.618346D+00 -0.559463D-01
        16   17   18   19   20
16 -0.128186D+01
17 -0.342452D+01 -0.160533D+01
18 -0.285375D+01 -0.375331D+01 -0.159510D+01
19 -0.890215D+00 -0.175818D+01 -0.299369D+01 -0.856900D+00
20 -0.472977D+00 -0.181973D+01 -0.160958D+01 -0.150738D+01 -0.178956D+01
21 -0.453040D+00 -0.209959D+01 -0.212928D+01 -0.143135D+01 -0.300889D+01
22 -0.684496D+00 -0.118711D+01 -0.939141D+00 -0.127046D+01 -0.593521D+00
23 -0.981621D+00 -0.237947D+01 -0.899766D+00 -0.147038D+01 -0.227611D+01
24 -0.846993D+00 -0.143259D+01 -0.986398D+00 -0.667693D+00 -0.151691D+01
25 -0.200952D+01 -0.152071D+01 -0.985352D+00 -0.273207D+00 -0.128932D+01
26 0.894399D-01 -0.592360D+00 -0.675465D+00 -0.860810D+00 -0.138100D+01
27 -0.234311D+00 -0.538403D+00 -0.152375D+01 0.156422D+01 -0.390209D+00
28 0.367075D+00 -0.104286D+01 -0.451108D+00 -0.758635D+00 -0.688277D+00
29 0.609224D+00 -0.622417D+00 -0.531678D+00 -0.499788D+00 -0.628491D+00
30 0.487288D+00 -0.170099D+01 -0.131278D+01 -0.258312D+00 -0.269073D+01
31 -0.274742D+00 -0.323730D+00 -0.281212D+00 -0.802388D+00 -0.528644D+00
32 0.131184D+00 -0.192894D+01 -0.134778D+01 -0.342570D+00 -0.175706D+00
33 -0.800579D+00 -0.452244D+00 -0.422096D+00 -0.292097D+00 0.677226D-01
34 -0.112765D+01 -0.438138D+00 0.204516D+00 -0.242507D+00 -0.171157D+01
35 -0.220508D+00 -0.459168D-01 0.165544D-01 0.242514D+01 -0.462437D+00
36 0.148966D+01 0.204826D+00 0.118630D+01 -0.419353D+00 -0.131831D+01
37 0.879826D+00 0.100042D+01 0.666865D+00 -0.508167D+00 -0.204062D+01
38 -0.128351D+01 0.293529D+00 0.360921D+00 -0.225723D+00 0.637916D+00
39 0.304617D+00 -0.754183D-01 0.146396D+00 0.227539D+00 0.477603D-01
40 -0.723166D+00 -0.553200D+00 -0.202640D-01 0.186629D+00 -0.105822D+01
41 -0.815140D+00 -0.820080D+00 -0.699115D+00 -0.507885D+00 -0.126009D+01
42 -0.678440D+00 -0.418185D+00 -0.530217D+00 -0.755222D-01 -0.392575D+00
43 -0.317929D+01 -0.290078D+00 -0.176022D+00 -0.143372D+00 0.125482D+00
44 0.240883D+01 0.114527D+00 -0.579632D+00 -0.164900D+01 -0.246494D+00
45 -0.249305D+01 0.174245D-01 0.382411D-01 0.278499D+00 0.267439D-01

46 0.656959D-01 -0.253853D+00 -0.256585D+00 0.147927D+00 -0.161522D+01
47 0.385645D+01 -0.267492D+00 0.306680D+00 0.116500D+01 -0.226579D+00
48 -0.102174D+01 -0.923571D+00 -0.430904D+00 -0.329108D+00 -0.168093D+01
49 0.258437D+01 0.799552D+00 0.144848D+00 -0.116348D+01 0.382447D+01
50 -0.170484D+00 -0.806122D+00 -0.565243D+00 -0.595938D+00 -0.415169D+00
51 -0.593509D+00 -0.720625D+00 -0.102270D+00 -0.197172D+00 -0.319305D+00
52 -0.587575D+00 -0.293356D+00 -0.932293D+00 0.632651D+00 -0.456673D+00
53 -0.188830D+01 -0.488471D+00 0.272944D+00 -0.432616D+00 -0.390512D+00
54 0.137542D+00 -0.146854D+00 -0.337843D-01 0.524219D+00 -0.191625D+00
55 0.128307D+00 0.394186D+00 0.721805D-01 -0.757440D+00 0.264525D+00
56 -0.189735D+00 -0.922110D+00 -0.474147D+00 0.564655D-01 -0.329379D+00
57 -0.641377D+00 0.188769D+00 0.344840D+00 -0.102176D+00 0.737270D+00
58 -0.201669D-01 -0.407357D+00 0.248136D+00 -0.829156D-02 -0.611984D+00
59 0.172071D+00 -0.283805D+00 -0.409872D+00 -0.361421D-01 -0.109967D+01
60 0.194660D+01 -0.524416D+00 -0.483053D-01 -0.230293D+00 -0.285244D-01
61 -0.300605D+00 -0.170742D+00 -0.825952D-01 0.176683D+00 0.261228D-01
62 -0.492034D+00 0.954523D+00 -0.776485D+00 -0.226770D+00 -0.696944D+00
63 0.284164D+00 -0.600329D+00 -0.178818D+00 -0.634480D+00 -0.214197D+00
64 0.120928D+01 0.117217D+00 0.414856D+00 -0.154097D+00 -0.292840D+00
65 0.648160D+00 -0.158682D+00 0.505199D-01 0.397353D+00 0.258181D+00
66 0.193565D+01 -0.364939D+00 -0.110510D+00 -0.146608D+00 -0.822694D-02
21 22 23 24 25
21 -0.163455D+01
22 -0.903006D+00 -0.471276D+00
23 -0.289833D+01 -0.112004D+01 -0.122167D+01
24 -0.176736D+01 -0.102361D+01 -0.116493D+01 -0.759577D+00
25 -0.104551D+01 -0.104574D+01 -0.181036D+01 -0.638511D+00 -0.981281D+00
26 -0.453208D+00 -0.628363D+00 -0.536424D+00 -0.264521D+01 -0.482720D+00
27 -0.435228D+00 -0.881245D+00 -0.472248D+00 -0.373183D+00 0.125667D+01
28 -0.120910D+01 -0.328075D+00 -0.191509D+00 -0.110954D+01 -0.921614D+00
29 -0.274271D+00 0.121632D-01 -0.240497D+00 -0.429982D+00 -0.449309D+00
30 -0.200893D+01 -0.428899D-01 -0.911692D+00 -0.907900D+00 -0.760419D+00
31 -0.390786D+00 -0.805791D+00 -0.425890D+00 -0.422393D-01 0.203321D-01
32 -0.142323D+01 0.135182D+01 -0.128578D+01 -0.118414D+01 -0.614795D+00
33 -0.114906D+01 -0.406960D+00 0.185616D+00 -0.763603D-01 -0.515246D+00
34 -0.113282D+01 -0.779767D+00 -0.500504D+00 -0.100727D+01 -0.807521D+00
35 -0.184844D+00 -0.903042D-01 -0.328946D+00 0.128307D+00 0.552236D-01
36 -0.170980D+01 0.398350D-01 -0.155866D+01 -0.811661D+00 0.360253D+00
37 -0.272882D+01 -0.116930D+00 -0.339449D+01 -0.111225D+01 0.580184D+00
38 0.774940D-01 -0.126002D+01 0.586734D+00 -0.709973D+00 0.185615D+00
39 0.118370D+01 -0.141960D+01 -0.656304D+00 -0.327827D+00 -0.196111D+00
40 0.103776D+00 -0.113741D+01 -0.757859D+00 0.102859D+00 -0.881227D+00
41 -0.675201D+00 -0.497946D+00 -0.983469D+00 -0.114049D+01 -0.316266D+00
42 -0.940865D+00 -0.334301D+00 -0.397340D+00 -0.418786D+00 0.357469D+00
43 -0.387717D+00 0.481876D+00 -0.607954D-01 -0.231009D+00 -0.102876D+01
44 -0.124153D+00 0.358180D-01 0.137002D+00 0.103231D+00 -0.488654D+00

45 0.217413D-01 -0.275121D+00 -0.122337D-01 0.827989D+00 0.221685D+00
46 -0.370050D+00 -0.737937D+00 -0.320745D+00 -0.336217D+00 -0.751649D+00
47 -0.332499D+00 -0.634473D+00 -0.256532D+00 -0.562483D+00 -0.259243D+00
48 -0.114366D+01 -0.952794D+00 -0.900046D+00 -0.340880D+00 -0.373612D+00
49 -0.316202D+01 -0.318884D+00 -0.279090D+00 -0.286812D+00 0.132487D+01
50 -0.404183D+00 -0.116390D+01 -0.232825D+00 0.892965D+00 -0.241391D+00
51 -0.539654D+00 -0.391022D+00 -0.164437D+00 -0.163475D+00 -0.296773D+00
52 -0.369854D+00 0.180846D+00 -0.474027D+00 0.157497D-01 0.279247D+00
53 -0.102883D+01 -0.144796D+00 -0.403917D+00 -0.452568D+00 0.603696D+00
54 -0.488391D+00 -0.258601D+00 -0.343211D+00 -0.309143D+00 0.364598D-01
55 -0.300651D+00 0.188425D+00 -0.510743D+00 -0.412419D+00 -0.493816D+00
56 0.974100D+00 -0.351296D-01 -0.394294D+00 -0.457346D+00 -0.396565D-01
57 0.971492D+00 -0.684855D+00 0.665605D-01 -0.625585D+00 0.729433D-01
58 -0.511555D+00 -0.114506D+00 0.985002D+00 -0.769421D+00 0.223158D+00
59 -0.343444D+00 -0.358720D-01 -0.511797D+00 -0.173011D-01 -0.113620D+00
60 -0.135988D+01 0.168699D+00 -0.801939D+00 -0.125913D+01 -0.685489D+00
61 -0.117381D+00 -0.189485D+00 -0.118499D+00 0.976479D-01 0.564724D-01
62 0.277011D+01 0.958713D+00 -0.482170D+00 -0.648044D+00 0.275992D+00
63 -0.441097D+00 -0.441334D+00 -0.288063D+00 -0.543468D+00 -0.570740D+00
64 -0.431650D+00 0.941691D-01 0.101492D+00 0.240127D-01 0.670603D-01
65 -0.194817D+00 -0.294099D+00 0.577972D+00 0.616024D-01 0.231077D-01
66 -0.288419D+00 0.170738D+00 0.940746D+00 0.971306D-01 0.507688D+00
        26   27   28   29   30
26 -0.124212D+01
27 -0.787015D+00 0.385896D+01
28 -0.432258D+00 0.167914D+00 -0.150176D+00
29 -0.388635D+00 0.223449D+01 0.578778D+00 0.393624D+00
30 0.463184D-01 -0.105318D+00 -0.587265D+00 0.816420D+00 -0.288938D+00
31 -0.439956D+00 0.234013D+01 0.765912D+00 0.365489D+00 -0.759431D-01
32 -0.250738D+00 -0.570626D+00 -0.385394D+00 0.585638D+00 -0.383539D-01
33 -0.255186D+00 -0.963473D-01 -0.254755D+00 0.443512D+00 0.843848D+00
34 -0.978825D+00 -0.643268D-01 -0.549751D+00 -0.186967D+00 -0.249397D+00
35 0.135391D+01 0.107095D+01 0.395847D-01 0.115359D+01 -0.380815D+00
36 0.540764D-01 0.237974D-02 0.446664D-01 0.442027D+00 -0.178569D+00
37 -0.232163D+00 0.125297D+00 0.387771D+00 0.472752D+00 -0.125795D+00
38 -0.106237D+00 -0.139440D+01 -0.759338D-01 -0.104366D+01 -0.397342D+00
39 -0.106734D+01 0.625024D+00 -0.588832D-01 0.747419D-02 -0.456327D-01
40 -0.785771D+00 0.214260D+00 -0.471087D+00 -0.821261D-01 -0.178770D+00
41 -0.936982D+00 -0.227734D+00 -0.614763D+00 -0.560845D+00 -0.735219D+00
42 -0.594957D+00 0.110767D+01 -0.928647D+00 -0.676361D-01 -0.269346D+00
43 -0.375766D+00 -0.285570D+00 -0.505906D+00 0.199538D+00 -0.807381D+00
44 -0.173909D+00 -0.188082D+00 -0.394718D+00 0.568506D+00 -0.115054D+01
45 -0.827735D+00 0.726703D+00 -0.133856D+00 0.779146D+00 -0.114091D+00
46 -0.153298D-01 0.912024D+00 -0.301830D+00 -0.216174D+00 0.807856D-01
47 -0.366476D+00 0.511574D+00 -0.560784D-01 0.508701D+00 0.590342D-01
48 -0.832592D+00 -0.161751D+00 0.231908D-01 -0.399221D+00 -0.357072D+00

49 0.216736D-01 0.217189D+00 -0.907960D-02 0.616470D+00 0.989481D+00
50 -0.486329D+00 0.400922D+00 -0.179177D+00 -0.237016D+00 0.279944D+00
51 -0.104048D+00 0.267029D+00 0.362445D+00 0.123036D-01 -0.179411D+00
52 -0.162756D+00 0.400383D+01 0.124750D+00 0.322351D+00 0.231680D+00
53 -0.395282D+00 0.173560D+00 -0.412307D+00 -0.337267D+00 -0.162969D+00
54 -0.263698D-01 0.225312D+01 0.511761D-01 0.491661D+00 0.152128D+00
55 -0.407176D+00 -0.200708D+00 -0.437490D+00 -0.453265D+00 -0.128110D+00
56 0.327010D-01 0.171628D+00 -0.207623D+00 0.305781D-01 -0.287899D-01
57 -0.284921D+00 -0.206431D+00 -0.147569D+00 -0.491479D-01 0.422681D-01
58 -0.234277D+00 0.697070D-01 -0.486796D+00 -0.394894D+00 -0.719146D+00
59 0.126777D+01 0.610919D+00 -0.732958D-01 -0.547488D-01 -0.617967D-01
60 0.163641D+00 -0.192247D+00 -0.346793D+00 0.361370D-01 -0.615577D+00
61 -0.334945D+00 0.589245D-01 -0.164109D-01 0.641131D-01 -0.168793D+00
62 -0.385728D+00 0.258622D+00 0.156444D+00 -0.974636D-01 -0.663295D+00
63 -0.213511D+00 -0.181479D+01 -0.346746D+00 -0.208941D+00 -0.662203D+00
64 0.309116D+00 0.192152D+00 0.525176D+00 0.344148D+00 0.243718D+00
65 0.329158D+00 -0.674903D-01 0.615594D+00 0.501142D+00 0.238557D+00
66 0.685851D+00 0.213706D+00 0.111704D+01 0.637591D+00 0.100999D+00

	31	32	33	34	35
31	0.311704D+00				
32	0.173054D+00	-0.372119D+00			
33	0.435191D-01	-0.119874D+01	-0.672225D+00		
34	-0.448224D+00	0.176340D-02	-0.390595D+00	-0.224707D+00	
35	-0.806306D+00	0.431615D+00	0.778549D+00	-0.519424D-01	0.405994D+02
36	-0.466809D-01	-0.730497D+00	-0.359744D-01	-0.219979D+01	0.851306D+00
37	-0.107057D+00	-0.570492D+00	0.203245D+00	-0.118334D+01	0.168885D+00
38	-0.137169D+00	-0.179099D+00	0.180237D-01	0.161887D+00	0.985256D+00
39	-0.118851D+00	-0.205607D+00	-0.124857D+00	-0.640470D+00	0.169392D+02
40	0.432712D-01	-0.181280D+00	-0.479283D+00	-0.228404D+00	0.126413D+00
41	-0.211003D+00	-0.114547D+01	0.620282D-01	-0.327241D+00	0.451874D+02
42	-0.117277D+00	-0.527820D+00	-0.249565D+00	-0.821796D-02	0.484039D+00
43	-0.166387D+00	-0.400513D+00	-0.466945D-01	-0.423194D+00	0.576816D+01
44	-0.343163D-02	-0.525986D+00	-0.906282D+00	-0.295044D+00	0.147981D+01
45	0.581356D+00	-0.378677D+00	-0.103161D+00	-0.263405D+00	0.131911D+02
46	-0.385811D-01	-0.262605D+00	0.509467D-01	0.610663D+00	0.134161D+00
47	-0.479751D+00	-0.436739D+00	-0.891240D+00	-0.495275D+00	0.799055D+01
48	0.572300D+00	-0.360008D+00	-0.123495D+00	-0.388161D+00	-0.499133D-01
49	-0.142315D+00	-0.750791D+00	-0.848256D+00	-0.506519D+00	0.304372D+01
50	-0.338287D+00	-0.161408D+00	-0.366744D+00	0.100453D+00	0.329905D+01
51	0.185989D+01	0.262083D+00	0.227647D+00	-0.112756D+00	-0.645400D-01
52	-0.161192D+01	0.931037D+00	-0.194406D+00	-0.193669D+00	0.331429D+00
53	-0.947197D-01	-0.166817D+01	0.155206D+01	-0.128374D+01	0.775813D+01
54	0.730353D+00	-0.401082D-01	0.299502D+00	0.985236D+00	0.266658D+00
55	-0.148981D+00	-0.460735D+00	-0.311348D+00	0.661360D-01	0.195917D+01
56	0.570345D+00	-0.315648D+00	0.486092D-01	-0.352672D+00	0.251890D+00
57	-0.612814D+00	-0.215626D-01	0.259035D+01	-0.936193D+00	0.183216D+02

58 0.172456D+00 -0.542120D+00 -0.336239D+00 -0.934904D+00 0.106252D+00
59 0.387697D+00 0.229202D+00 -0.175142D+00 0.332810D+00 0.143886D+00
60 0.462746D+00 0.629120D+00 0.322448D+00 0.418267D+00 0.208675D+00
61 0.209401D+00 0.111560D+00 0.282002D-01 0.804328D-01 0.473772D+01
62 0.353447D+00 -0.175791D+01 -0.742894D-01 -0.896781D-01 0.205540D+00
63 -0.925720D+00 -0.391248D+00 0.412038D+00 -0.145243D+00 -0.514964D+00
64 -0.579662D+00 0.382175D+00 0.195253D+00 0.138630D+00 0.693927D+00
65 0.126397D+00 0.485326D+00 0.110635D+00 0.473015D+00 0.143534D+01
66 -0.853257D+00 0.142148D+00 0.202931D+01 0.446904D+00 0.225373D+01
36 37 38 39 40
36 0.640297D+01
37 0.955432D+01 -0.444763D+00
38 0.234475D+01 0.738341D+01 0.371540D+02
39 -0.408932D-01 -0.351803D+00 0.596918D+00 -0.466978D+00
40 -0.118032D+01 -0.165268D+01 -0.162374D+00 -0.230204D+00 0.119046D+00
41 0.149382D+01 0.438519D+01 0.363307D+02 0.122257D+02 -0.733410D+00
42 -0.128620D+00 -0.239222D+00 -0.913867D-01 -0.453267D+00 -0.145096D+01
43 0.459764D+01 0.601519D+01 0.131703D+02 -0.320226D+00 -0.598396D+00
44 0.109968D+02 0.879433D+01 0.398965D+01 -0.851323D+00 -0.531923D+00
45 0.134912D+01 0.350339D+01 0.196753D+02 0.341564D+01 -0.276236D+00
46 0.113122D+00 -0.129961D+00 0.398329D+00 -0.237382D+00 0.510173D+00
47 0.456235D+01 0.303299D+01 0.951321D+00 -0.525671D+01 -0.562350D+00
48 -0.366081D+00 -0.491944D+00 -0.159124D+00 -0.479920D+00 -0.148288D+00
49 0.120576D+02 0.935814D+01 0.192273D+01 0.347376D+00 -0.645580D+00
50 0.115960D+01 0.186332D+01 0.118626D+02 0.971791D+00 -0.194360D+00
51 -0.629017D-01 -0.105058D+00 -0.947909D-01 -0.392658D+00 -0.342600D+00
52 -0.515122D+00 -0.754112D+00 -0.313726D+00 -0.221919D+00 -0.313408D+00
53 0.196388D+01 0.166482D+01 0.531500D+00 -0.190063D+00 -0.264317D+00
54 -0.360363D+00 -0.544073D+00 -0.420448D+00 0.766899D-02 -0.152691D+00
55 0.856264D+00 0.520359D+00 0.104755D+02 -0.284163D+00 -0.534391D-01
56 -0.401107D+00 -0.566656D+00 -0.662422D+00 -0.241056D+00 -0.133025D+01
57 0.388948D+00 0.380133D+00 0.143189D+01 0.155524D+00 0.305264D+00
58 -0.472208D+00 -0.752005D+00 -0.386027D+00 -0.489222D+00 -0.688728D+00
59 -0.114915D+01 -0.172917D+01 -0.133091D+00 -0.278529D+00 0.395208D+00
60 -0.903190D+00 -0.421198D+00 0.503276D+01 -0.259540D+00 0.702874D+00
61 0.109503D+01 0.821393D+00 0.325207D+01 0.375425D+00 0.282607D+00
62 -0.923026D+00 -0.162049D+01 -0.671807D+00 -0.149274D+00 -0.254822D+00
63 -0.125652D+00 -0.432702D+00 -0.696387D+00 -0.222620D+01 -0.341306D+00
64 0.539150D-02 -0.126580D+01 0.857593D+00 -0.102544D+01 0.250267D+00
65 0.446966D+00 -0.148456D+01 0.611714D+00 -0.146723D+00 0.164348D+01
66 -0.432613D+01 -0.789806D+01 -0.955357D-01 0.298804D-01 -0.106092D+01
41 42 43 44 45
41 0.442385D+02
42 -0.333929D+00 0.526115D-01
43 0.124156D+02 -0.505932D+00 0.141627D+01
44 0.199782D+01 -0.226851D+00 0.573331D+01 0.553331D+01

45 0.234706D+02 -0.665128D+00 0.468624D+01 0.274412D+01 0.217374D+01
46 -0.581976D+00 0.167205D+00 -0.819232D-01 0.276861D-01 -0.379313D+00
47 0.927117D+01 -0.569556D+00 -0.682904D+00 0.236971D+01 0.146978D+01
48 -0.819074D+00 0.160188D+00 -0.328750D+00 -0.523231D-01 -0.174978D+00
49 0.379667D+01 -0.372555D+00 0.174298D+01 0.983537D+01 0.788762D+00
50 0.147754D+02 -0.106966D+01 0.986459D+00 0.710138D+00 0.417841D+01
51 -0.875560D+00 -0.156389D+00 -0.305332D+00 0.773714D-01 -0.915433D-01
52 -0.629183D+00 0.535387D+00 -0.440212D+00 -0.593993D-01 -0.415781D+00
53 0.604934D+01 -0.677629D+00 0.964001D+00 -0.117280D+01 0.157403D+01
54 -0.548382D+00 0.873660D-01 -0.562910D+00 -0.218667D+00 -0.247124D+00
55 0.794395D+01 -0.503662D+00 -0.109449D+01 0.509252D+00 0.128964D+01
56 -0.608708D+00 -0.508917D+00 -0.428714D+00 -0.114021D+00 -0.417844D+00
57 0.729450D+01 0.536636D+00 0.200651D+00 0.114065D+00 0.190682D+01
58 -0.727158D+00 -0.604820D+00 -0.525730D+00 -0.198249D+00 0.381157D-02
59 -0.745363D+00 0.692688D+00 -0.191584D+00 0.940196D-01 0.168425D+00
60 0.124843D+00 -0.316759D+00 -0.812570D+00 0.400770D+00 -0.397556D+00
61 0.126057D+01 -0.148685D+00 0.156787D+00 -0.122916D+00 0.101639D+01
62 -0.140488D+01 -0.136369D+00 -0.503585D+00 0.130765D+00 -0.239040D+00
63 -0.148250D+01 -0.119677D+01 -0.340206D+01 -0.918574D+00 -0.680669D+01
64 0.296395D+00 0.496309D+00 -0.727184D+00 0.269582D+00 0.498565D+00
65 -0.788106D+01 0.437253D+00 -0.963855D+00 0.108666D+01 -0.139585D+01
66 0.148852D+01 0.672131D+00 -0.292121D+01 -0.126312D+01 -0.504231D+00

	46	47	48	49	50
46	-0.130892D+00				
47	-0.136390D+00	0.192985D+00			
48	0.765947D+00	-0.394796D+00	-0.713625D-01		
49	0.141896D+00	0.512764D+01	0.755871D-01	0.412537D+01	
50	-0.179982D+00	0.912476D+00	-0.178404D+00	0.913420D+00	0.447118D-01
51	-0.355440D-01	-0.343068D+00	0.139651D+00	0.239616D+00	-0.180081D+00
52	0.279886D+00	-0.402825D+00	-0.511822D-01	-0.100188D+00	-0.148071D+00
53	-0.293864D+00	0.115356D+01	-0.994247D-01	-0.305182D+00	0.720322D-01
54	0.173768D+00	-0.351895D+00	0.841063D-01	-0.288685D+00	-0.377656D+00
55	-0.431011D+00	-0.311697D+00	-0.438288D+00	-0.939527D-01	0.417961D+00
56	-0.520770D+00	-0.352109D+00	-0.324373D+00	-0.168789D+00	-0.222859D+00
57	0.104176D+00	0.136452D+01	0.166703D+00	0.546875D+00	0.234559D+00
58	-0.628176D-01	-0.368164D+00	-0.472094D+00	-0.174682D+00	-0.147550D+00
59	-0.233027D+00	-0.277956D+00	-0.533068D-01	0.680970D-01	-0.308660D+00
60	-0.316480D+00	-0.392332D+00	-0.334761D+01	-0.114915D+01	-0.546984D+00
61	-0.173794D+00	0.822521D+00	0.667410D+00	-0.198408D+00	0.786522D+00
62	-0.274630D+00	-0.438472D+00	0.208166D+00	-0.101174D-01	-0.223035D+00
63	-0.568252D+00	-0.139822D+01	-0.184045D+00	-0.688022D+00	0.858321D+00
64	0.886158D-01	-0.834682D+00	0.173423D+00	0.939395D+00	0.102188D+01
65	0.576190D+00	-0.354651D+00	0.473981D+00	0.122812D+01	0.562532D+00
66	0.437738D+00	-0.779412D+00	-0.486348D+00	-0.116300D+00	-0.116723D+01

	51	52	53	54	55
51	0.226642D+00				

```
52  0.172274D+00  0.733389D+00
53 -0.139834D+00 -0.333102D+00  0.699283D+00
54  0.306839D+00  0.370524D+00 -0.218525D-01  0.129058D+00
55 -0.396813D+00 -0.550846D+00  0.600093D+00 -0.804339D+00  0.410778D+00
56 -0.511772D+00  0.266668D+00 -0.531662D-01  0.575346D-01 -0.201673D+00
57  0.104926D+00 -0.207074D+00 -0.571941D+00  0.261284D+00  0.865131D-01
58 -0.265573D-01  0.530308D-02  0.187207D+00 -0.559566D-01 -0.544550D+00
59  0.805897D-01  0.229920D+00  0.218673D+00  0.136582D+00 -0.596248D-01
60 -0.364407D-01  0.172943D+00 -0.143501D+00  0.826873D-01 -0.409296D+00
61  0.187554D+01  0.114143D+00  0.103988D+01 -0.606141D+00  0.967512D+00
62  0.843329D-02  0.189060D+00  0.371128D+00  0.353588D+00 -0.851666D+00
63 -0.508910D+00 -0.927835D+00 -0.143803D+01 -0.419105D+00 -0.200156D+01
64 -0.101818D-01 -0.176583D+00  0.622955D+00  0.654288D+00  0.107358D+01
65 -0.166432D-01  0.578140D-01  0.135856D+01  0.226566D+00  0.109006D+01
66 -0.282415D+00  0.254295D+00 -0.754787D+00  0.333861D+00  0.623202D+01
       56          57          58          59          60
56 -0.200100D+00
57  0.309794D+00  0.123124D+01
58 -0.466628D+00  0.778866D+00 -0.189215D+00
59  0.130107D+00  0.722946D+00 -0.136088D+00  0.810439D-01
60 -0.833950D+00 -0.133773D+00 -0.160312D+01 -0.536145D+00  0.133366D+01
61  0.610322D-01  0.164766D+01 -0.775363D+00  0.371025D+00 -0.167033D+00
62 -0.826017D-01  0.849192D+00 -0.568830D+00  0.189313D-01 -0.301291D-01
63 -0.102893D+01 -0.501500D+00 -0.545028D+00 -0.102587D+01 -0.113886D+01
64 -0.323377D+00  0.127520D+01 -0.735250D+00 -0.176934D+00  0.497567D+00
65  0.344602D+00  0.287657D+01  0.492740D+00  0.816200D+00  0.165183D+00
66 -0.289195D+00  0.309762D+01 -0.803803D+00  0.812496D+00 -0.459665D+01
       61          62          63          64          65
61  0.331921D+00
62 -0.235734D+00 -0.705638D-01
63 -0.567138D+00 -0.181301D+01 -0.218211D+01
64  0.173813D+01 -0.447162D+00 -0.154316D+01  0.465802D+00
65  0.197583D+01  0.191625D+00 -0.415590D+00  0.374831D+01  0.151326D+01
66 -0.156745D+01  0.124727D+01 -0.687452D+01  0.521465D+01  0.169092D+01
       66
66  0.250020D+01
```

VITA

Jason Sandwisch was born in Vancouver, Washington in 1994. His family moved around until settling in Banks, Oregon, a small town in the suburbs of Portland, Oregon. Jason attended school in Banks until high school where he enrolled at Liberty High School in Hillsboro, where he graduated as a Salutatorian in 2013. Jason enrolled the following academic year at Oregon State University, having received the merit based academic achievement scholarship and chose to major in Chemistry. In the winter of 2014, he received the Undergraduate Research, Scholarship and the Arts engagement grant which funded his academic research with emeritus professor Kenneth Hedberg. While studying with Professor Hedberg Jason performed gas phase electron diffraction experiments, analyzed data and performed density functional theory Gaussian calculations. Jason continued to work with professor Hedberg throughout his time at Oregon State University. Later, collaborating with Professor Joseph Nibbler, Jason published 3 research articles with professor Hedberg. Also, during his time at Oregon State University, Jason worked in the materials science laboratory of Professor John Simonsen being responsible for the development of plant based biodegradable plastic and development of a UV curing resin to be used for digital light processing (DLP) 3D printing.

Jason received acceptance into the Ph.D. chemistry program at the University of Washington in the winter of 2017, upon which he joined Professor Chong Fang's femtosecond stimulated Raman spectroscopy group at Oregon State University. Jason's contributions with Professor Fang's group were published 2020. Jason graduated from Oregon State University in the summer of 2017 with a A.C.S. certified Bachelor of Science degree in Chemistry having received summa cum laude honors. Following graduation, Jason moved to Seattle and joined Professor Munira Khalil's research group where he conducted and developed ultrafast electronic vibrational spectroscopy to aid in the research and understanding of photoinduced excited state chemical reactions. In March of 2019 Jason received his Masters of Science degree in Chemistry from the University of Washington. In July 2023 Jason successfully defended his Ph. D. work. Jason married Jill Fenno in September of 2022 and they currently reside in Issaquah, Washington.